Elastocaloric Microcooling

Zur Erlangung des akademischen Grades eines
Doktors der Ingenieurwissenschaften
(Dr.-Ing.)

bei der Fakultät für Maschinenbau
des Karlsruher Instituts für Technologie (KIT)

genehmigte
DISSERTATION

von

Dipl.-Ing. Hinnerk Oßmer

To my parents

Abstract

Today, cooling or heat pumping is predominantly performed using two major technologies. Large-scale and household applications are mostly based on vapor compression, reaching high efficiencies but on the other hand promoting global warming due to the used refrigerants. Cooling on a small scale, as it is required, e.g., in power electronics, medicine, chemical and biological analysis, is often peformed by minaturization-compatible thermoelectric cooling, which is however rather in-efficient.

For these reasons, the search for energy-efficient, 'green' alternatives has recently lead to increased interest in solid-state cooling based on caloric effects. Among these, the elastocaloric effect exhibits particularly high temperature changes and material-level coefficients of performance (COP) exceeding 80% of the thermodynamic maximum. It is mechanically driven and based on a fully reversible first order phase transformation in pseudoelasic shape memory alloys (SMA). The aim of this thesis is to explore the potential of the elastocaloric effect for small-scale or 'microcooling' applications, making use of a favorable scaling behavior: On the one hand, transported heat per cooling cycle is directly proportional to the volume of elastocaloric material. On the other hand, surface-to-volume ratios increase upon miniaturization and may be further increased by using thin geometries, which leads to improved heat transfer.

In the first part of this work, suitable materials for elastocaloric microcooling are identified. The main challenges are the elastocaloric temperature change, mechanical performance and cyclic stability of the material. In addition, localized (Lüders-like) transformation behavior has to be considered. Several elastocaloric SMA materials are characterized by uniaxial tensile tests in combination with infrared thermography and digital image correlation. Thin geometries are selected for optimum heat transfer, which are at least ten times thinner than those in previous literature reports. Among the investigated materials, cold-rolled $30\,\mu\mathrm{m}$ thick $\mathrm{Ti}_{49.1}\mathrm{Ni}_{50.5}\mathrm{Fe}_{0.4}$ foils exhibit the highest elastocaloric temperature changes of $+20/-17\,\mathrm{K}$. The highest material COP of 15 is achieved by $20\,\mu\mathrm{m}$ thick sputter-deposited $\mathrm{Ti}_{55}\mathrm{Ni}_{29.6}\mathrm{Cu}_{12.6}\mathrm{Co}_{2.8}$ films. The slightly reduced elastocaloric temperature change of $+9/-12\,\mathrm{K}$ is compensated by a very narrow hysteresis. Furthermore, the films exhibit an extraordinary fatigue resistance due to a special microstructure. In both types of samples, rate-dependend formation and propagation of sharp temperature bands is shown to be closely related to Lüders-like strain bands. Under adiabatic conditions, a dense network of temperature bands occurs, leading to homogeneous temperature distribution after short equalization

time. Thermo-mechanical sample performance is closely reproduced in finite element simulation using a Tanaka-type phenomenological model.

The second part of the thesis is dedicated to the development of first-of-its-kind demonstrators for elastocaloric microcooling. A concept is introduced, in which SMA film and foil bridges are deflected out-of-plane in order to induce the elastocaloric effect. In contrast to other elastocaloric prototypes, only a single linear actuator is required and no fluids are involved. Heat transfer between the SMA and a solid heat sink and source is achieved by heat conduction in direct contact. Work recovery is implemented by coupling two SMA bridges to form an antagonistic pair. Devices are operated following an inverse Brayton cycle at frequencies up to $0.75\,\mathrm{Hz}$ due to limitations of the actuator. The highest temperature lift of $9.4\,\mathrm{K}$ is achieved using $\mathrm{Ti}_{49.1}\mathrm{Ni}_{50.5}\mathrm{Fe}_{0.4}$ foil bridges. Lumped-element simulation indicates that higher temperature lifts may be reached at higher operating frequencies. The highest specific cooling power of $5.1\,\mathrm{W\,g^{-1}}$ is reached using sputter-deposited $\mathrm{Ti}_{49.6}\mathrm{Ni}_{50.4}$ films. Device-level COPs are in the order of 3.

The results show that efficient elastocaloric cooling may be achieved by an entirely solid-state based approach using thin SMA foils and films. The presented approach is targeted at microcooling, but may also be used for meso-scale applications by massive parallelization in distributed device arrays.

Kurzfassung

Die meisten heutzutage verwendeten makroskopischen Kühlgeräte und Wärmepumpen sind Kompressionskältemaschinen mit recht hohen Wirkungsgraden, die aufgrund der verwendeten Kühlmittel jedoch zur globalen Erwärmung beitragen. Für die lokale Kühlung, z.B. in Leistungselektronik, Medizintechnik, chemischer und biologischer Analyse, werden wegen ihrer Miniaturisierbarkeit oft thermoelektrische Elemente verwenden. Deren Wirkungsgrad ist allerdings eher gering.

Aus diesen Gründen hat die Suche nach effizienten, 'grünen' Alternativen in jüngerer Zeit Festkörperkühltechnologien in den Fokus gerückt, die auf kalorischen Effekten basieren. Dabei ermöglicht insbesondere der elastokalorische Effekt besonders hohe Temperaturänderungen und materialseitige Wirkungsgrade (COP) von über 80% des thermodynamisch Möglichen. Der Effekt ist mechanisch getrieben und basiert auf einer Phasenumwandlung erster Ordnung in Formgedächtnislegierungen (FGL). Ziel dieser Arbeit ist es, das Potential des elastokalorischen Effekts für Miniaturanwendungen oder 'Mikrokühlung' zu untersuchen. Dabei wird das vorteilhafte Skalierungsverhalten des Effekts genutzt: Zum einen ist die transportierte Wärmemenge pro Kühlzyklus direkt proportional zum Volumen des elastokalorischen Materials. Zum anderen nimmt bei der Miniaturisierung das Oberfläche-zu-Volumen-Verhältnis zu und lässt sich durch die Wahl dünner Geometrien noch weiter steigern, was der effektiven Wärmeübertragung zugute kommt.

Im ersten Teil der Arbeit werden geeignete Materialen für elastokalorische Mikrokühlung identifiziert. Die wichtigsten Herausforderungen sind dabei die elastokalorische Temperaturänderung, das mechanische Verhalten sowie die zyklische Stabilität des Materials. Daneben spielt lokalisiertes (Lüders-artiges) Transformationsverhalten eine Rolle. Verschiedene elastokalorische FGL-Materialien werden in Zugversuchen in Kombination mit Infrarot-Thermographie und digitaler Bildkorrelation untersucht. Um eine effektive Wärmeübertragung zu gewährleisten, werden Proben mit dünner Geometrie ausgewählt, die weniger als ein Zehntel der Dicke von bisher in der Literatur beschriebenen Materialien aufweisen. Unter den untersuchten Materialien zeigen kaltgewalzte $Ti_{49.1}Ni_{50.5}Fe_{0.4}$-Folien der Dicke $30\,\mu m$ den größten Heiz-/Kühleffekt von $+20/-17\,K$. Die höchste Materialeffizienz von 15 wird mit gesputterten $Ti_{55}Ni_{29.6}Cu_{12.6}Co_{2.8}$-Filmen der Dicke $20\,\mu m$ erreicht. Der etwas geringere elastokalorische Effekt von $+9/-12\,K$ wird in diesem Material durch eine sehr schmale mechanische Hysterese ausgeglichen. Zudem sind die Filme aufgrund einer speziellen Mikrostruktur außergewöhnlich

ermüdungsarm. Für beide Proben wird gezeigt, dass die ratenabhängige Ausbildung scharfer Temperaturbänder eng mit Lüders-artigen Dehnungsbändern zusammenhängt. Unter adiabatischen Bedingungen bildet sich ein dichtes Netzwerk von Temperaturbändern, das innerhalb kurzer Zeit zu einer homogenen Temperaturverteilung verläuft. Das thermo-mechanische Probenverhalten wird in Finite-Element-Simulationen mit einem phänomenologischen Tanaka-Modell nachgebildet.

Der zweite Teil der Arbeit beschäftigt sich mit der Entwicklung neuartiger Demonstratoren zur elastokalorischen Mikrokühlung. Es wird ein Konzept vorgestellt, in dem freistehende Brücken aus FGL-Film/Folie aus der Ebene heraus ausgelenkt werden, um den elastokalorischen Effekt zu induzieren. Im Vergleich zu anderen elastokalorischen Prototypen wird für den Betrieb nur ein einziger Linearmotor benötigt und das Konzept kommt ohne Flüssigkeiten aus. Der Wärmetransport zwischen der FGL und einer festen Wärmequelle und -senke erfolgt über Wärmeleitung im direkten Kontakt. Durch das Koppeln zweier Brücken zu einem antagonistischen Paar wird in jedem Operationszyklus mechanische Arbeit zurückgewonnen. Die Demonstratoren werden entsprechend einem thermodynamischen Brayton-Zyklus betrieben, die Frequenz ist durch den verwendeten Aktor auf etwa $0.75\,\mathrm{Hz}$ beschränkt. Der höchste Temperaturhub von $9.4\,\mathrm{K}$ wird mit $\mathrm{Ti}_{49.1}\mathrm{Ni}_{50.5}\mathrm{Fe}_{0.4}$-Folien erreicht, die höchste spezifische Kühlleistung von $5.1\,\mathrm{W}\,\mathrm{g}^{-1}$ mit gesputterten $\mathrm{Ti}_{49.6}\mathrm{Ni}_{50.4}$-Filmen. Leistungszahlen (COP) auf Geräteebene liegen in der Größenordnung von 3.

Diese Ergebnisse zeigen, dass effizientes elastokalorisches Kühlen in einem vollständig festkörperbasierten Ansatz mit dünnen FGL-Folien und Filmen erreicht werden kann. Das vorgestellte Konzept ist auf Mikrokühlung ausgerichtet, kann durch massive Parallelisierung aber ebenso gut in mesoskopischen Anwendungen zum Einsatz kommen.

Publications

Parts of this thesis and related work have already been published

in scientific journals:

- **H. Ossmer**, F. Lambrecht, M. Gültig, C. Chluba, E. Quandt, and M. Kohl, "Evolution of temperature profiles in TiNi films for elastocaloric cooling", *Acta Materialia* **81** (2014) 9–20

- M. Gueltig, **H. Ossmer**, M. Ohtsuka, H. Miki, K. Tsuchiya, T. Takagi, and M. Kohl, "High Frequency Thermal Energy Harvesting Using Magnetic Shape Memory Films", *Advanced Energy Materials* **4** (2014) 1400751

- **H. Ossmer**, C. Chluba, M. Gueltig, E. Quandt, and M. Kohl, "Local Evolution of the Elastocaloric Effect in TiNi-Based Films", *Shape Memory and Superelasticity* **1**[2] (2015) 142–152

- C. Chluba, **H. Ossmer**, C. Zamponi, M. Kohl, and E. Quandt, "Ultra-Low Fatigue Quaternary TiNi-Based Films for Elastocaloric Cooling", *Shape Memory and Superelasticity* **2** (2016) 95–103

- **H. Ossmer**, C. Chluba, S. Kauffmann-Weiss, E. Quandt, and M. Kohl, "TiNi-based films for elastocaloric cooling – Fatigue life and device performance", *APL Materials* **4**[6] (2016) 064102

- **H. Ossmer**, F. Wendler, M. Gueltig, F. Lambrecht, S. Miyazaki, and M. Kohl, "Energy-efficient minature-scale heat pumping based on shape memory alloys", *Smart Materials and Structures* **25** (2016) 085037

- **H. Ossmer**, and M. Kohl, "Stretch to actively cool", *Nature Energy* **1**[10] (2016) 16159   *(News&Views article)*

- M. Gueltig, F. Wendler, **H. Ossmer**, M. Ohtsuka, H. Miki, T. Takagi, and M. Kohl, "High Performance Thermomagnetic Generation based on Heusler Alloy Films", *Advanced Energy Materials* (2016) 1601879

in conference proceedings:

- **H. Ossmer**, C. Chluba, B. Krevet, E. Quandt, M. Rohde, and M. Kohl, "Elastocaloric cooling using shape memory alloy films", *Journal of Physics: Conference Series* **476** (2013) 012138

- M. Gueltig, **H. Ossmer**, M. Ohtsuka, H. Miki, K. Tsuchiya, T. Takagi, and M. Kohl, "Thermomagnetic actuation by low hysteresis metamagnetic Ni-Co-Mn-In films", *Materials Today: Proceedings* **2S** (2015) S883–S886 *(peer-reviewed)*

- **H. Ossmer**, S. Miyazaki, and M. Kohl, "The elastocaloric effect in TiNi-based foils", *Materials Today: Proceedings* **2S** (2015) S971–S974 *(peer-reviewed)*

- **H. Ossmer**, S. Miyazaki, and M. Kohl, "Elastocaloric heat pumping using a shape memory foil device", *Proceedings of the 18th International Conference on Solid-State Sensors, Actuators and Microsystems (TRANSDUCERS)* (2015) 726–729

as conference contributions (presented by myself):

- **H. Ossmer**, C. Chluba, B. Krevet, E. Quandt, M. Rohde, and M. Kohl, "Elastocaloric Cooling using Shape Memory Alloy Films", *The 13th International Conference on Micro and Nanotechnology for Power Generation and Energy Conversion Applications (PowerMEMS)*, December 3–6, 2013, London, UK *(oral presentation)*

- **H. Ossmer**, S. Miyazaki, and M. Kohl, "The Elastocaloric Effect in NiTi-based Foils", *International Conference on Martensitic Transformations (ICOMAT)*, July 6–11, 2014, Bilbao, Spain *(oral presentation)*

- **H. Ossmer**, F. Lambrecht, C. Chluba, E. Quandt, and M. Kohl, "Evolution of Temperature Profiles During NiTi-Film-Based Ferroelastic Cooling", *Materials Science and Engineering (MSE)*, September 23–25, 2014, Darmstadt, Germany *(poster presentation)*

- **H. Ossmer**, S. Miyazaki, E. Patoor, and M. Kohl, "Shape Memory Alloys for Solid-State Microcooling", *Energy, Science & Technology (EST) Kongress*, May 20–22, 2015, Karlsruhe, Germany *(poster presentation)*

- **H. Ossmer**, S. Miyazaki, and M. Kohl, "Elastocaloic Heat Pumping using a Shape Memory Alloy Foil Device", *The 18th International Conference on Solid-State Sensors, Actuators and Microsystems (Transducers)*, June 21–25, 2015, Anchorage, Alaska (USA) *(oral presentation)*

- **H. Ossmer**, C. Chluba, E. Quandt, and M. Kohl, "Elastocaloric Cooling by Ultra-Low Fatigue SMA Films", *European Symposium on Martensitic Transformations (ESOMAT)*, September 14–18, 2015, Antwerp, Belgium *(oral presentation)*

- **H. Ossmer**, S. Miyazaki, and M. Kohl, "Elastocaloric Micro Heat Pumping", *MRS Spring Meeting & Exhibit*, March 28 – April 1, Phoenix, Arizona (USA) *(oral presentation)*

Contents

Contents

1 Introduction

1.1 Motivation

In ancient times, humans had to rely on natural ressources of cold whenever they needed it, e.g., to cool beverages or preserve food. The Romans, for example, used to carry ice and snow from the mountains and stored it in special pits in the ground. Thanks to the tremendous technological evolution, today cooling is performed by machines, and whole industries as well as our every day life depend on them. The universal spread of refrigerators, air conditioners and the like, however, leads to an enormous energy consumption. To give an example, in the year 2013 the operation of cooling and air conditioning devices accounted for 38% of primary energy consumption in buildings of the United States of America [1]. Considering the technical advance and population growth in emerging countries like China, India or Brazil, the global energy consumption related to cooling applications will certainly increase further in the future. Hence, energy efficiency is a serious concern.

The vast majority of present-day cooling applications is based on vapor compression, in which a fluid refrigerant is repeatedly forced through a phase change between liquid and gas [2]. Due to its technical maturity, the efficiency of vapor compression – expressed by the coefficient of performance – reaches quite high values of up to 60% of the thermodynamic maximum, but many of the refrigerants are considered environmentally harmful or health-threatening and require special disposal.

Besides the above-mentioned macroscopic applications, many technical devices and applications require cooling and active temperature control on a small scale – referred to as *microcooling* in this thesis. In an ongoing trend of miniaturization, more functionality is achieved on a smaller space using less material. In terms of microelectronics, the enormous increase in functional density is described by the famous Moore's law, stating that the packing density of transistors is doubled every two years [3]. The high packing density, in turn, is associated with an increased heat dissipation density. In other applications, e.g., Lasers, Infrared and other detectors, in the bio-medical field and novel lab-on-chip systems, active local cooling and precise temperature control are required. Since vapor compression is too bulky for these applications, microcooling is partly realized by *passive* structures like heat pipes [4–6] and micro heat exchangers [7–10]. When *active* cooling is required, the choice often falls upon thermoelectric cooling. Research on the latter has made considerable progress in recent years and elements

with very small dimensions have become available. However, due to fundamental limitations related to the so-called figure of merit (ZT), as well as increasing parasitic heat flows in small dimensions, the energy efficiency of thermoelectric cooling is rather low [11].

The search for efficient, non-toxic and safe alternatives has recently drawn attention to a group of cooling technologies referred to as *ferroic cooling*, which are based on caloric effects in solid-state materials [12]. Very similar to vapor compression, cooling is performed by a refrigerant medium undergoing phase change. Only, in this case both of the involved phases are solid. In *elastocaloric cooling* – which is the topic of this thesis – the cooling process is driven by mechanical forces. The refrigerant is a *shape memory alloy* (SMA) like TiNi, which is commercially available, affordable and widely used in medical applications due to its bio-compatibility. On the material level, elastocaloric cooling may reach more than 80% of the Carnot efficiency, which is the theoretical maximum achievable by any heat pumping process [13].

The motivation of this work is to explore the feasibility of elastocaloric cooling or heat pumping for miniaturized applications. When this thesis was started in the year 2012, only one elastocaloric demonstrator was published worldwide. It has been developed at the University of Maryland and had the size of a car. However, due to a favorable scaling behavior (latent heat is proportional to volume), the elastocaloric effect is very well-suited for down-scaling. In addition, the increasing surface-to-volume ratio in small dimensions allows for more efficient heat transfer.

1.2 Objectives

The main objectives of this work are twofold: First, suitable materials for elastocaloric (micro-)cooling have to be identified and a profound understanding of their thermo-mechanical behavior has to be achieved by *material characterization*. The materials are fabricated and provided by cooperation partners and include TiNi-based, Cu-based and magnetic shape memory alloys. The elastocaloric effect, mechanical performance and local effects associated with strain band formation are studied by tensile tests combined with infrared thermography. In order to obtain a better understanding of the sample behavior under various experimental conditions, sample performance is *simulated* using a phenomenological finite element model of the Tanaka type.

The second main objective, besides identification of proper materials, is the *engineering* task of utilizing these to perform actual heat pumping. Concepts for elastocaloric cooling on the miniature scale have to be developed in order to accomplish the separation of hot and cold temperature flows. Important aspects are heat transfer and heat losses, an economical use of the mechanical driving force,

as well as simplicity of device layouts in order to allow for miniaturization by state-of-the-art fabrication technology.

1.3 Structure of this work

In the following chapter, relevant background information regarding refrigeration, shape memory alloys, experimental methods and other basic principles is provided.

The third chapter is dedicated to the state-of-the-art in ferroic cooling. The different caloric effects and corresponding material classes are introduced, before strategies and approaches for utilizing these effects in technical applications are discussed with an emphasis on elastocaloric cooling.

In the fourth chapter, thin samples of elastocaloric materials are characterized experimentally, while their thermo-mechanical behavior is simulated within the fifth chapter.

In chapter six, device concepts for elastcaloric microcooling are developed and first-of-its-kind demonstrators are built up and characterized.

Results are reviewed and discussed in the last chapter.

2 Basic principles

In this chapter, general information relevant to the present work is given. In the beginning, basic heat transfer modes are introduced, followed by a brief overview of selected cooling technologies. Subsequently, shape memory alloys (SMA) and their material properties are discussed, as these represent the most promising material class for elastocaloric cooling. Sample fabrication methods are introduced, which allow for fabrication of thin SMA samples appropriate for microcooling. Finally, experimental methods, measurement setups and procedures used in this work are explained.

2.1 Heat transfer

According to the laws of thermodynamics, the amount of energy in a closed system is conserved, but energy may be converted from one form to another (e.g., thermal, mechanical, chemical, electric etc.). Thermal energy is a measure for the nondirectional kinetic energy of the particles in matter. Consequently, the temperature scale has an absolute zero point, which is defined as $0\,\mathrm{K}$ by the international Kelvin scale. Since all physical systems strive towards thermodynamic equilibrium, heat does (voluntarily) only flow from a hot to a cold reservoir, which is an irreversible process as it increases entropy. However, heat may be transported from a cold to a hot reservoir (i.e. the entropy is decreased) within a *sub-system* at the cost of the remaining system. In our everyday life, this task is performed by devices like refrigerators, air conditioners and heat pumps. All of these devices rely on the principles of heat tranfer, which takes essentially place by *conduction*, *convection* and *radiation* [14]. While the first one occurs in any cooling device and the second one in those involving a fluid (or simply being subjected to surrounding air), the latter becomes dominant only at high temperatures considerably above room temperature. However, radiation of infrared light provides a convenient way of contact-less temperature measurement.

2.1.1 Thermal conduction

Thermal conduction can be regarded as diffusion of thermal energy and occurs in all phases of matter. In solids, thermal conduction is dominated by vibrations of the crystal lattice referred to as phonons (in insulators), and by motion of free electrons (in the case of metals), whereas in fluids it is based on elastic impact and

collision of particles. Conduction is most efficient in solid phase due to the tight bonding and close packing of atoms, whereas interatomic distances are larger in liquids and gases.

According to Fourier's law, the local heat flux density $\vec{q}$ is proportional to the temperature gradient ∇T and the material's thermal conductivity κ:

$$\vec{q} = \kappa \nabla T \tag{2.1}$$

Under steady-state conditions, thermal gradients are stable and do not change in time. In the general case of a transient state, conduction is described by the heat equation:

$$\dot{q_V} = \rho c_p \frac{\partial T}{\partial t} - \nabla \cdot (\kappa \nabla T) \tag{2.2}$$

The equation shows that the volumetric heat $\dot{q_V}$ depends on the heat capacity c_p, density ρ and thermal conductivity κ of a material, as well as spatial gradient and time-dependent change of temperature. Whenever perturbation of a steady-state temperature distribution occurs, e.g., by a change of thermal boundary conditions, the appearance or disappearance of heat sources and sinks inside the volume, heat conduction acts until steady-state conditions are established again.
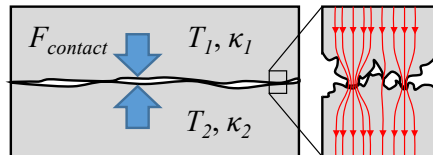
Figure 2.1: The thermal contact resistance between two bodies depends on contact force and contact area. It is increased by waviness (left) and microscopic roughness (zoom-in on the right) of the contacting surfaces (compare Ref. [15]).

If two solid bodies at different temperatures T_1 and T_2 are brought into physical contact, conductive heat transfer proceeds in between them. Typically, a steep temperature gradient results across the interface. The reason is the thermal contact resitance: Due to waviness and microscopic roughness of the contacting surfaces, the surface area through which heat may be transferred is considerably lower than the macroscopic interface area, as schematically shown in Fig. 2.1. Strictly speaking, thermal connection consists of a multitude of point contacts established by individual surface atoms [16]. Thermal contact resistance depends on the properties of the involved materials, interface area and contact force [17] and may be increased by introducing thermal interface materials [15, 18].

2.1.2 Convective heat transfer

Convection describes heat tranfer associated with mass tranfer due to macroscopic (advection) or individual particle movement (diffusion). It is the most dominant heat transfer mechanism in fluids, which generally have a lower heat conductivity than solids.

When temperature gradients are present in a fluid, thermal expansion leads to density variations. These, in turn, create a macroscopic fluid flow counteracting the gradient, referred to as *natural convection*. The fluid flow may also be created by external forces, e.g., by a fan or a pump, which is then called *forced convection*.

The heat flow from a solid body subjected to convective heat transfer is approximately described by

$$\dot{q} = h_{conv} A (T - T_{amb}) \tag{2.3}$$

where h_{conv} is the heat transfer coefficient, A the surface area exposed to convection, T the body's surface temperature and T_{amb} the ambient temperature. Typical heat transfer coefficients for air convection are in the range of 10 to $100\,\mathrm{W\,m^{-2}\,K^{-1}}$.

2.1.3 Thermal radiation

Thermal radiation refers to the transfer of energy (heat) by electromagnetic waves and is emitted by any body at a temperature larger than absolute zero. In contrast to conduction and convection, thermal radiation does not rely on matter for transport and can also propagate in vacuum. The most instructive example is sunlight reaching the earth and greatly influencing its climate and atmospheric temperature.

Due to conservation of energy, the sum of spectral absorption α, reflection ρ and transmission τ is unity ($\alpha + \rho + \tau = 1$) and the emissivity ε is equal to spectral absorption ($\varepsilon = \alpha$). In a so-called black body, reflection and transmission are zero.

Electromagnetic radiation shares properties of waves and particles. It is emitted in quasi-particles called photons. A photon of the wavelength λ has the energy $E = hc/\lambda$, where c is the speed of light and h the Planck constant. Thermal radiation reveals a continuous dispersion of photon energies (rather than having a single wavelength like, e.g., laser light). The spectral density emitted by a black body (having $\varepsilon = \alpha = 1$) in thermal equilibrium is described by Planck's law, which follows from energy quantization:

$$u(\lambda, T) = \frac{2hc^2}{\lambda^5} \cdot \frac{1}{e^{hc/k_B T \lambda} - 1} \tag{2.4}$$
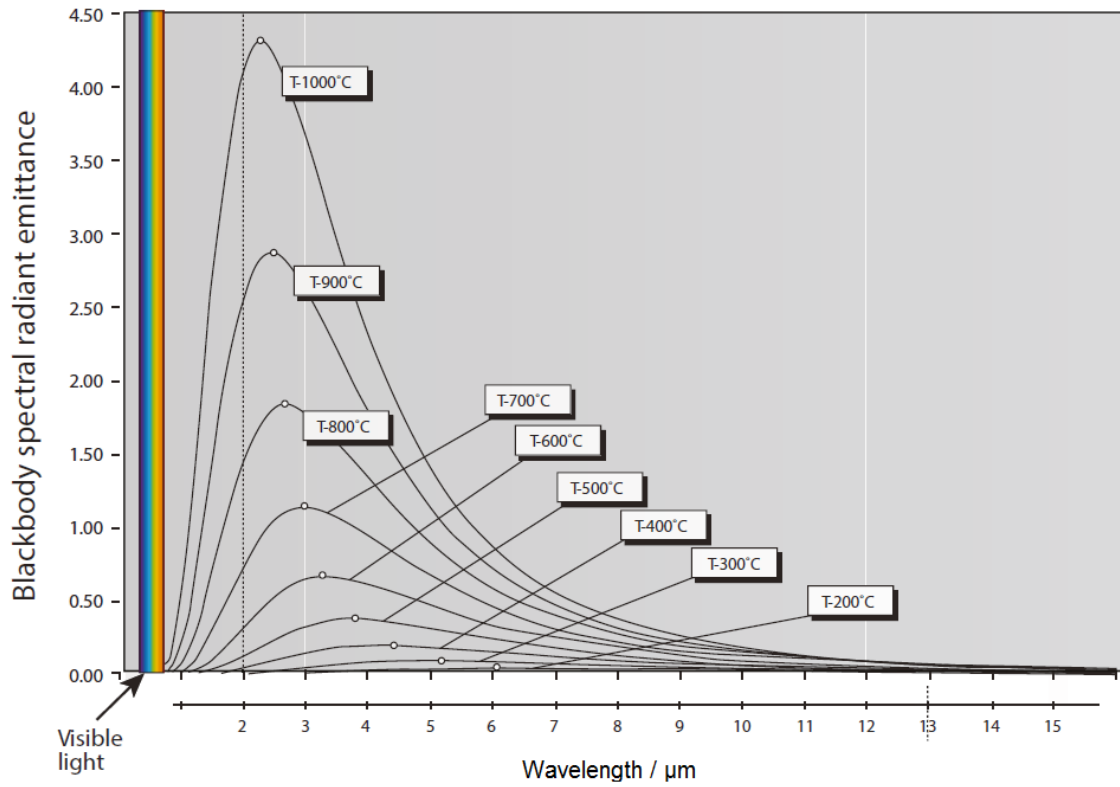
Figure 2.2: Visualization of Planck's law of radiation (modified from Ref. [19], ©FLIR Systems, AB).

where T is the body's temperature and k_B is Boltzmann's constant. The temperature dependence of black body radiation is visualized in Fig. 2.2. It can be seen that spectral density exhibits a temperature-dependent maximum. According to Wien's displacement law, the wavelength of maximum emission is inversely proportional to the absolute temperature:

$$\lambda_{max} = \frac{b}{T} \tag{2.5}$$

This circumstance can be used to estimate the temperature of a body from the thermal radiation it is emitting. Under ambient conditions, the emission peak is typically found in the infrared (IR) range, which is exploited, e.g., in infrared thermography. Significant thermal radiation at wavelengths visible for the human eye, on the other hand, occurs at temperatures above $500\,°\mathrm{C}$.

The total output power that a (grey) body with surface area A emits at a temperature T is decribed by the Stefan–Boltzmann law:

$$P = \varepsilon \cdot \sigma \cdot A \cdot T^4 \tag{2.6}$$

In this case, the emissivity $\varepsilon \leq 1$ accounts for the fact that most real bodys do only emit a fraction of ideal black body radiation. The propotionality factor σ is called Stefan–Boltzmann constant.

2.1.4 Thermal equivalent circuits

In systems under steady-state conditions, heat transfer can be described in a very similar way as electric conduction. In this case, temperature adopts the role of a voltage and heat flow is equivalent to electric current. The thermal coupling of elements within the system is described by thermal resistances, which may be combined in series or in parallel just as in electric circuits. Table 2.1 gives an overview of the thermal resistances associated with the different modes of heat transfer. The equations follow Newton's law of cooling, stating that the heat flow from a body to the environment is proportional to the temperature difference $(T_{surf} - T_{amb})$ between the body's surface temperature T_{surf} and the ambient temperature T_{amb}. In the case of radiative heat transfer, the heat transfer coefficient is given by $h_r = \varepsilon\sigma(T_{surf}^2 + T_{surr}^2)(T_{surf} + T_{surr})$, where T_{surr} is the surface temperature of surrounding objects emitting thermal radiation [20].

Thermal equivalent circuits are used in so-called lumped element models to model and predict the heat transfer in a system.

Similarly, the heat capacity of elements with negligible thermal gradient (i.e. heat transfer within the element is much faster than heat exchange with the surrounding) is treated as a single thermal capacitance. In analogy to the behavior of capacitors in electric circuits, such elements typically approach a steady state following a simple exponential evolution in time.

Table 2.1: Description of heat transfer by thermal resistances in purely resistive thermal circuits [20].

Transfer mode	Heat tranfer rate	Thermal resistance
Conduction	$\dot{q} = \frac{\kappa A}{L}(T_1 - T_2)$	$\frac{L}{\kappa A}$
Convection	$\dot{q} = h_{conv}A_{surf}(T_{surf} - T_{amb})$	$\frac{1}{h_{conc}A_{surf}}$
Radiation	$\dot{q} = h_r A_{surf}(T_{surf} - T_{surr})$	$\frac{1}{h_r A_{surf}}$

2.2 Cooling technologies

In this section, two of the most important cooling technologies shall be introduced: Vapor compression and thermoelectric cooling. The state-of-the-art in ferroic cooling, which is based on caloric effects, is described in more detail in Chapter 3. For an overview over further cooling technologies, the reader may refer to the reviews in Refs. [1, 21, 22].

Pumping heat from a cold to a hot reservoir may be achieved by a number of thermodynamic cycles. Since, according to the second law of thermodynamics, heat spontaneously only flows in the opposite direction (i.e. from hot to cold), these cycles require additional work input, as shown schematically in Fig. 2.3 (a). The efficiency of a refrigeration or heat pumping cycle is quantified by its *coefficient of performance*, stating the ratio of transported heat Q to the required work input W:

$$COP = \frac{Q}{W} \tag{2.7}$$

The transported heat is either the heat Q_C absorbed from the cold reservoir or the heat Q_H released to the hot reservoir, depending on the application-dependent desired effect.

2.2.1 Carnot refrigeration cycle
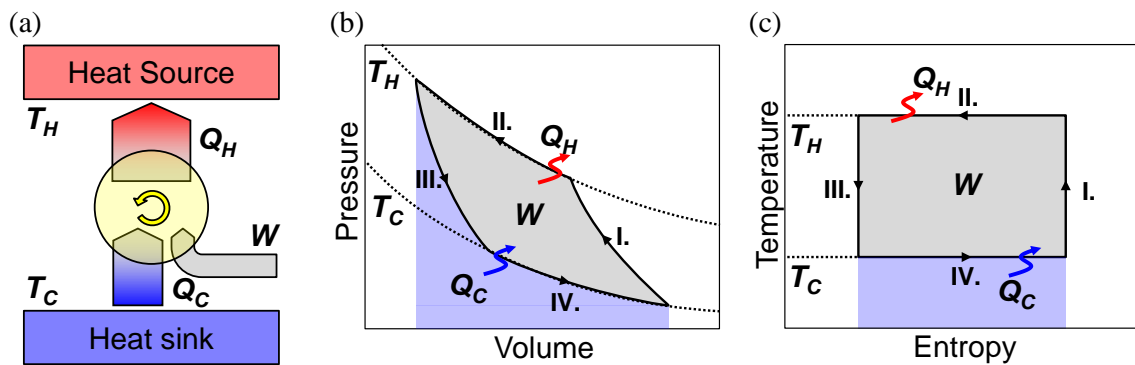
Figure 2.3: (a) Schematic of a general cyclic process for pumping heat from a cold to a hot resevoir. (b) pV-diagram and (c) TS-diagram of the reverse Carnot cycle.

The thermodynamic heat pumping cycle with the highest possible efficiency is the Carnot refrigeration cycle or reversed Carnot cycle. The cycle is visualized in the volume-pressure and temperature-entropy diagrams in Fig. 2.3 (b,c). In the first step (I.), the refrigerant is isentropically compressed and thereby heats up from T_C to T_H. To achieve this, external work W has to be introduced to the system. In the second step (II.), heat Q_H is released from the refrigerant to the heat source at constant temperature T_H (i.e. isothermally). In the third step (III.), the refrigerant is expanded isentropically, cooling down from T_H to T_C. In the last step (IV.), heat Q_C is isothermally absorbed from the heat souce at T_H. All four steps are fully reversible, i.e. free of friction or other losses. Steps I. and III. take place under perfect thermal insulation (i.e. adiabatically).

The required work input can be calculated from the closed integral over the pV- or TS-trajectory:

$$W = \oint P \cdot dV = \oint T \cdot dS = (T_H - T_C) \cdot \Delta S \qquad (2.8)$$

The coefficients of performance for cooling (refrigeration) and heating (heat pumping) by the inverse Carnot cycle are given by:

$$COP_{Carnot}^{cool} = \frac{T_C}{T_H - T_C} \qquad (2.9a)$$

$$COP_{Carnot}^{heat} = \frac{T_H}{T_H - T_C} \qquad (2.9b)$$

The Carnot COPs represent the maximum cooling/heat pumping efficiencies that may be obtained by any thermodynamic cycle at the given sink and souce temperatures T_H and T_C, respectively. As the cycle is a theoretical construct involving only reversible processes, it cannot be achieved in a real device. However, comparing other refrigeration cycles with respect to the Carnot cycle provides a measure of how close those cycles approach the ideal theoretical limit.

2.2.2 Vapor compression
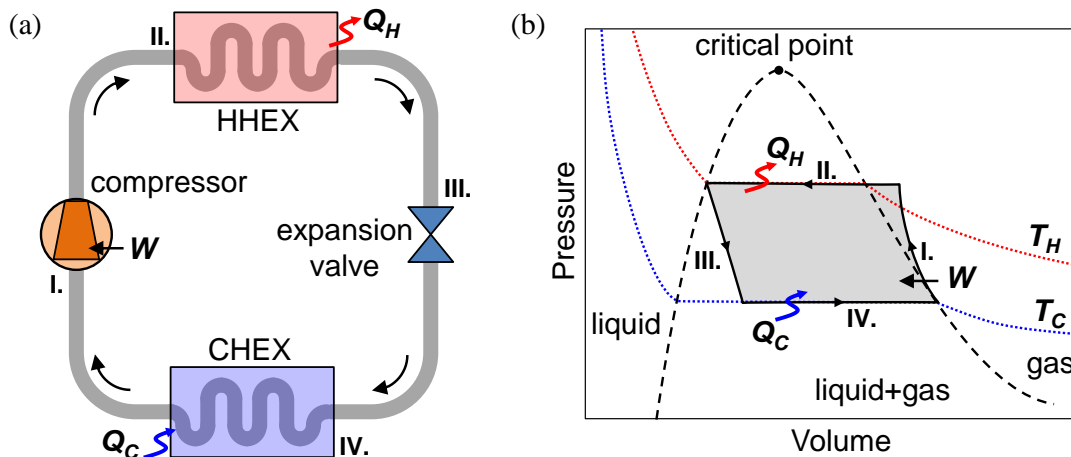
Figure 2.4: (a) Schematic vapor compression cycle and (b) corresponding pV-diagram. The cycle comprises the steps (I.) compression, (II.) heat release in the hot heat exchanger (HHEX), (III.) expansion, and (IV.) heat absorption in the cold heat exchanger (CHEX).

As already indicated in the introduction, the most common process used for industrial and domestic cooling and heat pumping today is the vapor compression cycle [1, 2]. In a vapor compression device, a fluid refrigerant is contained in a closed fluid system, in which it is repeatedly forced through phase changes between liquid and gas, making use of the refrigerant's large evaporation enthalpy.

The schematic vapor compression cycle and the corresponding pV-diagram are shown in Fig. 2.4. In the first step (I.) the refrigerant, which is in the state of saturated vapor, is isentropically compressed and thereby increases its temperature from T_C to a temperature above T_H. For this, a compressor is used which requires external energy input W. In the second step (II.), the superheated vapor is guided through a condenser at T_H acting as hot heat exchanger (HHEX). Here, the vapor condenses under constant pressure and thereby releases latent heat. In the next step (III.), the resulting saturated liquid is guided through an expansion valve or throttle. The abrupt decrease of pressure leads to partial evaporation (flash evaporation) of the refrigerant and to an adiabatic cooling from T_H to T_C. The fluid mixture is further led into the evaporator (IV.) acting as cold heat exchanger (CHEX). Here, the remaining liquid evaporates at constant pressure and thereby absorbs latent heat.

In order to increase COP, several more advanced cycle schemes have been proposed, including subcooling cycles, expansion loss recovery cycles, and multistage cycles [2]. Although a number of approaches have been made [23–26], miniaturization of vapor compression devices is generally difficult due to the lack of compact compressors [27].

Today, hydrochlorofluorocarbons (HCFC) like R-22, which has been the dominant refrigerant in domestic applications, and hydrofluorocarbons (HFC) like R-134A, which is widely used in cars, are mostly used for vapor compression. In contrast to HCFC (which are being banned in the European Union), HFC do not promote ozone layer depletion, but they still have a much higher global warming potential than CO_2 (e.g., by a factor of 1430 in the case of R-134A [28]). Ammonia, which is toxic, is used in large-scale industrial cooling. CO_2 may also be used as a refrigerant, but has special requirements on the fluid circuit due to its high vapor pressure. Other gases like propane and butane are highly flammable.

2.2.3 Thermoelectric cooling

Thermoelectric cooling (TEC) is a solid state cooling technology based on the Peltier effect [28–31]. The Peltier effect refers to the phenomenon that a heat flow $\dot{Q}$ is generated at the junction of two conductors made from the materials A and B, when a current I is applied (Fig. 2.5 (a)):

$$\dot{Q} = (\Pi_A - \Pi_B) \cdot I \tag{2.10}$$

where Π_A and Π_B are the Peltier coefficients of the two materials. In this case, the free electron gas may be considered as the 'working fluid'. The thermoelectric heat flow is partly counteracted by heat flows due to Joule heating within the materials ($P = I^2 \cdot R$) as well as thermal conduction. The inverse effect of the Peltier effect is the Seebeck effect, which is used for power generation and temperature measurement (Fig. 2.5 (b)). If two electrically conductive materials are
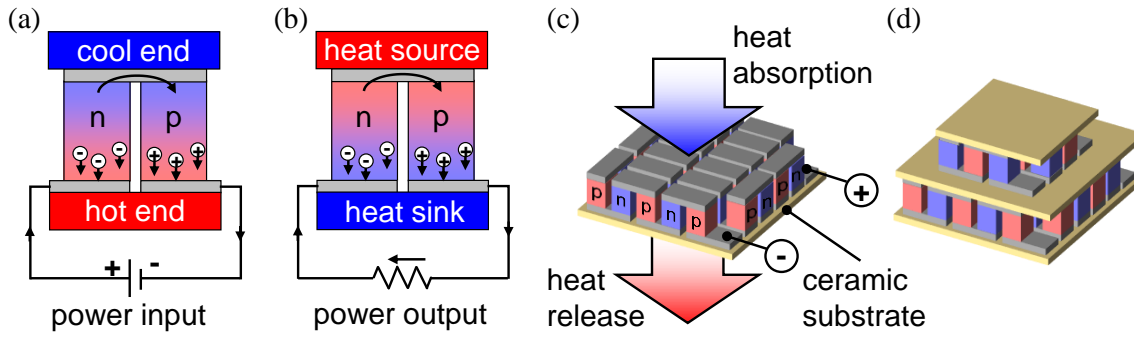
Figure 2.5: (a) A thermoelectric element supplied with a voltage pumps heat from a cold to a hot reservoir (Peltier effect). (b) A thermoelectric element subjected to a temperature gradient produces a voltage (Seebeck effect). (c) Large numbers of thermo junctions are connected electrically in a series to increase cooling power. (d) Thermoelements are stacked to increase temperature lift.

joined at one end, and a temperature difference ΔT is applied between the joint and the two free ends, a voltage ΔV will form between the ends:

$$S = -\frac{\Delta V}{\Delta T} \tag{2.11}$$

The proportionality constant S is called Seebeck constant. Under certain conditions, Peltier and Seebeck effect are related by the simple equation $\Pi = T \cdot S$. Due to these two effects, a thermoelectric element can be equally used as an electrically driven cooler or heat pump (Peltier effect) and as a thermally driven energy harvester (Seebeck effect). To increase the pumping power in a real TEC element, many individual thermocouples, which are thermally connected in parallel and electrically in a series, are integrated between two ceramic base plates that form a thermoelectric element (Fig. 2.5 (c)). In order to increase temperature lift, several TEC may be stacked (Fig. 2.5 (d)). Multistage TEC may be also integrated in a plane [32].

A central measure for the performance of a thermoelectric element at the temperature T is the dimensionless figure of merit ZT:

$$ZT = \frac{S^2}{\kappa} \cdot \sigma \cdot T \tag{2.12}$$

As can be seen from the formula, the ZT parameter is proportional to the square of the Seebeck coefficient S and to the electrical conductivity σ, but inversely proportional to the thermal conductivity κ. In other words, a TEC material should be a good thermal conductor in order to keep Joule heating at a minimum, but at the same time a bad thermal conductor to limit parasitic heat flows back from heat sink to source. Since all three involved material parameters are interrelated, the search for efficient TEC materials leads to conflicting design criteria. Today,

heavily doped semiconductors that can be doped n-type as well as p-type are predominantly used for TEC. Highest ZT values of up to 2.4 at room temperature are reached with bismuth telluride and related alloys. New trends go in the direction of quantum superlattices [33, 34], which however are still far from application.

Since the topic of this thesis is aimed at small-scale cooling as well, a more detailed list of current TEC applications shall be given here [28, 29]:

- Stabilization of laser diodes

- Cooling of infrared (IR) and charge-coupled device (CCD) detectors

- Noise reduction in integrated circuits

- Microprocessor cooling [35]

- Medical applications: Diagnostic medical equipment, hot/cold therapy pads, insulin coolers

- Biological applications: Polymerase chain reaction systems for deoxyribonucleic acid (DNA) multiplication

- Military applications: IR guided missiles, night sight

- Portable cooler boxes and beverage coolers

- Climate control in car seats

- Water condensation systems [36]

The maximum coefficient of performance of a TEC can be approximately expressed by [31]:

$$COP_{max} = \frac{T_C}{T_H - T_C} \cdot \frac{\sqrt{1 + ZT} - 1}{\sqrt{1 + ZT} + \frac{T_C}{T_H}} \tag{2.13}$$

where T_C and T_H are the temperatures of heat source and sink. As can be seen, the COP approaches the Carnot COP (Eq. 2.9a) for an infinite ZT. In real TEC devices, however, the COP hardly reaches values exceeding 2 [31]. In an article of Bell, it was pointed out that a ZT value of 2 would already open up a number of additional applications such as CPU cooling, but such high ZT have only been demonstrated in laboratory-scale so far [28]. Serious doubts have therefore been formulated that thermoelectric cooling will ever reach significantly higher coefficients of performance [11]. The cost per Watt of cooling power in TEC is still considerably higher than for vapor compression and other alternatives.

The advantages of TEC are the direct conversion of electricity into cooling, long lifetime without maintenance, reliability, compactness, as well as emission-free, silent and vibration-free operation (since no moving parts are involved). The

technology is furthermore compatible with MEMS (micro-electromechanical systems) technology and general miniaturization [37–40]. Today, thermoelectric cooling is predominantly used for small-scale applications where the low efficiency can be accepted or alternative solutions are out for question for other reasons.

2.3 Shape memory alloys

A special class of metal alloys exhibiting a range of fascinating multi-functional properties are the so-called shape memory alloys (SMA) [41]. These alloys owe their name to the fact that they can 'remember' a pre-defined shape after apparent plastic deformation, as will be explained below. Besides actuation and medical applications, SMA may be used for solid state cooling. In the following, general properties of SMA will be introduced, whereas the specific elastocaloric properties will be discussed in Chapter 3.

A selection of common SMA materials is indicated on the timeline in Fig. 2.6. Most of the alloys can be roughly assigned to one of the main groups of Cu-based, Fe-based an Ni-based SMA. The first known shape memory alloy was Au-Cd, discovered in 1932 by A. Ölander. However, in 1961 Buehler and co-workers discovered the shape memory properties of binary TiNi at the US Naval Ordnance Laboratory, which became famous under the trade name 'Nitinol' and today is the by far most common SMA in technical applications due to its superior functional properties.
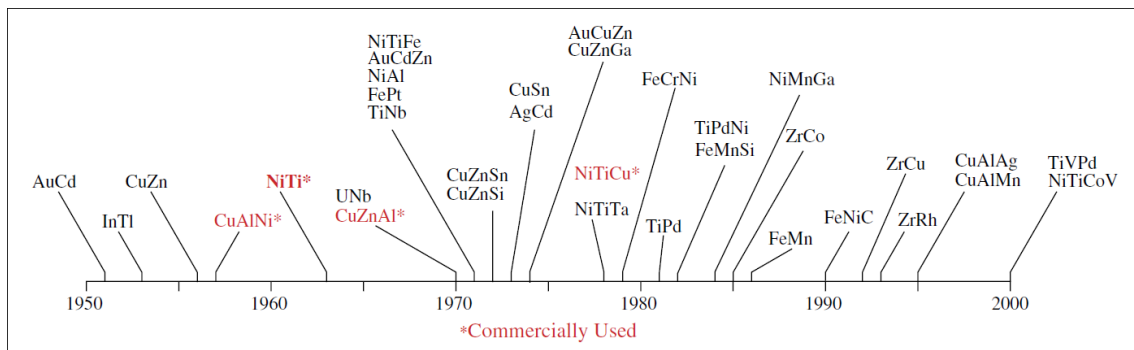
Figure 2.6: Several shape memory alloys (SMA) in chronological order of their discovery. ©2008, Society for Experimental Mechanics [42].

All the technically important material effects of shape memory alloys are based on a solid state phase transformation, which also makes these materials predestinated candidates for solid-state cooling based on the elastocaloric effect. The phase transformation occurs between a high-temperature austenite (A) phase with cubic B2 lattice and a low-temperature martensite (M) phase with orthorombic (B19) or monoclinic (B19') lattice (depending on the material), which has a lower symmetry. The schematic unit cells of each phase are shown in Fig. 2.7. The transformation is usually of first order, i.e. nucleation and growth based,

and furthermore diffusionless and fully reversible (in ideal materials), since it is based on shear deformation of lattice planes during which each atom is preserving its nearest neighbors. Due to its reduced symmetry, the martensitic unit cell can be oriented in different directions, which are referred to as variants. The binary TiNi alloy, for example, has 24 different variants. Compared to a cubic unit cell, the B19 (/B19') unit cell has one elongated diagonal axis, whereas the other axes are shortened. In macroscopic crystal lattices of (thermally-induced) martensite, usually a self-accommodated mixture of variants is found, which is called a twinned state. In case all variants are oriented in the same direction (or in approximately the same direction, in the case of polycrystals), the material is referred to as de-twinned and may reach deformations (strain) in the order of 10% with respect to the geometry in austenite state. The cubic austenitic unit cell on the other hand has only one possible orientation, since all symmetry operations result in an identical cell.
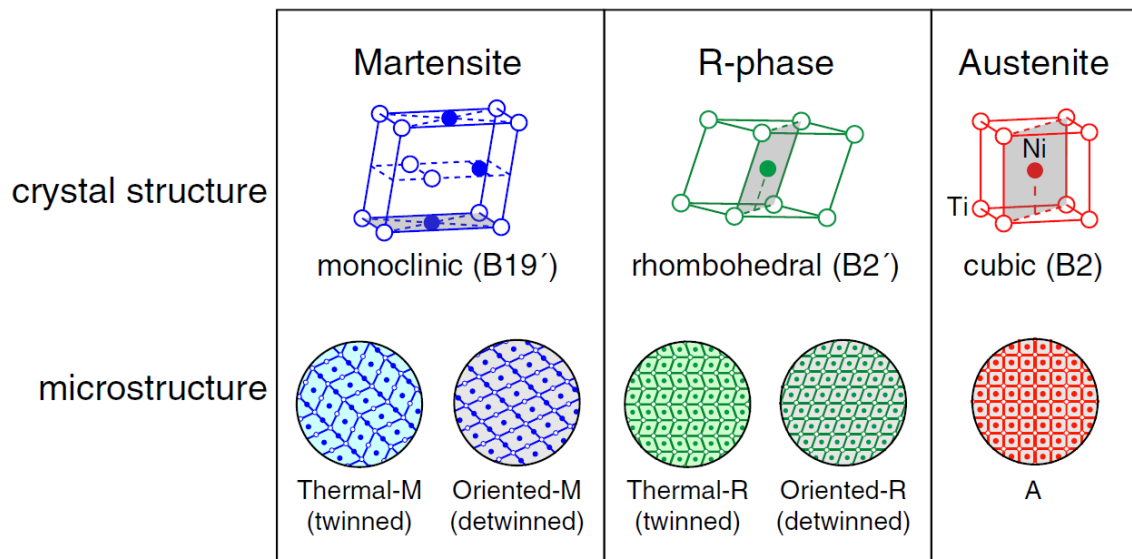
Figure 2.7: Unit cells and schematic crystal lattices of martensite (M), R-phase and austenite (A) phase. ©2008, Society for Experimental Mechanics [42].

2.3.1 Thermal phase transformation

The crystal lattice in which a SMA exists at a given temperature is determined by the free energy of each phase. The state with the lowest free energy is thermodynamically preferred. A schematic free energy diagram is shown in Fig. 2.15 (a) below (Section 2.3.6). The Gibbs potential G of both phases depends on the inner energy U, entropy S, temperature T and the strain and stress tensors ε and σ:

$$G^{A,M} = U^{A,M} - S^{A,M}T - \varepsilon^{A,M}\sigma \tag{2.14}$$

The free energy curves of martensite and austenite intersect at the temperature T_0. The martensite phase is stable below this temperature, whereas the austenite

phase is stable above. However, in real materials a certain activation energy is required, inducing thermal hysteresis. In addition, the transformations extend over a certain temperature range. The start and finish temperatures A_s and A_f of the M→A transformation are shifted to higher temperatures, whereas the start and finish temperatures M_s and M_f of the A→M transformation are shifted to lower temperatures. The transformation from martensite to austenite is endothermal, whereas the reverse transformation is exothermal. In certain TiNi-based alloys, an intermediate phase occurs between austenite and martensite, which is commonly referred to as R-phase due to its rhombohedral lattice (see Fig. 2.7). The R-phase shows a similar twinning behavior as the martensite phase, but length changes in the de-twinned state are much smaller.

A common way of determining the phase transformation properties is differential scanning calorimetry (DSC). The obtained curves reveal characteristic peaks for each occuring phase transformation. Fig. 2.8 shows the DSC diagrams of two commercial NiTi shape memory wires. In one case, the transformation proceeds in a single step from martensite to austenite, whereas in the other case the austenite-martensite transformation proceeds via the intermediate R-phase: A→R→M. During forward transformation, a single peak is observed, since the peaks of R-phase and austenite are overlayed.
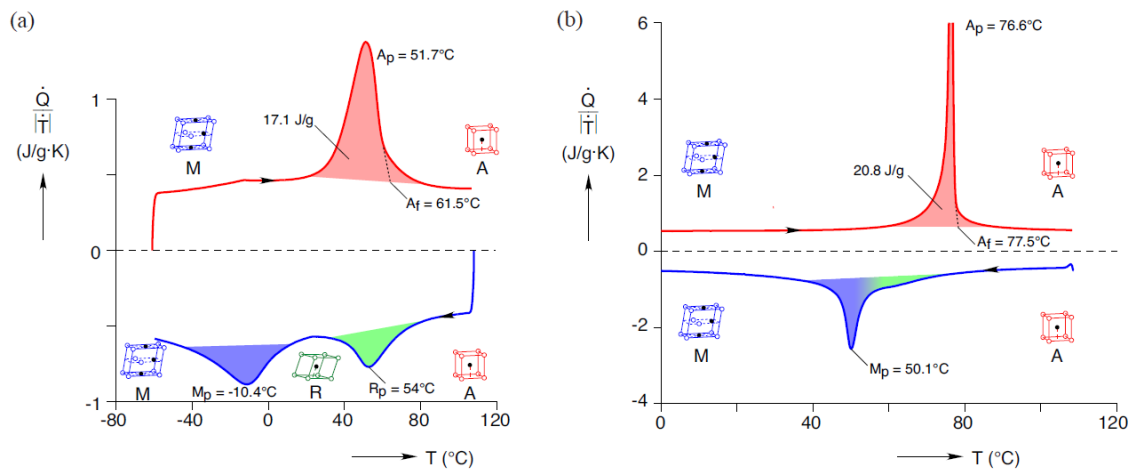
Figure 2.8: Differential scanning calorimetry (DSC) characteristics for two flexinol samples exhibiting (a) a two-step and (b) a single step phase transformation. Schematic unit cells of martensite (M), R-phase and austenite (A) are indicated. Both samples show shape memory effect at room temperature (RT). ©2009, Society of Photo Optical Instrumentation Engineers [43].

Phase transformation in SMA also influences other physical properties, which thus can be used in order to determine phase transformation temperatures as an alternative or supplement to DSC measurements. A common method is the temperature-dependent measurement of electrical resistance $R(T)$. In pure M and pure A state, the resistance increases approximately linearly with temperature for common shape memory alloys. In the temperature regime of phase

transformation, however, strong deviations from linear behavior is observed, often including a resistance decrease with increasing temperature. In case R-phase is involved in the transformation, temperature intervals of increased resistance are found. Some exemplary DSC and $R(T)$ curves may be found, e.g., in Refs. [44, 45].

The phase transformation temperatures and the involved phases depend on alloy composition as well as fabrication procedure and can therefore be tuned in a certain range. In the case of TiNi-based alloys, phase transformation temperatures decrease with increasing Ni content [46, 47]. Transformation temperatures are also affected by oxygen and carbon impurities [48–50] and may be tuned by thermal treatments [51, 52].

2.3.2 Shape memory effect
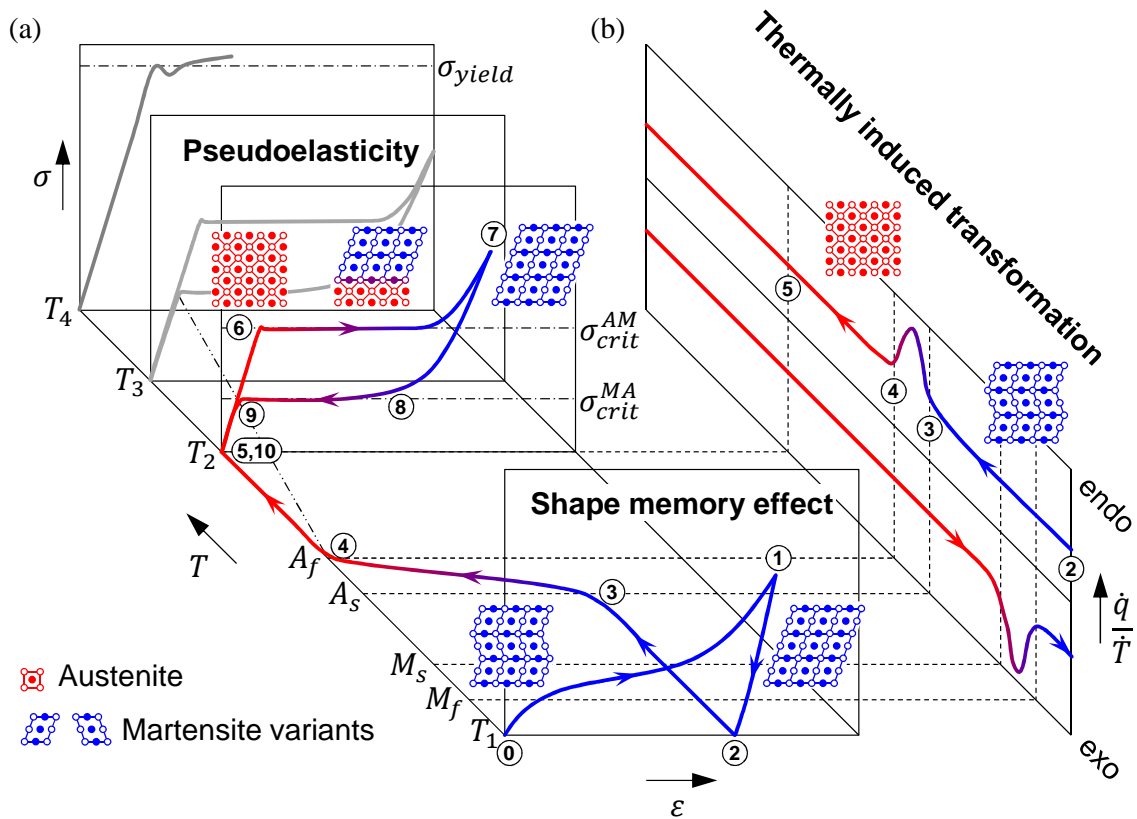
Figure 2.9: (a) Schematic trajectories of shape memory effect and superelasticity in 3-dimensional parameter space of strain (ε), stress (σ) and temperature (T). (b) For comparison, a schematic DSC characteristic of thermally induced phase transformation is indicated on the right.

The eponymous shape memory effect (SME) made shape memory alloys famous and allows them to recover a pre-defined shape, which seems to be lost after

apparent plastic ('pseudoplastic') deformation. The effect occurs in materials in the martensite phase, i.e. at temperatures below M_f. It is characterized experimentally by temperature-dependent tensile tests. A schematic trajectory in the strain-stress-temperature parameter space is shown in Fig. 2.9. In order to prepare a SMA component for technical use of the memory effect, a desired shape is imprinted in the austenitic state, i.e. by annealing at high temperature. Then, the component is cooled down to a temperature $T_1 < M_f$, whereupon it will transform to twinned martensite whithout changing its macroscopic shape. Starting from the stress- and strain-free state (0), an external force is applied in one direction, e.g., by a counteracting spring. With increasing stress in the material, martensitic variants are oriented in direction of the force and strain increases until a de-twinned state is reached (1). Upon releasing the external force, the strain slightly decreases due to elastic unloading of the de-twinned martensite, but the SMA component remains 'pseudoplastically' deformed (2). In order to reset the macroscopic shape to its initial state, the component is heated up. In the temperature interval between A_s (3) and A_f (4), the transformation from martensite to austenite takes place and all the martensite variants return to the austenitic cubic lattice, recovering the macroscopic imprinted shape. In order to start the cycle again, the material is cooled down to a temperature below M_f ((4→0), trajectory not shown in the graph). Since the pseudoplastically deformed shape from the previous cycle is not remembered, the effect is more specifically referred to as one-way SME. The effect finds wide application in electrically and temperature-controlled actuation due to its superior work density and simple operation principle [53–57].

2.3.3 Pseudoelasticity

The second important effect in SMA, occuring at temperatures above the austenite finish temperature A_f, is pseudoelasticity (also called superelasticity) which is related to a *stress-induced* phase transformation. The effect is essential for elastocaloric cooling, as described in chapter 3. A schematic trajectory is included in Fig. 2.9. Starting at a temperature $T_2 > A_f$ in the strain- and stress-free state (5), a uniaxial force is applied to a SMA component. Initially, the stress in the material increases linearly with strain since the austenitic lattice is elastically deformed in the direction of force (5→6). As soon as a material-specific critical stress σ_{crit}^{AM} is exceeded (6), the stress-induced transformation from austenite to martensite (SIM) begins. The stress remains constant although strain is further increased. The resulting stress plateau (6→7) is a direct consequence of the localized transformation behavior that will be decribed in section 2.3.4. At the end of the plateau, the material is fully transformed to martensite, in which all variants are oriented in the direction of applied external force, i.e. fully detwinned. Upon further increase of strain, stress also increases due to elastic loading of the martensite lattice (7). If now the external force is released (7→8), stress initially decreases linearly with decreasing strain due to elastic unloading of oriented martensite. When reaching

the critical stress σ_{crit}^{MA}, a second stress plateau occurs (8→9), which corresponds to the reverse transformation from stress-induced martensite to austenite and is shifted to a lower stress compared to the forward plateau. This hysteresis is the mechanical equivalent of the thermal hysteresis (see above). By completely removing the external force, the material is elastically unloaded in the austenite until a stress-free state is established (10). In an ideal, fatigue-free material, states (5) and (10) are identical and the initial shape of the SMA component is fully recovered.

Since R-phase also holds the capability of variant orientation, more complicated stress-strain characteristics may arise for materials exhibiting a two-step transformation. An overview over possible characteristics is given in Fig. 2.10.
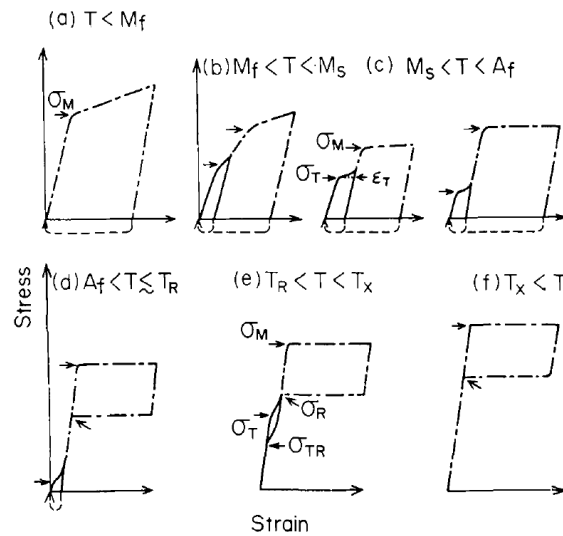
Figure 2.10: Stress-strain characteristic of a pseudoelastic TiNi alloy involving austenite (A), R-phase and martensite (M) phase, in dependence of temperature. ©1986, The Metallurgical Society of AIME / Springer [58].

Pseudoelastic behavior is observed in a certain temperature range above A_f. In case the material is loaded and unloaded at a higher temperature $T_3 > T_2$ (Fig. 2.9), the plateau stresses σ_{crit}^{AM} and σ_{crit}^{MA} are shifted to higher values. If the temperature is increased too high above A_f, the critical stress for SIM transformation becomes higher than the yield stress σ_{yield} of the material. Hence, irreversible plastic deformation and ultimately fracture of the austenitic material occur rather than a pseudoelastic stress-plateau.

The temperature dependence is described by the Clausius-Clapeyron equation:

$$\frac{d\sigma}{dT} = -\frac{\Delta S}{\Delta \varepsilon_T} = -\frac{\Delta H}{\Delta \varepsilon_T T} \tag{2.15}$$

where σ is the critical stress and $\Delta \varepsilon_T$ the transformation strain (i.e. the width of the pseudoelastic plateau). ΔS and ΔH are the specific entropy change and enthalpy of the transformation (see, e.g., Ref. [60]). In a certain temperature range,
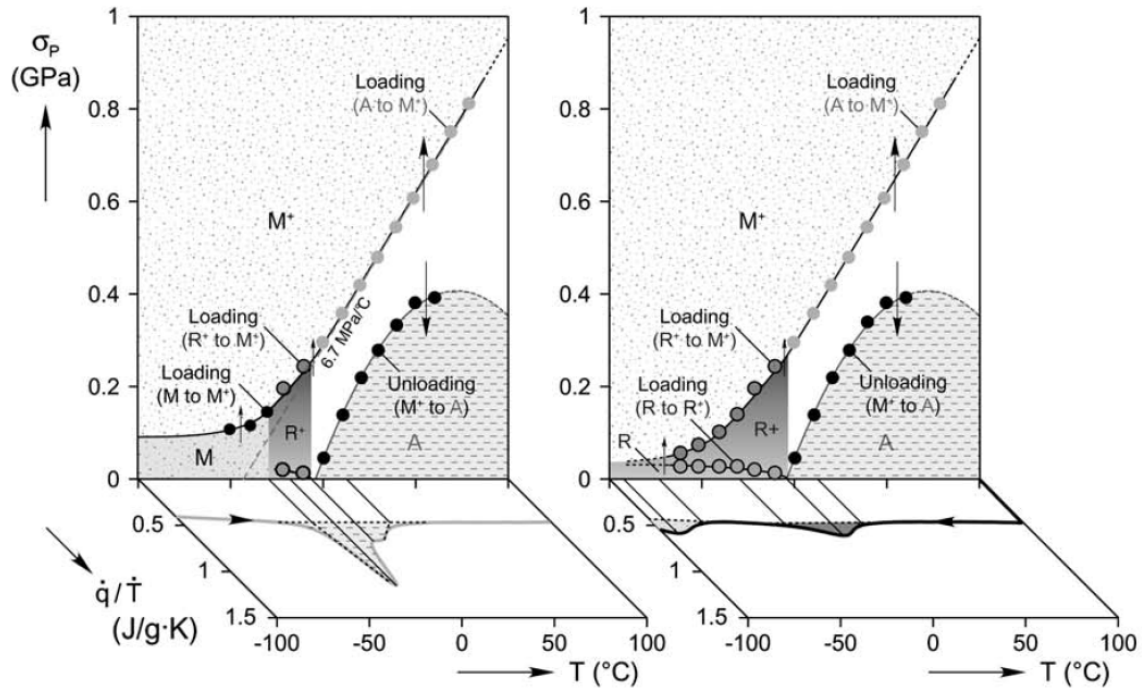
Figure 2.11: Stress-temperature phase diagram for a pseudoelastic NiTi wire based on experimentally obtained critical stresses. Clausius-Clapeyron coefficients are obtained by linearly approximating the temperature dependence of critical stresses. DSC characteristics for heating (left) and cooling (right) are included for comparison. ©2009, Society for Experimental Mechanics [59].

the correlation of critical stresses and ambient temperature is approximately linear. In this case, the proportionality constants or Clausius-Clapeyron coefficients for forward (loading) and reverse transformation (unloading) can be obtained from experimental data by determining critical stresses at different temperatures – see e.g. Fig. 2.11. In the vicinity of phase transformation temperature A_f, critical stresses become small and linearity does no longer apply. The case of zero stress coincides with the thermally induced phase transformation, allowing a comparison of tensile test data and results form DSC.

As a consequence of the Clausius-Clapeyron relation, pseudoelasticity exhibits a ponounced rate-dependency. Critical stresses during mechanical loading may not only be increased by rise of the ambient temperature, but also by *self-heating* of the material due to the elastocaloric effect. In case latent heat is released faster than it can be transferred to the ambient, sample temperature increases constantly and the pseudoelastic plateau (which is horizontal under quasi-static conditions) adopts a positive slope. In the same way, critical strains for reverse transformation are lowered due to *self-cooling*. Because of these effects, the area enclosed by the stress-strain trajectory increases and the damping capacity of the material reaches a maximum under adiabatic conditions [61–63].

The ability to recover large pseudoelastic strains in the order of $10\,\%$, endure high forces as well as the biocompatibility of TiNi-based alloys due to an intrinsic

TiO$_2$ surface film open up a number of technical applications for pseudoelastic SMA materials. These are for example medical components like stents, artificial heart valves, retainers for teeth or broken bones, antennae, indestructible glasses frames and damping components in tools and buildings [56, 64–67].

2.3.4 Lüders-like bands
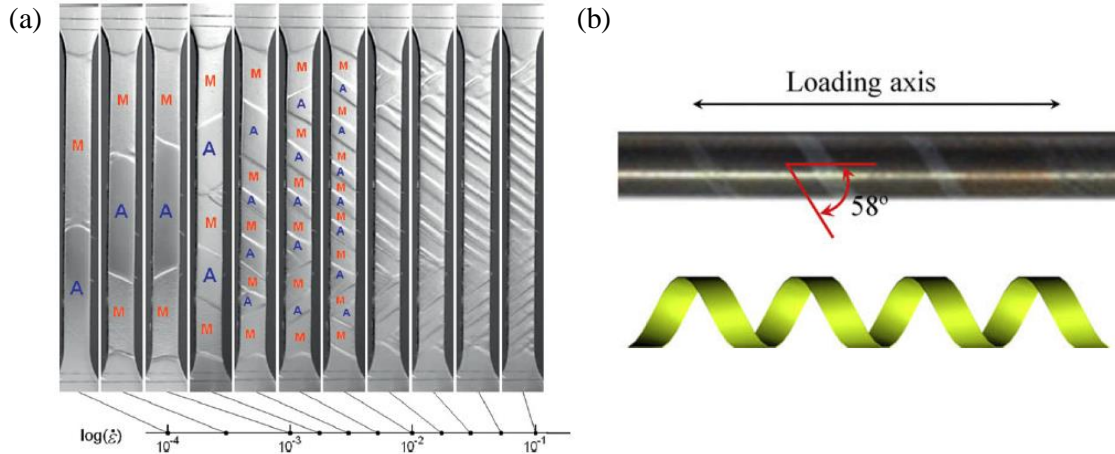
Figure 2.12: Lüders-like strain bands observed by optical method in TiNi-based alloys. (a) Sheet sample (©2010, Elsevier Ltd. [68]), (b) tube sample (©2010, Acta Materialia Inc. / Elsevier [69]).

The pseudoelastic stress-strain behavior described above is a direct result of the nucleation-growth based, heterogeneous character of the stress-induced martensitic phase transformation. In a typical displacement-controlled tensile experiment, the sample length is increased/decreased during loading/unloading by changing the distance between both sample ends. Initially, this leads to a homogeneously increasing strain throughout the sample (see (5→6) in the schematic stress-strain characteristic of Fig. 2.9). At a certain point (6), the critical stress for *nucleation* of a martensitic seed interface is reached and a sharp band of martensite is formed, having a considerably higher local strain in tensile direction than the surrounding austenite regions[1]. This strain band, also referred to as *Lüders band*, has a characteristic inclination angle with respect to loading direction, which depends on sample geometry (Fig. 2.12). Upon further increase of the sample length (6→7), the martensitic region grows by *propagation* of its two limiting phase fronts, since the critical stress for interface propagation is slighly lower than that for nucleation of a new interface (assuming that the experiment takes place under quasi-isothermal conditions) [70]. When the end of the resulting stress plateau is reached, the martensitic region expands over the whole sample and a further increase of sample length again leads to a homogeneous strain increase.

[1]Note that in case of a tensile experiment, the martensitic strain band has a decreased cross-section (necking), whereas its cross-section is increased in a compressive experiment.

Qualitatively the same behavior is observed while unloading by nucleation of an austentitic seed in the martensitic matrix. In this case, the critical stress for interface nucleation is *lower* than that for propagation. During loading, nucleation typically takes place at one or both sample ends due to the thermal and mechanical boundary conditions, whereas during unloading nucleation is preferred at locations where the last A-M-interface has disappeared before (history effect) [70, 71]. This is due to changes in microstructure (e.g., defects created during forward transformation) or remaining A-M interfaces (in case of incomplete transfromation).
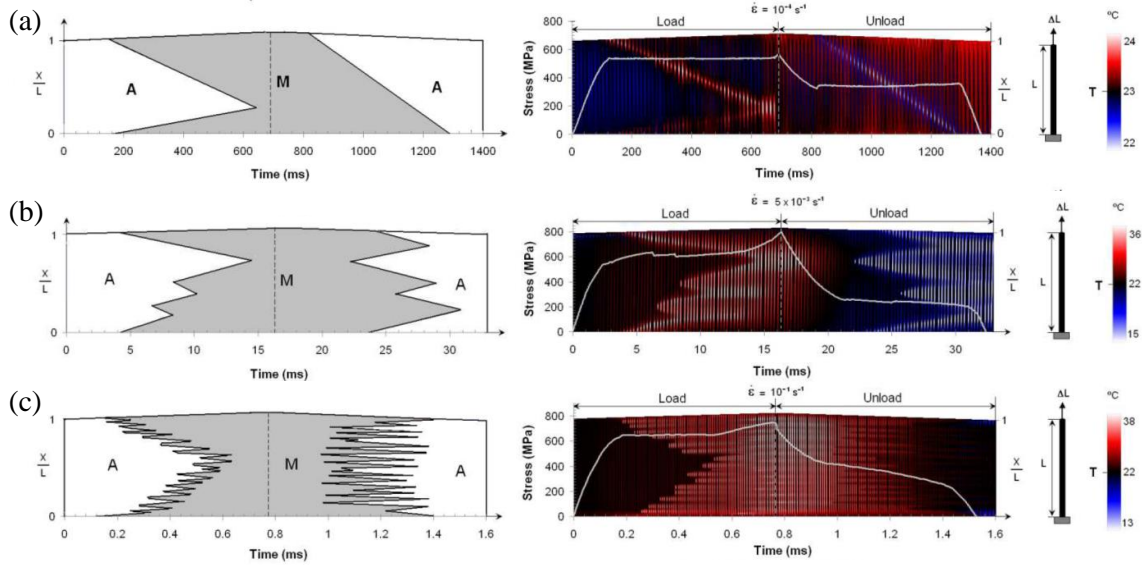
Figure 2.13: Number of Lüders bands in a NiTi wire sample as a function of strain rate. On the right, a chronological series of infrared images is shown. The diagrams on the left indicate the interpretation in terms of martensite (M) and austenite (A) phase. Figures adapted from Ref. [71]. ©2010, InTech.

In case the experiment is not performed under quasi-static (isothermal) conditions, the dynamics of band formation are affected by the elastocaloric effect. The growth of a martensitic region during loading leads to a *self-heating* at the moving interfaces due to release of latent heat. This, in turn, increases the critical stress and the nucleation of a new interface in a colder part of the sample becomes more favorable than the propagation of existing interfaces. The same effect is observed due to *self-cooling* at the interfaces of a growing austenitic region during unloading. Consequently, when the end displacement rate (strain rate) of the tensile experiment is increased, the number of M-A-interfaces inreases as well [70, 71]. The effect is exemplarily shown in Fig. 2.13. In case of n coexisting interfaces, all interfaces tend to propagate at the same average speed c (assuming homogeneous sample properties), which is related to the end-displacement rate $\dot{\delta}$ and the transformation strain ε_T [72]:

$$c = \frac{\dot{\delta}}{n \cdot \varepsilon_T} \tag{2.16}$$

Besides strain rate, Lüders-band formation strongly depends on experimental conditions like loading mode (tension vs. compression, shear, bending, torsion), strain- or stress-controlled loading, cycle number, ambient temperature with respect to the material's A_f temperature [73], as well as texture [74].

The vast majority of studies on Lüders-like band formation in SMA has been performed on polycrystalline, binary NiTi-based alloys with sightly different compositions. Band formation has been observed in flat sheet or ribbon samples having thicknesses of $160\,\mu m$ to $2\,mm$ [68, 70, 75–81], in tubes with wall thicknesses of 110 to $500\,\mu m$ [69, 82–85] as well as wires with diameters of 500 to $700\,\mu m$ [71, 86]. The band inclination with respect to loading direction was observed to be around $55°$ for flat samples [70, 73]), $90°$ in thick bars and wires [72, 73] and spiral-shaped in an angle of $58°$ for thin-walled tubes [69]. Besides these TiNi-based materials, Lüders bands have been furthermore observed in TiNiCu [87] and TiNiCuV ribbons [88] as well as single-crystalline NiFeGa [89, 90] and CuZnAl samples [91].

Lüders-like bands have been studied in different samples under a variety of loading conditions by optical methods [68, 70], digital image correlation (DIC) [75, 76, 80, 90, 92–94], infrared (IR) thermography [68, 70, 71, 77, 78, 86, 88, 90, 95–97], in-situ electron backscattering diffraction (EBSD) [69] and combinations of those. In research on elastocaloric cooling, IR thermography is of particular interest, since it allows for spatially resolved and contact-less temperature measurements. IR thermograms have furthermore been used to estimate local heat sources and sinks in-situ [79, 85, 87] as well as for 'InfraRed Image Correlation' [81].

2.3.5 Fatigue life and hysteresis

A sufficiently long lifetime is crucial for most technical application of functional materials like SMA. However, many SMA suffer from fatigue, which is one of the main factors hindering progress in commercialization. The occuring phenomena may be separated into structural and functional fatigue. Structural fatigue refers to a breakdown of the mechanical integrity of the material, e.g., due to crack nucleation, growth and ultimately fracture. Functional fatigue, on the other hand, describes the loss of desired functional properties such as recoverable strain, damping capacity or elastocaloric effect size. Under cyclic loading, materials with poor fatigue resistance often accumulate remanent strain, pseudoelastic plateaus degrade and the damping capacity is reduced. The latent heat was shown to decrease due to cyclic (thermally as well as stress-induced) phase transformation in certain materials [98, 99].

In the past, fatigue life in NiTi and other SMA was predominantly associated with microstructure, which is strongly influenced by the fabrication procedure [58, 100–102]. Fatigue may result from both, thermally induced and stress-induced phase transformation. In the context of elastocaloric cooling, the material performance under cyclic mechanical loading is essential. One of the main sources of

fatigue is the accumulation of defects, which may be favored by crystallographic mismatch between the phases (see below), but also by impurities and inclusions within the SMA matrix, and act as nucleation sites for crack formation. In case of anisotropic material properties, e.g., due to the fabrication method, a texture-dependence of fatigue behavior may be observed [100]. A second important parameter is the grain size in polycrystalline materials. Usually, fine-grained materials (with or wihout fine inclusions) show a more favorable fatigue performance [100, 103]. On the other hand, the converse effect is observed in oligocrystals with so-called 'bamboo structure'. In such crystals, triple grain boundaries are omitted which also improves fatigue life [104–109]. Inclusions as well as defects and grain boundaries may pin martensite-austenite interfaces during transformation and thus increase hysteresis. Materials with large hysteresis, on the other hand, are usually associated with poor fatigue resistance.

Besides the volumetric microstructure, surface quality plays an important role as well, since a rough suface may also act as nucleation centers for cracks [110]. Surface qualitiy may be improved, e.g., by electrochemical polishing [111, 112]. When a SMA is pseudoelastically cycled in a wet or liquid surrounding, fatige may be increased by electrochemical reactions at the surface [113–115], which has to be considered in medical applications as well as elastocaloric devices involving a heat transfer fluid.
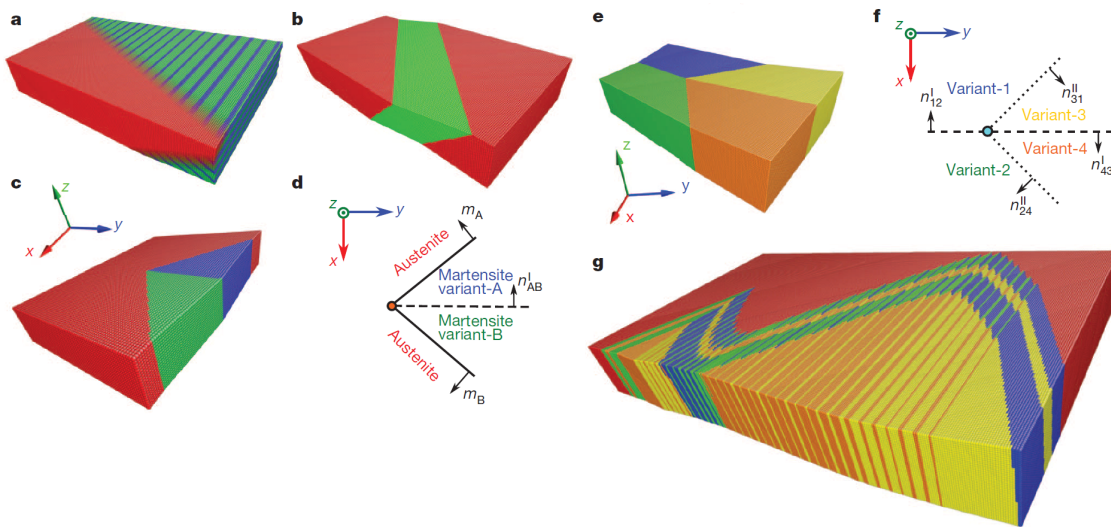
Figure 2.14: Various phase boundaries between martensite variants (blue, green, yellow, orange) and austenite (red). (a) Planar phase boundary with transition layer between austenite and twinned martensite. (b) Planar phase boundary between austenite and a single martensite variant for a material with $\lambda_2 = 1$. (c,d) Triple junction,(e,f) quad junction and (g) riverine microstructure in a material fullfilling all three compatibility criteria. ©2013, Macmillan Publishers Ltd. [99].

In recent years, there has been a growing recognition that fatigue life in SMA does not only depend on defects and grain structure (which are controlled by fabrication procedure and the phase diagram of the alloy system), but is rather

determined by crystallographic compatibility of the phases involved. Since the martensitic phase transformation is nucleation-growth driven, interfaces between austenitic and martensitic regions have to be formed during both, forward and reverse transformtion. In a general SMA, the lattice parameters of A and M phase differ, leading to a certain lattice mismatch at the interface. The mismatch is compensated by the formation of fine laminated mixtures of martensite variants, often including branching twins, as well as a transition layer between the twinned martensite and the austenite [116]. A typical interface layer is sketched in Fig. 2.14 (a). The free energy of the interface is then given by the bulk free energy difference of the phases, the interfacial energy of the twin boundaries and the elastic energy stored in the transition layer [117]. These additional contributions to the free energy have to be overcome (or dissipated) during thermally or mechanically induced phase transformation and lead to the hysteresis observed in real SMA. Such an interface is likely to produce an increasing number of defects in case of cyclic transformation.

In the geometric non-linear theory of martensite (GNLTM), the lattice of each martensite variant is mapped to the austenitic lattice by a transformation tensor U describing the deformation of the unit cell.[2] The transformation tensor has the three eigenvalues λ_1, λ_2 and λ_3 which are by convention ordered by size (e.g., $\lambda_1 \leq \lambda_2 \leq \lambda_3$). Several conditions for crystallographic compatibility between A and M phase are derived from the properties of the tranformation tensor.

The first condition that has been widely accepted for a long time states that the determinant of the transformation tensor should be unity:

$$det U = \lambda_1 \lambda_2 \lambda_3 = 1 \tag{2.17}$$

This condition describes nothing more than volume conservation and is immediately comprehensible, since, e.g., the formation of a martensitic nucleus in an austenitic matrix involves additional elastic energies due to mechanical constraints in case of a volume change.

The second condition concerns the middle eigenvalue:

$$\lambda_2 = 1 \tag{2.18}$$

---

[2] As an example, the cubic-to-orthorhombic (B2→B19) transformation has six possible martensite variants. The transformation tensors in case of face-diagonal stretch for each of the six variants are [116]:

$$U_1 = \begin{bmatrix} \beta & 0 & 0 \\ 0 & \frac{\alpha+\gamma}{2} & \frac{\alpha-\gamma}{2} \\ 0 & \frac{\alpha-\gamma}{2} & \frac{\alpha+\gamma}{2} \end{bmatrix}, U_2 = \begin{bmatrix} \frac{\alpha+\gamma}{2} & 0 & \frac{\alpha-\gamma}{2} \\ 0 & \beta & 0 \\ \frac{\alpha-\gamma}{2} & 0 & \frac{\alpha+\gamma}{2} \end{bmatrix}, U_3 = \begin{bmatrix} \frac{\alpha+\gamma}{2} & \frac{\alpha-\gamma}{2} & 0 \\ \frac{\alpha-\gamma}{2} & \frac{\alpha+\gamma}{2} & 0 \\ 0 & 0 & \beta \end{bmatrix},$$

$$U_4 = \begin{bmatrix} \beta & 0 & 0 \\ 0 & \frac{\alpha+\gamma}{2} & \frac{\gamma-\alpha}{2} \\ 0 & \frac{\gamma-\alpha}{2} & \frac{\alpha+\gamma}{2} \end{bmatrix}, U_5 = \begin{bmatrix} \frac{\alpha+\gamma}{2} & 0 & \frac{\gamma-\alpha}{2} \\ 0 & \beta & 0 \\ \frac{\gamma-\alpha}{2} & 0 & \frac{\alpha+\gamma}{2} \end{bmatrix}, U_6 = \begin{bmatrix} \frac{\alpha+\gamma}{2} & \frac{\gamma-\alpha}{2} & 0 \\ \frac{\gamma-\alpha}{2} & \frac{\alpha+\gamma}{2} & 0 \\ 0 & 0 & \beta \end{bmatrix},$$

where $\alpha = a/a_0$, $\beta = b/a_0$, $\gamma = c/a_0$. a, b and c are the lattice parameters of the orthorombic martensite and a_0 is the lattice parameter of the cubic austenite.

In case this condition is fulfilled, the austenite is directly compatible with a single variant of martensite. Hence neither twinned martensite nor a transition layer are required in order to accomodate the lattices and the interface is atomically sharp (Fig. 2.14 (b)). Materials with a middle eigenvalue of one are therefore expected to show particularly low hysteresis. Indeed such materials have been found by combinatorial research on ternary TiNiCu, TiNiPd as well as quaternary TiNiCuPd alloys [44, 116, 118]. Interestingly, hysteresis was observed to be very sensitive to the actual λ_2 value following an univerals law with a sharp minimum at $\lambda_2 = 1$ [117] and quite independent of volume mismatch (given by $detU$) and other material properties [116].

Besides the above, there is a third group of conditions referred to as 'cofactor conditions'[3] stating that the lattice system allows for "an infinite number of compatible interfaces between austenite and finely twinned martensite" [117] so that these can coexist in arbitrary volume fractions, if the cofactors are zero. Schematic microstructures are indicated in Fig. 2.14 for martensitic type I twins (c,d), type II twins (e,f) as well as a 'riverine' structure consisting of austenite and different martensite variants. A material that closely meets the middle eigenvalue as well as the cofactor conditions is $Zn_{45}Au_{30}Cu_{25}$ [99].

Recently, novel fatigue-free SMA thin films based on Ti-rich TiNiCu(Co) alloys have been developed at the University of Kiel [98, 103, 120–122]. Sputter-deposited samples with a thickness of about 20 µm and the compositions $Ti_{54}Ni_{34}Cu_{12}$ ($A_f = 65\,°C$) and $Ti_{54.7}Ni_{30.7}Cu_{12.3}Co_{2.3}$ ($A_f = 9\,°C$), the latter being particularly interesting for elastocaloric microcooling, have been shown to withstand ten million pseudoelastic loading cycles without any signs of fatigue [120]. The materials closely fulfill all three compatibility conditions. However, an additional effect further improves reversibility: Due to stoichiometric titanium excess, Ti_2Cu precipitates are formed within the matrix, which have epitaxial interfaces with the B2 as well as with the B19 lattice [120, 122]. While the low cofactors promote reversible growth, the precipitates act as nucleation centers during phase transformation. In a further study, it was shown that fine-grained samples achieve a much higher structural stability than more coarse-grainded samples of the same composition, presumably due to a finer martenstic variant structure resulting in a less rough surface of twinned martensite [103].

2.3.6 Modelling of shape memory alloys

A variety of theoretical models have been established in order to model, understand and predict the behavior of shape memory alloys. These models approach the mechanisms in SMA at all length scales between the atomic level and macroscopic samples, and are capable of treating single crystalline as well as polycrystalline samples.

---

[3]The mathematical details will not be discussed here. The reader may refer to [99, 117, 119] and references given therein.

The detailed mechanisms of lattice deformation during phase transformation like transition pathways and deformation modes on the atomic scale are treated by first-principle calculations [123–126]. Micromechanical approaches describe the crystallographic mechanisms on the grain scale, considering chemical, mechanical and thermal energy contributions [127, 128]. These models are very powerful and povide a deep understanding of microstructural mechanisms in SMA. On the other hand they are far too complex and computationally expensive to handle the macroscopic behavior of whole samples or devices.

Therefore, a number of macroscopic continuum models have been introduced, treating the sample behavior based on homegenized, averaged material properties (which are, however, based on microscopic considerations) [129, 130]. Two important groups of macro-models shall be briefly described in the following.
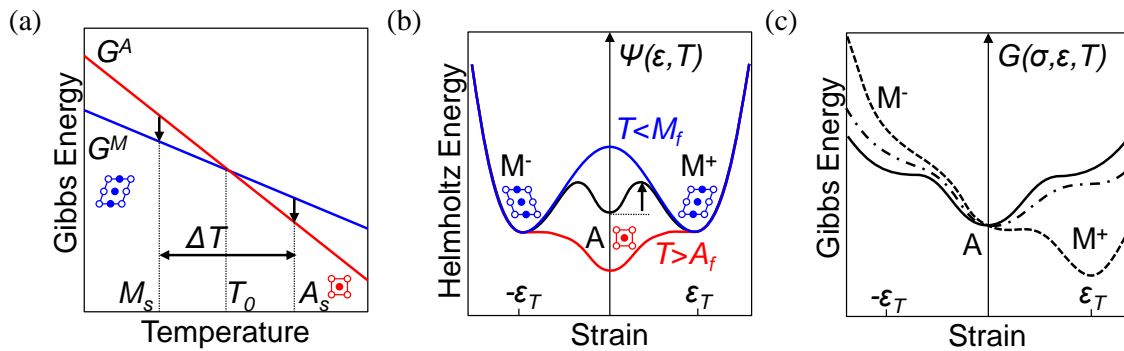
Figure 2.15: (a) Schematic Gibbs free energy potentials of austenite (A) and martensite phase (M) as a function of temperature. (b) Helmholtz free energy as a function of strain for three different temperatures as indicated. (c) Gibbs free energy as a function of stress and strain at a temperature $T > A_f$. Compare Refs. [131, 132].

Thermodynamics-based free energy models   Some models treat the behavior of SMA as thermally activated processes based on Gibbs free energy. One representative of this group is the Seelecke-Müller-Achenbach model [132–134]. A schematic one-dimensional energy landscape of a stress-free SMA as a function of strain is shown in Fig. 2.15 (b). The energy landscape may exhibit up to three local minima in the temperature regime of phase coexistence (black curve), corresponding to the austenite phase (A) at $\varepsilon = 0$ and two variants of martensite phase (M⁻, M⁺) at the transformation strain $\varepsilon = \mp\varepsilon_T$.[4] These local minima are described by parabola in the model, which are separated by potential wells. When decreasing the temperature, the central minimum rises with respect to the outer minima, until completely vanishing at $T = M_f$ (blue curve) – now, only the two martensite variants are thermodynamically stable. When, on the other hand, in-

---

[4]Note that the assumption of two variants (associated with tension and compression) is a simplification. In reality, the number of martensitic variants is larger, e.g., 24 in the case of TiNi.

creasing the temperature, the outer minima rise until vanishing at $T = A_f$. Then, austenite becomes the thermodynamically stable phase.

The case of pseudoelastic loading at a temperature above A_f is shown in Fig. 2.15 (c). In this case, the energy landscape is increasingly tilted with increasing applied stress σ.[5] The potential of the martensite variant M$^+$ oriented favorably to the tensile direction decreases, whereas the potential of M$^-$ increases. At some point, the variant M$^+$ becomes energetically more favorable than the austenite – stress-induced martensite is formed. In order to transit from one phase to another ($\alpha \rightarrow \beta$), the potential well separating the two corresponding free energy minima has to be overcome. This process is described as thermally activated, hence the transition probability is proportional to the Boltzman factor depending on potential well height $\Delta G_{\alpha\beta}$ and temperature T (k_B being the Boltzman constant):

$$p_{\alpha \rightarrow \beta} \propto e^{-\frac{\Delta G_{\alpha\beta}}{k_B T}} \tag{2.19}$$

These models establish a direct connection of sample behavior and continuum thermodynamcis, but certain parameters as the potential wells $\Delta G_{\alpha\beta}$ cannot be directly obtained from experimental data.
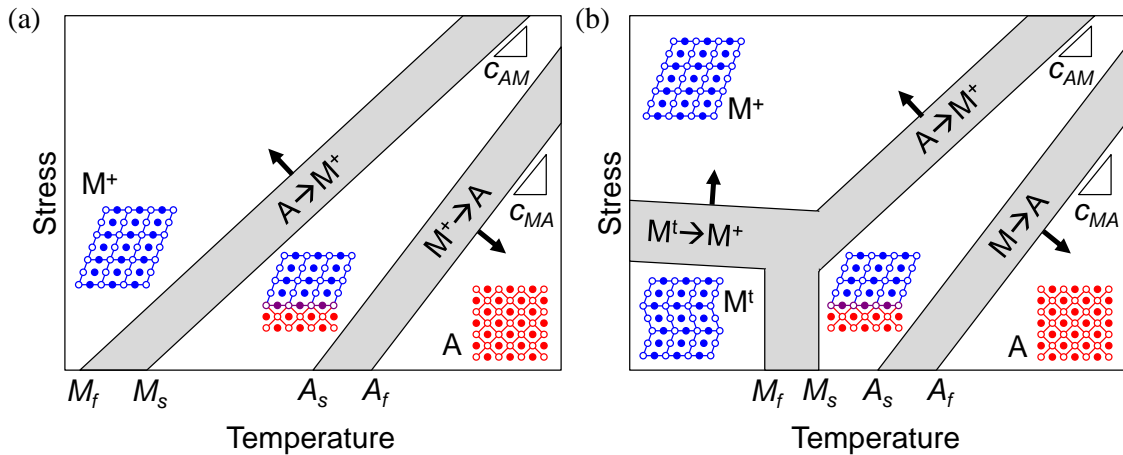
Figure 2.16: Schematic phase diagrams of constitutive shape memory models. (a) Tanaka-type model describing superelasticity. (b) Brinson-type model describing superelasticity and one-way shape memory effect. Compare Ref. [130]

---

[5]The Gibbs free energy G depends on the Helmholtz free energy Ψ by $G(\sigma, \varepsilon, T) = \Psi(\varepsilon, T) - \varepsilon\sigma$. In the Seelecke-Müller-Achenbach model, the Helmholtz free energy is defined piecewise by parabola representing the involved phases: $\frac{E_M}{2}(\varepsilon + \varepsilon_T)^2$ for the M$^-$ variant, $\frac{E_A}{2}\varepsilon^2 - \Delta\beta(T)$ for the austenite and $\frac{E_M}{2}(\varepsilon - \varepsilon_T)^2$ for the M$^+$ variant. E_A and E_M represent the elastic moduli of austenite and martensite and $\Delta\beta(T)$ the temperature-dependent potential height of austenite with respect to martensite. Parabola are connected by transition regions representing the potential wells. See Ref. [132] for details.

Phenomenologic constitutive models   In order to be able to simulate SMA behavior based on experimentally determined parameters, several phenomenological models have been proposed, which are based on schematic temperature-stress phase diagrams, as shown in Fig. 2.16. In these models, the dynamics of phase transformation are described by a coupled set of macroscopic constitutive equations, which are essentially a mechanical law representing stress-strain behavior and a kinetic law describing the evolution of phase fractions (e.g., of de-twinned martensite) as a function of stress and temperature [130, 135].

The first such model was introduced by Tanaka and Nagaki [136–138]. It is a one-dimensional model based on a simple phase diagram as indicated in Fig. 2.16 (a), which considers only two phases (M,A). The phase diagram comprises two phase transformation regions – one describing the forward A→M and the other the reverse M→A transformation – whose slope is given by the Clausius-Clapeyron coefficients c_{AM} and c_{MA} of the considered material. In between the transformation region, a two-phase region is found, where both phases may coexist and their phase fractions depend on thermo-mechanical sample history. Tanaka-type models have been extended to 2D [139] and 3D to simulate SMA microactuators [140, 141], as well as (in a first attempt) the elastocaloric effect in thin samples [142].

A number of similar constitutive models have been developed by different authors. A comparison is given in Refs. [130, 135]. It was shown that the differences between the models result predominantly from the employed kinetic law and less from the mechanical assumptions (rule of mixture). In the model of Brinson et al. [143, 144], the phase diagram is slightly modified to include twinned as well as de-twinned martensite (compare Fig. 2.16 (b)). The model was extended to 3D by combining the above constitutive models with microplane theory, in which a number of representative crystal planes is considered rather than all possible crystallographic variants [145, 146]. In contrast, Patoor et al. included all 24 martensitic variants in their 3D micro-macro model [147].

Simulation of Lüders bands   Different approaches have been followed in order to capture the localized phase transformation behavior in SMA, including sharp interface models [148, 149], phase field models [150–153] and other continuum approaches [154, 155]. Some recent one-dimensional models include the effects of self-heating and cooling and are capable of predicting the increasing number of Lüders bands with increasing strain rate [156–158].

2.4 Sample fabrication

Shape memory alloys, in particular binary NiTi or 'Nitinol', are nowadays commercially available in many different geometries including bulk parts, wires, tubes, sheets, foils and films or coatings. Actuation is mostly performed by wires and

coil-shaped springs, whereas medical stents are fabricated from tubes. For elastocaloric cooling, on the other hand, flat geometries are of particular interest, as they allow for efficient heat transfer due to a large surface-to-volume ratio. In the following, the most common fabrication methods for SMA sheet material with low thickness will be described.

Fabrication of SMA usually begins with the production of an ingot having the desired alloy composition. For this purpose, high purity elemental metals are weighted, mixed and melted together. A typical setup is shown schematically in Fig. 2.17 (a): The pure metals are placed in a graphite crucible and melted under inert gas atmosphere by inductive heating. Special care has to be taken to omit the entry of oxygen, carbon and other impurities, since these strongly affect the properties of the SMA [49, 50, 159]. The molten alloy is poured into a mold having the desired shape of the work piece. In order to achieve a homogeneous alloy, often several breaking, mixing and remelting steps are performed [46].
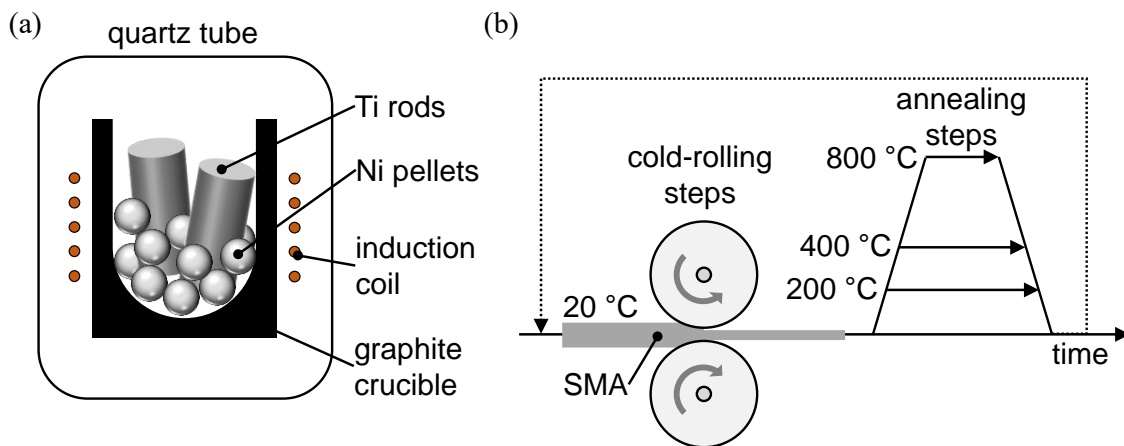
Figure 2.17: (a) Fabrication of a shape memory alloy ingot by inductive melting under inert gas atmosphere (compare Ref. [159]). (b) Schematic cold rolling process. The SMA ingot is thinned by several rolling steps at ambient temperature, followed by annealing steps (compare Ref. [101]).

2.4.1 Cold rolling

Starting from a stoichiometric ingot, fabrication of thin SMA sheets, bands and foils is commonly achieved by cold-rolling (Fig. 2.17 (b)). Cold-rolling is a top-down fabrication method based on plastic deformation of the processed material, which should not be too brittle. TiNi-based foils, for example, can be fabricated with minimum thicknesses between 100 and $20\,\mu\text{m}$. In contrast to hot-rolling, thinning takes place at a temperature below the re-crystallization temperature of the material – usually at ambient temperature – which allows for more precise thickness control. Since the achievable volume change by cold-working is limited, several consecutive rolling steps followed by heat treatment steps are per-

formend. Cold-rolling induces defects in the material, leading to so-called work-hardening and improving structural stability [101]. An additional heat treatment step may be performed to (partly) re-crystallize the microstructure and adjust phase transformation properties [52, 160]. Due to the directionality of the process, cold-rolled materials may exhibit a textured microstructure and strongly anisotropic properties [74, 94, 161–163]. Samples fabricated by cold-rolling will be referred to as 'foils' in the following.

2.4.2 Sputter deposition
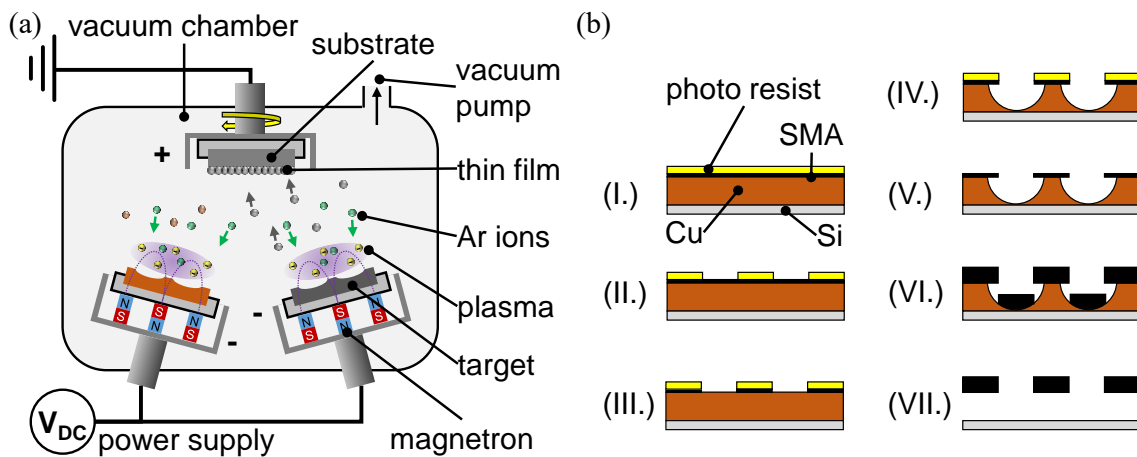
Figure 2.18: (a) Schematic setup for DC magnetron sputtering with two targets. (b) Structuring of SMA film samples by the mushroom process (compare Ref. [164]).

A second common fabrication method for thin SMA material is sputter deposition, which is a physical vapor deposition (PVD) method. Since it follows a bottom-up approach, films and coatings having very low thicknesses down to fractions of an atomic monolayer may be produced, whereas fabrication of thicker layers (up to $100\,\mu\mathrm{m}$) is more time-consuming. Films having very high purity and containing no inclusions may be produced. As in cold rolling, sputter deposition starts with a stoichiometric target of the desired alloy. The target is mounted on a magnetron and placed in a vacuum chamber, which also contains the substrate for film deposition, facing the target – see schematic in Fig. 2.18 (a). The chamber is evacuated by pumps and then filled with a process gas, e.g., Ar. Subsequently, a DC (direct current) voltage is applied between substrate and target, accelerating positive Ar ions towards the target. The impact of Ar ions, in turn, knocks out metal atoms from the target, which are deposited on the substrate and other surfaces of the setup. Due to the magnetic field of the magnetron, a plasma is formed and contained closely above the target, making the process more efficient. The use of several targets at the same time (as indicated in the schematic) allows to vary the film composition and produce films with stoichiometry gradients. Since as-deposited SMA films are amorphous, one or several annealing

steps are performed after sputter deposition. Temperature and duration are adjusted to obtain the desired properties of the films, e.g., grain size, phase transformation temperatures and the formation of precipitates [103]. Samples produced by sputter deposition will be referred to as 'films' throughout this thesis.

A special process – called the *mushroom process* – was developed at the University of Kiel, in which the substrate is structured prior to deposition of SMA films [164]. The schematic process is depicted in Fig. 2.18 (b). In the first step (I.), a sacrifical copper layer and a thin SMA seed layer are sputter-deposited on a silicon substrate, which is then covered with a photo resist by spin coating. In the second step (II.), the photo resist is patterned by ultraviolet (UV) photolithography. Then, the structure of the resist is transferred to the SMA seed layer by a wet etching step (III.). The sacrificial Cu layer is wet-etched as well, using a different etching solution which does not attack the SMA (IV.), before the remaining photo resist is removed (V.). Since the Cu etching step is isotropic, the process results in semi-freestanding SMA patterns carried by the remaining Cu fillets, whose cross-section resembles the shape of a mushroom. In the next step (VI.), further SMA material is sputtered onto the pre-structured substrate, until the desired film thickness is reached. In the last step (VII.), the remaining Cu of the sacrificial layer is removed and freestanding, readly structured SMA films are obtained.

2.4.3 Melt-spinning

A third fabrication method for thin SMA samples is melt-spinning. SMA material is molten in a furnace, e.g., by induction heating, and guided by a nozzle towards a cooled wheel turning at high velocity. As soon as the molten SMA contacts the wheel, it solidifies, forming a thin band. The process may be continuously driven and theoretically allows for production of bands with infinite length. The thickness is adjusted by temperature and turning velocity of the wheel. An advantage of the melt-spinning method is the ultra-rapid cooling, leading to homogeneous distribution of chemical elements [165]. The resulting bands are amorphous, so that a subsequent annealing step is applied to induce (partial) re-crystallization of the SMA.

2.5 Experimental methods

The fundamental property of a SMA material for elastocaloric cooling is superelasticity, i.e. the capability of stress-induced phase transformation. Therefore, in a first step phase transformation properties are determined by temperature-dependent electrical resistance measurements, as well as differential scanning calorimetry. The latter also allows for determination of latent heats and specific heat capacities. Subsequently, samples are subjected to uniaxial tensile tests at

various strain rates. A number of mechanical parameters (E_A, E_M, σ_{crit}, ε_T, hysteresis), as well as the cyclic behavior of the material are determined from these measurements. Simultaneously to the tensile tests, infrared thermography is performed to observe temperature changes and local temperature distribution. The local strain distribution is obtained from digital image correlation evaluation of optical images.

The respective experimental methods, procedures as well as setups will be briefly described in the following.

2.5.1 Differential scanning calorimetry
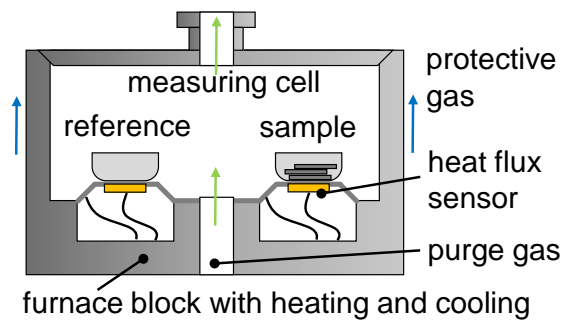
Figure 2.19: Schematic of differential scanning calorimetry (DSC) setup.

Differential scanning calorimetry (DSC) is a method widely employed to determine the phase tranformation properties of SMA [42] and many other material classes. The basic setup of a differential scanning calorimeter is shown schematically in Fig. 2.19. The setup consists of a temperature-controlled chamber, in which two small pans are placed – one containing the sample material and the other one left empty to serve as a reference. During the experiment, temperature is increased (or decreased) at constant rate and the heat flows into or out of both pans are measured. The pans are chosen to have approximately the same mass, so that the heat flow *difference* between them represents the heat flow associated with the sample material. For a material with constant heat capacity, the measured signal will be constant. However, in case an exothermal (or endothermal) reaction occurs, the decreased (increased) heat flow can be seen as a peak in the measurement – compare, e.g., Fig. 2.8. A standard test method for characterizing TiNi-alloys (as representative SMA) is decribed in ASTM norm F2004-05 [166] whereas additional practical advises are given in Ref. [42]. By convention, the austenitic and martensitic start and end temperatures A_s, A_f, M_s and M_f are determined by the tangent rule.[6] The latent heat of a transformation is also determined by DSC by integrating the area between the transformation peak and a flat baseline connecting the regions to the left and right of the peak.

---

[6]According to the tangent rule, each transformation temperature is determined by the intersection point of a tangent on the curve far from the transformation with a tangent through the steepest flank of the observed peak.

In this work, measurements are performed using a Netsch Phoenix DSC 204, which allows for cooling down to $-100\,°C$ by cold nitrogen gas, and to below $-180\,°C$ using liquid nitrogen. Gaseous nitrogen is also used as purge and protective gas to prevent sample oxidation. At least $7\,mg$ of sample material is inserted to an aluminum pan. Pieces of SMA films and foils are carefully stapeled inside the pan to guarantee good thermal contact, before the pan is closed with a pierced cap. Measurement usually consists of a heating step from the lowest to the highest temperature of the intended temperature range, a cooling step and a second heating step. Heating / cooling rate is $\pm10\,K\,min^{-1}$. When switching from heating to cooling and vice versa, temperature is held constant for $2\,min$ in order to assure stationary conditions. After the measurement, transformation temperatures and latent heat are determined using the proprietary Netsch Analysis software.

The same DSC setup is also used for determination of heat capacity at constant pressure c_p. The procedure is described in ASTM norm E1269-11, as well as in German DIN 53765 [167, 168]. In order to obtain reliable results, sample mass is increased to at least $30\,mg$ and heating/cooling rate is increased to $\pm20\,K\,min^{-1}$. An additional measurement on a synthetic sapphire standard, using the same aluminum pan and the same temperature program as for the sample, is required for calibrated evaluation of c_p. Heat capacity measurement are only meaningful for temperature intervals, in which no phase transformation takes place in the sample, since the sensible heat cannot be separated from latent heat. A method for determining c_p even in a temperature interval of phase transformation is modulated DSC [169, 170], which however was not accessible for the present work.

2.5.2 Electrical resistance measurement

Since electrical resistance sensitively depends on crystal lattice, stress-induced phase transformation in SMA is associated with characteristic changes of the resistance curve [171, 172]. Resistance measurements as a function of temperature are therefore a common method for determining phase transformation temperatures.

Here, electrical resistance is measured by the four-probe method, having the advantage of ruling out contact resistances of the experimental setup. For this purpose, four electrical contacts are attached in a line to the surface of the SMA sample. A current I is applied to the outer contacts (I^+, I^-). The voltage drop U between the inner contacts (U^+, U^-) is then measured and the electrical resistance R is calculated according to Ohm's law: $R = U/I$. Contacting of the sample is obtained by spring probe contacts. In some cases, electrical contact is instable due to an oxide layer at the sample surfaces. This problem can be solved by carefully polishing the surface and, in some cases, changing from spring contacts to wire bonds.

In order to measure electrical resistance as a function of temperature, the sample is placed in a cryostat with active temperature control, operated under vacuum of about 2×10^{-2} mbar. Temperatures between $-185\,°\text{C}$ and $300\,°\text{C}$ can be achieved by injecting a flow of (liquid) nitrogen and by electrical heating, respectively. Measurements are controlled by a custom LabView script and conducted under quasi-static conditions: Prior to each measurement point, stabilization of the temperature and sample resistance is awaited.

The temperature-dependent resistance curves of SMA exhibit characteristic changes in slope, whenever the sample undergoes a structural change, e.g., due to phase transformation. Phase transformation temperatures are estimated by the tangential method: Tangents are fitted to the linear sections of the curve and intersection points are interpreted as transformation temperatures.

2.5.3 Temperature measurement

In principle, every temperature-dependent physical quantity can be used for temperature measurement, like length change of solid bodies or volume change of fluids due to thermal expansion, phase transformation properties of materials, electrical resistance, contact voltage or emission of electromagnetic waves.

The SI unit for temperature measurement, the degree Kelvin, is defined based on the triple point of water, which is at $273.16\,\text{K}$ per definition. The absolute zero point of temperature is at $0\,\text{K}$ which is equal to $-273.15\,°\text{C}$.
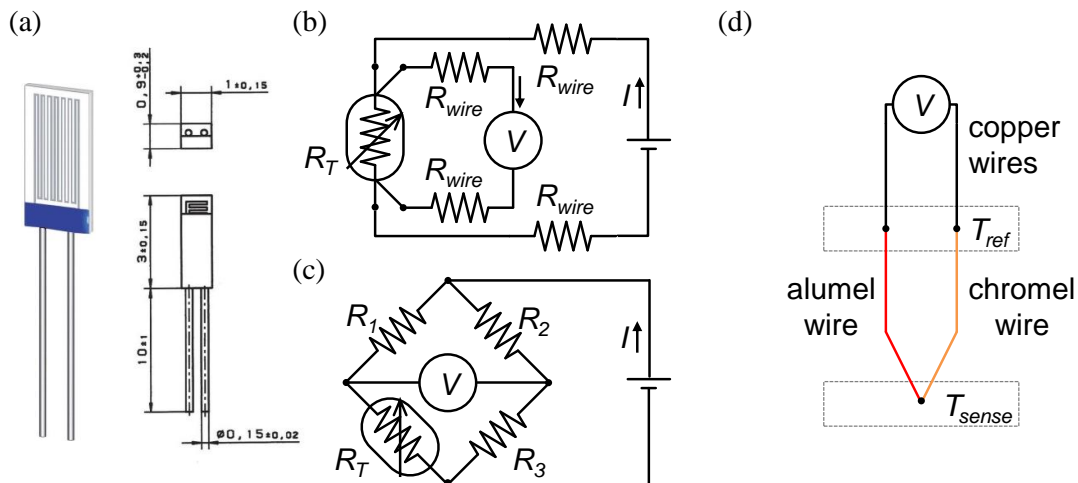
Figure 2.20: Temperature sensors delivering an electric output signal. (a) Typical thin-film Pt100 sensor. For exact readout, a four-wire circuit (b) or a Wheatstone bridge (c) is used. (d) Function principle of a thermocouple.

Resistance thermometers or resistance temperature detectors (RTD), make use of the fact that the electrical resistance of conducting materials is temperature dependent. In materials like pure metals and some doped ceramics, the resistance increases with increasing temperature, since the increasing lattice vibrations hinder the propagation of conduction electrons. Hence these materials have a positive temperature coefficient (PTC). The temperature coeficient α_0 is defined based on the electrical resistances R_0 and R_{100} at $0\,°\mathrm{C}$ and $100\,°\mathrm{C}$, respectively, assuming a linear increase:

$$\alpha_0 = \frac{R_{100} - R_0}{R_{100} \cdot 100\,°\mathrm{C}} \tag{2.20}$$

Due to its high corrosion resistance and a very stable resistance-temperature relationship over a large temperature range, platinum is a popular material for the realization of PTC sensors. Thin wires are wound around a glass or ceramic core, or meandering thin film circuit paths are structured on a ceramic substrate. In the case of a Pt100 sensor, the resistance R_0 is $100\,\Omega$, and the temperature coefficient is $3.851 \cdot 10^{-3}°\mathrm{C}^{-1}$.[7]

Resistance thermometers are read out by supplying a current and simultaneously measuring the (temperature-dependent) voltage drop over the resistance. In the simplest case, this is done over a two-wire connection. Since connecting wires, solder joints and other circuit components have an electrical resistance by their own, four wire measurements are performed to eliminte these disturbances (Fig. 2.20 (b)). Another way of obtaining very accurate measurements of small resistance / temperature changes is the use of a Wheatstone bridge (Fig. 2.20 (c)).

Advantages of RTDs are the high accuracy and stability, low drift and wide applicable temperature range. Disadvantages are the self-heating induced by the measuring current, response times in the order of seconds due to the relatively high mass, as well as limited accuracy at very low and very high temperatures.

Thermocouples are the second type of temperature sensor widely used in industry and research besides RTDs. These are based on the thermoelectric effect or Seebeck effect (Eq. 2.11) – see Section 2.2.3 for explanation.

Thermocouples have the advantage of being self-powered. On the other hand, accuracy is limited to about $1\,\mathrm{K}$, since voltages are typically in the microvolt range. One end of the thermocouple has to be held at a defined reference voltage (e.g., by placing it in iced water). Thermocouples can be fabricated from different material

---

[7]For extended temperature ranges, the norm DIN EN 60751 defines the following non-linear approximations of the resistance characteristic [173]:

$$R_T = R(T) = R_0(1 + A \cdot T + B \cdot T^2), \quad T \in (0 \ldots 850\,°\mathrm{C}) \tag{2.21a}$$

$$R_T = R_0(1 + AT + BT^2 + C(T + 100\,°\mathrm{C})T^3), \quad T \in (-200 \ldots 0\,°\mathrm{C}) \tag{2.21b}$$

with $A = 3.9083 \cdot 10^{-3}°\mathrm{C}^{-1}$, $B = -5.775 \cdot 10^{-7}°\mathrm{C}^{-2}$ and $C = -4.183 \cdot 10^{-12}°\mathrm{C}^{-4}$.

pairs. A common general-purpose thermocouple is the K type couple, using the alloys chromel and alumel and having a sensitivity of about $41\,\mu V\,°C^{-1}$.

2.5.4 Tensile test
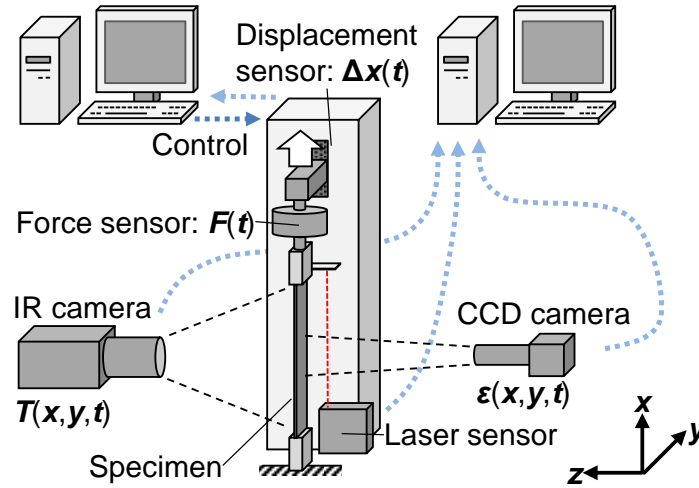
Figure 2.21: Schematic of tensile test setup.

The mechanical properties of shape memory alloys are determined in uniaxial tensile tests [59]. In a rod of a general elastic material, the local dependence between stress σ and strain ε is described by Hooke's law:[8]

$$\sigma = \varepsilon E \tag{2.22}$$

This dependency is in analogy to a linear spring, where the elastic modulus E takes the role of a spring constant. In a typical tensile experiment on a sample with length L_0 and cross-sectional area A, the averaged strain over the whole sample or *engineering strain* is calculated by dividing the length change ΔL by the initial lenght: $\varepsilon = \Delta L/L_0$. The term 'strain' will be mostly used in the sense of an engineering strain throughout this thesis. The stress is calculated by dividing the applied force F by the sample cross-section: $\sigma = F/A$.

In this work tensile tests are carried out using a Zwicki Line tensile test machine (Zwick Roell) equipped with a spindle drive motor and a $50\,N$ force sensor having a resolution of $0.25\,N$. The displacement measurement is performed by an internal sensor inside the spindle drive at a resolution of $0.25\,\mu m$. A schematic of the setup is shown in Fig. 2.21. In conrast to other investigations based on dogbone-shaped samples, rectangular samples are used here, having a typical free length of $L_0 = 15\,mm$ and cross sections of 0.03 to $0.06\,mm^2$. Sample ends

---

[8]In the general formulation, stress and strain are tensors, which however shall be omitted here for sake of simplicity.

are attached in a sandwich between two alumina plates of $0.5\,\mathrm{mm}$ thickness using two-component epoxy adhesive (EPO-TEK 353ND), which is cured at $120\,°\mathrm{C}$. Alumina plates are then connected to the stationary and movable sample holders of the tensile test machine. Compared to direct clamping, stress peaks at the sample fixitation are thus omitted. For tensile test on brittle samples, a special frame includig linear guidance in tensile (x) direction is constructed in order to elminiate shear and bending loads acting upon the sample (Fig. 2.22 (a)). The same frame is later used for demonstrator characterization (see Chapter 6).
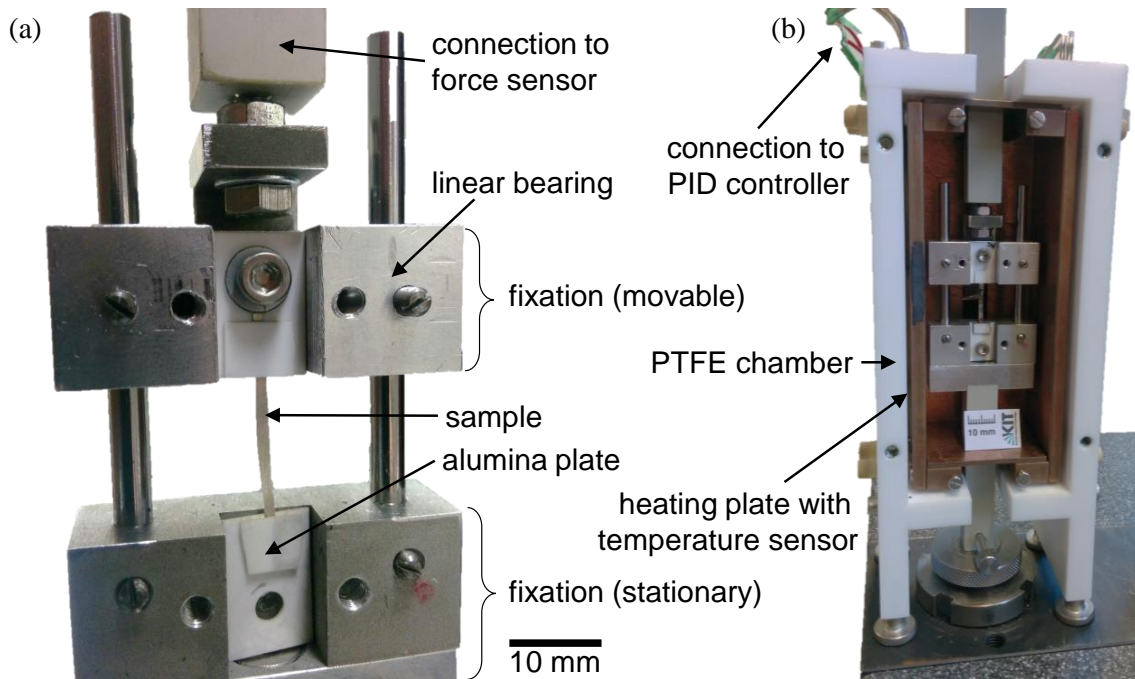
Figure 2.22: (a) Sample mounted to sample holder with linear guidance. (b) Heating chamber in open state (cover plate not shown).

In order to determine Clausius Clapeyron coefficients, tensile tests have to be performed at different ambient temperatures. For this purpose, a heating chamber is built, consisting of an outer housing made from PTFE (polytetrafluoroethylene or 'Teflon') for thermal insulation, as well as an inner shell made from copper plates (Fig. 2.22 (b)). The copper plates to the left and right of the sample contain heating wires and thermocouples for temperature control. Temperature is adjusted and stabilized by a PID (proportional–integral–derivative) controller. The sample holder is placed inside the chamber and connected to the tensile test machine by PEEK (polyether ether ketone) bars. Then the chamber is closed by a PTFE cover plate containing a glas window for optical inspection of the sample. The opposite wall of the chamber contains an infrared-transparent germanium window.

In the usual case, tensile tests are performed at ambient temperature in air without using the heating chamber. Experiments are carried out in displacement-control mode, hence the sample elongation is increased and decreased linearly in

time. The strain rate $\dot{\varepsilon}$ is varied between 10^{-4} and $2\,\mathrm{s}^{-1}$. It is calculated from the displacement rate and the initial sample length:

$$\dot{\varepsilon} = \frac{1}{L_0}\frac{dL}{dt} \tag{2.23}$$

Note that this rate again refers to the averaged engineering strain. Experiments are carried out cyclically by moving the sample end between a *loading* and an *unloading* point. The loading point is displacement-controlled. The unloading point is force-controlled to avoid buckling of the sample in case that plastic strain occurs. The force is set to $1\,\mathrm{N}$, which corrsponds to between 17 and $33\,\mathrm{MPa}$, depending on sample cross-section. A typical tensile test is performed as follows:

1. Apply small pre-load of $1\,\mathrm{N}$ in order to avoid buckling.

2. Load sample at constant rate $\dot{\varepsilon}$ until the specified maximum strain ε_{max} is reached ($\varepsilon_{max} = L_{max}/L_0$).

3. Hold position constant for $10\,\mathrm{s}$ to allow for temperature equalization.

4. Unload sample at constant rate $\dot{\varepsilon}$ until the pre-load of $1\,\mathrm{N}$ is reached.

5. Hold force constant for $10\,\mathrm{s}$ to allow for temperature equalization.

6. Start with 2. again, until specified number of cycles is reached.
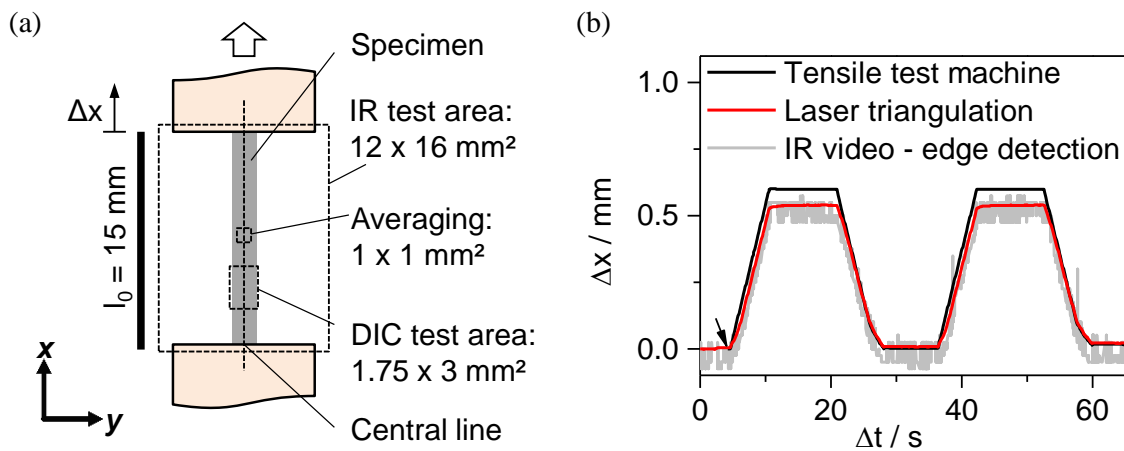
Figure 2.23: (a) Schematic of tensile test sample. Test areas for infrared (IR) thermography and digital image correlation (DIC) are indicated. (b) Sample elongation Δx versus time measured by tensile test machine, Laser triangulation sensor and IR edge detection. Time axes are correlated based on the first slope rise (indicated by arrow).

During tensile expriments, samples are monitored by an infrared camera and a CCD camera, both mounted on xyz-stages for precise alignment with respect to the sample. Depending on the experiment, either one or both of the cameras are used. As CCD and IR image acquisition is not performed on the same computer

that controls the tensile test machine, the time axis of data sets is synchronized by using the point in time, where loading begins (Fig. 2.23 (b)).

As a comparison of the different displacement measurements – using the tensile test machine, the IR camera and an additional Laser triangulation sensor – shows, the displacement measurement of the tensile test machine has a systematic error in the order of 10% due to the measurement principle of the force sensor and elastic components in the setup (Fig. 2.23 (b)). However, since data correction using alternative displacement signals is only possible in some cases, raw data from the tensile test machine is used for evaluation to maintain consistency between datasets.

2.5.5 Infrared thermography

Infrared thermography makes use of the thermal radiation described in Section 2.1.3 for thermal imaging. Infrared (IR) light covers the wavelength range of about 0.9 to $14\,\mu m$ of electromagnetic radiation and is invisible for the human eye. In contrast to the temperature sensors decribed above, IR thermography allows for contact-less and spatially resolved temperature measurement. Similar to digital cameras, IR cameras contain a detector comprising a two-dimensional focal plane array of individual pixels. Detectors may essentially be separated in two groups: thermal detectors and quantum detectors. The latter are based on an internal photoelectric effect. They achieve the highest sensibility and allow for frame rates in the kHz range, but are rather expensive and require active cooling (another application for microcooling!). In comparison, thermal detectors like uncooled microbolometer detectors are much cheaper and do not require active cooling. In each pixel, temperature is measured based on the change of a physical property, e.g., electrical resistance, of the (metal or semiconductor) detector material caused by radiant energy. Independent of the IR detector type, IR transparent optics have to be used, which are fabricated, e.g., from silicon or germanium.

Since most real objects do not behave like perfect black-bodys, and are furthermore surrounded by atmosphere, the total radiative power W_{tot} received by an IR camera pointed at an object with a radiative power of W_{obj} can be expressed as

$$W_{tot} = \varepsilon \cdot \tau \cdot W_{obj} + (1 - \varepsilon) \cdot \tau \cdot W_{amb} + (1 - \tau) \cdot W_{atm} \qquad (2.24)$$

where ε is the emissivity of the object, τ is the transmissivity of the atmosphere, W_{amb} is the radiative power of objects in the surroundings (whose thermal radiation is reflected by the object) and W_{atm} is the radiative power of the atmosphere [19]. In the present work, the distance between sample and close-up lense of the IR camera is only $60\,mm$, so that the impact of the atmosphere is negligible. However, the emissivity of typical metal surfaces (including SMA samples) is typically

quite low. Therefore, sample surfaces are covered by a thin layer of graphite spray in order to increase emissivity up to 0.98.

In this work, a FLIR A655sc infrared camera is used, having an uncooled microbolometer detector with a spectral range of 7.5 to $14\,\mu m$ (long-wavelength infrared). The thermal sensitivity and accuracy are $< 50\,mK$ and $\pm 2\,°C$, respectively. The camera has a detector resolution of 640×480 pixels and a maximum frame rate of $200\,Hz$. It is equipped with a close-up lense, resulting in a spatial resolution of $25\,\mu m\,pixel^{-1}$. The corresponding field of view is $12 \times 16\,mm^2$, as indicated in Fig. 2.23 (a). The proprietary analysis software ('ResearchIR') allows for producing false-color thermal images (as shown in Chapters 4 and 6), extracting line profiles and calculating average temperatures over rectangular/circular regions of interest.

2.5.6 Digital image correlation

Digital image correlation (DIC) provides a method for calculating spatially resolved, two-dimensional maps of local strain [174, 175]. In this work, DIC is used to observe Lüders-like strain bands in pseudoelastic samples. A series of greyscale images of a sample region of interest is acquired during tensile tests. In DIC evaluation, a grid of points is defined in a reference image (e.g., the first one). These points are then tracked in all the other images by taking a tile of pixels around each point in the reference image and finding the position with the highest cross-correlation in each of the remaining images. Local strains are then calculated from the distance change between neighboring points of the grid. Hence, the method is invariant to rigid displacement of the sample. In order for the cross-correlation algorithm to work, the observed surface has to exhibit a speckle pattern (or other distinguishable features) which is stable from image to image.

In this work, images for DIC evaluation are acquired with a CCD camera (mvBlue-fox124G, Matrix Vision) having a resolution of 1200×1600 pixels and a maximum frame rate of $10\,Hz$. A microscope lense is attached to the camera, yielding in a spatial resolution of $2.5\,\mu m$. In order to create a speckle pattern, the observed sample surface is covered with a thin layer of graphite spray thinned with isopropanol. The sample is illuminated by an LED lamp in close proximity, which may increase sample temperature by several $°C$. Images are acquired using a custom Labview script. At the same time, the script acquires a position measurement of the upper sample fixation using a Laser triangulation sensor (Panasonic HL-G103S) with a spatial resolution of $0.5\,\mu m$. This position signal is used to correlate DIC data with tensile test data (see Fig. 2.23). DIC evaluation is performed using a modified version of the Matlab code provided by C. Eberl [176] (see also Ref. [175]). The script allows for defining the point grid, eliminating points that could not be tracked correctly, and exporting colored strain maps. The size of each tile

for cross-correlation is 30×30 pixels, hence the spatial resolution of the strain maps is $75\,\mu m$.

3 Ferroic cooling – state of the art
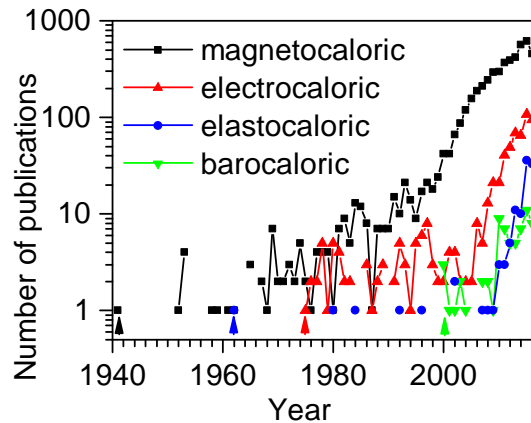
Figure 3.1: Evolution of the annual number of publications on caloric effects in scientific journals and conference proceedings (logarithmic scale). Earliest publication on each effect is marked by arrow. Based on research on Scopus publication database [177].

Due to the various shortcomings of present-day cooling and heat pumping technologies (see Introduction and Section 2.2), interest in proper alternatives is strongly growing; research efforts are intensified and several countries launched extensive funding programms in order to boost progress [178]. One of the most promising directions of research is focused on so-called *ferroic cooling* technologies [1, 12]. These are based on *caloric effects* in ferroic materials associated with solid-to-solid phase transformations. Depending on the driving field, the effects are referred to as magnetocaloric, electrocaloric, elastocaloric or barocaloric effects. The latter two are often summarized as mechanocaloric effects. While magnetocaloric materials have already been investigated for several decades [179–184], a number of prototypes have been built [185–191] and first commercial products are under development [192, 193], research on the other caloric effects is still at its beginning. This can be seen from Fig. 3.1, showing how the annual number of publications on caloric effects evolved since the middle of the 20th century.[1] Recently, a number of review articles have been dedicated to caloric materials [12, 194–199] and design approaches for caloric cooling devices [22, 178, 200, 201].

---

[1]Meta-analysis based on publication database Scopus (Ref. [177], accessed 2016/06/11). Search was performed using the keywords 'magnetocaloric', 'electrocaloric', 'elastocaloric' and 'barocaloric' for search fields Title, Abstract and Keywords, and source types Journals and Conference Proceedings.

3.1 Caloric effects in ferroic materials
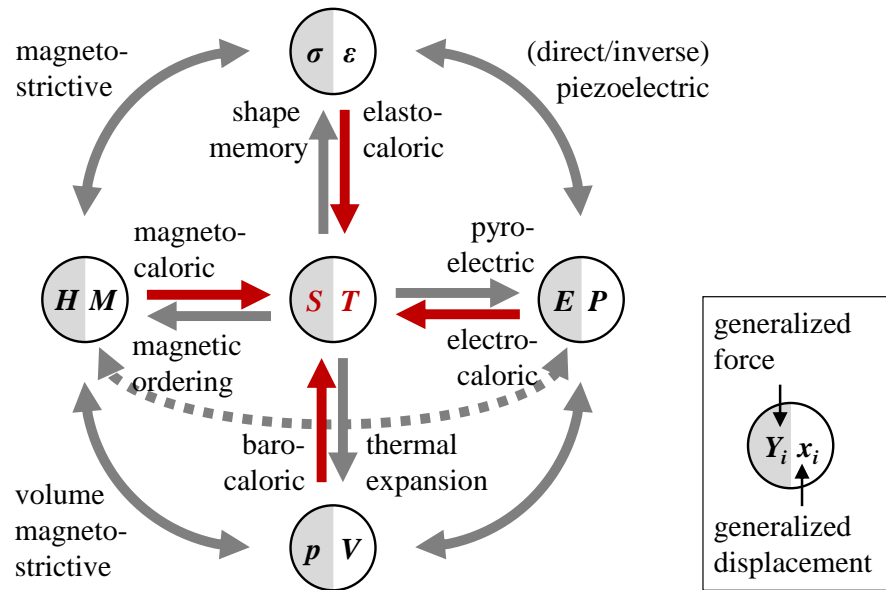
Figure 3.2: Schematic diagram of the complex coupling and interdependency of physical parameters in ferroic materials. Each circle represents a pair of driving field (generalized force) and order parameter (generalized displacement).

Caloric effects occur in many materials due to entropy changes induced by external fields. For instance, natural rubber and other polymers release heat upon stretching and cool down when they are relieved again [202–204]. However, the effect size is usually too low for technical applications. Considerable caloric effects – sometimes termed 'giant caloric effects' – are associated with solid-state phase transformations in ferroic materials. These materials are characterized by a diffusionless and reversible phase transformation. The caloric effect is particularly high in the case of first-order transformations, since in this case a small variation of external control parameters leads to considerable changes of extensive thermodynamic quantities. One of the phases in ferroic materials exhibits symmetry-breaking and a spontaneous long-range ordering of crystal axes, magnetic moments, electric dipoles etc., leading to the formation of domains. Due to this ordering, phase transformation may be driven not only by temperature, but also by external fields. The term 'ferroic materials' was created by Japanese physicist Kêitsiro Aizu [205] and hints at the analogy between magnetic ordering in ferromagnetics like iron (latin: *ferum*) and ordering phenomena, e.g., in ferroelectrics and (ferroelastic) shape memory alloys.

A thermodynamic system may be described by generalized forces (driving fields) $\{Y_i\}$ and displacements (order parameters) $\{x_i\}$, as well as temperature T. Each pair (Y_i, x_i) is formed by two conjugated thermodynamic quantities of the same tensorial rank, whose product has the dimension of an energy density. Table 3.1 gives an overview on the forces and displacements for the various caloric

Table 3.1: Comparison of the caloric effects in ferroic materials.

	Magnetocaloric	Electrocaloric
Driving field Y_i	Magnetic field H	Electric field E
Order parameter x_i	Magnetization M	Polarization P
Tensorial rank	1 (vector)	1 (vector)
Ordering entities	Magnetic domains	Polar domains
Dissipation	Eddy current heating	Joule heating
Material classes	Gd-based alloys, Heusler alloys, Mn-based alloys, La(Fe$_{13-x}$M$_x$)-based compounds, Manganites	Hydrogen-bonded ferroelectrics, ceramic perovskites, ferroelectric co-polymers, ferroelectric relaxors
Conventional effect	MnCoGeB$_{0.02}$ (24 K) [206]	(Pb$_{0.86}$La$_{0.08}$)(Zr$_{0.65}$Ti$_{0.35}$)O$_3$ (45 K) [207]
Inverse effect	Ni$_{50}$Mn$_{34}$In$_{16}$ (-2.2 K) [208]	La-doped Pb(Zr$_{0.95}$Ti$_{0.05}$)O$_3$ thin films (-5.5 K) [209]
Development state	Pre-industrial	First demonstrators

	Elastocaloric	Barocaloric
Driving field Y_i	Uniaxial stress σ	Hydrostatic pressure p
Order parameter x_i	Strain ε	Lattice cell volume V
Tensorial rank	2 (matrix)	0 (scalar)
Ordering entities	Crystallographic variants	(Magnetic domains)
Dissipation	Frictional heating	(Frictional heating)
Material classes	Conventional and magnetic shape memory alloys (ferroelastics)	Magnetic shape memory alloys
Conventional effect	Ti$_{49.5}$Ni$_{50.5}$ (58 K) [96]	Fe$_{49}$Rh$_{51}$ (10 K) [210]
Inverse effect	Fe$_{49}$Rh$_{51}$ (-5.12 K) [211]	LaFe$_{11.33}$Co$_{0.47}$Si$_{1.2}$ (-2 K) [212]
Development state	First demonstrators	Material research

effects. Based on Maxwell relations, the infinitesimal entropy change dS in a ferroic material resulting from infinitesimal changes in the driving fields $\boldsymbol{Y}_i$ may be expressed as follows [213]:

$$dS = \frac{C}{T}dT + \sum_{i=1}^{n} \left(\frac{\partial \boldsymbol{x}_i}{\partial T}\right)_{\{\boldsymbol{Y}_{j=1,\ldots,n}\}} \cdot d\boldsymbol{Y}_i \tag{3.1}$$

where C is the material's heat capacity at a constant value of the fields. In ferroic cooling, one (or several) of the generalized forces is used as a control parameter to induce caloric effects. The caloric effect size may be quantified either based on the associated entropy change ΔS in case of isothermal application of the field, or temperature change ΔT in case of adiabatic application of the field:

$$\Delta S(0 \rightarrow \boldsymbol{Y}_i) = \int_0^{\boldsymbol{Y}_i} \left(\frac{\partial \boldsymbol{x}_i}{\partial T}\right)_{\{\boldsymbol{Y}_{j=1,\ldots,n}\}} \cdot d\boldsymbol{Y}_i \tag{3.2a}$$

$$\Delta T(0 \rightarrow \boldsymbol{Y}_i) = \int_0^{\boldsymbol{Y}_i} \frac{T}{C} \left(\frac{\partial \boldsymbol{x}_i}{\partial T}\right)_{\{\boldsymbol{Y}_{j=1,\ldots,n}\}} \cdot d\boldsymbol{Y}_i \tag{3.2b}$$

In the general case that dissipative processes are involved, the entropy contains an additional irreversible contribution $\delta S_i \geq 0$ and the following equations apply to the total entropy and temperature change:

$$\Delta S(0 \rightarrow Y) \geq \int_0^Y \frac{\delta q}{T} = \int_0^Y dS - \delta S_i \tag{3.3a}$$

$$\Delta T^{irr}(0 \rightarrow Y) \geq \Delta T(0 \rightarrow Y) \tag{3.3b}$$

In the case of a first-order phase transformation, a discontinuity Δx of the generalized displacement occurs. The Clausius-Clapeyron relation describing the transformation also contains the (usually weak) temperature-dependence of dissipated energy E_{diss}:

$$\frac{dY}{dT} = -\frac{\Delta S}{\Delta x} + \frac{1}{\Delta x} \cdot \frac{dE_{diss}}{dT} \tag{3.4}$$

In *multiferroics*, two or more generalized foces/displacements are interdependent. For example, many magneto- and electrocaloric materials show also elasto- and barocaloric effects, since the magnetic and ferroelectric sub-systems strongly depend on the crystal lattice.

In case of conventional caloric effects, where the order parameter is large for the low-temperature phase and small for the high-temperature phase, the entropy change ΔS upon field application is negative and the temperature change ΔT is positive. However, in some materials the order parameter is higher for the high-temperature phase than for the low-temperature phase. In this case, *inverse caloric*

effects occur, characterized by $\Delta S > 0$ and $\Delta T < 0$ upon field application. Inverse caloric effects require a strong coupling between different degrees of freedom, i.e. a cross-response to the various external fields.
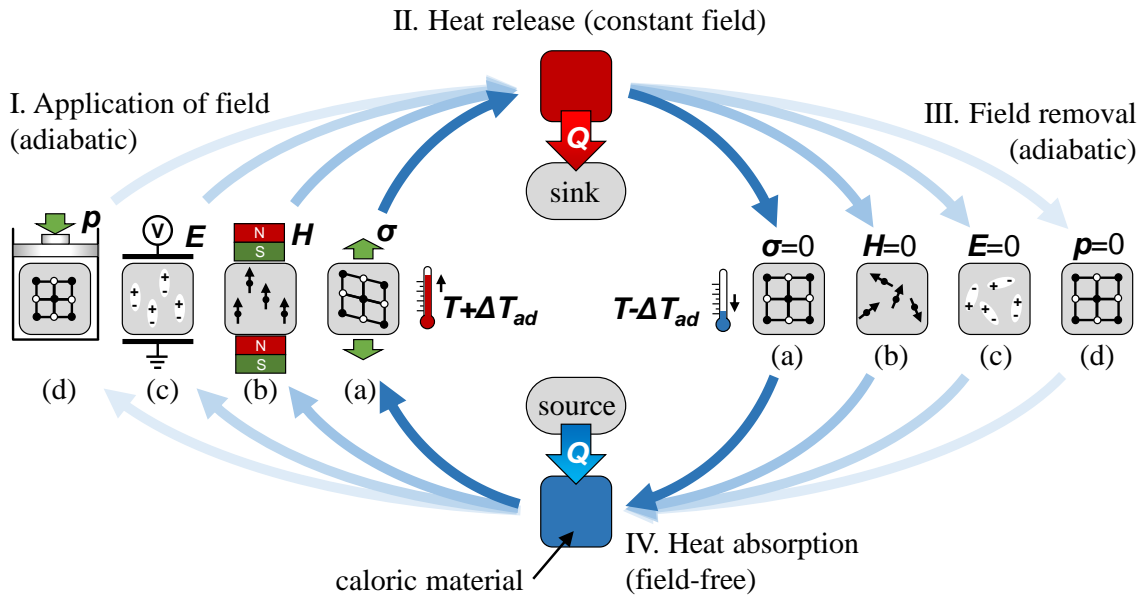
Figure 3.3: Schematic cooling cycle for (a) elastocaloric, (b) magnetocaloric, (c) electrocaloric and (d) barocaloric cooling.

A schematic cycle for cooling or heat pumping based on caloric effecs is shown in Fig. 3.3. The cycle consists of four basic steps. In the first step (I.) the driving field is applied to the caloric material in its high-temperature phase at an initial temperature T. The material undergoes field-induced phase transformation into the high-order phase (which, in the case of conventional caloric effects, is the low-temperature phase) and releases latent heat, since the transformation is exothermal. When field application is performed under adiabatic conditions, the material heats up to $T + \Delta T_{ad}^{load}$. In the next step (II.), the hot material is thermally connected to a heat sink, to which it transfers the heat Q^{hot} while the driving field is maintained constant. After disconnecting the heat sink again, the driving field is removed in the third step (III.) and the material undergoes endothermal reverse transformation back to the high-symmetry / low-order phase. If field removal is performed adiabatically, the material cools down to a temperature $T - \Delta T_{ad}^{unload}$ below the initial temperature. The generated cold is used in the fourth step (IV.) to absorb the heat Q^{cold} from a heat sink. A comparison with Fig. 2.4 reveals a close analogy to the vapor compression cycle. The difference is that caloric cooling is entirely solid-state based.

Except for the magnetocaloric effect, caloric effects have been studied predominantly on the material level until recently. In the following, the different caloric effects will be briefly introduced. Results on caloric materials are not reviewed here in detail – instead, few representative examples are mentioned. The focus will be on adiabatic temperature changes relevant for heat pumping applications

rather than entropy changes. The reader may refer to the review articles cited at the beginning of this chapter, as well as references given therein, for extensive overview tables of materials.

3.1.1 Magnetocaloric effect

In magnetocaloric materials, transition into a phase exhibiting increased magnetic ordering and a magnetization M is driven by application of a magnetic field H. Magnetocaloric effects are found in Gd-based alloys, Ni-Mn-Ga Heusler alloys and other Mn-based alloys, La(Fe$_{13-x}$M$_x$)-based compounds, Manganites as well as certain nanocomposites [182, 183]. Depending on the material, phase transformation may be of first or second order [214] and in some materials, sample behavior may be switched between both, e.g., by application of mechanical fields [200, 215]. In general, adiabatic temperature changes are strongly dependent on the applied field and are therefore limited in practical applications by the available (permanent or electromagnetic) magnets. A giant magnetocaloric effect of $24\,\mathrm{K}$ at a field of $5\,\mathrm{T}$ has been reported for MnCoGeB$_{0.02}$ showing a first-order transformation (Ref. [206], cited after [195]). However, for most magnetocaloric materials, the effect is considerably lower.[2] Gd-based alloys, which still represent the most commonly used material in magnetocaloric demonstrators [186], have relatively low heat capacities, supporting high temperature changes [180]. Magnetic Heusler alloys exhibit giant magnetocaloric effects, when the martensitic and ferromagnetic transition temperatures are close to each other [183, 215]. These alloys may exhibit both, conventional as well as inverse effect. The intrinsic magnetostructural coupling leads to a conventional caloric effect. However, in nearly stoichiometric Ni$_2$MnGa and certain Ni–Mn–Z alloys (with Z being Sn,In,Sb), the martensite phase has a lower magnetic moment than the austenite phase due to large magnetocrystalline anisotropy. In this case, a strong extrinsic coupling of structural and magnetic degrees of freedom (martensite variants and magnetic domains) at the meso-scale leads to an inverse magnetocaloric effect, changing into a conventional effect at sufficiently high applied fields [183, 194]. An inverse magnetocaloric effect of $-2.2\,\mathrm{K}$ (at a field of $5\,\mathrm{T}$ and initial temperature of $230\,\mathrm{K}$) was reported for Ni$_{50}$Mn$_{34}$In$_{16}$ [208]. For an overview of magnetocaloric effects in other materials, the reader may refer to Refs. [182, 183, 195, 217].

3.1.2 Electrocaloric effect

The electrocaloric effect is controlled by electric fields E, whereas the ordering parameter is the electrical polarization P. The effect was first discovered in Rochelle

---

[2]In an article published in 2010, Zverev et al. even predicted an ultimate upper bound of $18\,\mathrm{K}$ for the magnetocaloric effect [216].

salts in 1930. Electrocaloric effects occur in hydrogen-bonded ferroelectrics, ceramic perovskites, doped halides, ferroelectric co-polymers and ferroelectric relaxors [194, 195, 218]. In hydrogen-bonded ferroelectrics, phase transformation is order-disorder based, whereas it is of displacive nature in perovskites [195]. Giant electrocaloric effects occur close to the paraelectric-ferroelectric transition [194].

A major obstacle in reaching high electrocaloric effects is the electric breakdown field, which limits the driving field and causes adiabatic temperature changes to stay below $1\,\mathrm{K}$ in most bulk materials [219, 220]. Due to the inverse relation between breakdown field and sample thickness, considerably higher temperature changes may be reached in thin films. Giant (conventional) electrocaloric effects have been observed, for instance, in $0.45\,\mathrm{\mu m}$ thick $(\mathrm{Pb_{0.86}La_{0.08}})(\mathrm{Zr_{0.65}Ti_{0.35}})\mathrm{O_3}$ films (temperature change $45\,\mathrm{K}$ at an applied field of $120\,\mathrm{MV\,m^{-1}}$) [207] and in $80\,\mathrm{\mu m}$ thick Terpolymer/BNNSs/BST67 nanocomposite films ($50.5\,\mathrm{K}$ at $250\,\mathrm{MV\,m^{-1}}$) [221]. Inverse electrocaloric effects may occur in materials exhibiting an antiferroelectric-to-ferroelectric transformation [222]. A giant inverse effect of $-5.5\,\mathrm{K}$ at a field of $33.8\,\mathrm{MV\,m^{-1}}$ was found in $0.65\,\mathrm{\mu m}$ thick La-doped $\mathrm{Pb(Zr_{0.95}Ti_{0.05})O_3}$ thin films [209]. For a compilation of further electrocaloric material data, confer Refs. [195, 209, 219, 220, 222, 223].

3.1.3 Elastocaloric effect

The elastocaloric effect refers to an isothermal entropy or adiabatic temperature change in materials driven by mechanical fields, i.e. uniaxial tensile or compressive stress σ. The ordering parameter is the strain ε in this case.[3] In contrast to the magnetocaloric and electrocaloric effect, both driving field and ordering parameter are tensors of rank 2 in case of the elastocaloric effect. The effect was first discovered in natural rubber in the early nineteenth century and may also be observed in dry wood, many polymers etc. However, particularly high elastocaloric temperature changes are found in pseudoelastic SMAs undergoing a first-order phase transformation. These may be grouped into (non-magnetic) *conventional shape memory alloys* (which have been described in detail in Section 2.3) and *magnetic shape memory alloys* [197, 199]. The use of magnetic [225] and non-magnetic SMAs [226] for solid-state cooling was first proposed in the early 2000s.

Most conventional SMAs are either based on Cu-alloys or TiNi-alloys. These materials exhibit a first-order transition between a low-symmetry (B19 or B19') martensitic and a high-symmetry (B2) austenitic phase. The specific volume of both phases is approximately identical. The corresponding entropy change of the transition is purely vibrational, i.e. associated with lattice vibrations (phonons).

---

[3]In material characterization experiments and elasocaloric demonstrators, stress-induced martensitic transformation is often strain- instead of stress-controlled for practical reasons. It has been shown that in case of reasonably low mechanical hysteresis, the isothermal entropy change is the same for both loading modes [224].

Giant elastocaloric effects have been observed in $Cu_{83}Al_{14}Ni_3$ single crystals ($14\,K$ at an applied stress of $150\,MPa$) [227] and in polycrystalline $Ti_{49.5}Ni_{50.5}$ belts ($58\,K$ at an applied stress of $1300\,MPa$) [96]. For the TiNi-based alloys it has been shown that latent heat (and thus elastocaloric temperature change) depends on alloy composition [47] as well as oxygen and carbon impurity levels [48–50]. A particular advantage of elastocaloric cooling based on SMA is the exceptionally large temperature span in which the effect occurs. For instance, $Cu_{68}Zn_{16}Al_{16}$ has been shown to exhibit temperature changes of 5 to $7.5\,K$ within a temperature window of $130\,K$ (i.e. at ambient temperatures between 210 and $340\,K$) [228].

Elastocaloric effects induced by tensile and compressive loading have been labeled direct and reverse effect, respectively, by some authors [195]. However, due to the crystallographic properties of SMA, both loading modes lead to formation of stress-induced martensite and thus to a positive (conventional) temperature change. A truly inverse elastocaloric effect of $-1.1\,K$ has been observed recently in $Ti_{49}Ni_{51}$ samples containing aligned Ti_3Ni_4 precipitates [229]. In this case, precipitates create compressive stress within the microstructure and application of an external uniaxial load leads to partial stress relieve, inducing endothermal reverse martensitic transformation. Above a certain stress threshold, the effect becomes conventional.

Besides non-magnetic SMAs, many Fe-based SMAs (e.g., Fe-Pd, Fe-Pt) and Heusler alloys (e.g., Ni-Mn-Ga) exhibit magnetic properties in combination with shape memory behavior. These alloys also exhibit elastocaloric effects, but the entropy change includes vibrational as well as magnetic contributions – the materials are multiferroics. Magnetic SMAs may be further subdivided into ferromagnetically ordered and so-called metamagnetic SMAs exhibiting weak magnetic coupling of the martensite phase. In contrast to conventional SMAs, the phase transformation in metamagnetic SMAs often involves a volume change of up to 1.2% [196], making the materials also barocaloric. Giant elastocaloric effects are found, for instance, in $Ni_{50}Fe_{19}Ga_{27}Co_4$ single crystals ($10\,K$ at a compressive load of $300\,MPa$). Inverse elastocaloric effects are observed in melt-spun $Ni_{55}Fe_{16}Ga_{29}$ and $Ni_{50}Mn_{40}Sn_{10}$ films [230]. A giant inverse elastocaloric effect of $-5.12\,K$ has been reported for $Fe_{49}Rh_{51}$ [211].

An overview on elastocaloric effects in different materials is given in Table 3.2. Further compilations of elastocaloric material data are given in Refs. [195, 197–199, 201].

3.1.4 Barocaloric effect

Barocaloric effects are induced by hydrostatic pressure p. They occur in magnetic shape memory alloys exhibiting first-order magnetostructural transitions, which are associated with a volume change $\Delta V/V_0$. Hence, barocaloric materials are automatically multicaloric. A giant barocaloric effect in the order of $10\,K$ has been estimated for $Fe_{49}Rh_{51}$ at a pressure of $2.5\,kbar$ [210]. An inverse effect

Table 3.2: Elastocaloric effect in selected materials. Legend: SC – single crystal, PC – polycrystal, Dim. – smallest dimension (thickness or diameter Ø), ΔT_{load} / ΔT_{unload} – temperature change upon loading (l) and unloading (u), $\Delta \sigma$ – applied stress, $\Delta \varepsilon$ – applied strain.

Material	Crystal	Dim. [mm]	ΔT_{load} [K]	ΔT_{unload} [K]	$\Delta \sigma$ [MPa]	$\Delta \varepsilon$ [%]	Ref.
$Ni_{50.1}Ti_{49.9}$	PC	Ø1.07	28		900	7	[72]
Ni-Ti	PC	Ø3.0	25.5	-17	550	8	[13]
Ni-Ti	PC	Ø0.7	25	-21	700	6	[86]
$Ni_{55.8}Ti_{45.2}$	PC	0.2	14	-12.5	450	4.2	[231]
$Ti_{49.5}Ni_{50.5}$	PC	0.38	58	-54	1300	8	[96]
$Ni_{45}Ti_{47.25}Cu_5V_{2.75}$	PC	0.5	10	-9	500	4	[88]
$Cu_{83}Al_{14}Ni_3$	SC	1.0	14	-14	150	7.7	[227]
$Cu_{63.1}Zn_{33.8}Sn_{3.1}$	SC	1.0	12	-12	150	> 5	[232]
$Cu_{68.13}Zn_{15.74}Al_{16.13}$	SC	Ø3.0		-6.5	110	8	[91]
$Cu_{68}Zn_{16}Al_{16}$	PC	1.4		-7	250	7.1	[228]
$Fe_{49}Rh_{51}$	PC	0.27	-5.17		529	0.3	[211]
$Fe_{68.8}Pd_{31.2}$	SC	3.3	1.9	-2.3	-100	-1.5	[233]
$Fe_{68.8}Pd_{31.2}$	SC	3.3	3.1	-3.1	-200	-3	[234]
$Ni_{50}Fe_{19}Ga_{27}Co_4$	SC	4.0		-10	-300	-4.8	[235]
$Ni_{54}Fe_{19}Ga_{27}$	PC	5.0	5.0	-6.2	-170	-3.5	[236]
$Ni_{45.7}Mn_{36.6}In_{13.3}Co_{5.1}$	PC	3.0	3.5	-3.5	-100	-1.25	[237]
$Ni_{45}Mn_{44}Sn_{11}$	PC	Ø3.0	4	-5.7	-250	-1.3	[238]
Natural rubber		0.05	2	-4		500	[202]
Natural rubber		0.1	5.5	-8.7	1.5	600	[239]
Latex rubber		0.6	14	-14		700	[240]

of $-2\,\mathrm{K}$ is observed in $LaFe_{11.33}Co_{0.47}Si_{1.2}$ at a load of $1\,\mathrm{kbar}$ [212]. Depending on the magnetic ordering of high-temperature and low-temperature phase, various combinations of inverse/conventional barocaloric and inverse/conventional magnetocaloric behavior may occur [197].

3.1.5 Toroidocaloric effect

Besides the four main caloric effects described above, a further, more exotic group of caloric effects has been introduced in literature: the torroidocaloric effects including electrotoroidic, magnetotoroidic and piezotoroidic effects [241]. All ferroic effects are based on a symmetry breaking. In ferroelectrics, symmetry is broken by the loss of spatial inversion symmetry, in ferromagnetics by the loss of time reversal symmetry and in ferroelastics the rotational symmetry of the lattice is broken. In ferrotoroidic materials, both spatial inversion and time reversal

symmetries are simultaneously broken, when a long-range order of magnetic-vortex-like structures is established [242, 243]. Ferrotoroidic ordering has been observed in a number of materials inclunding $LiCo(Po_4)_3$, $Ba_2CoGe_2O_7$, $MnTiO_3$ and $MnPS_3$. However, experimental conditions have been rather impractical (i.e. very low temperatures and high magnetic fields) and a direct measurement of torroidocaloric temperature changes has not yet been reported.

3.1.6 Multiferroic effects

In multiferroic materials, caloric effects may be induced by various driving fields [244–247]. As already mentioned above, multi-caloric effects are likely to occur in magnetically or ferroelectrically ordering materials upon mechanical driving fields, since lattice structure strongly affects the magnetic and electronic subsystems. Magnetic - ferroelectric coupling has also been observed [248]. These materials imply interesting options for ferroic cooling. On the one hand, caloric effects may be increased by applying more than one driving field at once. Also, advanced cooling cycles involving a combination of direct and inverse caloric effects may be envisioned in order to increase temperature lift. On the other hand, a combination of different driving fields may be used to tune and adjust a ferroic phase transition to the desired operation conditions [200].

3.1.7 Performance metrics

Material performance metrics

The caloric effect size is quantified in terms of adiabatic temperature change ΔT_{ad}, isothermal entropy change ΔS and associated isothermal heat Q. Different approaches may be followed to determine these properties from experimental data [194, 195, 222]. *Indirect methods* are based on a thermodynamic analysis of the influence of temperature and field on the local order parameter. The *Maxwell method* makes use of Eq. 3.2a and the *Clausius-Clapeyron method* (applicable only for first-order transitions) is based on the Clausius-Clapeyron equation (neglecting dissipative effects):

$$\frac{dT}{dY} = -\frac{\Delta x}{\Delta S} \tag{3.5}$$

In *quasi-direct methods* the entropy change is calculated from the heat capacity as a function of temperature measured in special calorimeters at constant applied field:

$$\Delta S = S(T, Y) - S(T_0, Y) = \int_{T_0}^{T} \frac{1}{T} \frac{\dot{Q}(Y)}{\dot{T}} dT \tag{3.6}$$

Unlike the entropy change, temperature is an experimentally accessible quantity, so that field-induced adiabatic temperature changes may be measured by *direct methods*, for instance by attaching temperature sensors to the surface of a caloric

sample or monitoring the sample with an infrared camera. Isothermal heat may also be measured directly by dedicated calorimetric setups allowing for variation of the driving field at constant temperature:

$$\Delta S = S(T,Y) - S(T,0) = \frac{1}{T} \int_0^Y \frac{\dot{Q}(T)}{\dot{Y}} dY \tag{3.7}$$

In the above equations, $\dot{Q}$, $\dot{T}$ and $\dot{Y}$ represent the heat flux, cooling/heating rate and field change rate.

In analogy to the coefficient of performance of cooling cycles, a material's coefficient of perormance COP_{mat} (sometimes also referred to as material's efficiency η) may be defined, which is given by the ratio of heat Q released/absorbed due to a caloric effect, and the work W needed to drive the effect [195]:

$$COP_{mat} = \frac{|Q|}{|W|} \tag{3.8}$$

Some authors derived the heat Q from DSC measurements of the thermally induced phase transformation which may however lead to an overestimation of the stress-induced effect. Therefore, it was proposed to calculate the heat from sample mass m, heat capacity c_p and adiabatic temperature change ΔT by $Q = mc_p\Delta T$ [226]. The work is obtained by numerical integration of the generalized force-displacement trajectory (e.g., the stress-strain characteristic of elastocaloric materials).

The refrigerant capacity is a further performance measure, which is approximately given by the product of entropy change ΔS and temperaure change ΔT [213]:

$$R = \int_{\Delta T} \Delta S(T) dT \simeq \Delta S \Delta T \tag{3.9}$$

For elastocaloric materials, the definition of an 'elastocaloric cooling strengh' $|\Delta T|/|\Delta\sigma|$ was proposed [197].

Device performance metrics

Similar to the performance metrics for elastocaloric materials (see above), several performance metrics have been defined, which quantify the performance of a caloric heat pumping device.

The coefficient of performance of a caloric cooling device/system is defined as the ratio of cooling (/heating) power $\dot{Q}$ and power input $\dot{W}$ for driving the device [214]:

$$COP_{system} = \frac{\dot{Q}}{\dot{W}} \tag{3.10}$$

Using the material COP normalized by the Carnot COP, Φ_{mat}, and a parameter Φ_{sys} expressing the perfectness of system integration, the system COP may be expressed as [22]:

$$COP_{system} = COP_{Carnot} \cdot \Phi_{mat} \cdot \Phi_{sys} \tag{3.11}$$

The temperature lift is defined as the temperature difference between sink and source:

$$\Delta T_{lift} = T_{sink} - T_{source} \tag{3.12}$$

Further considerations regarding device/system performance may be found in Ref. [22].

3.2 Device concepts and demonstrator development

In the following, practical aspects, design concepts and demonstrator developments of caloric cooling devices shall be described. The focus is put on elastocaloric demonstrators, which will be described in detail. Prior to that, selected concepts from other caloric cooling technologies will be briefly introduced. Some of the concepts are universal and may be used with all of the caloric effects, whereas others are specific to the respective caloric effect. Considering the large number of demonstrators developed during the last decades especially in the field of magnetocaloric refrigeration, only selected aspects will be discussed below for the non-elastocaloric technologies.

3.2.1 Magnetocaloric devices

First prototypes for magnetocaloric refrigeration at room temperature have been introduced already in the year 1976, reaching an impressive temperature lift of $47\,\mathrm{K}$ [249]. Inspired by these first successes, a number of magnetocaloric designs and device concepts have been proposed and built during the following decades – see Refs. [185, 186, 191] for an overview. In the following, some general trends, important device concepts, as well as prototypes for microcooling shall be briefly introduced.

Scarpa et al. proposed a classifications scheme of demonstrators based on geometries, type of magnetic source, magnetocaloric material and the relative motion of the active elements of magnetocaloric devices [190]. During device operation, the magnetocaloric material has to be cyclically exposed to and removed from a magnetic field. Synchronously, hot and cold heat flows have to be separated, which is mostly accomplished using a heat transfer fluid. A particularly crucial (though specific) task in magnetocaloric cooling is the design and dimensioning of permanent or electromagnetic magnets providing the driving field [187, 191]. Elaborate permanent magnet assemblies have been developed, which create regions of maximum magnetic field alternating with field-free regions. A general drawback of the technology is the reliance on rare earth materials for fabrication of strong permanent magnets. In order to subject the magnetocaloric material to magnetic field changes, either the material or the magnet has to be moved. This is done in a rotary or recipocating (displacive) manner [186]. Electromagnets bear the additional possibility to switch the field on and off electrically. Different thermodynamic cycles have been proposed for the operation of magnetocaloric devices, including the inverse Brayton cycle [22, 250, 251]. By implementing active magnetic regeneration (see below), magnetocaloric devices reach temperature lifts between a cold and a hot end considerably higher than the adiabatic temperatue change of the material. Temperature lifts of up to $80\,\mathrm{K}$ have been reached using superconducting magnets and $42\,\mathrm{K}$ using permanent magnets. Maximum cooling powers and operation frequencies in state-of-the-art demonstrators are $600\,\mathrm{W}$ and $10\,\mathrm{Hz}$, respectively [186]. In almost all demonstrators, Gd has been used as active material.

Active magnetic regeneration.   A central concept used in virtually all modern magnetocaloric devices is the so-called active magnetic regeneration (AMR) [252, 253]. Regeneration provides a solution for the issue of low adiabatic temperature change in most magnetocaloric materials, which are usually by an order of magnitude lower than temperature changes required for technical applications. Already the first demonstrator by Brown (1976) reached a temperature lift of $47\,\mathrm{K}$ thanks to regeneration, although the adiabatic temperature change of Gd, the active material, is only $14\,\mathrm{K}$ at an applied field of $7\,\mathrm{T}$. The term 'active' refers to the fact that the refrigerant itself (i.e. the caloric material) acts as regenerator. As the concept is universal and may be applied to other caloric effects as well, Fig. 3.4 shows a general scheme of the active regeneration cycle. The setup comprises a regenerator bed containing the caloric material, a fluid channel guiding a heat transfer fluid through the bed by pumps or pistons, as well as a cold and a hot heat exchanger (CHEX, HHEX) at the two ends of the bed, respectively. The heat pumping cycle consists of four steps. During the first (I.), the driving field (in this case a magnetic field) is applied to the caloric material, inducing exothermal phase transformation and a temperature rise within the material. In the second step, heat tranfer fluid is pumped in one direction along the bed (e.g., rightwards), transporting heat to the HHEX while the field is held constant. Inside the regenerator bed each section of caloric material passes heat to its right
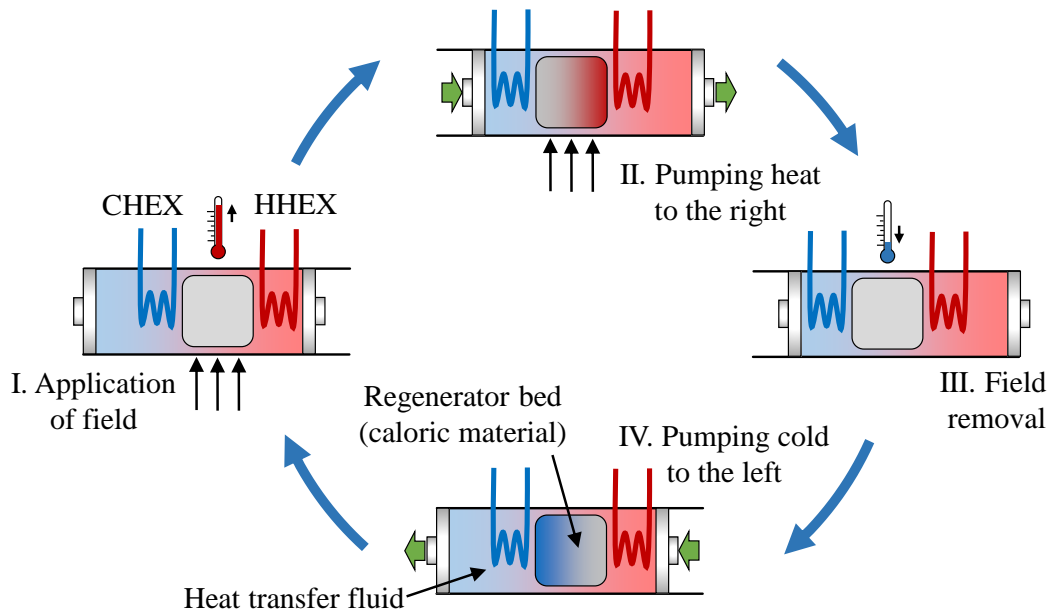
Figure 3.4: Schematic heat pumping cycle for active caloric regeneration. (I.) Application of the driving field induces heat release of the caloric material within the regenerator bed. (II.) Heat transfer fluid is pumped rightwards at constant applied field, transporting heat towards the hot heat exchanger (HHEX). (III.) Removal of driving field leads to heat absorption by the caloric material. (IV.) Fluid is pumped leftwards, transporting cold towards the cold heat exchanger (CHEX). A temperature gradient is established along the regenerator bed.

neighboring section, a temperature gradient results. In the third step (III.), the driving field is removed, leading to endothermal reverse transformation of the caloric material. The generated cold is transported to the CHEX in the fourth step (IV.) by pumping the heat transfer fluid leftwards through the regenerator bed. Due to the temperature gradient along the regenerator bed, each portion of caloric material is operated around its own individual 'ambient' temperature. The temperature lift between CHEX and HHEX is no longer dependent on the active material's adiabatic temperature change, but rather on geometrical properties and thermal insulation of the regenerator. In magnetocaloric cooling, plates or a loose filling of spheres, pellets or particles of magnetocaloric material are inserted into the regenerator bed in order to increase the surface for heat exchange. For each regenerator setup, an optimum packing density (regenerator porosity), particle size, mass-flow rate of the heat transfer fluid and operation frequency have to be found [254, 255]. In order to operate the active material under optimum conditions, regenerator beds may be filled with a functionally graded series of magnetocaloric materials (adapted to the temperature gradient during operation) rather than a homogeneous filling by a single material.

Thermal diode. Recently, a thermal diode mechanism has been proposed for magnetocaloric cooling, which is based on a combination of caloric materials and

(a)

(b)
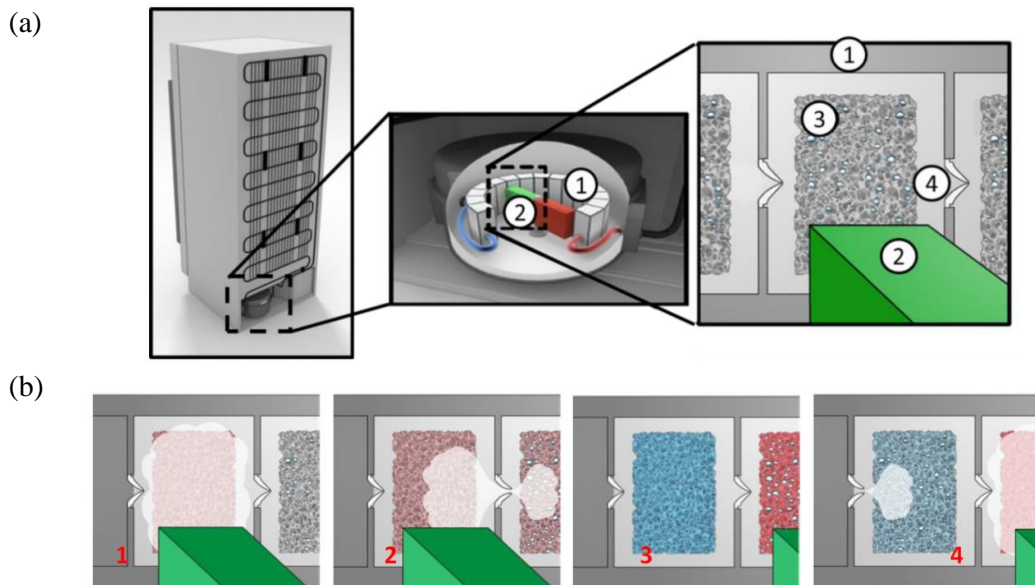
Figure 3.5: Schematic magnetocaloric cooling device comprising a thermal diode mechanism based on heat pipes. (a) The system replaces the compressor in a conventional refrigerator. Basic components are (1) heat pipe chamber, (2) magnet, (3) caloric material and (4) check valve. (b) Operation steps are (1) application of magnetic field, (2) vaporization of fluid due to magnetocaloric heating, (3) removal of magnetic field, (4) condensation of fluid due to magnetocaloric cooling. Modified from Ref. [256]. ©2016, K. Bartholomé.

heat pipes [256, 257] and might also be used with the other caloric effects. The cycle is schematically shown in Fig. 3.5. The caloric material is placed in a number of chambers connected in a series. Within each chamber, heat pipe conditions are established and the chambers are connected by check valves allowing fluids only to flow in one direction (e.g., rightwards). During operation, forward and reverse transformation of the caloric material are induced by field application in one chamber after the other, e.g., by arranging the chambers around a rotating permanent magnet. Each time the forward caloric effect is induced in a chamber, a certain amount of heat pipe fluid is evaporated by the released latent heat, the pressure increases and vapor is transferred to the right neighboring chamber through the check valve. When, on the other hand, the reverse caloric effect occurs in a chamber, vapor is condensated, the pressure drops and additional vapor enters from the left neighboring chamber through the check valve. Hence, the thermal diode mechanism allows to pump vapor in a circuit just as in vapor compression, but using caloric materials instead of a compressor. As an alternative to the heat pipe concept, solid-state based thermal diode mechanisms using thermoelectric elements have been proposed [188, 258].

Magnetocaloric microcooling devices. A comparison of the magnetocaloric properties of thin films, melt-spun ribbons and microwires with those of corre-

sponding bulk samples reveals that the magnetocaloric effect in small or low-dimensional samples is inferior to that in bulk material [165]. However, thin film fabrication techniques like melt spinning provide the advantage of ultra-rapid quenching during fabrication, which helps to better control stoichiometry. Despite the reduced magnetocaloric effect, several author presented approaches for magnetocaloric microcooling of electronics chips etc. Most of the studies are simulation-based, but some preliminary test setups have been fabricated. Silva et al. proposed a thermal diode mechanism using materials whose thermal conductivities are magnetic field-dependent [259]. The mechanism is expected to allow for a temperature lift of $2.5\,\mathrm{K}$ and a COP of about 1.5 under ideal conditions. Ghirlanda et al. and Kim et al. designed a micro-machined magnetocaloric microcooler including a microchannel heat exchanger fabricated by MEMS technology [260–262]. In preliminary test using $\mathrm{Gd_5(Si_2Ge_2)}$ as active material, an anti-freeze fluid (propylene glycol) as heat transfer fluid and a moderate magnetic field of $1.2\,\mathrm{T}$, the device achieved a cooling ΔT by $-9\,\mathrm{K}$ when operation was started at an initial temperature of $-11\,\mathrm{°C}$. Microchannel-based devices using LaSrMnO as active material have been simulated by Pereira et al. [263, 264]. Silva et al. investigated several heat exchange fluids for use in magnetocaloric microcoolers and concluded that gallium is the optimum heat transfer fluid for operation at $5\,\mathrm{kHz}$ [265]. For slower operation frequencies around $50\,\mathrm{Hz}$, water becomes the better heat transfer fluid. However, gallium and mercury have been discarded due to their toxicity.

3.2.2 Electrocaloric devices

At present, the number of published electrocaloric demonstrators is still low – a review article of Kitanovski et al. cited five demonstrators in 2015 [178]. Device concepts focus on the two concepts of active electrocaloric regeneration and thermal diodes, which have been discussed above for magnetocaloric cooling [220]. In the thermal diode concept, temperature lift may be increased by stacking several electrocaloric films and interdigit electrodes in the direction of thermal gradient. The resulting devices are very similar to piezoelectric stacks widely used for precision actuation. Since the thermal conductivity of typical electrocaloric materials (ceramics and polymers) is relatively low, advanced stack geometries including fluid channels have been proposed [220].

Electrocaloric microcooling devices   In contrast to the magnetocaloric effect, the scaling behavior of the electrocaloric effect upon miniaturization is very favorable. As described above, considerably higher electric fields may be applied to thin films, compared to bulk samples, which drastically increases the electrocaloric effect (e.g., temperature change). Just as for the macroscopic demonstrators, thermal diodes or heat switches and active regeneration are considered as heat transfer mechanisms in electrocaloric microcooling devices. Thin heat
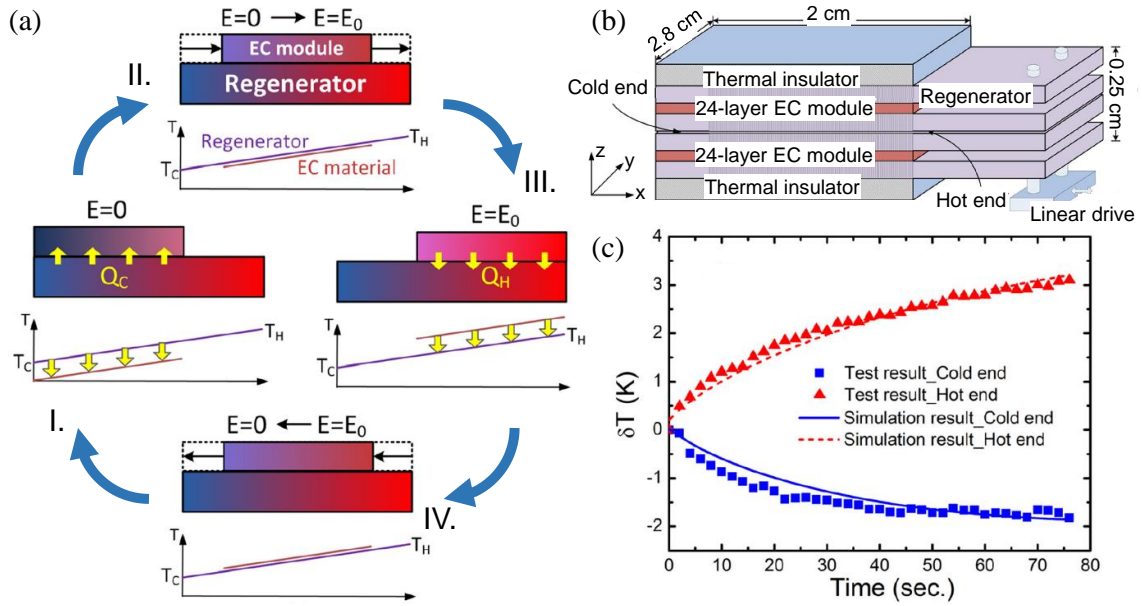
Figure 3.6: Solid-state based electrocaloric microcooling demonstrator based on active electrocaloric regeneration. (a) Heat pumping cycle. (b) Schematic of the device. (c) Temperature evolution of heat source and sink as a function of time. Modified from Ref. [266]. ©2013, American Institute of Physics / AIP Publishing.

switches may be realized using liquid crystal films with anisotropic thermal conductivity, which are controlled by the same electric field as the electrocaloric film [267]. A ratio of 5 to 10 between heat conductivities in the 'open' and 'closed' state of the heat switch would already allow for heat pumping devices competitive with state-of-the-art thermoelectric coolers. Thermal contact switching might also be achieved by simple solid-to-solid contact between the active material and heat source/sink, controlled by a compact linear actuator [268]. An entirely solid-state-based, $20\,\text{mm}$ long electrocaloric microcooler based on the regeneration principle was simulated and built by Gu et al. [266, 269]. The device, which is schematically shown in Fig. 3.6 (b) contains two 24-layer electrocaloric modules (each layer having a thickness of $8\,\mu\text{m}$) fabricated from high energy electron irradiated poly(vinylidene fluoridetrifluoroethylene) 68/32mol% (ei-copolymer). During operation, four $500\,\mu\text{m}$ thick steel plates are shifted forth and back in x-direction between the electrocaloric modules instead of a heat transfer fluid. After $80\,\text{s}$ of operation at $0.5\,\text{Hz}$ and an electric driving field of $100\,\text{MV}\,\text{m}^{-1}$, the hot end of the device is heated by $2.25\,\text{K}$, whereas the cool end is cooled by $-2.15\,\text{K}$ with respect to the ambient (Fig. 3.6 (c)). The temperature span could be further increased to $6.6\,\text{K}$ by doubling the operation frequency. For comparison, the adiabatic temperature change of the active material, measured at an electric field of $160\,\text{MV}\,\text{m}^{-1}$, is $20\,\text{K}$.

3.2.3 Elastocaloric devices

In this section, elastocalorics-specific design concepts, as well as first demonstrators that have actually been realized, will be described. Since elastocaloric cooling only recently entered the focus of research interest, most of the demonstrators have been developed in parallel to this thesis. None of the devices is dedicated especially to microcooling, though many of the design concepts may as well be transferred to small-scale applications.

The main challenges in constructing an elastocaloric heat pumping device are (1) application of the driving field and (2) separation/direction of heat flows. Application of tensile or compressive forces requires physical contact of the active material to a reasonably strong actuator, making filled beds of granular material unfeasible. Due to the high pseudoelastic strains, the active material changes its dimensions considerably during each operation cycle. Engineers found different solutions for these challenges, as will be reviewed below. The elastocaloric material in wire, tube, plate or belt shape is loaded either in tensile, compressive or bending mode. Heat is transported via air convection, in solid-to-solid contact or with the help of a (pumped or stationary) heat transport fluid (HTF). In order to direct the heat flow, either heat source and sink are stationary while the active material (or the auxiliary heat transfer fluid) is moved, or vice versa.

The most common thermodynamic cycle for elastocaloric cooling is the inverse *Brayton cycle*, consisting of (I.) an adiabatic (isentropic) loading step for stress-induced phase transformation, (II.) a heat release step at constant stress until the elastocaloric material has reached the heat sink temperature T_h, (III.) an adiabatic unloading step and (IV.) a heat absorption step at constant stress, during which the material adopts the temperature of the heat source T_c. The inverse Stirling cycle is very similar, except that loading (I.) and unloading step (III.) proceed isothermally instead of adiabatically. Alternative cycles are discussed in literature, including combinations of the Brayton and Stirling cycle, as well as modified versions with internal heat recovery [201, 270].

In principle, an elastocaloric heat pump can be obtained by simple reverse operation of a SMA-based heat engine [201, 271]. A comprehensive review of such heat engines is found in Ref. [272]. Although the first continuously operating device was described in 1975 [273], first patent applications considering SMA for cooling and heat pumping have been submitted as recently as the early 2000s [274, 275].

It took another decade, until a state-funded project (DOE ARPA-E DEAR0000131) was started at the University of Maryland (USA), leading to several first-of-its kind demonstrators [276] with, however, rather low temperature lifts [195, 277] and sparse documentation in scientific literature. In the following years, a priority program of the German Science Foundation (DFG SPP1599, [278]) regarding ferroic cooling initiated demonstrator development projects at Saarland University [279] and Karlsruhe Institute of Technology (KIT) [142]. A further project

was started at the Technical University of Denmark (DTU) based on experience in magnetoclorics. These demonstrators and the underlying concepts will be described in the following.

Circulating elastocaloric medium

(a) Hugenroth 2002

(b) Browne 2013

(c) Cui 2012
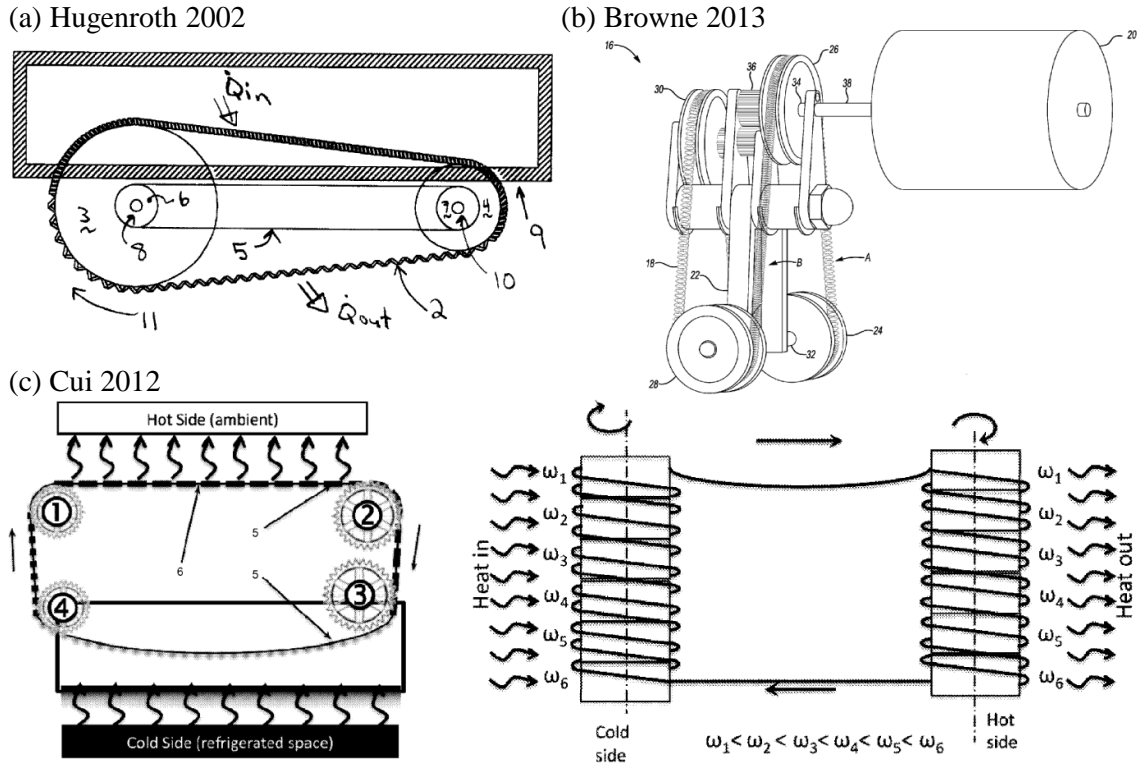
Figure 3.7: Elastocaloric demonstrator and designs for tensile loading of closed SMA loops in continuous operation. Loading and unloading is achieved by guiding the loop around two wheels rotating at different angular velocities. (a,b) SMA springs [274, 280], (c) chain of SMA elements (left) and wire loop (right) [281].

As said before, the first drafts for elastocaloric cooling devices were inspired by heat engines which act in just the reverse manner, i.e. converting a temperature gradient into motion. Many of these devices were designed to create a rotary motion and contain either closed loops or arrays of SMA elements undergoing a periodic, circulating motion. Thus, the corresponding heat pumping designs are also closest to vapor compression: In both cases the refrigerant (fluid or SMA) circulates through stationary heat exchangers, while periodically undergoing mechanically (pressure or uniaxial force) induced phase transformation.

In Fig. 3.7, several designs from patent applications are shown, in which a closed loop of SMA material is guided over two cylinders or gear-wheels rotating at different angular velocities ω_1 and ω_2. In case the first wheel rotates slower than the second one ($\omega_1 < \omega_2$), the SMA string has to elongate while passing from

(a) Cui 2012

(b) Ikegami 2014

(c) Takeuchi 2010

(d) Saylor 2012 (after Qian 2015)

(e) Schmidt et al. 2016
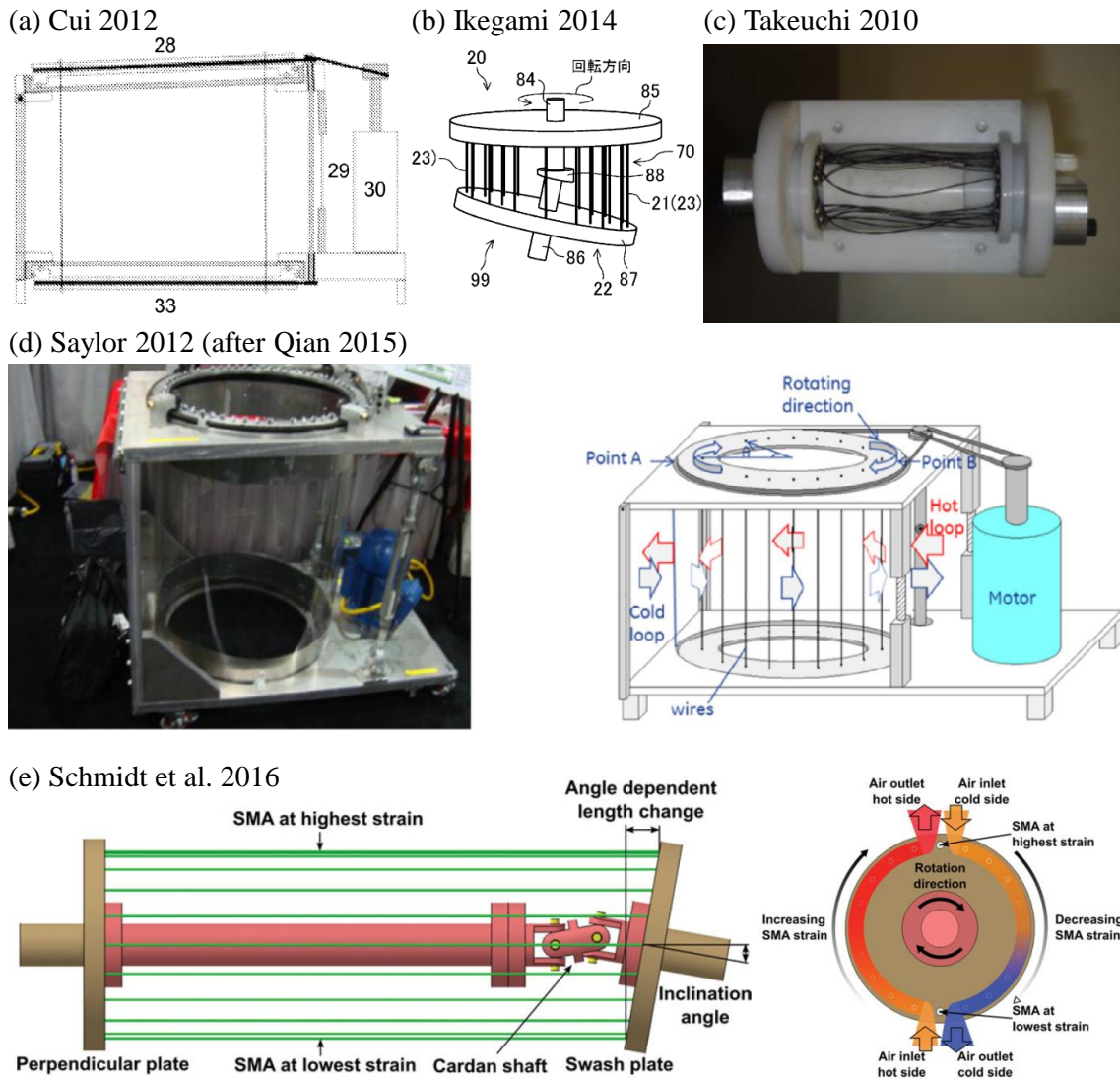
Figure 3.8: Elastocaloric demonstrator and designs for tensile loading of circulating SMA elements in continuous operation: Drum layout. (a,b) Patent drawings of Cui et al. [281] and Ikegami et al. [282]. (c) First generation (manual operation, $35\,\text{W}$) and (d) second generation demonstrator (motorized, $1\,\text{kW}$) at the University of Maryland [201, 276]. (e) Modified design by Saarland University, containing a Cardan shaft (©2016, Taylor and Francis [270]).

the first to the second wheel, undergoing stress-induced phase transformation and releasing heat.[4] When passing from the second back to the first wheel, the material is allowed to relax and cools down due to reverse transformation. The same principle may be realized by wheels with different diameters instead of different rotating velocities.

In another design which was proposed by several authors, a number of SMA wire strings is attached between two rings, resulting in a drum-shaped device (Fig. 3.8). The two rings are then tilted with respect to each other in such a way that a length change occurs between the strings at the closest and the most distant location of both rings. The strain change is adjusted to the transformation strain of the employed material. When now both rings are rotated around their central axis synchronously, each string is periodically strained and released, leading to heat release at the strained side and heat absorption at the relaxed side of the drum. The heat/cold is transported to the desired places by two directed air flows. The first reported elastocaloric demonstrators dating back to the years 2010 and 2012 belong to this device category (Fig. 3.8 (c,d), [201, 276]), though their performance is not reported in literature. Another prototype is currently being built at Saarland University [270].
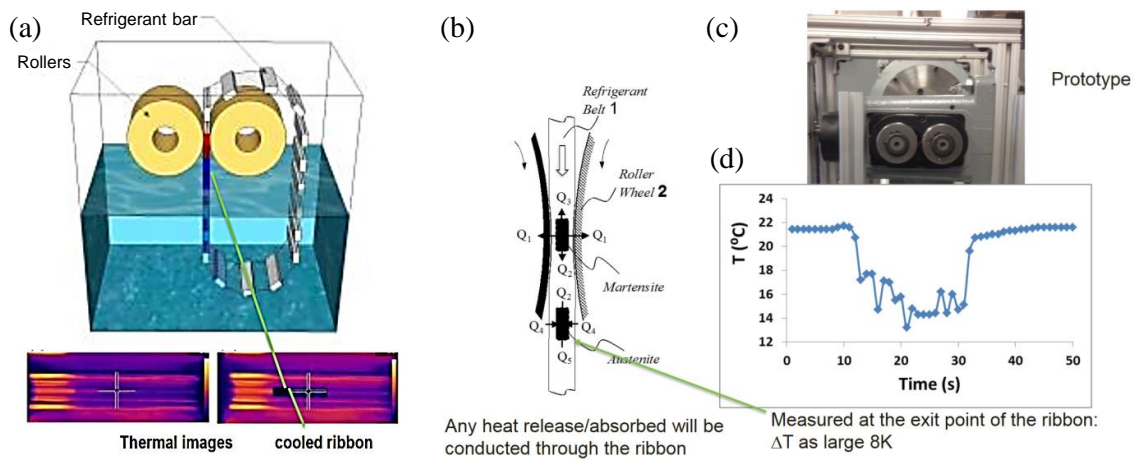
Figure 3.9: Elastocaloric demonstrator for compressive loading of circulating SMA elements in continuous operation. (a) Schematic device design, (b) operation principle: SMA elements are squeezed between two cylinders, (c) experimental setup, (d) cooling of an individual SMA segment upon stress release. ©2016, I. Takeuchi [276].

A third design, currently under development at the University of Maryland, proposes loading in compressive instead of tensile mode [276]. A number of SMA plate elements is connected to a loop (refrigerant belt). The belt is then placed in between two rotating cylinders which are used to squeeze the SMA elements. Under operation, the belt and the cylinders rotate, leading to heat release of the

---

[4]The length-per-second passed on by the first wheel is lower than the length-per-second pulled by the second wheel.

circulating SMA elements when squeezed and heat absorption upon stress release.

Loading in compressive mode – solid-to-fluid heat transfer
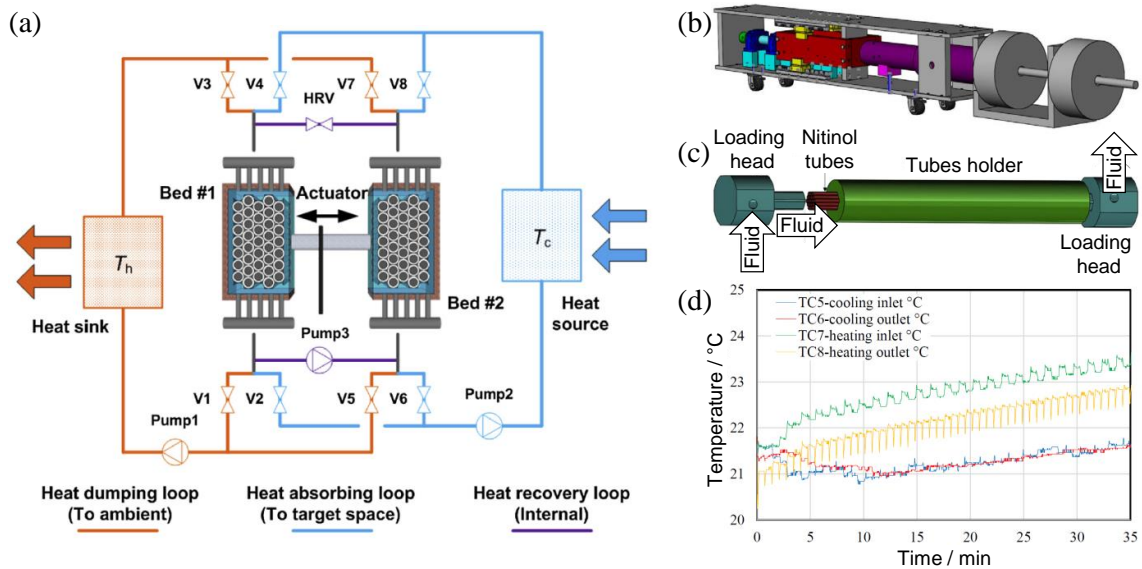
Figure 3.10: Elastocaloric demonstrator for loading a bed of SMA tubes in compressive mode. Heat is transported to a sink and source by a heat transfer fluid. (a) Schematic of the fluidic circuit (©2015, Elsevier Ltd. and IIR [271]); (b) first generation demonstrator actuated by screw jack (computer model); (c) container for tensile loading of NiTi tubes; (d) temperature evolution of sink and source (maximum temperature lift configuration) [277].

A research team around Ichiro Takeuchi at the University of Maryland developed a series of large-scale elastocaloric demonstrators, in which the SMA active medium is loaded in compressive mode. The authors pointed out that compressive loading reaches a higher material COP than tensile loading of NiTi wires, and that compressive loading furthermore increases the material's life span by inhibiting crack growth [13]. Heat transfer is realized by a heat transfer fluid (HTF) guided by a fluidic system. Note that the HTF is not undergoing phase transformation as in vapor compression, but is solely used to transfer heat from the active material to the hot and cold heat exchangers.

A schematic setup of the compressive cooling system is shown in Fig. 3.10 (a). The basic constituents are two independent beds of elastocaloric material, which are mechanically connected with each other to form an antagonistic pair, an actuator, a heat source and sink. A fluidic circuit including valves and pumps is used to direct the heat tranfer fluid. The fluidic circuit consists of three independent loops: two for coupling of the SMA with heat source and sink and an additional connection between the SMA beds for heat recovery (see below).

The system is operated following a reverse Brayton cycle [283]. During the first step, the first (peviously stress-free) SMA bed is adiabatically loaded by applying a compressive force (isentropic process) and heats up due to A→M transformation. At the same time, the second bed (previously in maximum stress state) is adiabatically unloaded and cools down due to M→A reverse transformation. During this step, mechanical work is transferred from the second to the first bed in addition to the work of the linear actuator. In the following, second step, heat is transported from the first bed to the heat sink and cold is transported from the second bed to the heat source with the help of the heat transfer fluid so that each of the beds adapts the temperature of the connected temperature reservoir (sink/source). Since now the first bed still has a higher temperature than the second bed (due to the temperature lift between sink and source), an additional internal heat recovery (HR) step involving HTF is performed to equalize the temperatures of both beds. During the third and forth step, the roles of the two beds are just reversed: By appropriate switching of valves, the first bed (being unloaded) is connected to the heat source, whereas the second bed (being loaded) is connected to the sink.

In a preceding simulation study, Qian et al. pointed out that the performance of the system depends on total cycle duration as well as HTF flow rate during heat recovery, and that there is a setup-specific optimum. While in case of short cycle durations, heat transfer is the limiting factor and a high HR flow rate increases performance, in case of long cycle durations HR itself becomes the limiting factor and slow flow rates improve the performance. In general, the device COP is increased by more effective heat transfer (i.e. for longer cycle durations) and more reversible HR; a maximum achievable COP of 4 at a temperature lift of $10\,\mathrm{K}$ is predicted [283]. In a further parametric study, system peformance is investigated for inverse Brayton cycle and inverse Stirling cycle (i.e. isothermal loading instead of adiabatic loading). Device coefficients of performance are calculated for three different SMA materials and different geometric parameters of the tubes. In all cases, the COP is shown to increase with increasing heat recovery efficiency, as well as with increasing heat transfer effectiveness. The COP decreases, however, with increasing temperature lift [271]. A third parameter variation study based on a multi-objective genetic algorithm, considering further design optimizations, predicted a maximum COP of 4.1 and a maximum temperature lift of $27.8\,\mathrm{K}$ to be achiebable with the compressive setup [284].

The authors emphasize the important difference between granular active material beds as used, e.g., in magnetocaloric refrigeration, and monolithic SMA elements in elastocaloric cooling. In the latter case, the high heat conductivity of the active material is expected to prevent the formation of temperaure gradients along the material bed.[5] Therefore, a heat recovery cycle is proposed for transferring heat between two elastocaloric material beds operated at a phase shift of one half-cycle. The cycle is analogous to a traditional counter-flow heat transfer process

---

[5]However, a temperature gradient along the SMA bed is crucial for active regeneration, as will be described in section 3.2.3.

and increases system efficiency. Guidelines for the design of such a heat recovery cycle are given in Ref. [285].

In the first-generation prototype (Fig. 3.10) (b), NiTi tubes with a length of $254\,\text{mm}$, outer diameter of $5\,\text{mm}$ and wall thickness of $500\,\mu\text{m}$ are employed as active medium. The tubes are arranged in two bundles of ten tubes each, forming the two SMA beds (Fig. 3.10) (c)). Loading is performed by two stepping motors in axial direction of the tubes. The required force for phase transformation was $6.7\,\text{kN}$ per tube. Specially designed holders and loading heads were used to stablilize the bundles and to guide water as heat transfer fluid trough the tubes. The maximum temperature lift between source and sink was determined to about $1.5\,\text{K}$ in adiabatic mode. In this case the times for loading/unloading, heat transfer to source/sink and heat recovery were $1\,\text{s}$, $9\,\text{s}$, $25\,\text{s}$, repsectively. When on the other hand artificially reducing the temperature lift to zero by external heating/-cooling of source/sink, a maximum cooling power of $46\,\text{W}$ was achieved [277].

The relatively low temperature lift was partly attributed to thermal losses of the SMA beds. Therefore, advanced layouts have been proposed, in which the SMA tube bundles are thermally insulated by polymer layers. Furthermore, advanced tube geometries including tube-in-tube and rod-in-tube combinations are proposed in order to increase SMA surface-to-volume ratio as well as SMA-to-HTF mass ratio [284, 286].

In a second device generation, Qian et al. are up-scaling their compressive thermoelastic cooling system by increasing the number of SMA tube beds from two to four, each containing 19 NiTi tubes (length of $254\,\text{mm}$, outer diameter $4.72\,\text{mm}$, wall thickness $50\,\mu\text{m}$). The mechanical linear drive is replaced by two hydraulic cylinders, increasing the available force while at the same time being more compact. Based on simulation, maximum COP and maximum temperature lift are predicted to be 11.0 and $24.6\,\text{K}$, respectively [287].

Loading in tensile mode – solid-to-solid heat transfer

A device concept based on tensile loading of an SMA ribbon and solid-to-solid heat transfer was developed at Saarland University in the framework of the research program DFG SPP1599. An experimental setup was designed with an emphasis on scientific understanding and thermodynamic analysis rather than commercial application [288]. The basic components are an SMA ribbon sample ($\text{Ni}_{50.8}\text{Ti}_{49.2}$, dimensions $90 \times 3.6 \times 0.5\,\text{mm}^3$) clamped on both ends, two metal blocks serving as heat sink and source, an electromagnetic linear drive (peak force $1.2\,\text{kN}$) for loading of the SMA and two additional actuators for displacing heat source and sink (sidewards and upwards motion). The copper blocks of sink and source have slightly curved surfaces in order to facilitate contact to the SMA and a heat capacity approximately 46 times larger than that of the SMA ribbon. Loading force of the SMA, as well as contact forces between SMA and sink/source are measured by load cells.
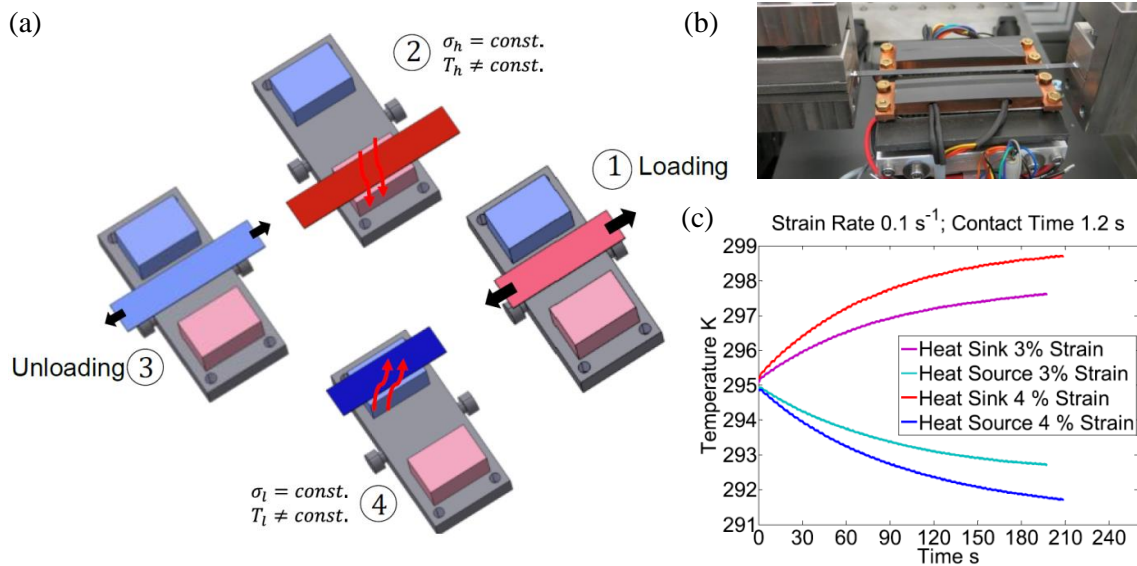
Figure 3.11: Elastocaloric demonstrator for tensile loading of a TiNi ribbon. Heat is transferred to source and sink by solid-to-solid contact. (a) Operation principle, (b) experimental setup (©2014, ASME [288]), (c) temperature evolution of heat sink and source during operation with a loading rate of $0.1\,\mathrm{s^{-1}}$ and a heat transfer time of $1.2\,\mathrm{s}$ (©2015, Elsevier Ltd. and IIR [289]).

In a conventional tensile test, the freestanding NiTi ribbon samples reached adiabatic temperature changes of $18.2\,\mathrm{K}$ and $-14.1\,\mathrm{K}$, respectively, while the time constant for temperature equalization with the environment is about $20\,\mathrm{s}$ (obtained by exponential fit). The NiTi ribbons required a training of 200 cycles in order to stabilize thermo-mechanic performance before being applied for heat pumping operation.

The schematic operation cycle is shown in Fig. 3.11 (a). In the first step, the freestanding SMA ribbon is mechanically loaded at a high strain rate in order to approach adiabatic conditions while inducing A→M phase transformation and self-heating. During the second step, the hot SMA is brought into contact to the heat sink by displacing the latter and pressing it against the ribbon from below. Heat is transferred during a specified heat transfer time by conduction between the contacting bodies, so that temperatures of SMA and sink equalize [290]. For the third step, the heat source is removed again and the freestanding SMA ribbon is unloaded adiabatically, leading to reverse transformation and elastocaloric self-cooling. The cold SMA is brought into contact with the heat source in the fourth step.

Contact forces were $11\,\mathrm{N}$ between ribbon and sink and $6\,\mathrm{N}$ between ribbon and source, the time constant for heat tranfer is about $0.2\,\mathrm{s}$ (obtained by exponential fit). The authors varied the operation parameters maximum strain ($3\%\ldots6\%$), strain rate ($0.1\,\mathrm{s^{-1}}$ was found to be sufficient for adiabatic conditions) and contact time for heat transfer ($0.6\,\mathrm{s},1.2\,\mathrm{s},2.0\,\mathrm{s}$). A temperature difference of about $8\,\mathrm{K}$ between sink and source is achieved after $210\,\mathrm{s}$ (60 cycles) under optimum con-

ditions [289]. The work input W of the device is estimated based on numerical integration of the force-distance characteristic of the SMA ribbon during loading [279], the heat absorbed from the sink Q_c by its temperature change and heat capacity. A coefficient of performance $COP = Q_c/W$ of 2.99 is obtained. If recovery of mechanical work during unloading is assumed (which is not implemented in the setup), the expected COP is 7.82 [288].

In a further study, the authors replaced the binary material with a newly developed quaternary $Ni_{45}Ti_{47.25}Cu_5V_{2.75}$ alloy showing low hysteresis [88], which has been identified as optimum material in an extensive alloy composition study [47]. The material reaches an adiabatic self-heating and cooling of $22\,\text{K}$ and $-21\,\text{K}$ in the conventional tensile test. Localized temperature profiles due to Lüders-like strain bands were shown to homogenize upon 100 cycles of mechanical training [88].

Besides the Brayton-like cooling cycle described above, the authors also discussed alternative cooling cycles based on combined adiabatic-isothermal loading and unloading (by bringing the SMA into contact to sink/source before the end of loading/unloading), or combinations of non-adiabatic loading with adiabatic unloading [270].

Loading in tensile mode – active regeneration (solid-fluid)

Very recently while this thesis is being finalized, Tušek et al. have been the first to present an elastocaloric demonstrator implementing the concept of active regeneration [291]. Beforehand, the authors have studied the cooling potential of such regenerative systems in a simulation study [292].

The operation principle of the device is shown in Fig. 3.12 (a). A regenerator element consisting of several TiNi plates is fixed between two clamps at the ends and placed in a flexible fluidic chamber with two inlets and two outlets (each two at the upper and lower end). Via the clamps, the regenerator is periodically loaded and unloaded in tensile mode by a screw drive motor to induce martensitic and reverse transformation. Synchronously, a heat transfer fluid is pressed through the upper inlet and lower outlet when the regenerator is hot and through the lower inlet and upper outlet when it is cold. This way, a net heat flow is created from the upper to the lower end, resulting in a temperature gradient along the SMA regenerator. Heat and cold are then transported to the hot (HHEX) and cold heat exchanger (CHEX) by the heat transfer fluid. The pumping is realized by a displacer in combination with four check valves.

The regenerator element is fabricated by stacking several dogbone-shaped TiNi plates having a thickness of $100\,\mu\text{m}$ with spacers in between and welding them together (Fig. 3.12 (b)). The thickness of the spacers is identical to the plate thickness, hence the regenerator porosity is 0.5. The plates have been polished and trained for several thousand cycles beforehand in order to stabilize and homogenize the elastocaloric effect [86, 110]. A flexible fluidic chamber is created around
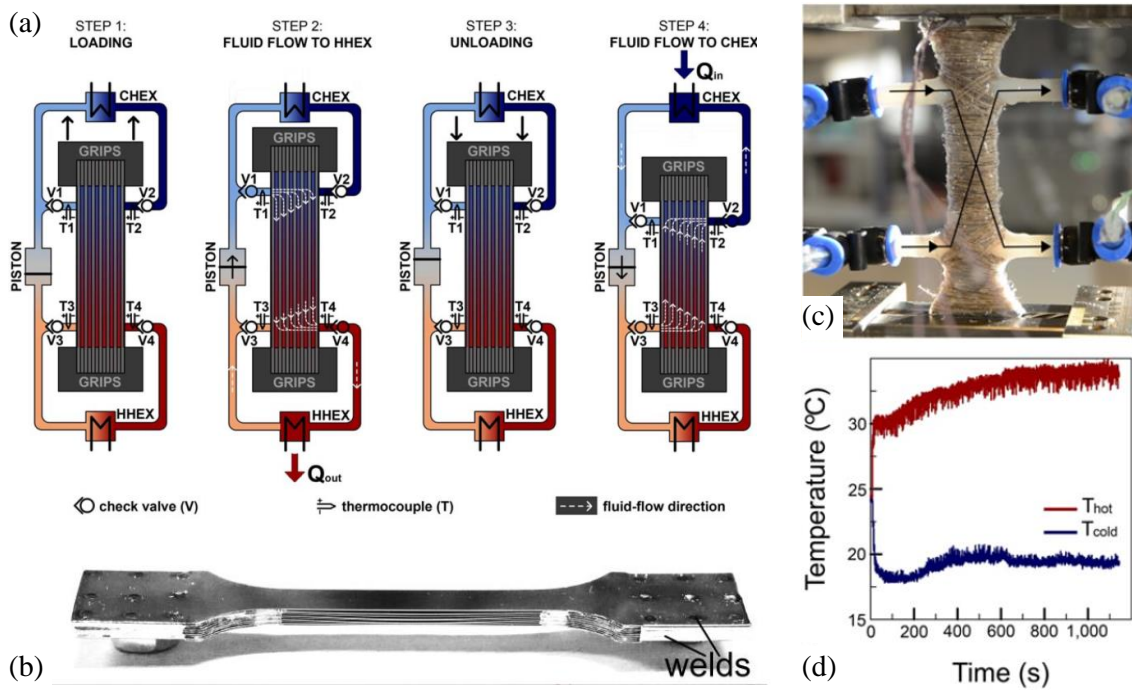
Figure 3.12: Elastocaloric demonstrator implementing active regeneration. Heat is transported to source and sink by a heat transfer fluid. (a) Schematic of the fluidic circuit and operation principle. (b) Array of dogbone-shaped TiNi plates acting as regenerator bed. (c) Experimental setup comprising flexible regenerator housing. (d) Temperature evolution of sink and source during operation. ©2016, Macmillan Publishing Group [291].

the regenerator by wrapping it in a thread soaked with silicone (PDMS) (Fig. 3.12 (d)).

Under optimum operation conditions, the device reaches a maximum temperature difference of $15.3\,\mathrm{K}$ on the water side [291], which is even higher than the adiabatic self-cooling of the material of $12.5\,\mathrm{K}$ [231]. The maximum heating power of the device is $800\,\mathrm{W\,kg^{-1}}$, the maximum COP (excluding the efficiency of the driving actuator) is 7. The results show that the (already high, compared to magnetocalorics) adiabatic temperature lifts of elastocaloric materials can be extended by employing the concept of active regeneration, paving the way for commercial applications which demand higher temperature lifts. Based on simulation, the authors point out that significantly higher mass flow rates of the HTF can be realized in TiNi-based elastocaloric regenerators, compared to the magnetocaloric reference material gadolinium, and that mass-specific elastocaloric cooling power is up to 20 times larger, allowing more compact device layouts [292].

(a) Hugenroth 2002
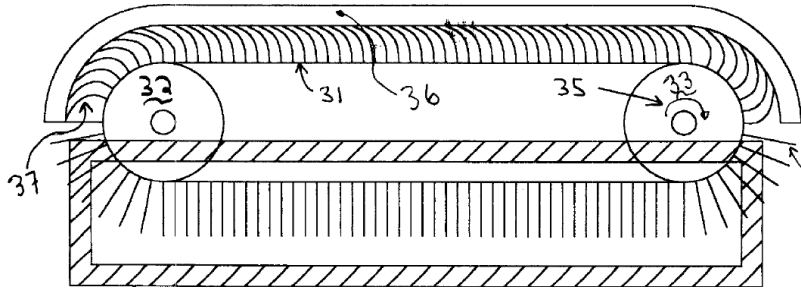
(b) Quarini 2002
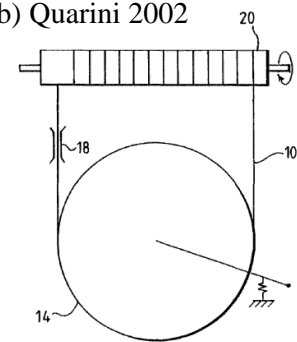
(c) Ullrich 2014
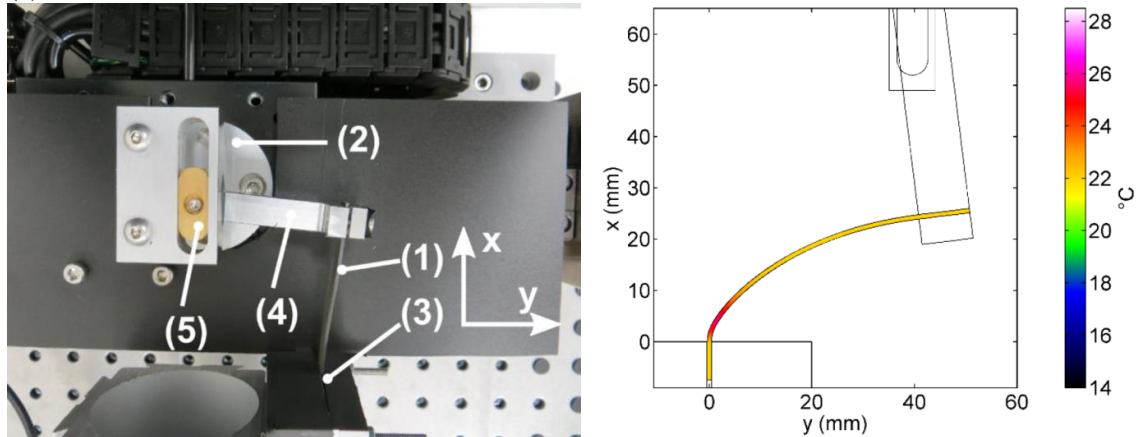
Figure 3.13: Elastocaloric demonstrator and designs for loading SMA in bending mode. (a) SMA elements attached to a circulating belt are bent and released [274]. (b) SMA wire is guided around a small and a big cyclinder in order to change bending radius [275]. (c) Experimental setup for bending of SMA plate sample (left) and simulated temperature distribution after bending (right) (©2014, ASME [293]).

Loading in bending mode

Besides compressive and tensile loading, bending has been considered as a third loading mode for inducing martensitic phase transformation in elastocaloric materials. Bending is essentially equivalent to compressive loading in the inner part of the bent piece of material, whereas tensile loading occurs in the outer region. In between both regions exists a neutral axis, which is deformed but neither compressed nor stretched. Compared to pure compression or tension, actuation forces are much lower, whereas the required stroke is higher. A disadvantage of bending-mode loading is that stress-induced phase transformation necessarily remains incomplete due to the resulting strain profiles and the neutral axis.

Two different concepts of how bending deformation may be performed in a continuously operating device are illustrated in Fig.3.13 (a) and (b). Both concepts date back to the first patent applications concerned with elastocaloric cooling [274, 275]. In the first example, a number of thin SMA plates is mounted perpen-

dicularly on a rotating belt. Bending is induced by letting the plates collide with a stopper. In the second example, different levels of bending are realized by guiding a closed SMA wire loop around two cylinders with considerably different radii. Thus, stress-induced martensitic and reverse transformation are induced by variation of the wire's bending radius.

Ullrich et al. constructed a scientific test setup for bending a TiNi plate (thickness $0.85\,\mathrm{mm}$) under defined conditions and studied the occuring elastocaloric effect by infrared thermography and finite element simulation [293]. The authors found that temperature changes of about $\pm 6\,\mathrm{K}$ occured in the NiTi plate close to the clamping, where bending forces were highest.

Comparison

The state-of-the-art of elastocaloric device concepts and prototypes has been reviewed within this chapter based on patents and scientific literature. The various concepts shall be briefly compared in the following. Table 3.3 gives an overview over the design choices regarding application of stress, operation mode, heat transfer mode, heat recovery (HR) and work recovery (WR).

Table 3.3: Comparison of prototypes and device concepts for elastocaloric cooling. In all prototypes, TiNi alloys have been used as active material. HR and WR refer to heat and work recovery, respectively.

Authors	Fig.	SMA	Force	Operation	Heat transfer	HR	WR
Hugenroth 2002 [274]	3.7	spring	tensile	continuous	solid-fluid	–	✓
Saylor 2012 [201]	3.8	wire	tensile	rotary	solid-air	–	✓
Takeuchi 2016 [276]	3.9	bulk	comp.	continuous	solid-liquid	–	–
Qian 2015 [271]	3.10	tube	comp.	oscillarory	solid-liquid	(✓)	✓
Schmidt 2015 [289]	3.11	ribbon	tensile	oscillatory	solid-solid	–	–
Tušek 2016 [291]	3.12	sheet	tensile	oscillatory	solid-liquid	✓	–
Hugenroth 2002 [274]	3.13	sheet	bending	continuous	solid-fluid	–	–
Ullrich 2014 [293]	3.13	ribbon	bending	oscillatory	solid-air	–	–
This work	–	foil	tensile	oscillatory	solid-solid	–	✓

The mode of stress application may have an impact on the cyclic stability of the elastocaloric material. Compressive loading is considered to be more material

friendly than tensile loading, since sample cross-section inceases instead of decreasing and crack propagation is hindered [13]. On the other hand, compressive loading implies strong thermo-mechanical contact to the sample, which may increase parasitic heat flows, and may furthermore not be applied to thin sample geometries. The most unfortunate loading mode is bending, since it leads to volume fractions of the SMA (neutral fiber) not taking part in phase transformation.

The operation mode determines which type of actuation is suitable for driving the elastocaloric heat pump. Continuous and rotary operation may be advantageous, because they are compatible with standard electromagnetic motors as well as gears for power transmission and furthermore do not involve rapid direction changes. For oscillatory concepts, linear motors (like electromagnetic linear drives, piezo stack actuators or hydraulic drives) may be more convenient, although a rotary motor could be used in combination with a crankshaft or eccentric tappet. In any case, the actuator has to be sufficiently strong and fast to allow for high cycling frequencies.

The heat tranfer mode has strong impact on the efficiency of heat transfer. Convective heat transfer between SMA and air is the most inefficient choice and should be avoided [201]. For bulk geometries, convective heat transfer times are easily in the order of minutes [13]. The fastest heat transfer is reached by using a heat transfer fluid, which furthermore provides a convenient way to transport heat from or to the cold and hot heat exchanger (source and sink), but requires additional channels, pumps and valves. Heat transfer in solid-to-solid contact might be a good alternative and allows for very simple device layouts. It depends crucially on the thermal contact resistance of the contacting surfaces.

Heat recovery (HR) is a central concept in caloric cooling in order to overcome the limits of the adiabatic temperature change [22]. Qian et al. proposed an internal heat recovery cycle [285] working similar to a cross-flow heat exhanger and allowing for device temperature lifts up to $2 \times \Delta T_{ad}$. Much higher temperature lifts become accessible by active regeneration, which has been applied with great success in magnetocaloric cooling for many years. Currently, the demonstrator of Tušek et al. is the only published device based on active elastocaloric regeneration.

A second central concept in elastocaloric cooling is mechanical *work recovery* (WR). The device coefficient of performance is considerably increased when the unloading work of the SMA is recovered. Work recovery may be reached by antagonsitically coupling two SMA elements, as it was done in the demonstrators of Qian et al. In many of the continuous/rotary concepts pesented above, work recovery may be implemented as well or is already included (compare Chapter 6).

Finally, the performance of the existing elastocaloric demonstrators shall be compared. Table 3.4 gives an overview of important parameters.[6] The device with

---

[6]Operation frequencies, temperature changes and specific heating/cooling powers have been derived from graphs and material/performance data, if not explicitly stated in the reference.

the highest COP and highest temperature lift is currently the active elastocaloric regenerator device. Parameters of the demonstrators developed within this thesis have been included for comparison.

Table 3.4: Comparison of the performance of prototypes for elastocaloric cooling. f – operation frequency, ΔT – temperature lift, $P_{h,c}$ – heating and cooling power, $COP_{h,c}$ coefficient of performance for heating and cooling.

Concept		Fig.	Material	f [Hz]	ΔT [K]	$P_{h,c}$ [W g^{-1}]	$COP_{h,c}$
Qian [277]	2015	3.10	Ni-Ti	0.03	1.5	0.20 , 0.16	$-$, $-$
Schmidt [289]	2015	3.11	Ni$_{50.8}$Ti$_{49.2}$	0.33	7.0	1.0 , 0.84	$-$, $-$
Tušek [291]	2016	3.12	Ni$_{50.7}$Ti$_{49.3}$	0.25	15.3	$-$, 0.782	$-$, 3.5
This [294]	work	6.20	Ti$_{49.1}$Ni$_{50.5}$Fe$_{0.4}$	0.76	9.4	4.5 , 2.9	4.9 , 3.1

4 Material characterization

The core element of every elastocaloric cooling device is the shape memory alloy constituting the active material. In the following, a selection of promising shape memory materials is characterized. In order to be suitable for elastocaloric cooling, materials have to be pseudoelastic at room temperature. Application in small-scale cooling additionally requires samples to be fabricated with at least one small dimension. This is achieved, e.g., in foil, film and wire geometries.

Device performance (Chapter 6) depends crucially on the performance of the active material. At least, three main challenges of material development arise from the requirements of practical applications regarding cooling power, energy efficiency and device lifetime [12]: (1) *elastocaloric effect size*, (2) *mechanical performance*, and (3) *cycle dependence*, which is related to training and fatigue. Since microcooling takes place in small dimensions, a fourth challenge consists in the understanding and control of (4) *local phenomena*.
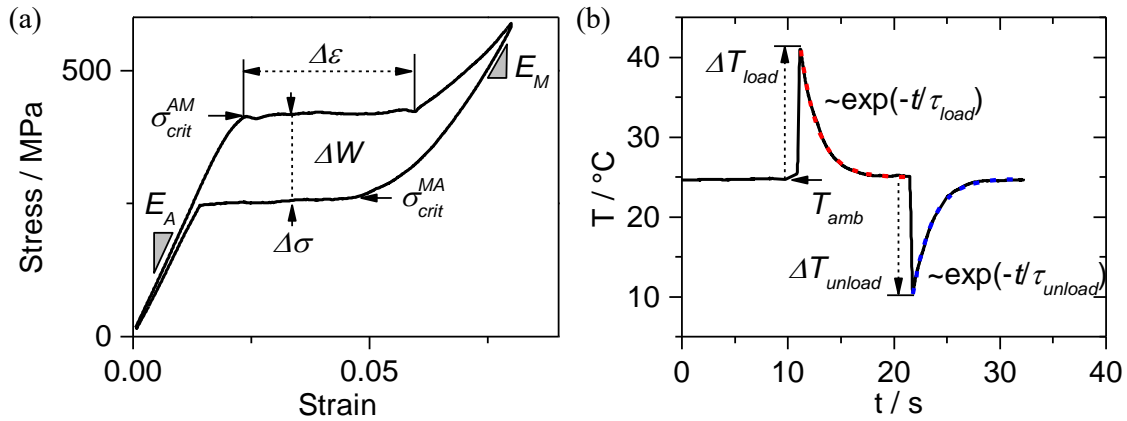
Figure 4.1: Determination of mechanical (a) and thermal parameters (b) from experimentally observed stress-strain characteristics and temperature change.

The materials investigated here belong essentially to the group of TiNi and TiNi-based alloys. In addition, one Cu-based alloy (wire) and one magnetic shape memory alloy (melt-spun film) are examined. An overview is given in Table 4.1. Samples are identified by three-digit numbers associated with each investigated material and lower-case letters for each individual sample (e.g., 006-d). Since in the case of sputter deposition, sample properties may vary between the different sample batches due to changing target composition, an individual number is assigned to each sputter deposition batch. Identification numbers are stated in the text and included in tables and figure captions in order to clearly indicate which

Table 4.1: Overview over investigated samples for elastocaloric microcooling. Legend: t – thickness, sput. – sputter-deposited, roll. – cold rolled.

Batch	Material	$t[\mu m]$	Fabrication / heat treatment
006	$Ti_{49.6}Ni_{50.4}$	19	sput., $10\,min$ @ $650\,°C$ + $10\,min$ @ $450\,°C$
008	$Ti_{49.6}Ni_{50.4}$	20	sput., $10\,min$ @ $650\,°C$ + $10\,min$ @ $450\,°C$
009	$Ti_{49.6}Ni_{50.4}$	20	sput., $10\,min$ @ $650\,°C$ + $10\,min$ @ $450\,°C$
019	$Ti_{49.6}Ni_{50.4}$	22	sput., $5\,min$ @ $650\,°C$ + $5\,min$ @ $450\,°C$
026	$Ti_{49.6}Ni_{50.4}$	16	sput., $5\,min$ @ $650\,°C$ + $5\,min$ @ $450\,°C$
030	$Ti_{49.6}Ni_{50.4}$		sput., $5\,min$ @ $650\,°C$ + $5\,min$ @ $450\,°C$
004	TiNiCu	18	sput.
010	TiNiCu	22	sput., $15\,min$ @ $700\,°C$
021	$Ti_{55.0}Ni_{30.7}Cu_{12.6}Co_{2.8}$	22	sput., $15\,min$ @ $700\,°C$
022	$Ti_{55.0}Ni_{30.7}Cu_{12.6}Co_{2.8}$	23	sput., $15\,min$ @ $780\,°C$
025	TiNiCuCo	20	sput.
028	$Ti_{54.7}Ni_{30.7}Cu_{12.3}Co_{2.3}$	18	sput., $15\,min$ @ $700\,°C$
031	TiNiCuCo	20	sput., $4\,min$ @ $730\,°C$ + $11\,min$ @ $700\,°C$
032	TiNiCuCo	39	sput., $4\,min$ @ $750\,°C$ + $11\,min$ @ $700\,°C$
018	$Ti_{49.1}Ni_{50.5}Fe_{0.4}$	30	roll., $30\,min$ @ $\{350, 400, 450, 500\}°C$
020	$Ti_{49.1}Ni_{50.5}Fe_{0.4}$	50	roll., $30\,min$ @ $\{350, 400, 450, 500\}°C$
040	$Ni_{54.9}Ga_{27.9}Fe_{17.1}$		melt-spun
030	TiNi	Ø254	Wire (commercial)
027	Cu-Al-Be	Ø400	Wire; Czochralski method, oligo crystal

data sets belong together. All materials are fabricated and provided by cooperation partners. The fabrication procedures are briefly described in chapter 2. The aim of this chapter is to characterize the selected materials, determine all crucial thermo-mechanical parameters and estimate the material's cooling potential. These include the elastic moduli E_A and E_M, plateau width $\Delta\varepsilon$, critical stresses of stress-induced and reverse transformation σ_{crit}^{AM} and σ_{crit}^{MA}, stress hysteresis $\Delta\sigma$, adiabatic temperature changes ΔT_{load} and ΔT_{unload}, as well as time constants τ for heat exchange with the environment. Fig. 4.1 shows how the parameters are derived from measured data. At the end of this chapter, experimental findings and their implications for elastocaloric cooling are discussed and compared.

4.1 Cold-rolled TiNiFe foils

A common method for producing shape memory material with thin geometry (i.e. sheet material) is cold rolling. Samples fabricated by this method are referred to as 'foils' in the following. As fabrication starts from a thicker workpiece by mechanic deformation, the material must not be too brittle. Also, material

properties are strongly influenced by rolling-induced texture. Cold-rolled TiNi-based sheets with thicknesses down to $50\,\mu m$ are commercially available and are employed, e.g., in stents and other medical products.

In the following, foil samples with a nominal composition of $Ti_{49.1}Ni_{50.5}Fe_{0.4}$ and a thickness of $30\,\mu m$ are investigated, which are provided by Shuichi Miyazaki from the University of Tsukuba. The low thickness imposes high demands on the fabrication process which are only met by very few suppliers. Samples are produced by cold-rolling with a final cold-rolling reduction of 40% and delivered in sheets of about $50 \times 150\,mm^2$. For tensile tests, samples having a width of $2\,mm$ and a length of $20\,mm$ are structured from the sheets. Three different structuring methods are tested for this purpose: Optical lithography in combination with chemical wet etching, laser cutting and mechanical cutting. Wet-chemical etching is performed using a mask of UV-structured positive resist (AZ4533) and a solution of hydrofluoric acid, nitric acid and deionized water for etching. Laser cutting is performed using a $20\,W$ Nd:YAG laser in pulsed mode.

(a) (b) (c)
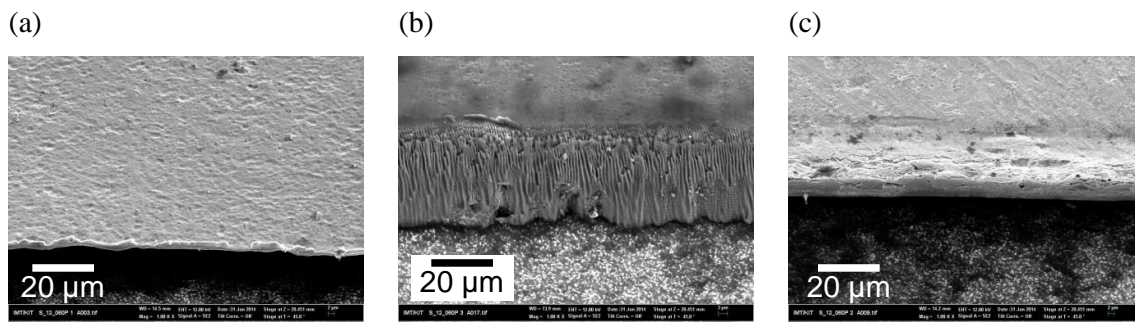
Figure 4.2: Comparison of structuring methods for TiNiFe foil samples produced by cold-rolling: (a) Lithography and chemical wet etching, (b) laser cutting, and (c) mechanical cutting. Images are obtained by scanning electron microscopy (SEM).

The resulting edge qualities are examined by scanning electron microscopy (SEM), as shown in Fig. 4.2. Smooth but corrugated edges are obtained by wet etching, and the sample thickness varies in the vicinity of the edge (Fig. 4.2 (a)). The reason is that a comparatively long etching time is required for the given sample thickness. Thus the resist layer partially peels off before the etching solution has fully penetrated the TiNiFe foil. The resulting samples have a slightly varying cross-section. The edge of the laser-cut sample, shown in Fig. 4.2 (b), is covered by fine striations induced by pulsed material removal. The striations might possibly act as nucleation sites for crack growth and are therefore not desired. In the case of mechanical cutting (Fig. 4.2 (c)), reasonably flat sample edges are obtained, therefore this method is employed for the following experiments. At this point it should be noted that edge quality and hence sample lifetime may be improved considerably through polishing procedures such as electro polishing [111, 112]. However, due to lack of the necessary equipment, unpolished samples were used. Sample lifetime (in the order of hundreds of cycles) is sufficient for characterization purposes.
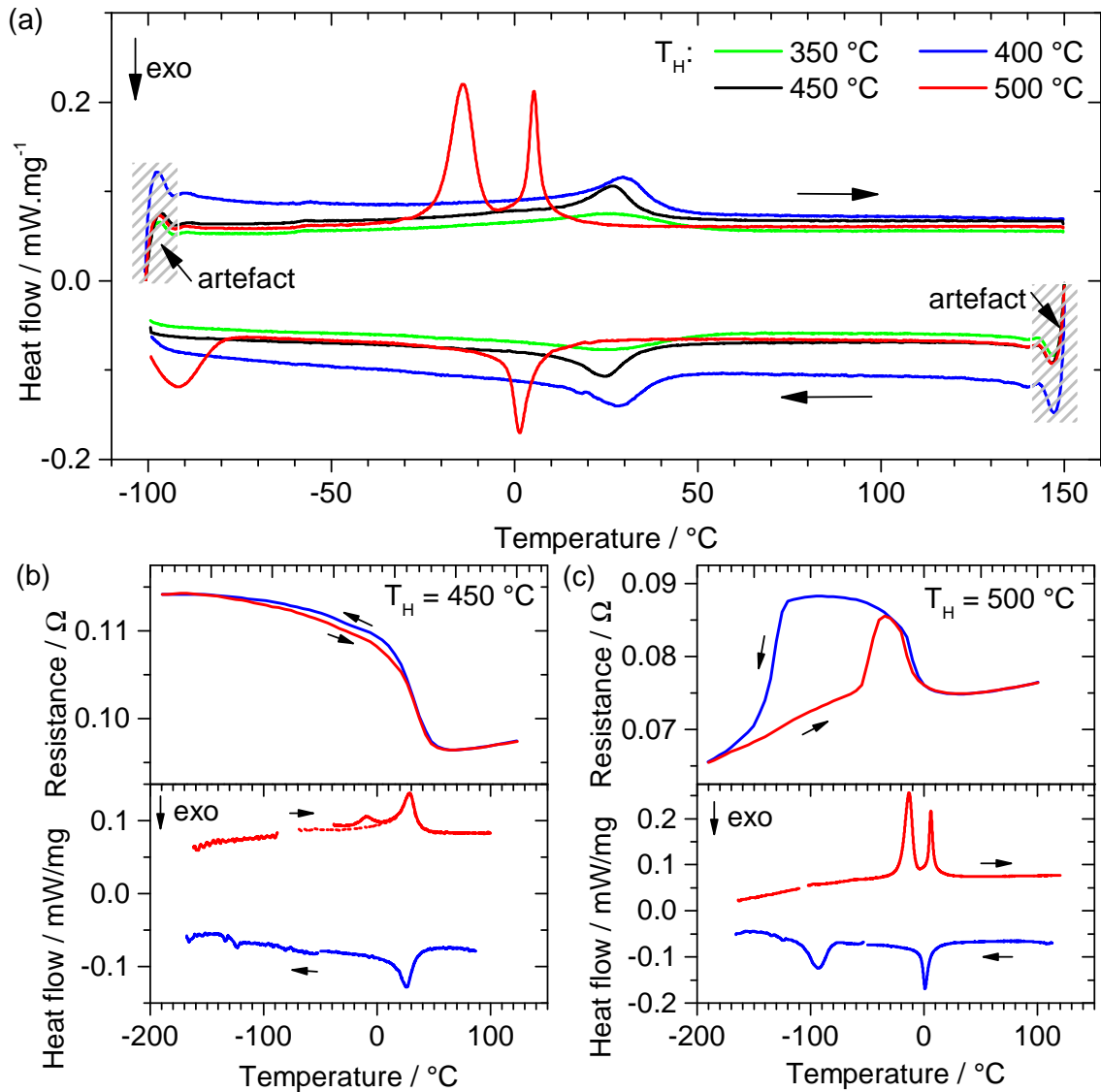
Figure 4.3: Thermally induced phase transformation properties of TiNiFe foil samples, characterized by differential scanning calorimetry (DSC) and electrical resistance measurement. Samples have been annealed for $30\,\text{min}$ at different temperatures T_H as indicated. (a) DSC measurements on four different samples (annealed at $T_H = 350, 400, 450$ and $500\,°\text{C}$) in the temperature range of -100 to $150\,°\text{C}$. (b) DSC and resistance measurement in the extended temperature range of -180 to $120\,°\text{C}$ for a sample annealed at $450\,°\text{C}$. (c) DSC and resistance measurement for a sample annealed at $500\,°\text{C}$. (Sample batch 018)

Thermal and electrical properties.   In order to adjust phase transformation properties and obtain superelastic behavior, as-fabricated foil samples require a heat treatment. For this purpose, samples are clamped between two metal plates fixed with screws and then placed in a quartz tube. The tube is sealed, flooded with N_2 gas and evacuated to a pressure below 1×10^{-4} mbar twice before being placed in a pre-heated oven in order to omit sample oxidation. In addition, a Ti foil is placed in between the metal plates as well, acting as an oxygen getter. Samples are left in the oven until reaching the final annealing temperature $T_H \in \{350, 400, 450, 500\}°C$ and then held at this temperature for 30 min. Then the quartz tube is removed from the oven and flooded with N_2 gas in order to quench the samples.

The resulting phase transformation temperatures are investigated by DSC and $R(T)$ measurements. As the results in Fig. 4.3 show, a two-step M→R→A as well as A→R→M transformation with A_f temperature below room temperature is observed in the case of $T_H = 500°C$. For heat treatments at 400 and $450°C$, a one-step transformation is observed, having peak temperatures close to room temperature and a small thermal hysteresis of a few Kelvin. However, when extending the temperature range of the DSC measurement, an additional peak occurs in the heating curve of the material with $T_H = 450°C$. Apparently, the second step of the phase transformation proceeds at temperatures below the measurement range of the DSC setup. In case of $T_H = 350°C$, phase transformation peaks are very broad and shallow, indicating that the annealing temperature was too low.
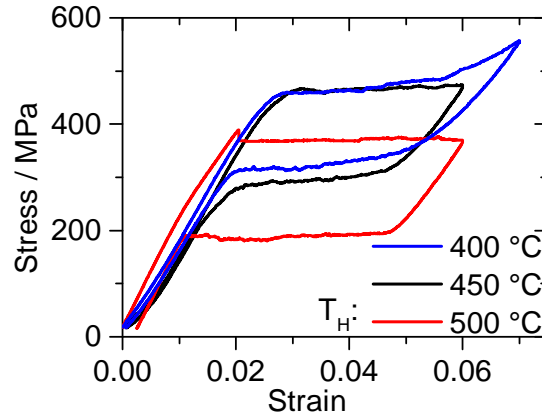
Figure 4.4: Stress-strain characteristics of TiNiFe foil samples annealed at different temperatures T_H as indicated. Loading was performed in RD at the strain rate 1×10^{-4} s^{-1}. Stress plateaus are considerably lower for sample annealed at $500°C$ compared to samples annealed at lower temperatures. (Samples 018-f,g,h)

Mechanical performance.   Since the samples annealed at 400, 450 and $500°C$ exhibit a phase transformation around or below room temperature, they are expected to be superelastic. For verification, tensile tests are performed for each ma-

terial at a very low strain rate of $1 \times 10^{-4}\,\mathrm{s}^{-1}$, samples being aligned in rolling direction. The results are shown in Fig. 4.4. All three samples exhibit pseudoelastic behavior with a closed stress-strain characteristic, i.e. attaining a strain of approximately 0% after a full cycle. This is important to notice especially for the samples annealed at $T_H = 400$ and $450\,°\mathrm{C}$. On the one hand, the DSC curves reveal a thermally induced phase transformation peaking right at room temperature. On the other hand, considerable stress is necessary in order to trigger the stress-induced phase transformation and upon unloading, the reverse transformation takes place completely. Although partial one-way shape memory effect could be expected based on the DSC measurement, it is not observed. For $T_H = 400$ and $450\,°\mathrm{C}$ the curves are similar, having a stress plateau at $460\,\mathrm{MPa}$ during loading and a stress hysteresis of 140 and $170\,\mathrm{MPa}$, respectively. The stress plateau of the sample with $T_H = 500\,°\mathrm{C}$ is considerably lower, at $370\,\mathrm{MPa}$, and the stress hysteresis is $190\,\mathrm{MPa}$. This difference seems plausible, if one assumes that R $\rightarrow$ B19 transformation takes place at lower temperatures for the samples with $T_H = 400$ and $450\,°\mathrm{C}$, compared to $T_H = 500\,°\mathrm{C}$. The end of stress plateau is reached at a strain of about 6% for all samples.

In order to examine the mechanical behavior of the samples at different ambient temperatures, quasi-static tensile tests are conducted in a heating chamber. Temperature is increased step-wise and temperature stabilization is awaited before each experiment. As Fig. 4.5 (a) shows, the stress plateaus rise with increasing temperature. From the temperature-dependent change of plateau height (Fig. 4.5 (b-d)), Clausius-Clapeyron coefficients are estimated by linear fits. These coefficients quantify the proportionality between thermally induced and stress-induced martensitic phase transformation. For $T_H = 400$ and $450\,°\mathrm{C}$, thermal hysteresis decreases with increasing ambient temperature and the coefficient for the forward transformation (4.5 and $5.6\,\mathrm{MPa\,K}^{-1}$) is lower than for reverse transformation (7 and $6\,\mathrm{MPa\,K}^{-1}$). This trend is not observed for the sample with $T_H = 500\,°\mathrm{C}$, where coefficients are around $7.5\,\mathrm{MPa\,K}^{-1}$.

Owing to the fabrication process, mechanical performance is expected to depend also on sample orientation with respect to rolling direction. Quasi-static tensile tests are performed on samples oriented in rolling direction (RD), transverse direction (TD, i.e. perpendicular to RD), as well as $45°$ to rolling direction. The resulting stress-strain characteristics are depicted in Fig. 4.6 (a). For loading in RD and $45°$ direction, the curves are virtually identical. In TD, however, the critical stresses (plateau heights) are increased, whereas the plateau width is decreased. The stress-strain characteristic in Fig. 4.6 (a) is a macroscopic curve based on engineering strain (i.e. averaged over the whole sample), like all stress-strain curves discussed before. In order to evaluate the transformation stresses and strains more precisely, a local stress-strain characteristic (for a particular point of each sample) is generated from digital image correlation (DIC) evaluation, as seen in Fig. 4.6 (b). From this curve it can be seen that in case of RD and $45°$ loading, stress-induced transformation sets in at a critical stress of about $450\,\mathrm{MPa}$. The plateau width $\Delta\varepsilon$, i.e. the strain difference between austenite and stress-induced martensite, is 4.1% in this case. In TD, the stress has to reach a higher critical value
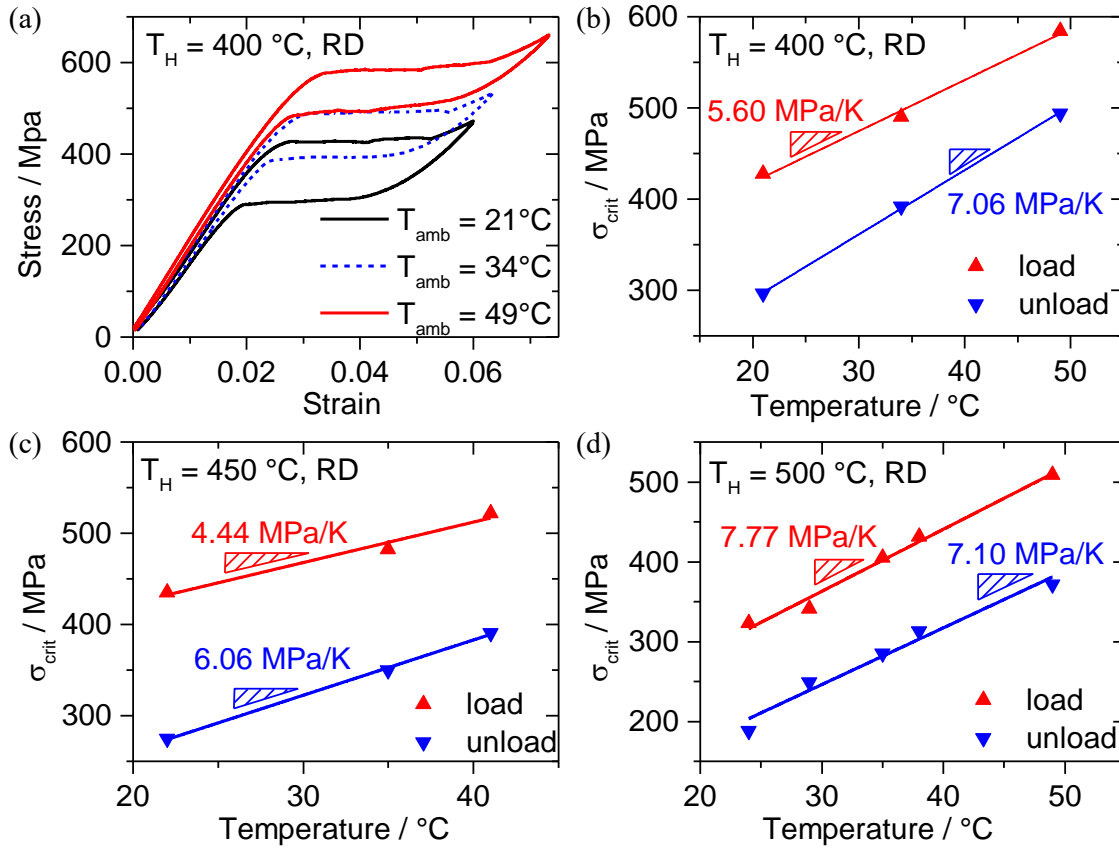
Figure 4.5: Mechanical performance of TiNiFe foil samples for different ambient temperatures T_{amb}. (a) Quasi-static stress-strain characteristics for a sample annealed at $400\,°C$. The strain rate is $1 \times 10^{-4}\,s^{-1}$. The stress values σ_{crit} of the superelastic plateaus during loading and unloading are plotted as a function of ambient temperature for the sample annealed at $400\,°C$ (a), $450\,°C$ (b) and $500\,°C$ (c). Clausius-Clapeyron coefficients $d\sigma_{crit}/dT$ are estimated from the slope of linear fits. (Samples 018-f,g,h)

of $520\,MPa$ in order to trigger phase transformation. The plateau width decreases to 2.6%. These observations are in qualitative agreement with results of Kim and Daly, obtained with cold-rolled TiNi samples having a thickness of $254\,\mu m$, i.e. ten times as thick as in the present work [74].

Strain bands. The observed stress-strain behavior including stress plateaus is due to the spatial and time-resolved course of stress-induced phase transformation in TiNi-based alloys [72]. The transformation proceeds in a highly localized manner, rather than homogeneously. These local effects are studied by in-situ digital image correlation (DIC) analysis. DIC is employed to generate local strain maps with respect to loading direction, which are shown as color-coded diagrams. Due to the limited field-of-view of the camera, only a representative sample area of about $3 \times 2\,mm^2$ (i.e. 20% of the full length) may be studied at once. Chronological time series of local strain profiles during loading and unloading in

(a)

(b)

(c)
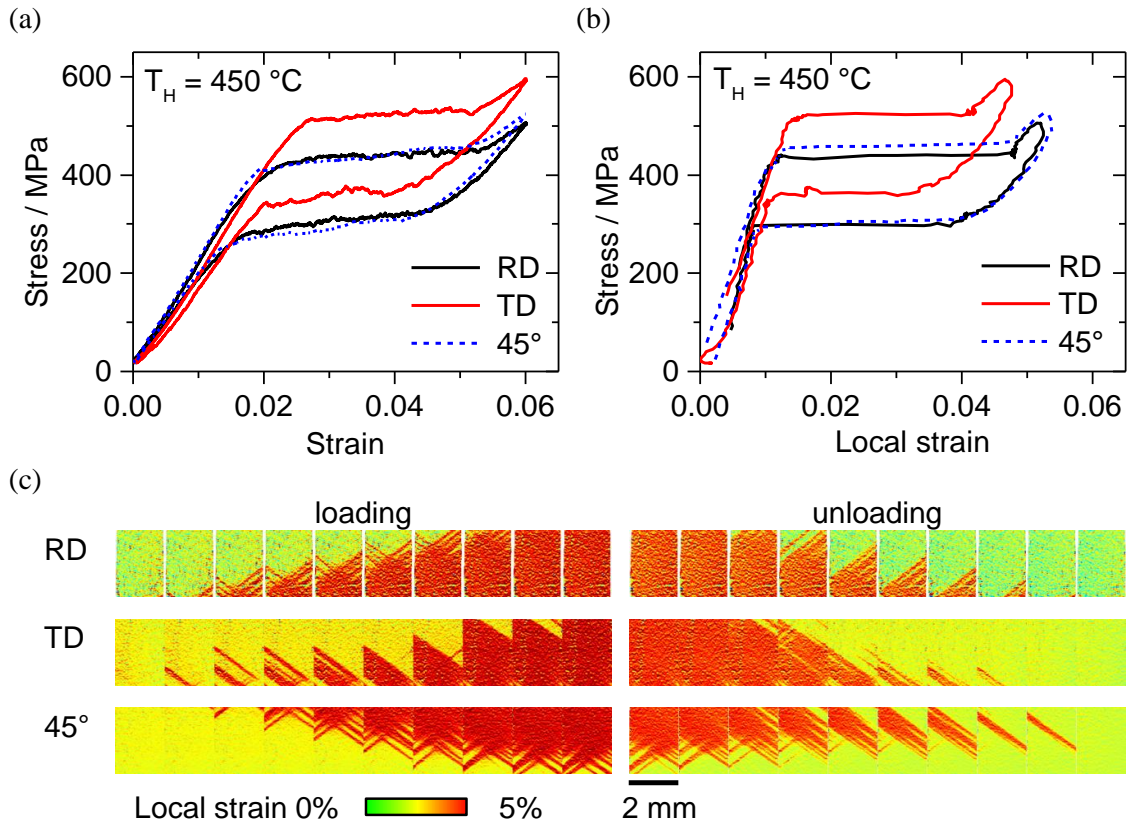
Figure 4.6: Mechanical performance of TiNiFe foil samples in dependence of rolling-induced texture. Samples are investigated by quasi-static tensile test at a strain rate of $1 \times 10^{-4}\,\mathrm{s}^{-1}$ in rolling direction (RD), transverse direction (TD) and $45°$ to rolling direction. (a) Macroscopic stress-strain characteristics. (b) Local stress-strain characteristics near sample fixation determined by DIC. (c) Chronological series of local strain maps, obtained by DIC evaluation near the sample fixation. Compare Ref. [295]. (Samples 018-a,b,c)

RD, TD and $45°$ direction are shown in Fig. 4.6 (c). In all cases, a strain band enters the observed area at some point during loading, grows in size and finally covers the whole area at the end of the loading step. Regions with increased strain level (red in the color code) are interpreted as predominantly transformed to martensite (all the variants being aligned close to loading direction), whereas regions of lower strain (green/yellow) are predominantly in austenite phase. Both regions are divided by sharp interfaces with a strain discontinuity $\Delta\varepsilon$, which are aligned in a characteristic angle of $\pm 55°$ with respect to loading direction. For TD loading, one of the two possible orientations dominates, whereas for RD and $45°$ loading intersecting interfaces of both orientations are observed.

Elastocaloric performance.   Up to now, experiments have been performed under quasi-static conditions in order to observe the mechanical behavior independently of self-heating and cooling effects. However, for elastocaloric cooling ap-
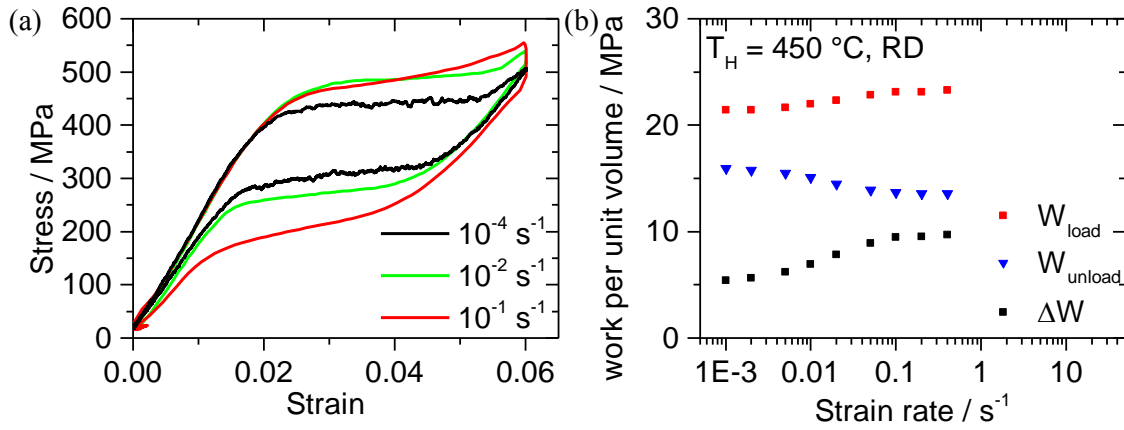
Figure 4.7: Mechanical performance of TiNiFe foil samples as a function of strain rate. (a) Stress-strain characteristics for different strain rates. (b) Mechanical works W_{load} an W_{unload} for loading and unloading, as well as work input $\Delta W = W_{load} - W_{unload}$ as a function of strain rate (logarithmic scale). (Sample 018-a)

plications, these effects are essential. The mechanical performance of the material determines the work input for a cooling cycle and has to be investigated under realistic strain rates. Fig. 4.7 (a) exemplarily shows the stress-strain characteristics of a sample loaded at different rates. In the quasi-static case, stress plateaus are approximately horizontal. When the strain rate is increased, the plateaus gradually become steeper and the stress is higher at the end of loading. During the time interval of constant strain, the sample temperature equalizes with the environment and the stress drops to the level reached at the end of quasi-static loading. Then, upon unloading, the plateau stress drops lower than in the adiabatic case. Hence, the area enclosed by the loading and unloading trajectory increases with increasing strain rate, until the strain rate is so high that the adiabatic limit is reached. The mechanical work of loading and unloading, obtained from stress-strain characteristics by numerical integration, is shown in Fig. 4.7 (b). The difference of both quantities can be interpreted as the work input $\Delta W = W_{load} - W_{unload}$ of a full load-unload cycle. The work input increases with strain rate, until adiabatic conditions are reached at a strain rate of $0.2\,\mathrm{s}^{-1}$. In the isothermal limiting case, ΔW reduces to the dissipated work due to irreversible processes. The strain rate of the adiabatic limit contains information about the thermal coupling of the sample to the ambient: at the respective strain rate, heat generation and absorption due to phase transformation are considerably faster than heat exchange with the environment, e.g., by air convection and heat conduction through the clamping.

In literature, a hysteresis maximum at an intermediate strain rate was reported rather than a saturating maximum hysteresis in the adiabatic limit [61, 62]. The difference is caused by the fact that, in contrast to the present work, temperature equalization was not awaited between loading and unloading step in these studies.

(a) loading

(b) unloading

2 mm   27 °C   40 °C   13°C   23°C
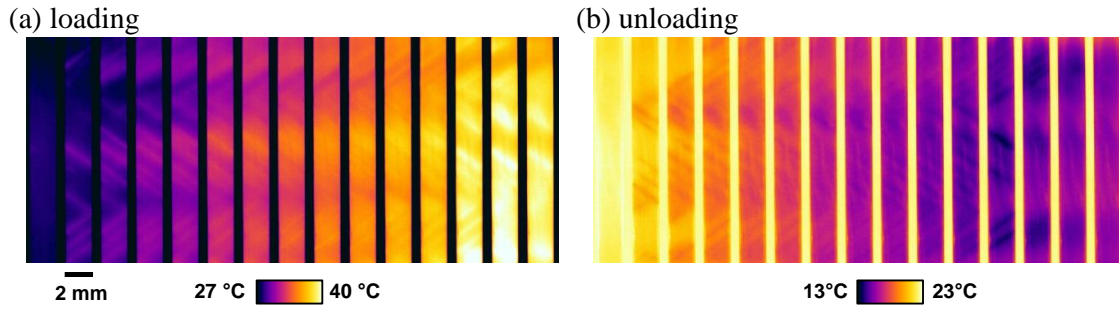
Figure 4.8: Chronological series of temperature profiles of TiNi foil samples annealed at $450\,°C$ during tensile test in RD at a strain rate of $0.02\,\mathrm{s}^{-1}$. The time step between two adjacent thermograms is $80\,\mathrm{ms}$. Compare Ref. [295]. (Sample 022-a)

Temperature bands. During strain rate-dependent experiments, the temperature distribution of the sample is monitored by an infrared camera. A chronological series of thermograms of a tensile test sample is shown in Fig. 4.8. The diagrams reveal self-heating of the sample during superelastic loading and self-cooling during unloading. On closer inspection, the thermograms reveal a number of fine temperature bands. These bands are related to the localized character of the phase transformation and will be examined in more detail in section 4.2.2 on the example of sputter-deposited films. The time-dependent temperature evolution is obtained by averaging over a test area of $1 \times 1\,\mathrm{mm}^2$ in the sample center. A selection of temperature evolution curves of a sample annealed at $500\,°C$ for different strain rates is shown in Fig. 4.9 (a). For increasing strain rate, self-heating and cooling take place in shorter time intervals and the (absolute) temperature change reached at the end of loading/unloading increases. The peak values are plotted as a function of strain rate for samples with different annealing temperatures in Fig. 4.9 (b-d). The adiabatic limit may be confirmed from the diagrams based on the observation that peak temperatures do not increase when increasing the strain rate above $0.2\,\mathrm{s}^{-1}$. The highest adiabatic temperature changes ΔT_{ad} of $22\,\mathrm{K}$ during loading and $-17\,\mathrm{K}$ during unloading are reached in case of $T_H = 500\,°C$. For $T_H = 450\,°C$, peak temperature changes are similar, but about 1 to $2\,\mathrm{K}$ lower. The lowest effect size is observed for $T_H = 400\,°C$. Measurements performed in RD and TD reveal that the orientation of sample texture plays a minor rule for the elastocaloric temperature change, the differences lying well within the natural scatter between samples.

After reaching the peak values, sample temperature equalizes with the environment following an exponentially decaying trend. The time constant for heat transfer, obtained from exponential least-squares fit to the data, is about $1.5\,\mathrm{s}$.

Training and fatigue. Finally, the dependence of mechanical and thermal performance on cycle number is investigated, since cyclic stability is crucial for any practical application. An extensive fatigue study lies beyond the scope of this work, but a cyclic experiment comprising 100 cycles shall be discussed in the
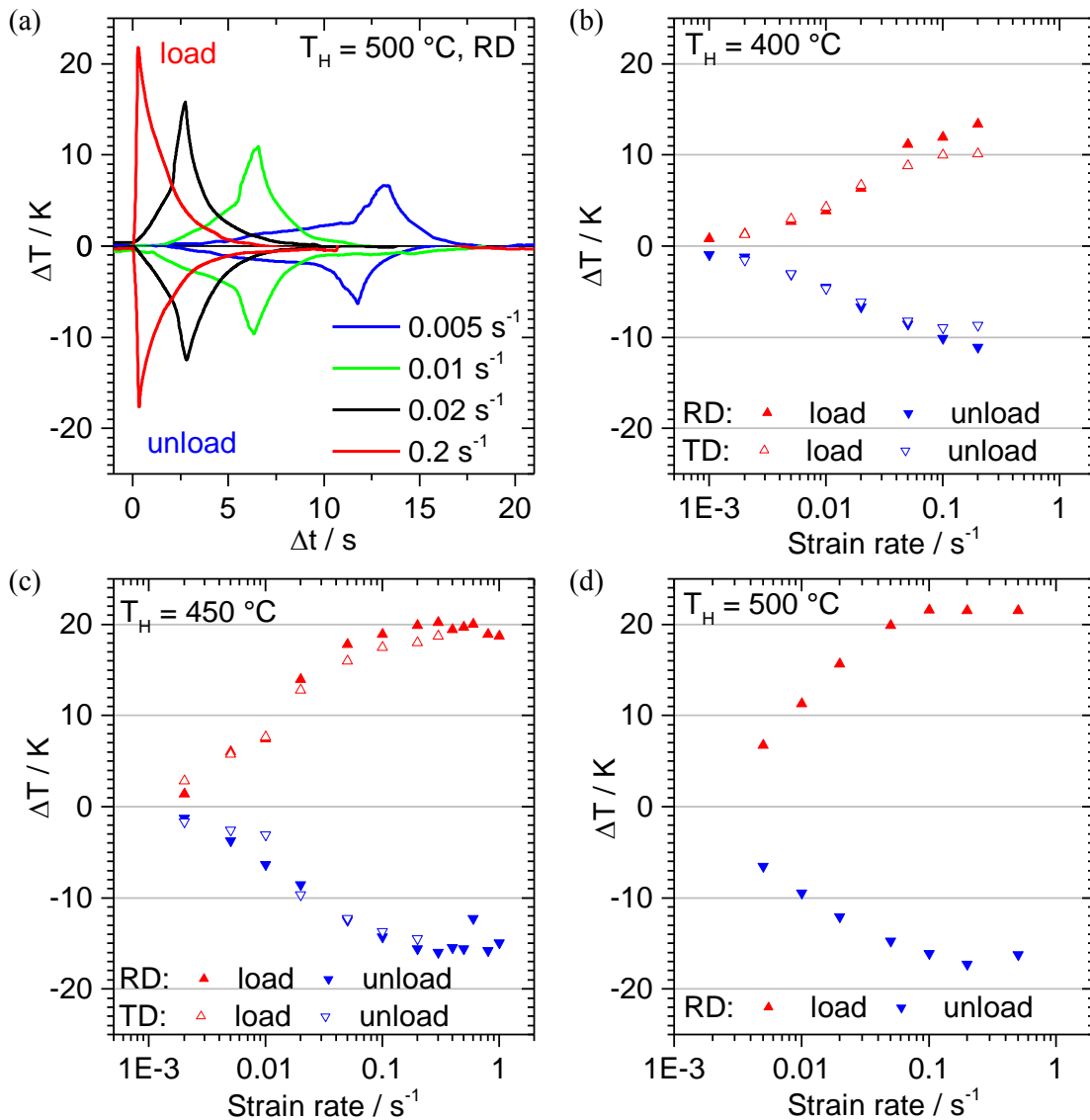
Figure 4.9: Elastocaloric temperature change of TiNiFe foil samples as a function of strain rate. (a) Time-dependent temperature change due to self-heating and cooling during loading and unloading for various strain rates as indicated. Sample annealed at $T_H = 500\,°C$ and loaded in RD. Peak temperature changes upon loading and unloading as a function of strain rate for samples annealed at $500\,°C$ (b), $400\,°C$ (c) and $450\,°C$ (d). Loading direction (RD/TD) is indicated. Compare Ref. [295]. (Samples 018-g,a,b,h,i)
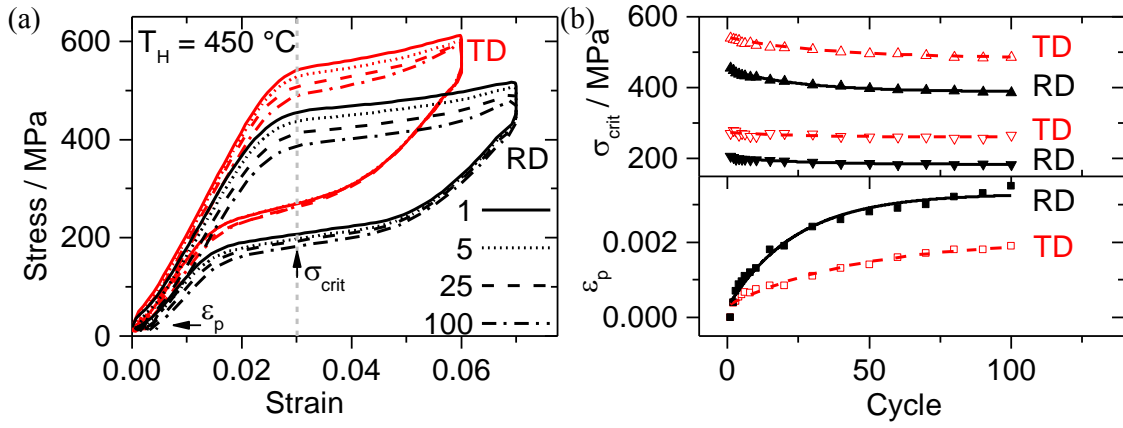
Figure 4.10: Mechanical performance of TiNiFe foil samples as a function of cycle number for loading directions RD and TD. Samples are trained for 100 cycles at a strain rate of $0.1\,\text{s}^{-1}$. (a) Stress-strain characteristics of cycle 1, 5, 25 and 100 as indicated. (b) Superelastic plateau stresses σ_{crit} measured at 3% strain during loading and unloading, as well as plastic strain ε_p as a function of cycle number. Exponential fits of data are included as solid and dashed lines. TiNiFe foil samples in dependence of loading direction. Compare Ref. [294]. (Samples 018-j+k)

following. Experiments are performed on two samples annealed at $450\,°\text{C}$ and loaded at a strain rate close to the adiabatic limit in RD and TD, respectively. The stress-strain characteristics are shown in Fig. 4.10 (a). For both samples, the stress plateau during loading and, to a lower extend, during unloading decreases with increasing cycle number. Cycle-to-cycle deviation is highest for the first cycles and then decreases continuously. In order to quantify this stabilization process, the critical stresses determined at a strain of 3%, as well as the plastic strain accumulated at the end of each cycle are analyzed in Fig. 4.10 (b). Data is approximated by exponential fits, which are included as dashed lines. Within 100 cycles, the plateau stress of forward transformation decreases by 10% for TD and by 14% for RD loading. The decrease of the reverse transformation plateau is weaker, namely by 5% and 12% in TD and RD, respectively. After every cycle, a small amount of plastic deformation is accumulated. In TD, a moderate plastic strain ε_p of 0.14% is reached after 100 cycles. In RD, plastic deformation is approximately doubled. The stabilization cycle number, obtained from exponential fits, is roughly 30 cycles. The cycle-dependent elastocaloric effect size is analyzed by IR measurements, which do not reveal a pronounced impact of training on the peak temperature changes.

Pseudoelastic subloops. At the end of this section, the correlation of latent heat release/absorption and pseudoelastic sub-loops shall be investigated. In a number of publications on SMA actuation and also elastocaloric cooling, it is proposed to limit the strain range of application in order to increase the material's lifetime [291, 296]. Therefore it is important to know which consequences the limitation of strain range has on the elastocaloric effect size. The stress-strain char-
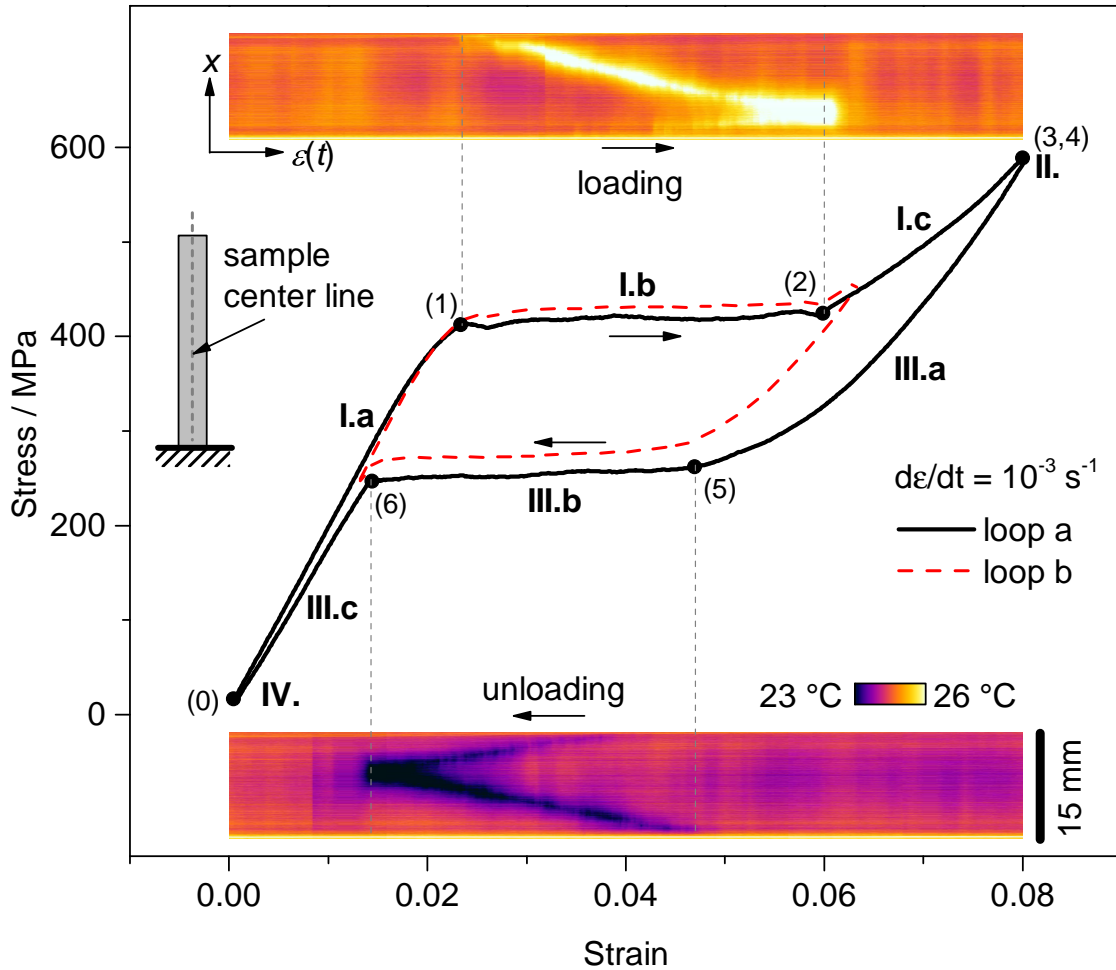
Figure 4.11: Stress-strain characteristics of a TiNiFe foil sample annealed at $T_H = 450\,°C$ and loaded at a strain rate of $1 \times 10^{-3}\,s^{-1}$ in RD: full loop (solid line) and subloop comprising only superelastic plateaus (dashed line). The inset shows the temperature evolution along the center line of the sample as a function of strain during loading and unloading. (Sample 018-m)

acteristic in Fig. 4.11 shows the four steps of the cooling cycle (compare chapter 3): I. stress-induced phase transformation (loading), II. heat release, III. reverse transformation (unloading) and IV. heat absorption. The loading and unloading step are further subdivided into elastic deformation of austenite (I.a, III.c), stress plateaus (I.b, III.b) and elastic deformation of martensite (I.c, III.a). Obviously, the elastic loading (I.c) and unloading curve (III.a) of the stress-induced martensite do not coincide. The time-dependent temperature evolution of the sample during the experiment is included as colored inset in 4.11. The diagram shows the temperature profile in x-direction along the sample center for each strain value during loading and unloading. Pronounced localized temperature bands are observed in sections I.b and III.b of the stress-strain characteristic. These sections may also be accessed by a stress-strain subloop (indicated as red dashed line in the plot) instead of the full loop. However, weak temperature changes are

observed beyond the stress plateaus as well, showing homogeneous instead of localized distribution.

In a further experiment, smaller stress-strain subloops are investigated by tensile test and infrared thermography. The results for a moderate and a high strain rate are shown in Figs. 4.12 and 4.13. At the lower strain rate of $1 \times 10^{-3}\,\mathrm{s}^{-1}$ only two temperature bands are observed at the same time (compare Fig. 4.11). For subloop e in the lower strain range, temperature changes are only observed at the upper sample end, subloop f results in temperature bands in the sample center and subloop g yields localized heating/cooling only at the lower sample end. However, in all three cases a weak homogeneous heating/cooling of the entire sample is observed in addition. The same homogeneous temperature change is also observed for subloops c and d before, as well as h, i and j after the stress plateau region. This result indicates that a certain volume fraction of the elastocaloric material is undergoing phase transformation independently from the dominating Lüders-like transformation. In case of the higher strain rate of $0.2\,\mathrm{s}^{-1}$ the number of thermal bands increases and the bands are distributed more evenly for the respective subloops, but the effect is very similar. The temperature changes associated with the stress-strain subloops are shown as a function of strain in Fig. 4.14. The homogeneous temperature changes are considerably lower than the localized temperature changes, but the associated stress-strain subloops are also much more narrow.

The above experiments show that in case of subloops within the strain region of the stress plateaus, only part of the sample shows localized temperature change with the maximum effect size. Hence, these subloops might possibly represent a more gentle treatment of the superelastic material, compared to the full stress-strain loop. However, part of the heat pumping / cooling performance of the material is not accessed and the exact location of maximum temperature change cannot be controlled. The experiments furthermore show that even outside of the plateau region, latent heat is released and absorbed by the material. These homogeneous temperature changes are associated with volume fractions of the SMA remaining in the austenitic state even beyond the end of the forward stress plateau, which are referred to as residual austenite or 'lazy austenite' [45, 297, 298]. Similarly, individual grains or volume fractions may transform to martensite even prior to the stress plateau onset when they have already been prestrained by the surrounding matrix.
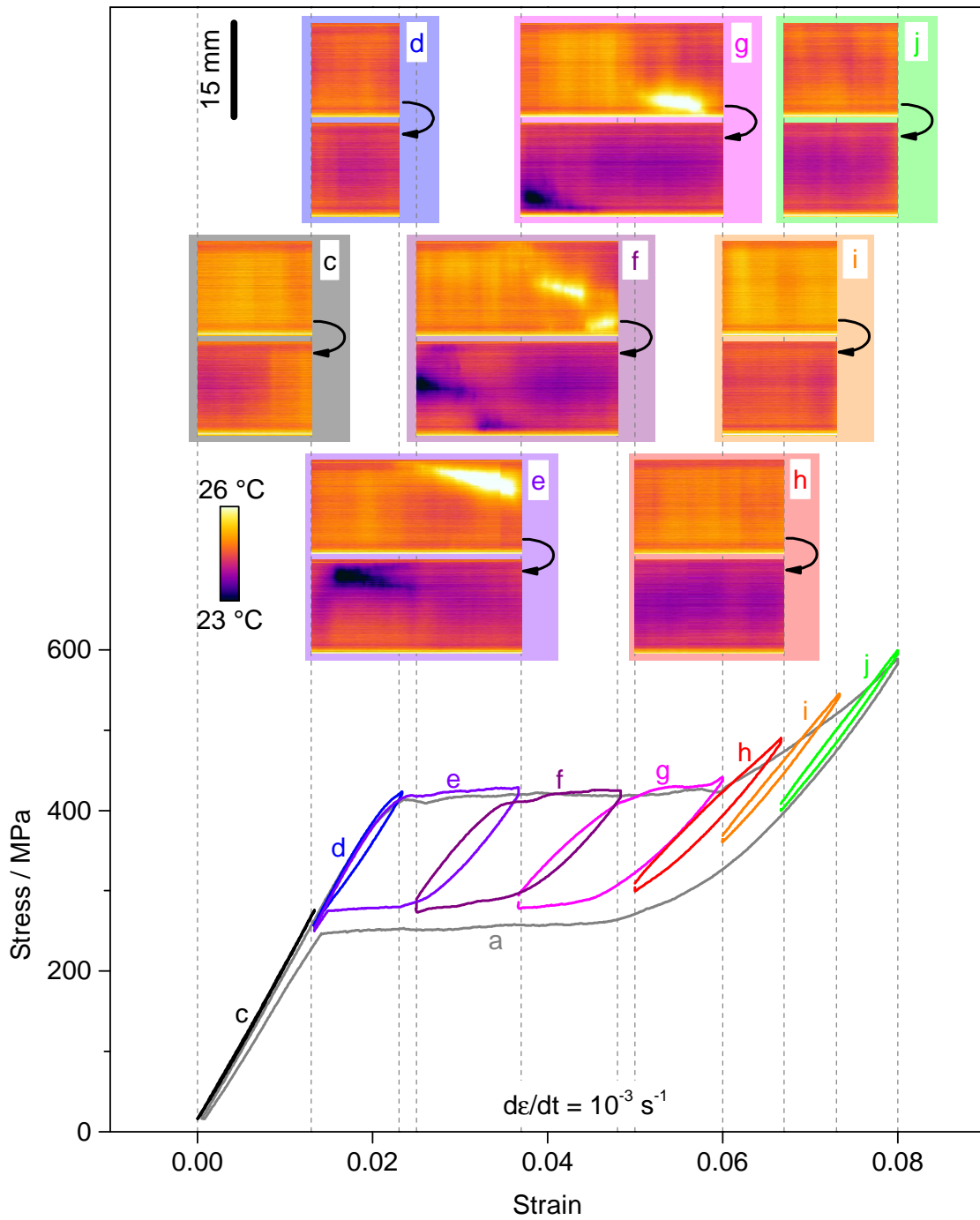
Figure 4.12: Stress-strain characteristics for a TiNiFe foil sample annealed at $T_H = 450\,°\text{C}$ (strain rate $1 \times 10^{-3}\,\text{s}^{-1}$, loading in RD): subloops for several strain intervals. The insets show the temperature evolution along the center line of the sample as a function of strain during loading and unloading for each respective subloop. (Sample 018-m)
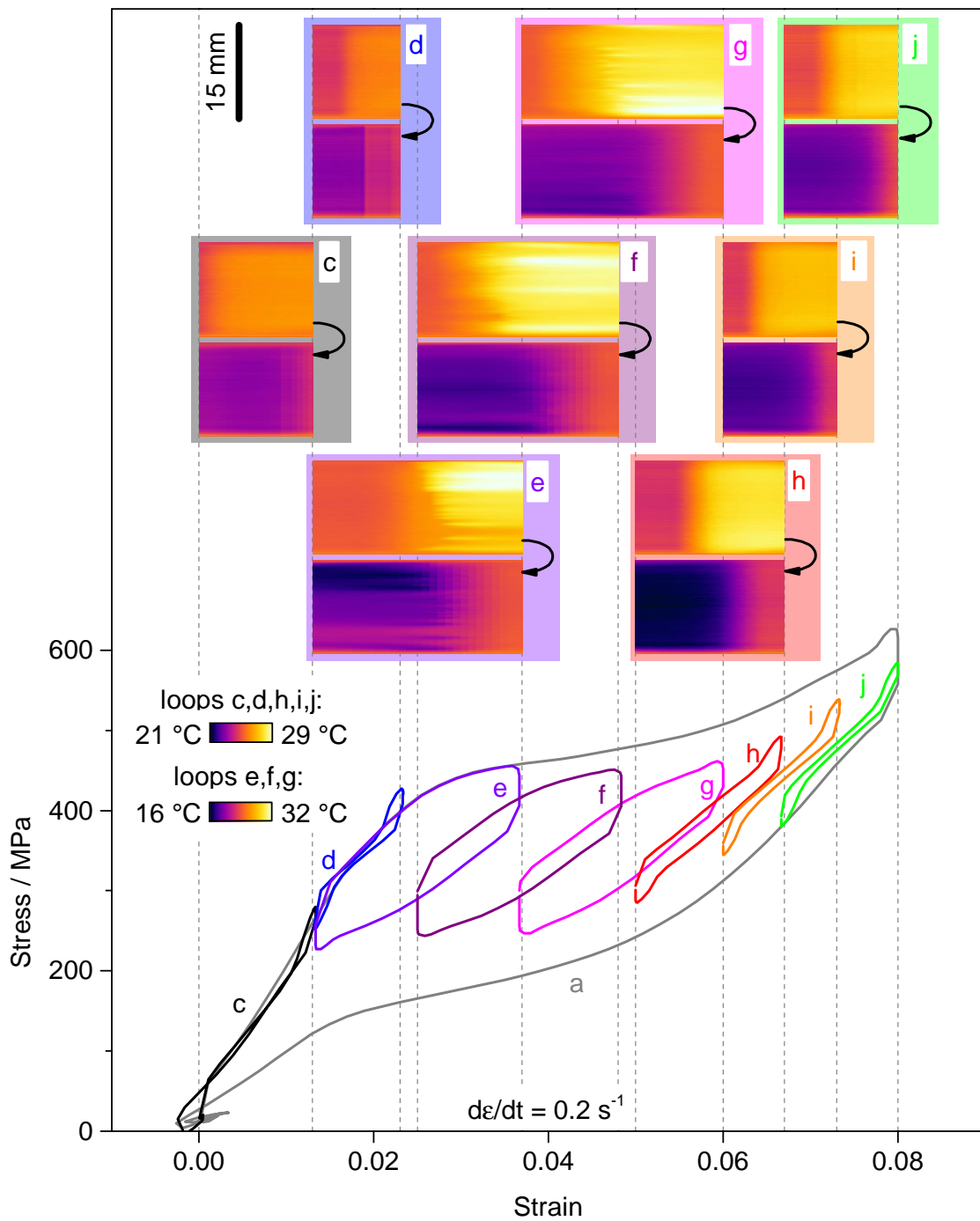
Figure 4.13: Stress-strain characteristics for a TiNiFe foil sample annealed at $T_H = 450\,°C$ (strain rate $0.2\,s^{-1}$, loading in RD): subloops for several strain intervals. The insets show the temperature evolution along the center line of the sample as a function of strain during loading and unloading for each respective subloop. (Sample 018-m)
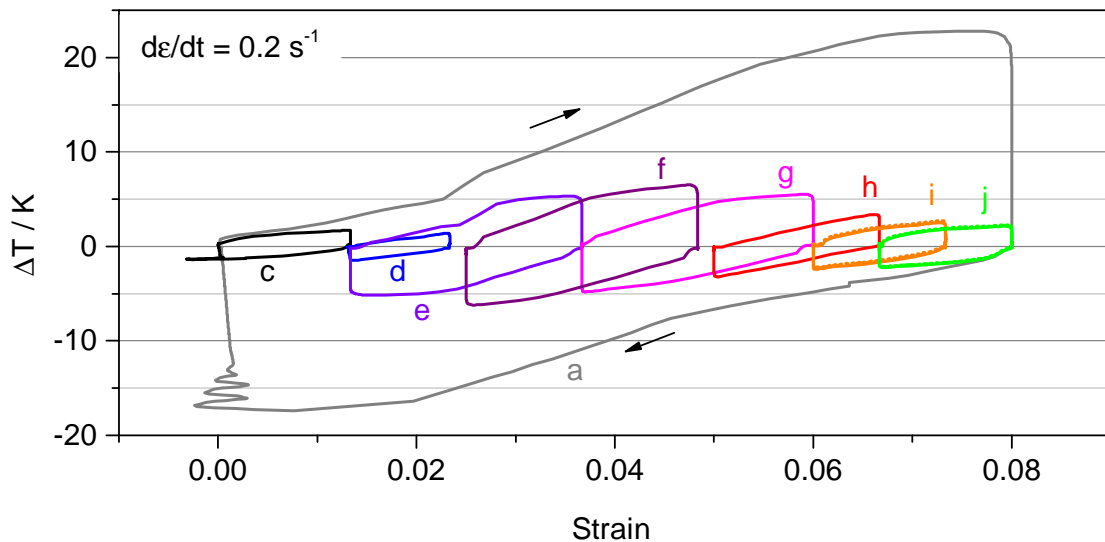
Figure 4.14: Temperature-strain characteristics for TiNiFe foil sample annealed at $T_H = 450\,°C$ (strain rate $0.2\,\mathrm{s}^{-1}$, loading in RD): subloops for several strain intervals. (Sample 018-m)

4.2 Sputter-deposited films

In contrast to cold-rolling, sputter deposition is an additive process which is capable of producing arbitrarily thin samples (down to individual atomic monolayers) which are furthermore free of inclusions. Samples produced by this method will be referred to as 'films' in the following. Sputter-deposited TiNi-based films with binary, ternary and quaternary composition are provided by the group of Eckhard Quandt from the University of Kiel (CAU).

Although thinner samples are possible, sample thickness is adjusted to about $20\,\mu m$ in order to enable proper handling. Samples are structured already during sputter deposition by the so-called 'mushroom process' [164]. Sample dimensions are $1.75\,mm$ in width and $25\,mm$ in length.

4.2.1 TiNi films

Binary TiNi is a well-known standard material for sputter deposition. Samples with a thickness of $20\,\mu m$ are produced by DC magnetron sputtering from a $Ti_{53.2}Ni_{46.8}$ target. The resulting sample stoichiometry, determined by XRD on a selected sample, is $Ti_{49.6}Ni_{50.4}$. After sputter deposition, a two-step heat treatment is applied to the initially amorphous films, comprising a rapid thermal annealing at $650\,°C$ for $10\,min$ and at $450\,°C$ for another $10\,min$.
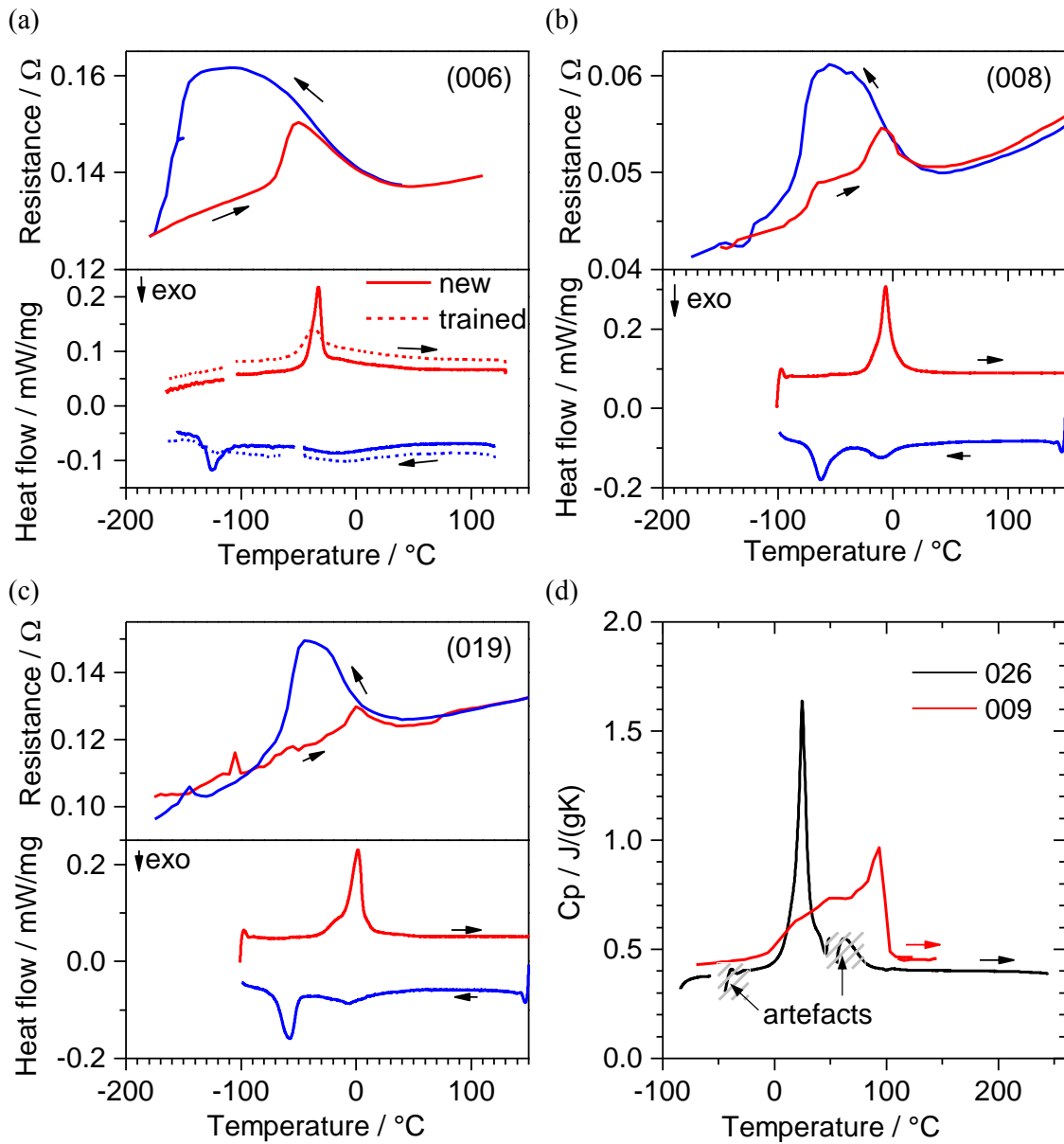
Figure 4.15: Thermally induced phase transformation properties of TiNi film samples, characterized by differential scanning calorimetry (DSC) and electrical resistance measurement: sample batches 006 (a), 008 (b) and 019 (c). Heat capacity c_p is determined by DSC for sample batches 009 and 026 (d). Compare Ref. [299].

Thermal and electrical properties. Since batch sizes are comparatively small, samples from different fabrication batches are investigated in the following. Target composition changes over time, therefore samples naturally show a certain scatter in material properties. DSC and electrical resistance measurements are performed for sample batches 006, 008 and 019 in order to determine thermal phase transformation properties (Fig. 4.15). A comparison reveals that samples 008 and 019 show very similar behavior. Both samples undergo a two-step phase transformation upon cooling with a shallow peak in the DSC curve at $-10\,°C$ followed by a somewhat bigger peak at $-60\,°C$. The latent heat of both peaks is determined to about $20\,\mathrm{J\,g^{-1}}$. Upon heating, the peaks of both transformation steps are superimposed to a single peak close to $-5\,°C$, having a latent heat of $20\,\mathrm{J\,g^{-1}}$ as well. The full set of transformation temperatures is presented in table 4.2. In the cooling part of the electrical resistance curve, a plateau of increased resistance is observed in the temperature range of -20 to $-50\,°C$. Such a resistance plateau indicates that the transformation from austenite to martensite proceeds via an intermediate R-phase. The behavior of sample batch 006 is different insofar as phase transformation temperatures are shifted to lower temperatures. A two-step transformation is observed, the first (higher temperature) peak at $-15\,°C$ in DSC being very broad and shallow. The second peak upon cooling is observed at $-125\,°C$. The latent heat is determined to about $5\,\mathrm{J\,g^{-1}}$. Upon heating, a single peak at $-35\,°C$ having a latent heat of $9\,\mathrm{J\,g^{-1}}$ occurs. In both cases, latent heat of the broad and shallow peak is not included, since the onset and end temperatures of this peak are hard to determine. The resistance measurement confirms the existence of a phase with elevated resistance between -80 and $-145\,°C$ upon cooling. Transformation temperatures estimated from resistance curves are summarized in Table 4.3.

Since calibrated heat capacity measurements require a higher amount of sample material than regular DSC measurements, c_p values are determined separately from sample batches 009 and 026. The curves shown in Fig. 4.15 (d) indicate that the heat capacity of binary TiNi films is in the order of 0.4 and $0.45\,\mathrm{J\,g^{-1}\,K^{-1}}$ and differences between martensite and austenite are negligible.

Mechanical performance. Quasi-static tensile tests are performed at room temperature for as-received samples. The stress-strain characteristics are shown in Fig. 4.16. All three samples show superelastic behavior with closed trajectory. The maximum strain is limited to 5% in order to avoid overloading of the samples, although the end of the stress plateau is not yet reached at this strain. Samples 008 and 019 behave quite similar. The critical stress for forward transformation is about $350\,\mathrm{MPa}$, stress hysteresis is $200\,\mathrm{MPa}$. In some cases, the stress plateau is not entirely horizontal, which may be a sign of varying film thickness or stoichiometry gradient along the loading direction. For sample 006 with lower transformation temperatures, the forward stress plateau is elevated, starting at $490\,\mathrm{MPa}$. The stress hysteresis of $130\,\mathrm{MPa}$ is somewhat smaller than for the other two samples. The different mechanical behavior is easily understood by
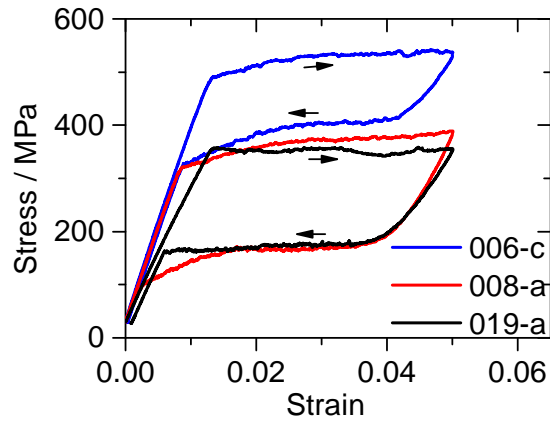
Figure 4.16: Quasi-static stress-strain characteristics for different sample batches of TiNi films (strain rate $1 \times 10^{-4}\,\mathrm{s}^{-1}$). Critical stresses are higher for sample 006, because the transformation temperatures are lower than for the other samples. (Samples 006-c, 008-a, 019-a)

the differences in (thermal) phase transformation temperatures: The higher the temperature difference between ambient temperature and martensite start temperature M_f, the higher the critical stress for A→M phase transformation. The relation between thermally and stress-induced transformation is descibed by the Clausius-Clapeyron coefficients. In order to estimate these, quasi-static tensile tests are performed for a sample of batch 019 at two different ambient temperatures. The evaluation of the stress-strain characteristics shown in Fig. 4.17 (a) reveals $d\sigma_{crit}/dT$ of 8.75 and $7.75\,\mathrm{MPa\,K}^{-1}$ for loading and unloading, respectively. Since only two data points are available for linear fit, these values have to be considered as rough estimates. Further measurements at different ambient temperatures could not be performed, because the stress-strain curve showed distinctive signs of degradation already during the third load-unload cycle (dash-dotted line in Fig. 4.17 (a)): Large plastic strain is accumulated and the curve is becoming rounder and steeper, so that a plateau stress cannot be defined in a meaningful way. Because training effects like this play such a major role in the sputter-deposited binary films, cycle dependence shall be discussed next.

Localized behavior and fatigue A cyclic tensile test experiment is performed at a strain rate of $0.02\,\mathrm{s}^{-1}$ on an as-produced sample (batch 019). The stress-strain characteristics of the first, second, third, as well as 20th cycle are shown in Fig. 4.18 (a). An increasing amount of plastic strain is accumulated from cycle to cycle. At the same time, the stress plateaus become steeper and the (initially sharp) transition from elastic regime to plateau is rounded out. The curve becomes more narrow, i.e. the area enclosed by the trajectory decreases. After 20 cycles, the sample has adopted a cigar-shaped characteristic and accumulated a plastic strain of 1.5%. The mechanical behavior stabilizes after several tens of cycles (depending on loading conditions).
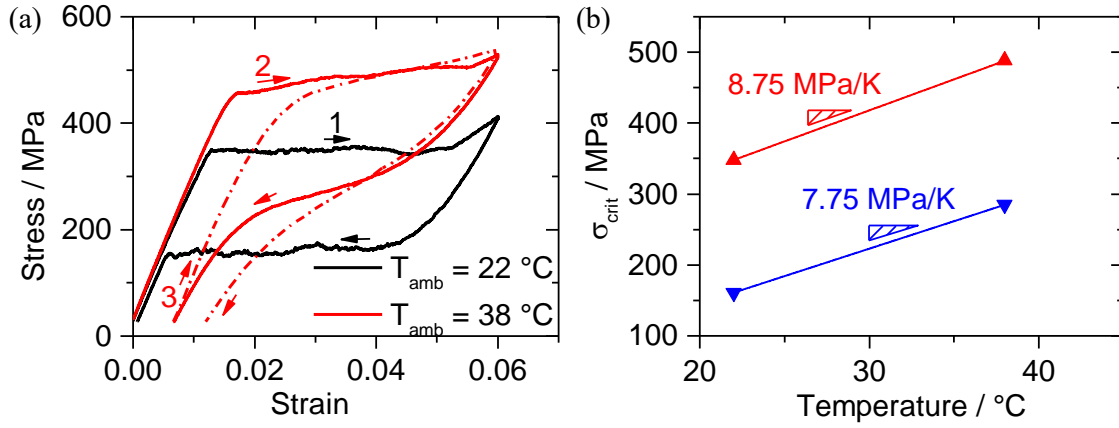
Figure 4.17: Mechanical performance of TiNi film sample as a function of ambient temperature T_{amb}. (a) Quasi-static stress-strain characteristics at a strain rate of $1 \times 10^{-4}\,\mathrm{s}^{-1}$. (b) Stress values σ_{crit} of the superelastic plateaus during loading and unloading as a function of T_{amb}. Clausius-Clapeyron coefficients $d\sigma_{crit}/dT$ for loading (red) and unloading (blue) are estimated from linear fits. (Sample 019-a)

Stress plateaus are a manifestation of Lüders-like transformation behavior including strain bands. Hence, vanishing of the plateaus is a sign of changes in local structure. In order to examine effects of training at the meso-scale, DIC analysis is performed to obtain local strain maps (Fig. 4.18 (b)). Within the first cycle, nucleation and propagation of strain bands is observed during both, loading and unloading. Bands are oriented at an angle of $55°$ with respect to loading direction. During the second loading step, strain bands occur again, but their interfaces are blurred. During unloading, however, the bands have virtually disappeared. In the following loading-unloading cycles, the local stress is observed to increase and decrease almost homogeneously throughout the investigated sample section. This observation indicates that the microstructure of the TiNi film samples is heavily affected by degradation in the course of mechanical training.

In order to study degradation at the local scale, X-ray diffraction (XRD) measurements are performed on an as-received (untrained) sample, as well as on the (trained) sample used for the cyclic tensile test experiment described above. The first order diffraction reflex is shown in Fig. 4.19. For the untrained sample, a double peak is observed, consisting of the 110 peak of the B2 phase and a smaller peak associated with a fraction of the sample in R-phase. The trained sample, on the other hand, reveals a considerably broader and shallower single peak. From this result, the conclusion is drawn that mechanical training induces a wide range of local stress states in the microstructure. Hence, reverse transformation is impeded in a number of grains or variants due to mechanical pinning of the phase interfaces at defects created by mechanical cycling, leading to plastic strain ε_p. On the other hand, local (internal) stress states support stress-induced transformation even for applied (external) stresses below σ_{crit}^{AM}, leading to vanishing of the stress plateaus.
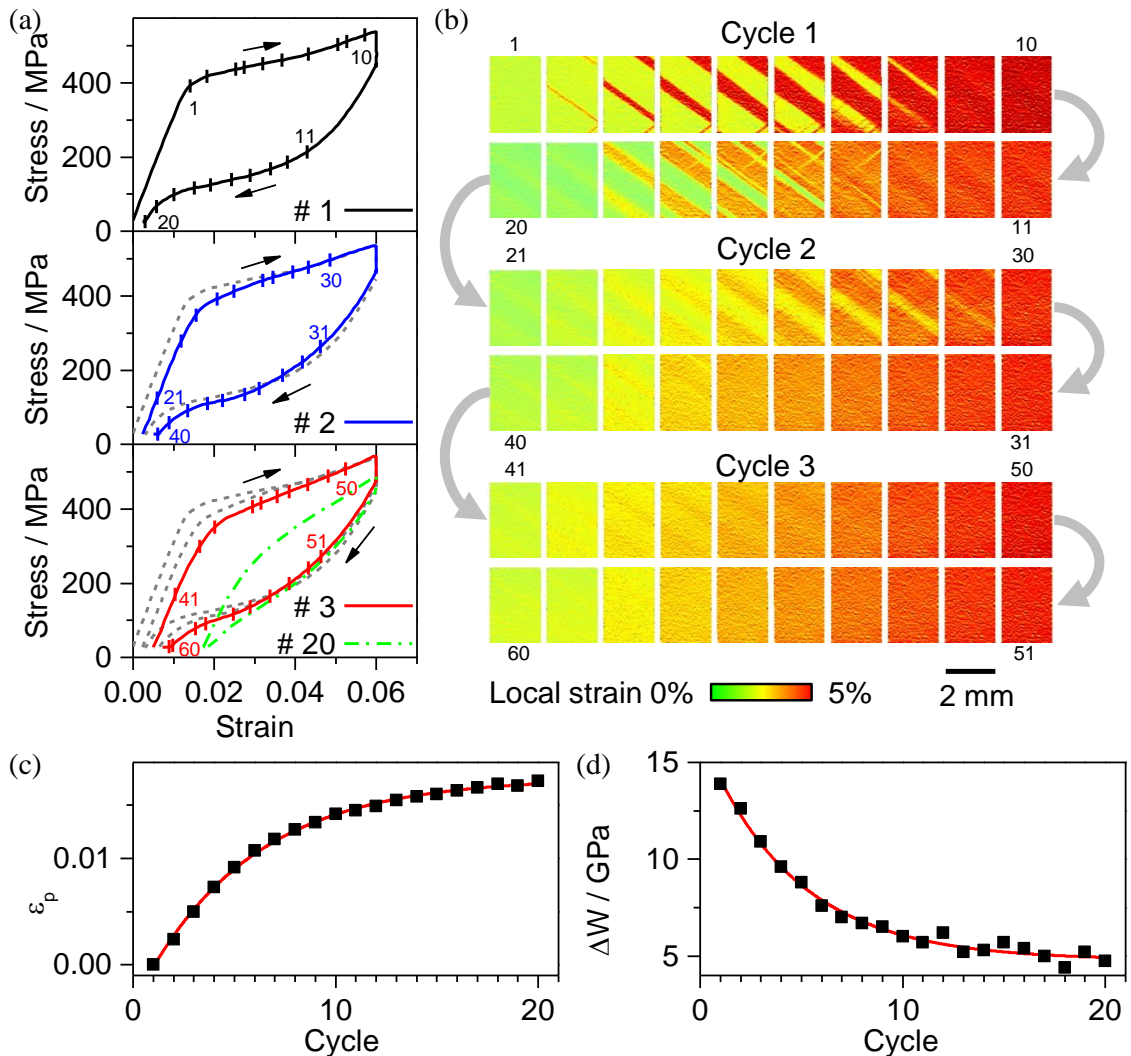
Figure 4.18: (a) Mechanical performance of TiNi film sample as a function of cycle number. Stress-strain curves of three successive loading-unloading cycles at a strain rate of $0.02\,\mathrm{s}^{-1}$ reveal a training effect leading to accumulation of plastic strain and vanishing of stress plateaus. After 20 cycles, a cigar-shaped characteristic is established (green curve). (b) Local strain maps obtained from DIC analysis of a representative sample section reveal the occurrence of strain bands during the first cycle and their gradual vanishing during the following cycles. Points of strain map acquisition are marked by ticks in the graphs. Plastic strain ε_p (c) and hysteresis area ΔW (d) stabilize with increasing cycle number. Exponential fits are included as red lines. Compare Ref. [300]. (Sample 019-c)
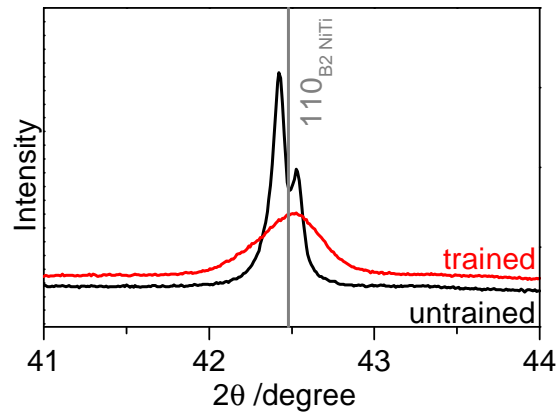
Figure 4.19: X-ray diffraction (XRD) investigation of TiNi film sample before and after mechanical training. A literature value for the (110) reflex of B2 phase in TiNi is included as a guide. Compare Ref. [301]. (Sample 019-c)

In the next step, the effect of training on elastocaloric effect size is studied. A tensile test is performed at an intermediate strain rate of $0.01\,\mathrm{s}^{-1}$ on an as-produced TiNi film sample of batch 006. In order to guarantee full transformation, the sample is loaded up to 10% strain in this case, which is well beyond the end of stress plateau. The stress-strain characteristic in Fig. 4.20 (a) reveals a plastic strain of 2% already after the first cycle. During the following cycles, the curve becomes increasingly cigar-shaped. The time-dependent strain, stress and temperature evolution in the sample center obtained from IR measurement by averaging over a test area of $1\,\mathrm{mm}^2$ are depicted in Fig. 4.20 (b). The peak temperature changes during loading and unloading decrease from cycle to cycle. A series of thermograms acquired during tensile test is shown in Fig. 4.20 (c). Time intervals I.-VI. of IR acquisition are marked in yellow in (b). During the loading step of the first cycle, a band of elevated temperature forms close to the lower clamping and then propagates upwards along the sample. About $1\,\mathrm{s}$ later, a second, smaller band forms close to the upper clamping and propagates downwards. Both bands meet in the upper third of the sample at the end of loading. During unloading, a single cold temperature band is observed, propagating downwards from the upper clamping towards the lower clamping. During the second and third load-unload cycle, temperature bands with a similar chronological sequence are observed, but the bands become increasingly diffuse. After a sufficient number of cycles, self-heating and cooling proceed approximately homogeneously, i.e. at the same time throughout the sample. The temperature peaks shown in Fig. 4.20 (b) occur at the moment when temperature bands pass the observed test area in the sample center. The decrease of elastocaloric effect size upon mechanical cycling is also detected by DSC measurement. A DSC curve for trained material (included as dashed line in Fig. 4.15 (a)) indicates that the peak of M→A transformation gets considerably broader and shallower due to training. The latent heat decreases from 9 to $5\,\mathrm{J\,g}^{-1}$. The peak of M($\rightarrow$R)→A transformation is barely visible in the curve of trained material. The degradation of elastocaloric effect size is also re-
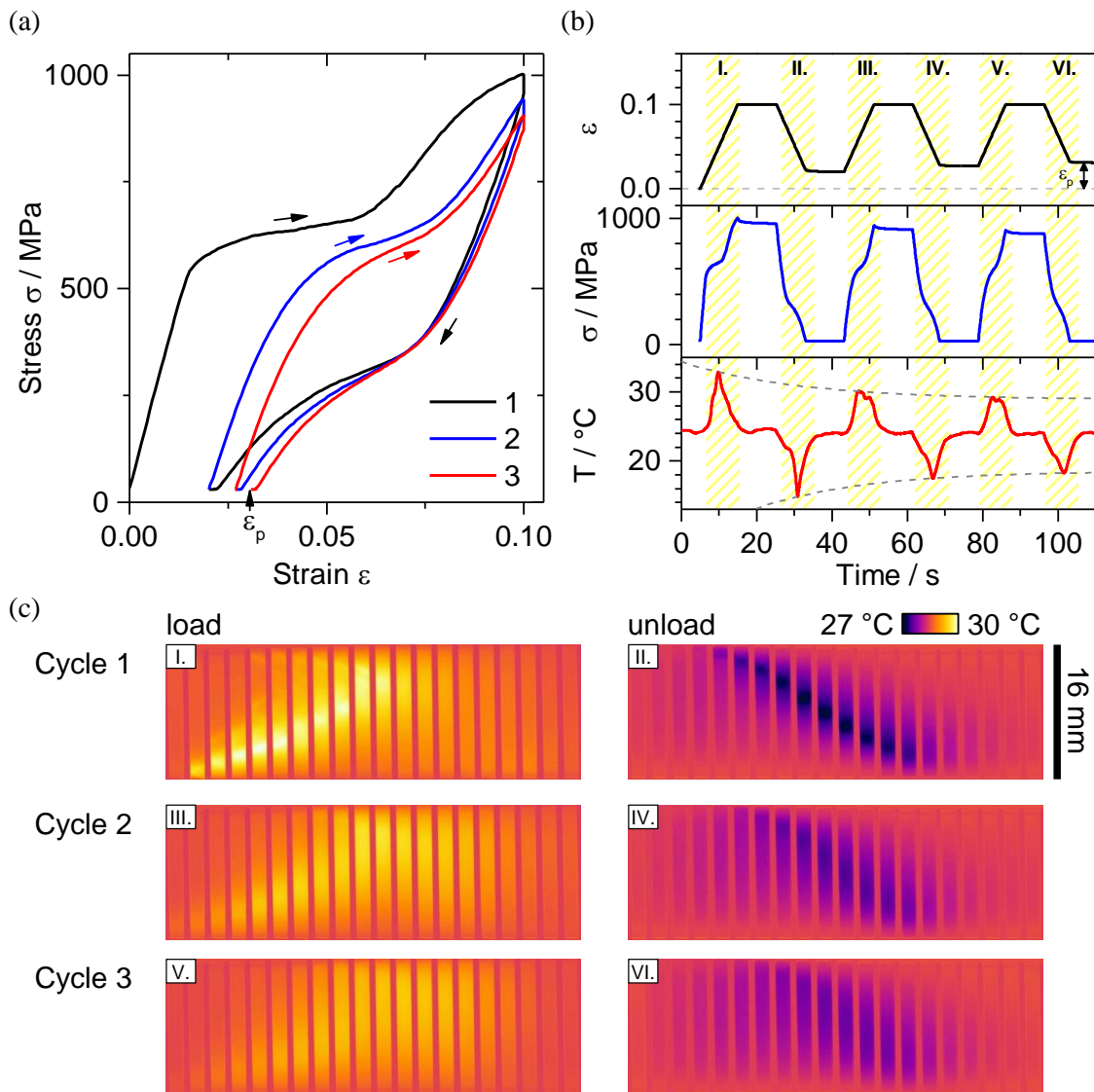
Figure 4.20: Elastocaloric effect of TiNi film samples as a function of cycle number. (a) Stress-strain characteristics during three cycles at a strain rate of $0.01\,\mathrm{s}^{-1}$. (b) Time-dependend course of strain, stress and temperature in the sample center, averaged over a test area of $1\,\mathrm{mm}^2$. (c) Chronological series of temperature maps of the sample obtained by IR thermography during loading and unloading. Intervals I.-VI. of image acquisition are indicated in (b). (Sample 006-f)

ported by Bechtold et al. [98].
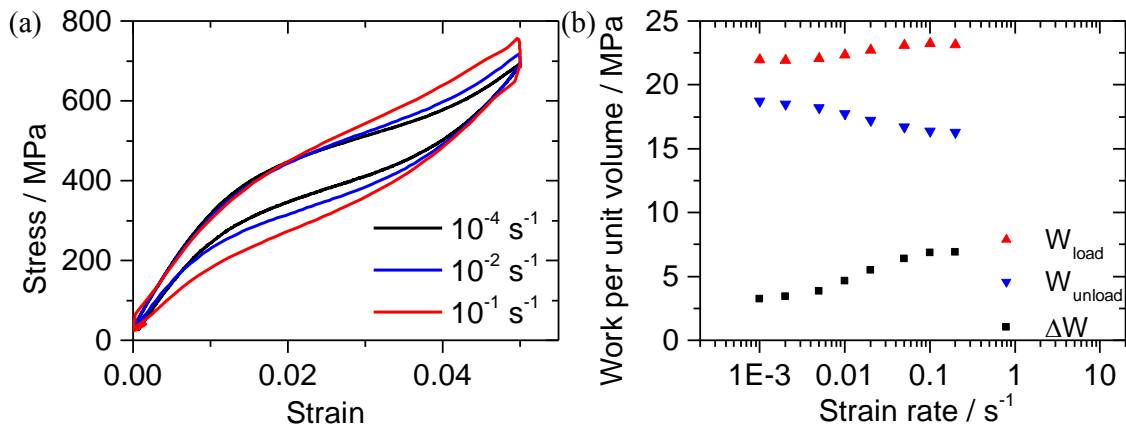
Figure 4.21: Mechanical performance of trained TiNi film sample as a function of strain rate. (a) Stress-strain characteristics for different strain rates. (b) Mechanical work W_{load} and W_{unload} for loading and unloading, as well as work input $\Delta W = W_{load} - W_{unload}$ as a function of strain rate (logarithmic scale). Compare Ref. [299]. (Sample 006-d)
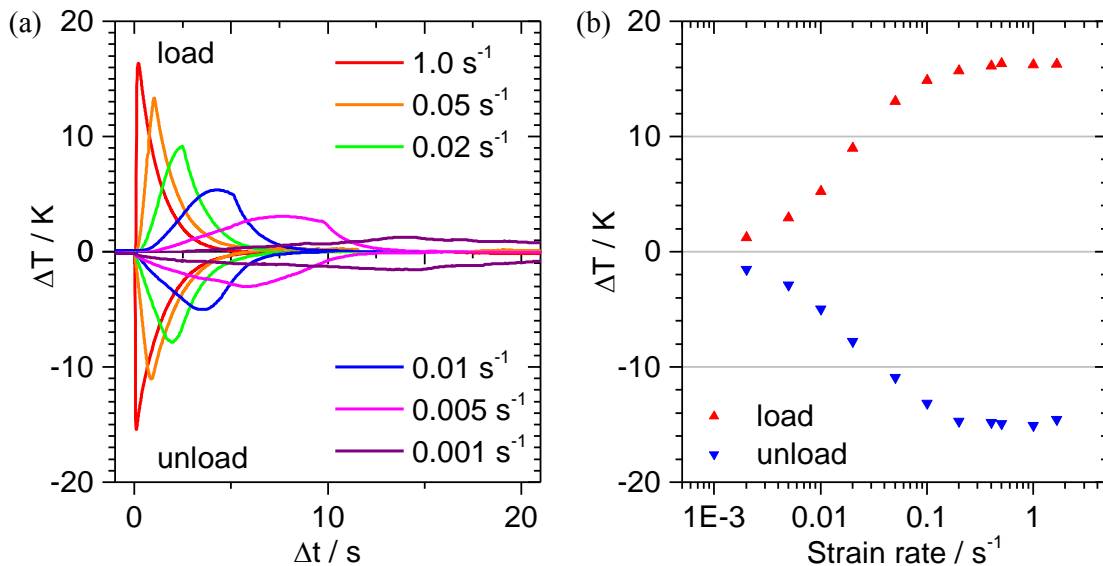
Figure 4.22: Elastocaloric temperature change of trained TiNi film sample as a function of strain rate. (a) Time-dependent temperature change due to self-heating and cooling during loading and unloading at different strain rates. Temperature is averaged over a representative test area of $1\,\mathrm{mm^2}$ in the sample center. (b) Peak temperature changes reached during loading as a function of strain rate. Compare Ref. [299]. (Sample 006-d)

Performance of trained samples.   It has been shown above that the superelastic performance of TiNi film samples severely depends on cycle number. Therefore the strain rate-dependent analysis of mechanical work input and elastocaloric

effect size is performed on trained samples in which the mechanical behavior has stabilized. Stress-strain characteristics obtained at different strain rates on a sample of batch 006 are shown in Fig. 4.21 (a). The curves are narrow and cigar-shaped. The area enclosed by the trajectory increases with increasing strain rate (see Fig. 4.21 (b)). Under adiabatic conditions, the mechanical work input is $6.9\,\mathrm{MPa}$. The elastocaloric effect size is studied in the same experiment by IR thermography. Time-dependent temperature evolution curves are obtained by averaging the temperature over a test area of $1\,\mathrm{mm}^2$ in the sample center. Temperature curves for different strain rates are shown in Fig. 4.22 (a), the resulting peak temperatures as a function of strain rate in Fig. 4.22 (b). In the adiabatic limit, which is reached at a strain rate of $0.2\,\mathrm{s}^{-1}$, the temperature change is $16\,\mathrm{K}$ during loading and $-15\,\mathrm{K}$ during unloading. For sample batches 008 and 019, results are in qualitative agreement, but work input is slightly higher and adiabatic temperature changes are lower. The time constant for temperature equalization, determined by exponential fit, is about $1\,\mathrm{s}$.

4.2.2 TiNiCuCo films

The sputter-deposited TiNi films described in the previous section show a considerable elastocaloric effect size, in the as-fabricated as well as in the trained state. However, strong cycle-dependent changes of mechanical performance complicate any practical application. A way of considerably stabilizing superelastic performance and thus improving sample lifetime is alloying of additional metals to the binary TiNi. Experiments at the University of Kiel revealed that Ti-rich ternary TiNiCu samples reach extraordinary cyclic stability, provided that the sample stoichiometry is carefully adjusted [98, 103, 120]. However, TiNiCu samples are not pseudoelastic at room temperature (compare Fig. 4.23 (a)), therefore fourth elements are added in order to lower phase transformation temperatures.

In the following, quaternary TiNiCuCo samples are investigated that are produced by DC magnetron sputtering following two slightly different procedures [300]. Films with the composition $\mathrm{Ti}_{55}\mathrm{Ni}_{29.6}\mathrm{Cu}_{12.6}\mathrm{Co}_{2.8}$ (determined by energy-dispersive X-ray diffraction; batch 028) are fabricated from a quaternary alloy target having the composition $\mathrm{Ti}_{58}\mathrm{Ni}_{24.5}\mathrm{Cu}_{14.7}\mathrm{Co}_{2.3}$. In addition, films with the composition $\mathrm{Ti}_{54.7}\mathrm{Ni}_{30.7}\mathrm{Cu}_{12.3}\mathrm{Co}_{2.3}$ (batch 022) are prepared by multilayer sputtering layers of $35\,\mathrm{nm}$ from a ternary $\mathrm{Ti}_{56}\mathrm{Ni}_{29}\mathrm{Cu}_{15}$ target in alternation with $1\,\mathrm{nm}$ from a Co target. In both cases, a rapid thermal annealing step is performed for sample homogenization and recrystallization. Annealing is performed at 780 and $700\,^{\circ}\mathrm{C}$, respectively, for $15\,\mathrm{min}$.

Thermal and electrical properties. DSC and electrical resistance measurements are shown in Fig. 4.23 for the two quaternary TiNiCuCo alloys (022 and 028), as
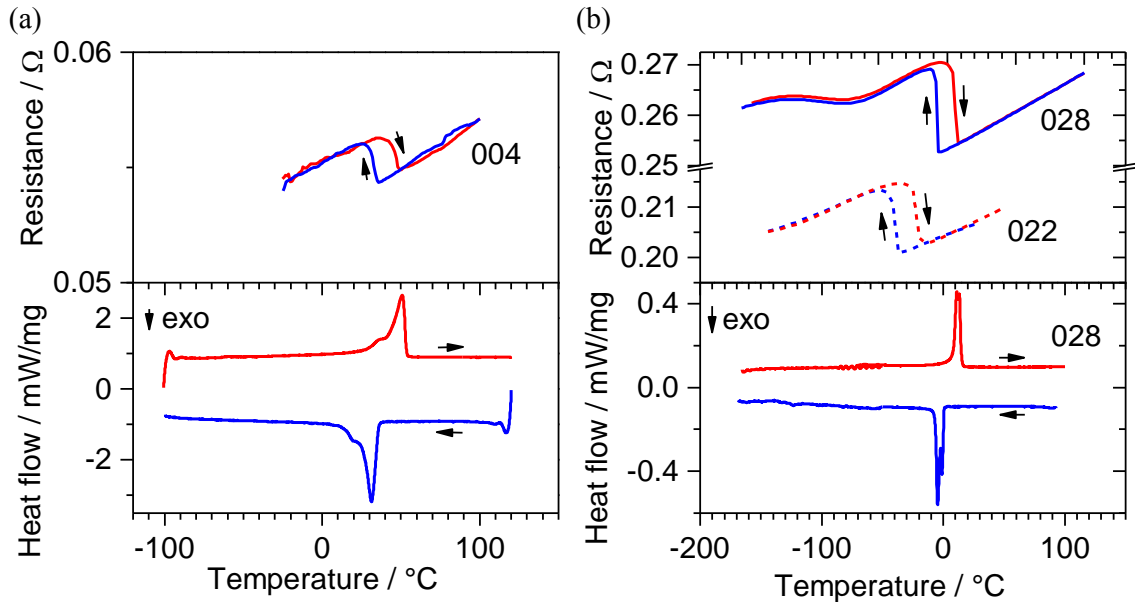
Figure 4.23: Thermally-induced phase transformation properties of TiNiCu(Co) film samples, characterized by differential scanning calorimetry (DSC) and electrical resistance measurement: ternary sample batch 004 (a), and quaternary sample batches 022 and 028 (b). Compare Ref. [300].

well as a ternary TiNiCu alloy (batch 004) for comparison. In the case of sample batch 022, sample material was not sufficient to perform a DSC measurement. In all three cases, a one-step transformation with small thermal hysteresis is observed. For the ternary alloy, transformation peak temperatures are $30\,°C$ upon cooling and $50\,°C$ upon heating, hence the material is not superelastic at room temperature. The latent heat is $12\,\mathrm{J\,g^{-1}}$. The quaternary sample 028 shows a transformation with very sharp peaks at $-5\,°C$ upon cooling and $10\,°C$ upon heating. Note that the A_f temperature is close to room temperature. The curve shows a narrow double peak, which is caused by slight inhomogeneity of the sample material and does not result from a two-step transformation. The latent heat of the transformation is $14\,\mathrm{J\,g^{-1}}$. In the case of sample 022, transformation temperatures are shifted to lower temperatures, A_f being about $-20\,°C$.

The heat capacities of TiNiCu (batch 010) and TiNiCuCo film samples (batch 026) are determined by DSC measurement as well, using a synthetic sapphire standard (see Fig. 4.24). The heat capacities are $0.47\,\mathrm{J\,g^{-1}\,K^{-1}}$ for the ternary and $0.4\,\mathrm{J\,g^{-1}\,K^{-1}}$ for the quaternary alloy, respectively. Differences between martensite and austenite are negligible in both cases.

Mechanical performance. Quasi-static tensile tests are performed for both quaternary film samples at a strain rate of $1 \times 10^{-4}\,\mathrm{s^{-1}}$. As a consequence of the different phase transformation temperatures, plateau stresses differ between both samples. Sample 022 shows a very narrow stress-strain characteristic with slightly
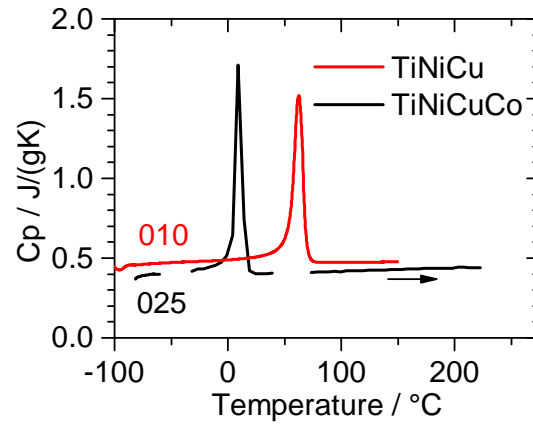
Figure 4.24: Mass-specific heat capacity of TiNiCu(Co) film samples. (Sample batches 010, 025)
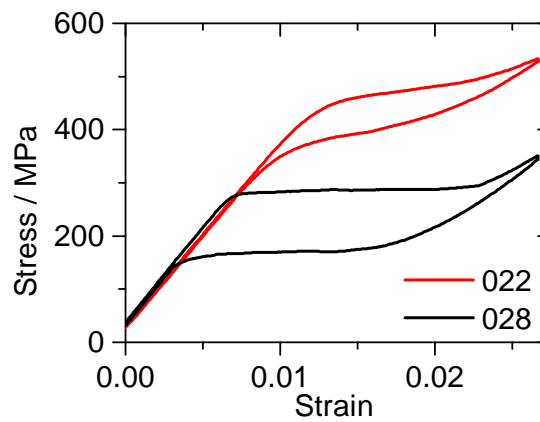
Figure 4.25: Quasi-static stress-strain characteristics for TiNiCuCo film samples of batches 022 and 028 (strain rate $1 \times 10^{-4}\,\mathrm{s}^{-1}$). Critical stresses are higher for sample 022, because the transformation temperatures are lower than for sample 028. (Samples 022-b, 028-a)

inclined stress plateau at a critical stress of $450\,\mathrm{MPa}$ and a low stress hysteresis of $70\,\mathrm{MPa}$ (Fig. 4.25). In the case of sample 028, the stress plateau occurs at a lower stress of $280\,\mathrm{MPa}$ and is almost horizontal. The stress hysteresis of $110\,\mathrm{MPa}$ is higher than for sample 022. For both samples, the end of the stress plateau is reached at about 2.25% strain. A further important difference between the two samples is the onset of the stress plateau, which is sharp for sample 028 but rounded out for sample 022. This observation is correlated with a different course of stress-induced transformation on the meso-scale. Sample 028 (showing the sharp plateau onset) develops strain bands with sharp interfaces, indicating a discontinuity of local strain during transformation. Sample 022, on the other hand, shows a homogeneous local stress distribution which is increasing continuously upon loading. Therefore, the strain rate-dependence of work input and elastocaloric effect size will be discussed in the following on the basis of sample 022 with lower transformation temperatures. Subsequently, local effects will be

discussed on sample 028.

Tensile tests at different ambient temperatures have been performed by Chluba et al. using a more advanced temperature control chamber than the one used herein. Therefore, the reader is referred to Ref. [121] for more information. Clausius-Clapeyron coefficients for the quaternary films are about $10\,\mathrm{MPa\,K^{-1}}$.
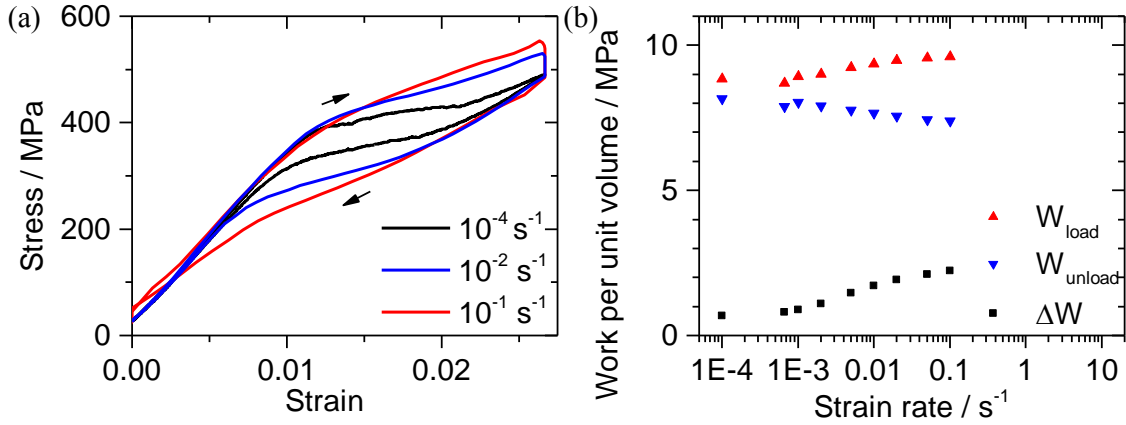
Figure 4.26: Mechanical performance of TiNiCuCo film sample (batch 022) as a function of strain rate. (a) Stress-strain characteristics for different strain rates. (b) Mechanical work W_{load} and W_{unload} for loading and unloading, as well as work input $\Delta W = W_{load} - W_{unload}$ as a function of strain rate (logarithmic scale). Compare Ref. [300]. (Sample 022-a)

Fig. 4.26 (a) shows stress-strain characteristics obtained at different strain rates on sample 022. The curves are very narrow. As already described for binary samples, the enclosed area between loading and unloading trajectory, representing the work input, increases with increasing strain rate (Fig. 4.26 (b)). Under adiabatic conditions, the mechanical work input is only $2.2\,\mathrm{MPa}$. The elastocaloric effect size observed in the same experiment by IR thermography is shown in Fig. 4.27. In the adiabatic limit, which is reached at a strain rate of $0.2\,\mathrm{s^{-1}}$, the temperature change is $9\,\mathrm{K}$ during loading and $-12\,\mathrm{K}$ during unloading. Remarkably, the effect size is by one third higher during unloading, compared to loading. This effect is unexpected and requires further research for explanation. A more pronounced cooling than heating was also reported for FePd and NiMnSn samples in literature [233, 238]. The time constant of temperature equalization, obtained by exponential fit, is slightly above $1\,\mathrm{s}$. Strain-rate dependent experiments are also performed for sample 028. However, since the phase transformation temperature A_f is closer to room temperature, reverse stress-induced phase transformation remains incomplete due to self-cooling, if strain rate is high enough.[1] The work input is higher, whereas the adiabatic temperature changes are smaller than for sample 022. Therefore, results are not presented here.

---

[1]Temperatures below A_f may be reached by self-cooling due to absorption of latent heat. In this case, reverse transformation is impeded and the sample partially remains in stress-induced martensite state until heat exchange with the environment has taken place.
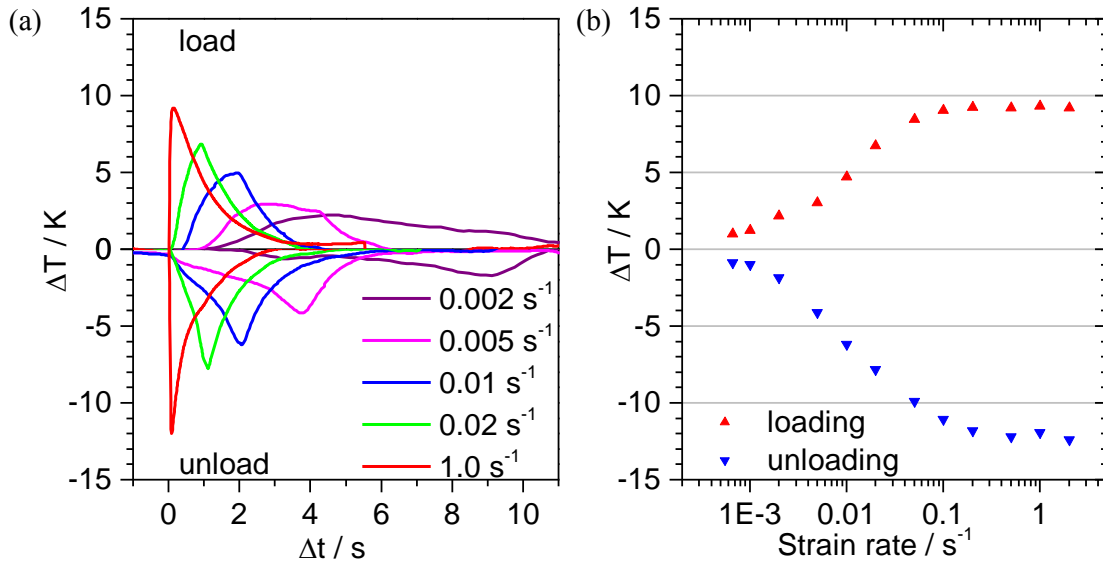
Figure 4.27: Elastocaloric temperature change of TiNiCuCo film sample (batch 022) as a function of strain rate. (a) Time-dependent temperature change due to self-heating and cooling during loading and unloading at different strain rates. Temperature is averaged over a representative test area of $1\,\mathrm{mm}^2$ is the sample center. (b) Peak temperature changes reached during loading and unloading $\Delta T_{load,unload}$ as a function of strain rate. Compare Ref. [300]. (Sample 022-a)

Strain bands. However, sample 028 provides an excellent example for the study of local phenomena, whereas sample 022 does not exhibit any sharp strain or temperature bands. In the following, a cyclic tensile test experiment is performed on a sample of batch 028 at a strain rate of $0.02\,\mathrm{s}^{-1}$, equivalent to that described in the previous section for binary TiNi films (compare Fig. 4.18). In Fig. 4.28 (a), stress-strain characteristics of three successive cycles are shown. The curves are virtually identical (except for a slight decrease of plateau height). The corresponding local strain maps obtained from DIC analysis are shown in Fig. 4.28 (b). Strain maps reveal the formation and propagation of strain bands with sharp interfaces, oriented at an angle of $\pm 55°$ with respect to loading direction. The pattern of strain bands is very similar, though not identical, from cycle to cycle. X-ray diffraction (XRD) measurements are performed on sample material before and after tensile testing. The measurement, shown in Fig. 4.29, reveals a double peak at a slightly smaller angle than the literature value for the (110) B2 phase peak of binary TiNi. In this case, the double peak is attributed to the B2 parent phase and Ti_2Cu precipitates. The location and width is evidently not affected by mechanical cycling. In a more detailed study on cyclic performance and microstructure, Chluba et al. show that sputter-deposited TiNiCuCo films actually withstand 10^7 training cycles without any degradation of mechanical performance [120].

Temperature bands. Due to the stable behavior upon cyclic loading, TiNiCuCo film sample 028 is suitable for a study of stress-induced temperature bands at
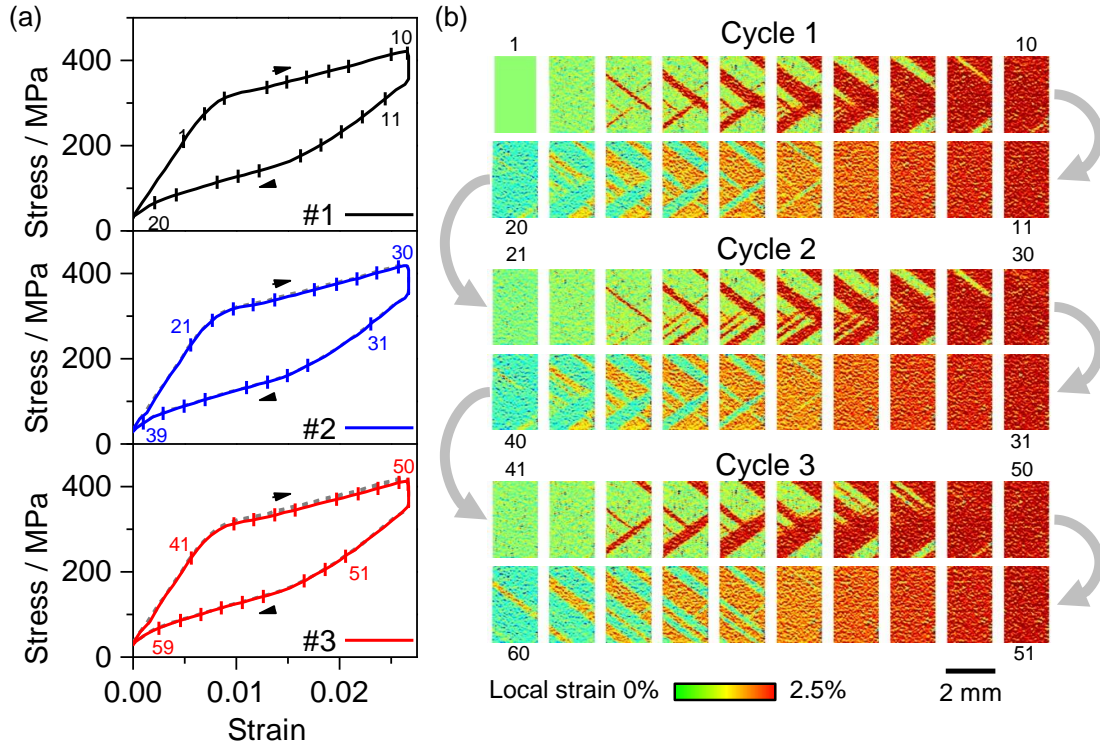
Figure 4.28: Mechanical performance of TiNiCuCo film sample (batch 028) as a function of cycle number. Close coincidence is observed for stress-strain curves of three successive load-unload cycles at a strain rate of $0.02\,\mathrm{s}^{-1}$ (left). Local strain maps obtained from DIC analysis of a representative sample section (right) reveal the reproducible occurrence of strain bands. Points of profile acquisition are marked by ticks in the graphs. Compare Ref. [295]. (Sample 28-d)
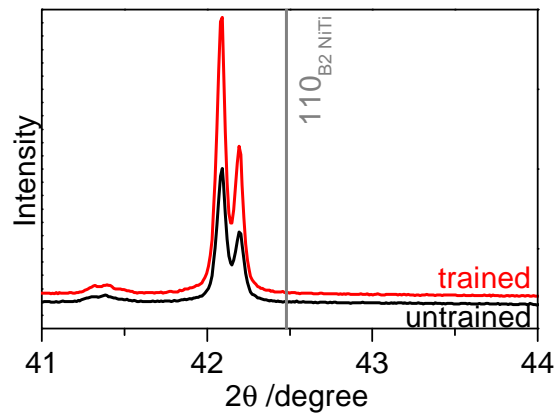
Figure 4.29: X-ray diffraction (XRD) investigation of TiNiCuCo film sample before and after mechanical training. A literature value for the (110) reflex of B2 phase in TiNi is included as a guide. Compare Ref. [301]. (Sample 028-d)
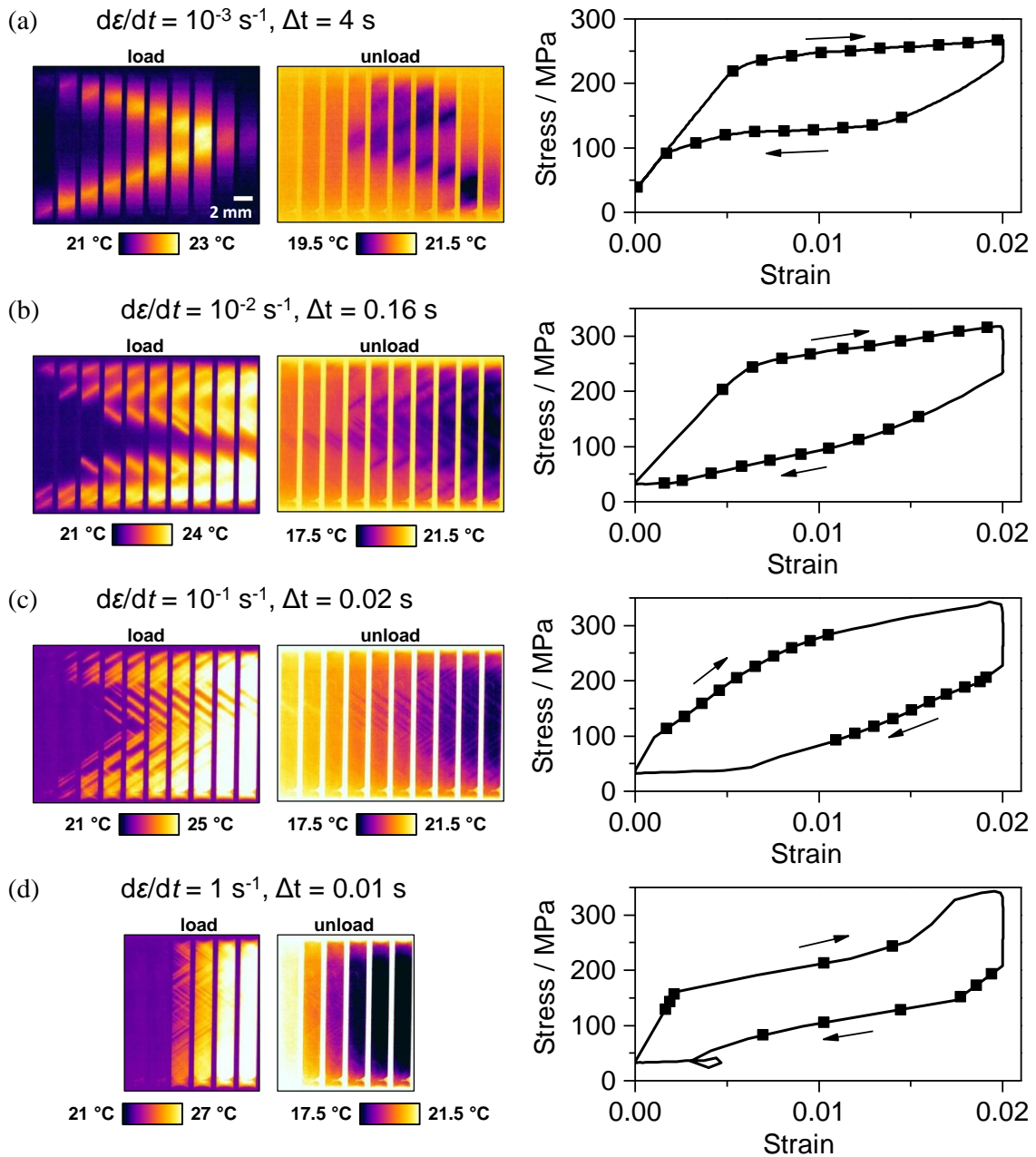
Figure 4.30: Spatially resolved temperature evolution of TiNiCuCo film sample (batch 028) as a function of strain rate. Chronological series of thermograms are obtained by IR thermography during loading and unloading at the strain rates 1×10^{-3} (a), 1×10^{-2} (b), 1×10^{-1} (c) and $1\,\mathrm{s}^{-1}$ (d). Time intervals Δt between two images, as well as associated position in stress-strain characteristic are indicated. Compare Ref. [300]. (Sample 028-d)

different strain rates, which shall be performed in more detail for this material. In contrast to the limited field-of-view of the DIC setup, IR thermography allows to observe the whole sample at once during tensile testing. In Fig. 4.30, chronological series of temperature maps acquired during loading and unloading at four different strain rates are shown. Strain rate is increased by a factor of ten from each experiment to the next. Upon loading at the slowest strain rate of $1 \times 10^{-3}\,\mathrm{s}^{-1}$ (Fig. 4.30 (a)), two hot temperature bands are observed, initiating close to the sample fixations and then propagating towards each other, until finally uniting in the sample center. The course of phase transformation is almost symmetric with respect to the sample center. Upon unloading, transformation takes the reverse course: Two cold temperature bands initiate in the center and then propagate towards sample fixation. Additional bands occur at a later stage of unloading. When increasing the strain rate (Fig. 4.30 (b,c) the number of bands increases. Hot bands initiate close to the fixation upon loading and occur in the sample center at a later stage. Upon unloading, the course is again reversed: First cold bands appear in the sample center, before covering the whole sample. At the highest strain rate of $1\,\mathrm{s}^{-1}$ (Fig. 4.30 (d)), the whole sample is covered by fine temperature bands within less than $10\,\mathrm{ms}$ (which is the temporal resolution of the IR camera) during both, loading and unloading. Within about $50\,\mathrm{ms}$, approximately homogeneous temperature profiles are established throughout the entire sample. The strain rate is well above the adiabatic limit in this case.

In order to make the correlation of local temperature evolution with stress and strain state of the sample more visible, a different evaluation of the IR data is performed. One-dimensional temperature profiles along the center line of the sample in x-direction are extracted from the data and plotted against the time axis, together with the engineering strain ε, stress σ and average temperature in the sample center T_{center}. The plots for the four strain rates are shown in Figs. 4.31-4.34. The tensile experiment is divided into four stages: I. mechanical loading, II. heat release time at constant strain, III. mechanical unloading, and IV. heat absorption time at constant stress. Stages II. and IV. are further subdivided into segments a and b, corresponding to mechanical loading and unloading in the elastic regime (a) and stress plateau regime (b). For the experiments at lower strain rates (Figs. 4.31 and 4.32), the temporal evolution of phase transformation can be seen most clearly. During the first part of the loading stage (I.a), strain and stress increase linearly, whereas the sample temperature remains at ambient level. As soon as the critical stress σ_{crit} is reached, the forward stress plateau is entered and first temperature bands form. In the course of stage I.b, temperature bands propagate through the sample (usually from the clamping inwards) and depending on strain rate, additional bands are formed. The sample temperature rises, until reaching a maximum at the end of the loading stage. During the (strain-controlled) equilibration stage II., the temperature profile along the sample is homogenized by internal heat conduction. The sample temperature falls back to ambient level due to heat exchange with the surroundings. At the same time, stress decreases due to the Clausius-Clapeyron relation. In stage III., unloading is performed. During sub-stage III.a the stress level decreases until
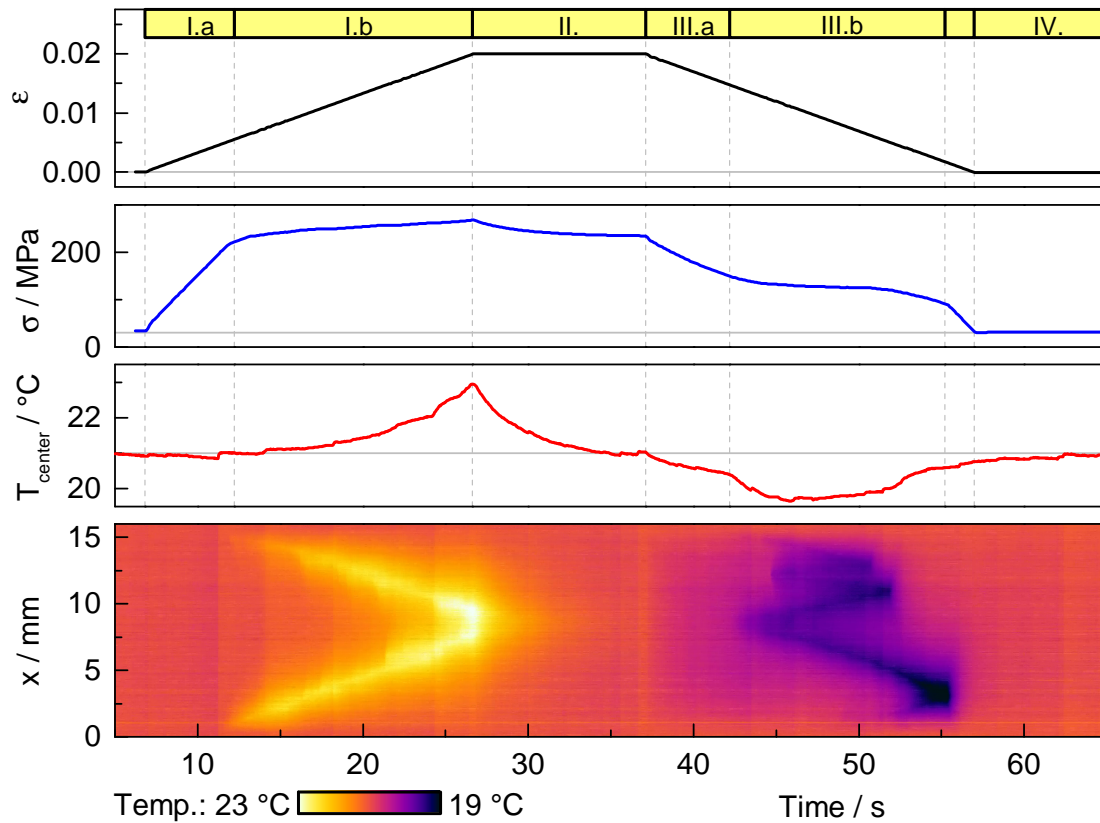
Figure 4.31: Propagation of temperature bands at a strain rate of $1 \times 10^{-3}\,\mathrm{s}^{-1}$. Colored diagram represents time-series of line profiles along the sample center. Temporal evolution of strain ε, stress σ, and average temperature T_{center} in the sample center are included. (Sample 028-d)

reaching the reverse stress plateau. The sample temperature slightly decreases in a homogeneous way. As soon as the stress plateau is entered in sub- stage III.b, cold temperature bands form and start to propagate across the sample. The lowest temperatures are reached at the end of stage III., when the sample is fully unloaded.[2] In subsequent stage IV. the temperature distribution is homogenized again and the temperature level rises back to ambient temperature. At the higher strain rates (Fig. 4.33 and 4.34), a clear distinction of elastic part and plateau part of the stages II. and IV. is not possible anymore, because the inclination of the plateaus increases. Also, due to the increasing number of temperature bands, quasi-homogeneous temperature distribution along the sample is reached within short time intervals.

In the particular case of sample 028, the temperature A_f is so close to room temperature that it can be reached by self-cooling of the sample (which is undesired for cooling applications). Hence, the reverse transformation from stress-induced martensite to austenite is self-inhibiting. Because the heat exchange stage IV. is

---

[2]Actually, this stage is stress-controlled and a small stress is maintained in order to avoid buckling of the sample.
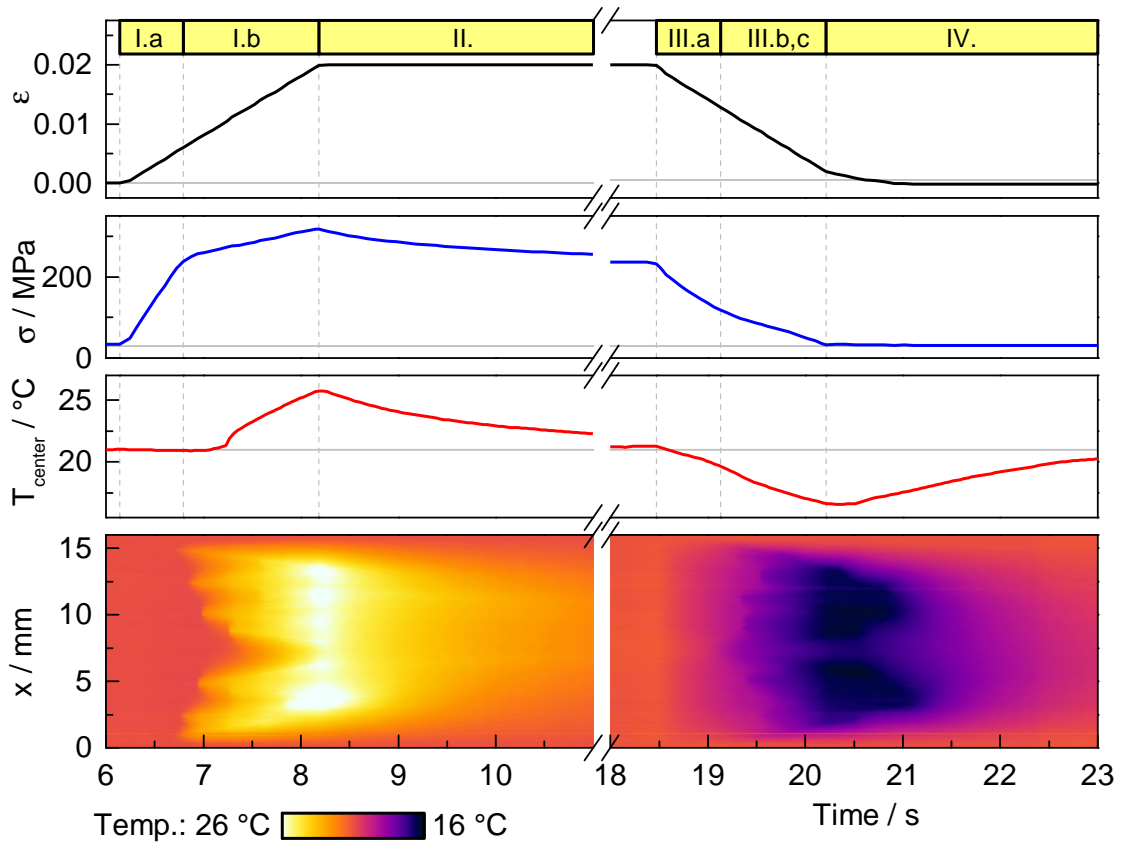
Figure 4.32: Propagation of temperature bands at a strain rate of $1 \times 10^{-2}\,\mathrm{s}^{-1}$. Colored diagram represents time-series of line profiles along the sample center. Temporal evolution of strain ε, stress σ, and average temperature T_{center} in the sample center are included. (Sample 028-d)

stress-controlled, full unloading to zero strain is achieved only after several seconds, when heat exchange and full reverse transformation have taken place.
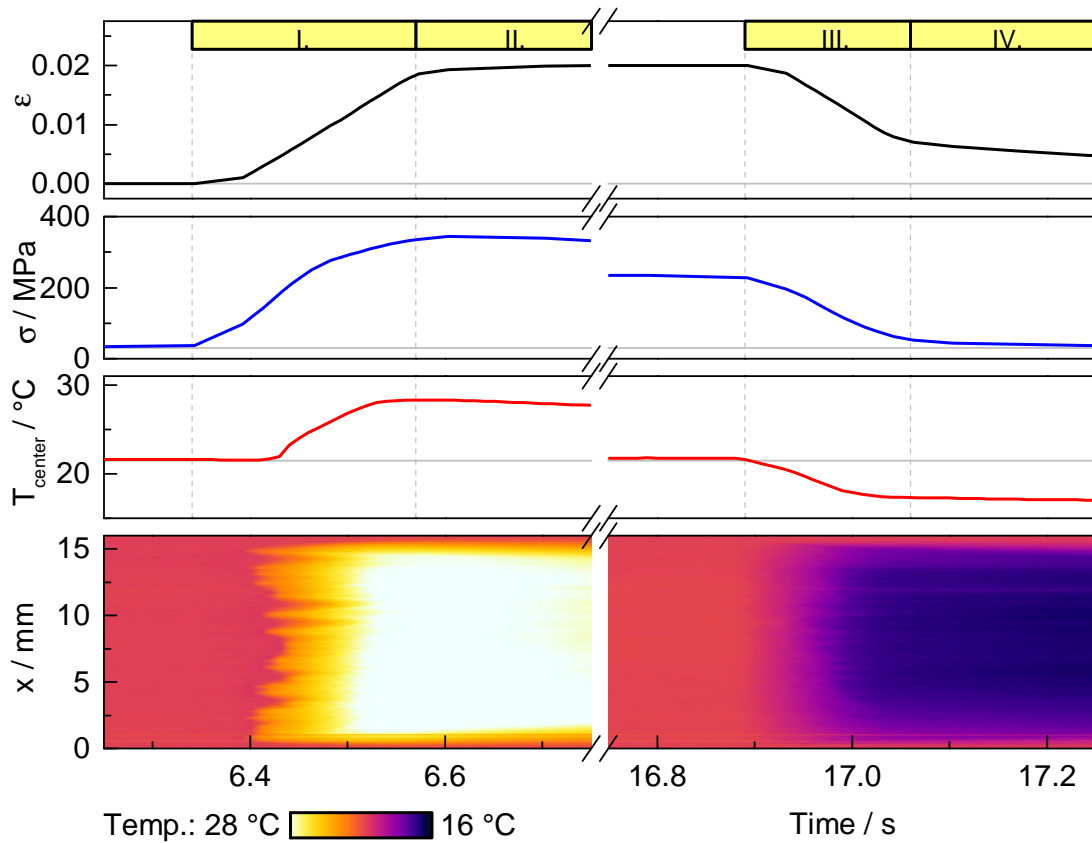
Figure 4.33: Propagation of temperature bands at a strain rate of $1 \times 10^{-1}\,\mathrm{s}^{-1}$. Colored diagram represents time-series of line profiles along the sample center. Temporal evolution of strain ε, stress σ, and average temperature T_{center} in the sample center are included. (Sample 028-d)
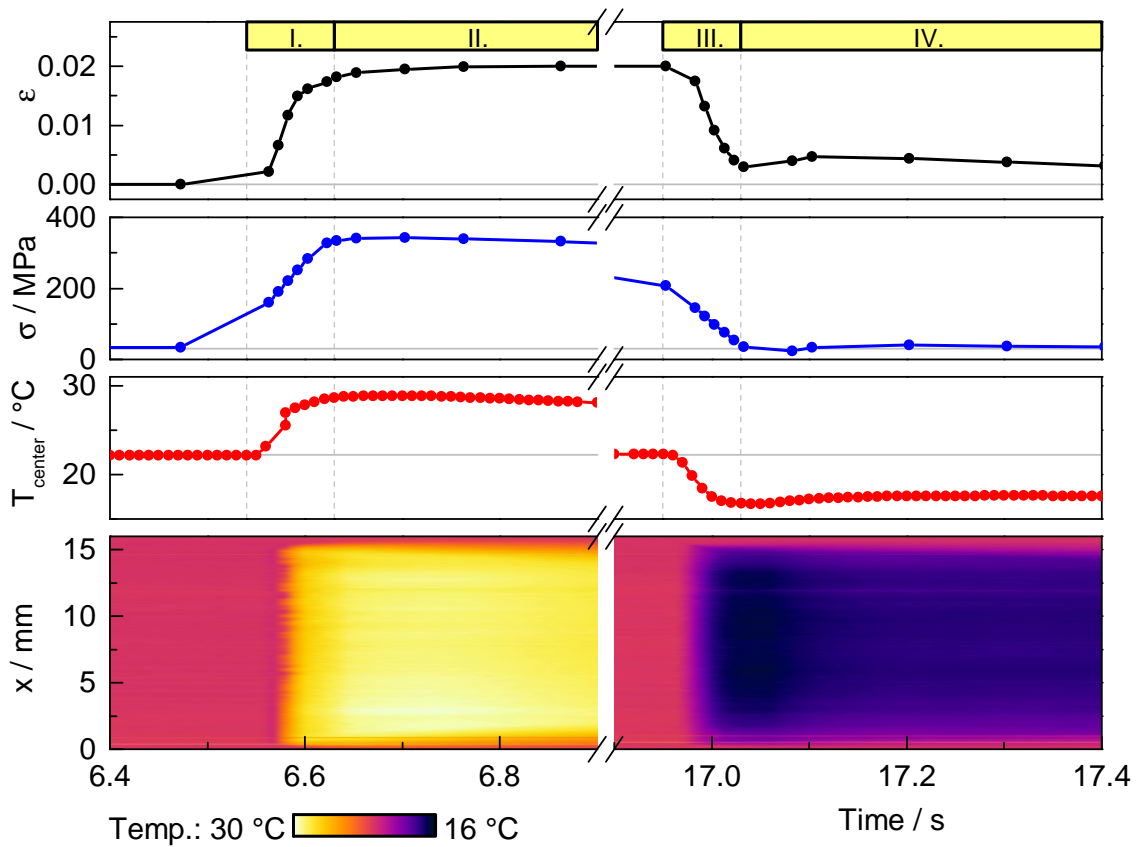
Figure 4.34: Propagation of temperature bands at a strain rate of $1\,\mathrm{s}^{-1}$. Colored diagram represents time-series of line profiles along the sample center. Temporal evolution of strain ε, stress σ, and average temperature T_{center} in the sample center are included. Data acquisition points of tensile test machine and IR camera are marked by bullets. (Sample 028-d)

4.3 **Melt-spun foils**

Besides sputter deposition and cold rolling, a further production route for thin SMA samples is melt spinning. A number of melt-spun samples of different alloys and compositions are provided by Volodymyr Chernenko (University of the Basque Country, Bilbao, Spain). Tensile tests are performed in order to identify alloys that show pseudoelasticity at room temperature. Since the samples are more fragile than TiNi-based foils and films, alumina plates are first mounted to the tensile test sample holder and then the melt-spun samples are attached to the plates in-situ at both ends using a fast curing adhesive. Due to the production process, samples have a cross-section varying along the length direction. The resulting stress peaks lead to increased brittleness during tensile testing.

Fig. 4.35 shows the result of a tensile test on a $Ni_{54.9}Ga_{27.9}Fe_{17.1}$ sample, which ended in sample fracture. Applied force and sample temperature (measured by IR thermography) are shown as a function of time. A change in slope of the force curve indicates the onset of a stress plateau, hence the sample is pseudoelastic. However, the sample broke before the end of the stress plateau was reached, therefore the transformation strain cannot be determined. Simultaneously to the onset of the stress plateau, the sample temperature rises due to elastocaloric self-heating. A temperature increase of $0.9\,K$ is reached before fracture occurs. Hence, the material is in principle feasible for elastocaloric cooling. Extensive study of the elastocaloric performance of the melt-spun samples has unfortunately not been possible.
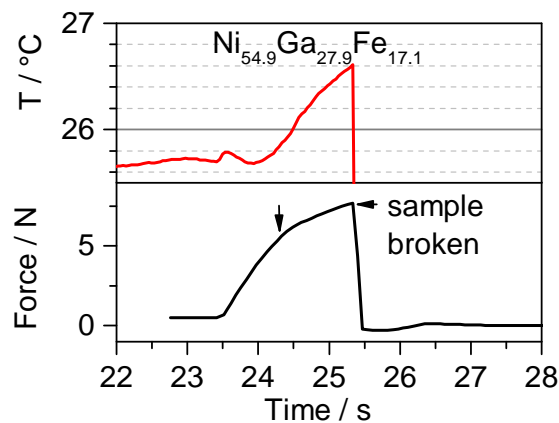
Figure 4.35: Tesile test result of a melt-spun $Ni_{54.9}Ga_{27.9}Fe_{17.1}$ sample showing the onset of a pseudoelastic plateau (marked by arrow) and elastocaloric self-heating. The tensile test ended in fracture of the sample before reaching the end of the plateau. (Sample 040-c)

Melt spinning may be a great technology to produce thin SMA bands in a cost-effective way and in large quantities in the future. However, the production process still has to be improved in order to overcome brittleness. A possible solution may be the production of thicker samples, which are then polished to obtain

smooth surfaces and uniform cross-section.

4.4 Wires

For comparison with the samples having flat geometry discussed above, two materials with wire geometry shall be investigated at the end of this chapter. Wire diameters have been chosen in such a way that overall actuation forces are similar as in the case of the TiNi-based foils and films. During tensile tests, wires are directly clamped to the machine instead of attaching them to alumina plates. The gauge length is $15\,\mathrm{mm}$, as in the tensile tests on the film and foil samples.

The circular cross-section of wires is unfavorable for elastocaloric cooling on a small scale. Firstly, the suface-to-volume ratio is much lower than for film and foil geometries, making heat exchange between the active material and heat sinks and sources ineffective. Secondly, the device concepts that will be developed in chapter 6 mostly rely on a flat geometry of the active material. However, it might be considered to produce flat bands from wires by flat rolling [302] or polishing.

4.4.1 TiNi wire

Since TiNi wires are commercially availible in reasonable quality and at a considerably lower price than TiNi film, foil and tube material, they serve as a kind of standard in literature on elastocalorics (see, e.g., Refs. [13, 86]). In the following, the elastocaloric performance of pseudoelastic TiNi wires shall be investigated for comparison. The wires characterized here are obtained from SAES Getters and have a diameter of $254\,\mathrm{\mu m}$.

Characterization by DSC reveals an A_f temperature of $4.2\,\mathrm{K}$ for the material. Similar to the cold-rolled TiNi foils annealed at $400\,^{\circ}\mathrm{C}$, the wire material shows a single peak with low thermal hysteresis and a latent heat of $3.8\,\mathrm{J\,g^{-1}\,K^{-1}}$ within the measured temperature range. Following the discussion in Section 4.1, it is assumed that this peak represents an intermediate R-phase transformation, and that a second transformation step at lower temperature was not captured by the measurement.

The quasi-static stress-strain characteristic shown in Fig. 4.36 (a) reveals pseudoelastic behavior. The forward plateau occurs at a high critical stress of $400\,\mathrm{\mu m}$ and extends over more than 7% strain. The work input ΔW, shown in Fig. 4.36 (b), is strongly rate-dependent and reaches $29.7\,\mathrm{MPa}$ in the adiabatic limit, which is more than three times the adiabatic work input of the cold-rolled TiNiFe foils discussed above.

The rate-dependent maximum temperature changes during loading and unloading are shown in Fig. 4.37. A maximum self-heating of $24.7\,\mathrm{K}$ and self-cooling of $-18.6\,\mathrm{K}$ is observed, which is slightly higher than for the cold-rolled foils. The
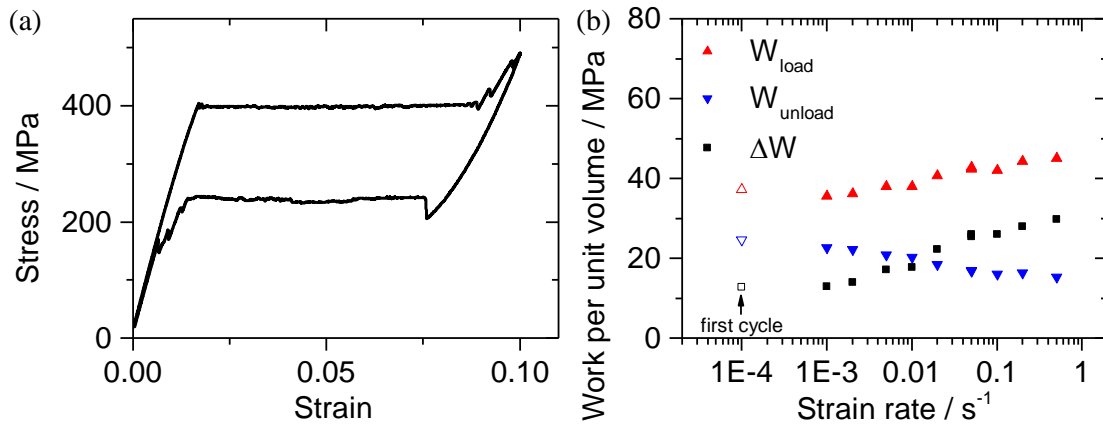
Figure 4.36: (a) Quasi-static stress-strain characteristic of a pseudoelastic TiNi wire at a strain rate of $10 \times 10^{-4}\,\mathrm{s^{-1}}$. (b) Loading, unloading and hysteresis work as a function of strain rate. Data points marked as open symbols are obtained from as-fabricated wire, full symbols represent data points obtained from trained wire. (Sample 029-a)

time constant for temperature equalization with the environment (obtained by exponential fit of the temperature decay measured by IR thermography) is $3\,\mathrm{s}$. The reason for this increased time constant is the low surface-to-volume ratio of $16\,\mathrm{mm^{-1}}$. For comparison, the cold-rolled foils discussed above have approximately the same cross-section as the wires, but a four times higher surface-to-volume ratio of $68\,\mathrm{mm^{-1}}$.

During forward and reverse stress-induced transformation, temperature bands occur in the TiNi wire samples. A more detailed investigation of the local effects in TiNi wires is given in the master thesis of Massy Mehran [303].
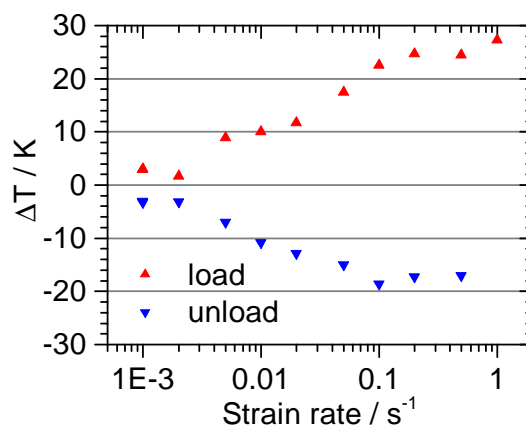
Figure 4.37: Maximum temperature change of a pseudoelastic TiNi wire as a function of strain rate. Temperatures are determined by IR thermography in a small test area in the center of the wire. (Sample 029-a)

4.4.2 CuAlBe wire

Finally, an alloy belonging to the group of Cu-based SMA shall be investigated. Oligocrystalline CuAlBe wires having a diameter of $400\,\mu m$ are provided by Etienne Patoor from the University of Lorraine (France). The wires are produced by the Czochralski method and have a so-called *bamboo structure*, which means that they consist of a number of mesoscopic single-crystalline grains stringed together in length direction. This microstructure is particular favorable in order to overcome structural fatigue [106].
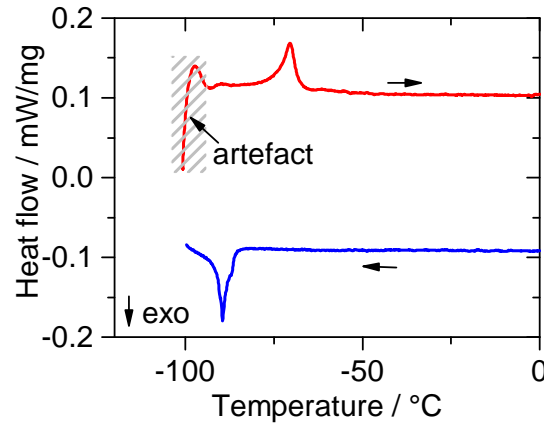
Figure 4.38: Differential scanning calorimetry measurement on an oligocrystalline CuAlBe wire sample. Hatched area marks measurement artefact. (Sample 027)

Thermal properties. DSC measurement (Fig. 4.38) reveals a single-step transformation with a low A_f temperature of $-74.1\,K$ and a peak-to-peak thermal hysteresis of $19\,K$. The latent heat is about $2\,J\,g^{-1}$.
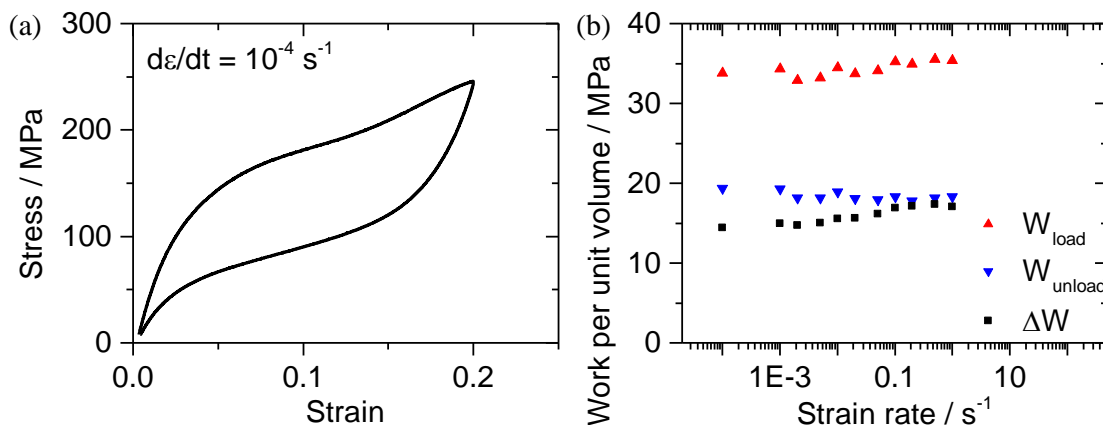
Figure 4.39: (a) Quasi-static stress-strain characteristic of a CuAlBe wire at a strain rate of $10 \times 10^{-4}\,s^{-1}$. (b) Hysteresis work as a function of strain rate. (Sample 027-b)

Mechanical performance. A number of tensile tests is performed, during which the maximum applied strain is increased step-wise. The maximum recoverable strain of the CuAlBe samples is four times as high as for all other investigated samples. Fig. 4.39 (a) shows a quasi-static stress-strain characteristic for a maximum strain of 20%. The critical stress of about $150\,\text{MPa}$ is much lower than for the TiNi-based materials investigated above. The work input ΔW shown in Fig. 4.39 (b) is only weakly rate-dependent. These observations, together with the low phase transformation temperatures, indicate that the Clausius-Clapeyron coefficients of the material must be very low. The transformation strain, on the other hand, is much higher than for the materials discussed above: Tensile loading is fully reversible for maximum strains of up to 25%, but due to the high change in cross-section, sample clamping becomes unreliable at high maximum strains.
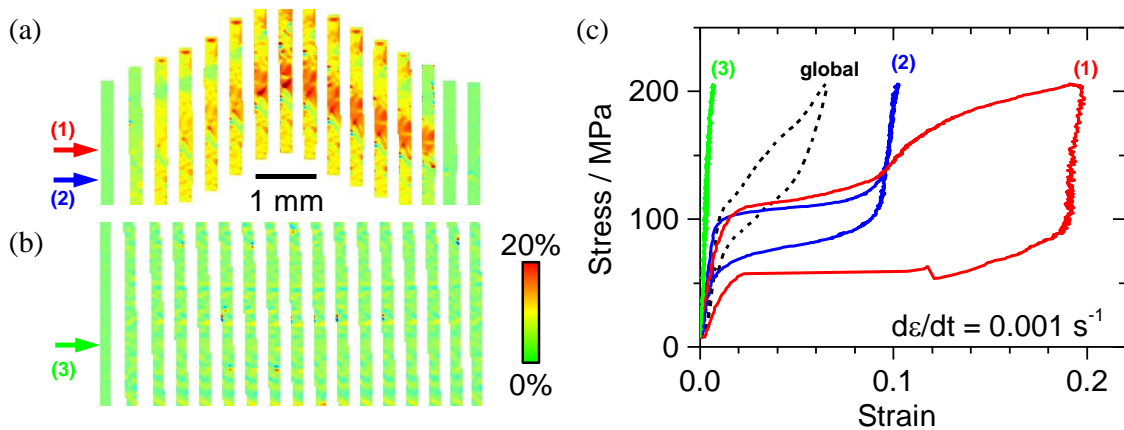
Figure 4.40: Chronological series of local strain profiles obtained by DIC at the upper end (a) and at the lower end (b) of a CuAlBe wire during two consecutive tensile tests at a strain rate of $2 \times 10^{-3}\,\text{s}^{-1}$ to a maximum strain of 0.06. (c) Local stress-strain characteristics at the locations (1)-(3) marked in (a) and (b), obtained from DIC data. The macroscopic stress-strain characteristic of the sample is shown as dashed line. (Sample 027-a)

Strain bands. DIC analysis is performed in order to invesigate local effects in the CuAlBe wires. Local strain maps of two different positions on a wire sample are shown in Fig. 4.40 (a) and (b). The sample was loaded up to a maximum strain of 6%, leaving the stress-induced phase transformation incomplete. Strain maps reveal that at the upper sample end, local strain bands occur, whereas the lower part of the sample remains nearly unstrained. Three points of interest are marked by arrows in the figure. Local stress-strain characteristics at these locations, calculated from DIC data, are shown in Fig. 4.40 (c). In addition, the macroscopic stress-strain curve of the sample (engineering strain) is included. Considering that the sample has a bamboo-like structure of large single-crystalline grains, these local mechanical characteristics may be interpreted as follows: Since the applied strain was not sufficient to induce full martensitic transformation of the whole sample, only some of the grains having favorable orientation and/or a

118

reduced cross-section, undergo phase transformation. Interestingly, one of the observed regions (1) is strained by 20%, whereas another (2) is strained only by 10%.[3] The third observed region (3) at the lower sample end, on the other hand, does not show any stress plateau but undergoes elastic deformation in the austenitic state.

(a) loading

(b) unloading

18 °C ▮▮▮ 38 °C

dε/dt = 1 s^{-1}
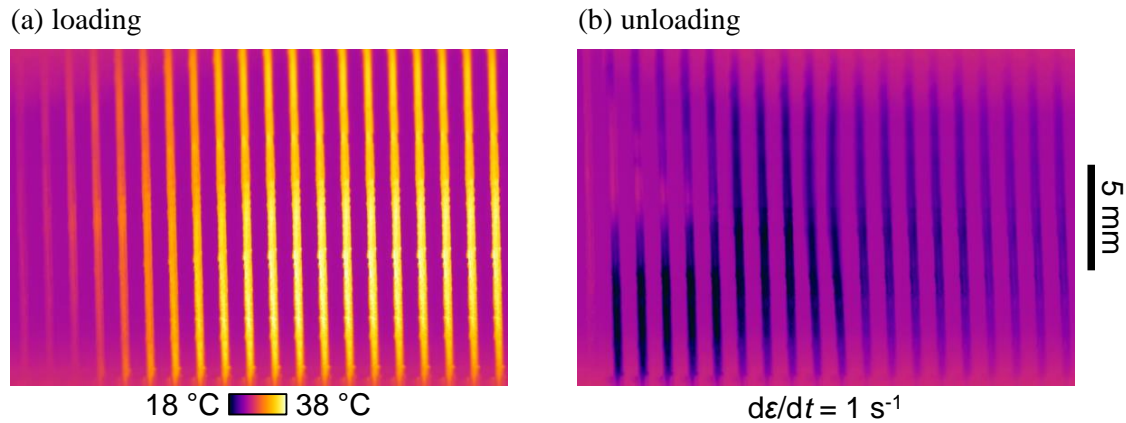
Figure 4.41: Chronological series of IR thermograms of a CuAlBe wire during (a) loading and (b) unloading at a strain rate of $1\,\mathrm{s}^{-1}$ to a maximum strain of 0.25. (Sample 027-c)
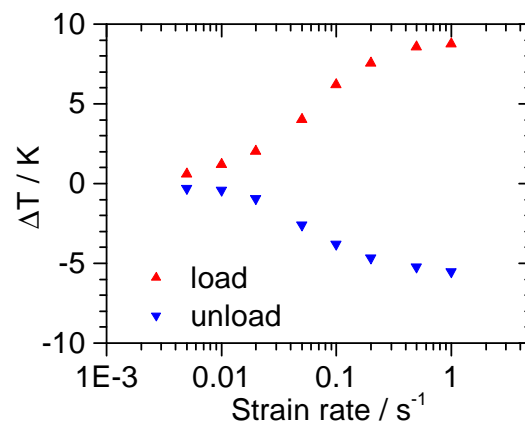
Figure 4.42: Maximum temperature change of a CuAlBe wire at a maximum strain of 0.2 as a function of strain rate. Temperatures are determined by IR thermography in a small test area in the center of the wire. (Sample 029-b)

Temperature bands and elastocaloric performance. In accordance with the local strain profiles, temperature profiles reveal localized behavior as well. Thermal bands can be seen in Fig. 4.41, showing a series of IR thermograms during loading and loading at a high strain rate of $1\,\mathrm{s}^{-1}$. For the IR experiment, a maximum strain of 25% was chosen to achieve nearly full phase transformation. The

---

[3]The first region shows an apparent two-step stress plateau, corresponding to two different critical stresses. This might be caused by reorientation of martensite variants [41].

maximum temperature changes are plotted in Fig. 4.42 as a function of strain rate. Under adiabatic conditions, a self-heating and -cooling of $8.8\,\mathrm{K}$ and $-5.5\,\mathrm{K}$ are observed, respectively.

Although the surface-to-volume ratio of the sample is $10\,\mathrm{mm}^{-1}$, which is the lowest value of all pseudoelastic samples investigated herein, the time constant for temperature equalization (obtained by exponential fit from IR data) is $1.37\,\mathrm{s}$. Hence, the time constant is almost identical to that of the cold-rolled TiNiFe foils. It is presumed that heat transfer is enhanced in the Cu-based alloy due to a higher thermal conductivity.

Due to their oligocrystalline properties, Cu-based wires may be an interesting option for elastocaloric cooling. Wires might be polished flat to further improve heat transfer. However, the latent heat is mush lower and the work input is more than douled with respect to typical TiNi-based alloys, leading to a significantly lower coefficient of performance. Also, the occuring high pseudoelastic strains pose severe challenges on the junction of SMA wire and device.

4.5 Discussion

In this section, the thermo-mechanical properties of the investigated materials are discussed with respect to elastocaloric microcooling applications. In some respects, the materials behave very similar, whereas they differ distinctively in others. The challenges introduced in the beginning regarding elastocaloric effect size, mechanical performance, cycle dependence and local effects are addressed one-by-one in the following.

Thermal and electrical phase transformation properties. Two measurement techniques have been employed in order to determine the properties of thermally induced phase transformation, namely DSC and temperature-dependent resistance measurement. Detailed phase transformation temperatures and values of latent heat of all investigated materials are listed in Tables 4.2 and 4.3. The results of both methods are in qualitative agreement. However, the exact values of transformation temperatures differ in some cases. As an explanation it has to be considered that two different physical phenomena are studied: changes in sample enthalpy due to release or absorption of latent heat in the case of DSC, and changes of electron conductivity related to the lattice structure, phonon states etc. in the case of resistance measurement. Also, the former is performed at a rather high temperature change rate of $10\,\mathrm{K\,min}^{-1}$, whereas the latter is performed under quasi-static conditions with the sample being in equilibrium. In addition, although care has been taken, deviations due to systematic measurement errors cannot be ruled out.[4] In the case of DSC, higher amounts of sample material are

---

[4]In the case of the electrical resistance measurement setup, the temperature sensor is not located directly at the sample. Hence temperature gradients throughout the experimental setup may

Table 4.2: Summary of phase transformation temperatures and latent heats of elastocaloric materials, determined by differential scanning calorimetry. Annealing temperature T_H of TiNiFe foils is indicated as superscript of the sample number. In case the DSC measurement reveals multiple peaks, peaks are numbered by roman letters (I,II).

Sample	Material	$T^{heat,I}_{(start,peak,finish)}$ [K]	$T^{heat,II}_{(start,peak,finish)}$ [K]	L^{heat} [J g^{-1}]
$018^{450\,°C}$	TiNiFe	(n.a. / -7.3 / n.a.)	(10.8 / 26.8 / 37.2)	(n.a. / 6.1)
$018^{450\,°C}$	TiNiFe	(15.2 / 24.0 / 33.2	-	6.8
$018^{350\,°C}$	TiNiFe	(-17.6 / 22.5 / 54.3	-	5.3
$018^{500\,°C}$	TiNiFe	(-21.3 / -14.0 / n.a.)	(n.a. / 5.2 / 8.1)	15.3
$018^{450\,°C}$	TiNiFe	(-19.3 / -9.9 / n.a.)	(n.a. / 24.5 / 33.0)	7.2
$018^{500\,°C}$	TiNiFe	(-21.1 / -13.3 / n.a.)	(n.a. / 6.0 / 9.3)	17.2
$018^{400\,°C}$	TiNiFe	(11.1 / 30.3 / 42.5)	-	7.2
$018^{450\,°C}$	TiNiFe	(-19.3 / -8.9 / -1.2)	(15.3 / 28.4 / 37.3)	(n.a. / 6.8)
006	TiNi	(-41.4 / -32.7 / -28.2)	(n.a. / -16.0 / n.a.)	(8.6 / n.a.)
008	TiNi	(-14.2 / -6.4 / 1.0)	(n.a. / -3.8 / n.a.)	20.0
019	TiNi	(-11.6 / 1.5 / 7.2)	-	18.9
004	TiNiCu	(26.8 / 50.8 / 53.6)	-	12.1
028	TiNiCuCo	(7.6 / 10.4 / 14.0)	-	13.7
027	CuAlBe	(-74.3 / -70.4 / -67.5)	-	1.9

Sample	$T^{cool,I}_{(start,peak,finish)}$ [K]	$T^{cool,II}_{(start,peak,finish)}$ [K]	L^{cool} [J g^{-1}]
$018^{450\,°C}$	(36.9 / 24.7 / 11.7)	-	-6.1
$018^{450\,°C}$	(32.2 / 22.1 / 14.5)	-	-7.5
$018^{350\,°C}$	(53.4 / 25.9 / -0.8)	-	-5.5
$018^{500\,°C}$	(6.4 / 1.4 / -2.2)	(-80.2 / -92.2 / n.a.)	(-7.8 / n.a.)
$018^{450\,°C}$	(32.4 / 22.8 / 12.9)	-	-6.1
$018^{500\,°C}$	(6.5 / 0.7 / -3.2)	(-81.1 / -93.4 / -109.4)	(-7.8 / -7.7)
$018^{400\,°C}$	(41.3 / 29.3 / 15.2)	-	-7.6
$018^{450\,°C}$	(35.5 / 25.7 / 13.2)	-	-7.6
006	(n.a. / -17.0 / n.a.)	(-115.5 / -125.3 / -133.3)	(n.a. / -5.0)
008	(9.7 / -10.8 / -26.9)	(-50.2 / -62.7 / -72.7)	-19.9
019	(27.9 / -5.4 / n.a.)	(-50.1 / -57.2 / -70.5)	-18.7
004	(35.9 / 31.5 / 13.1)	-	-12.3
028	(0.8 / -4.1 / -5.9)	-	-13.7
0.27	(-86.8 / -89.5 / n.a.)	-	-2.2

Table 4.3: Summary of phase transformation temperatures of elastocaloric materials, determined by electrical resistance measurement as a function of temperature.

Sample	Material	$T^{heat,I}_{(start,finish)}$ [K]	$T^{heat,II}_{(start,finish)}$ [K]	$T^{cool,I}_{(start,finish)}$ [K]	$T^{cool,II}_{(start,finish)}$ [K]
$018^{450\,°C}$	TiNiFe	n.a.	-	(30 / -1)	-
$018^{500\,°C}$	TiNiFe	(-55 / -40)	(-25 / 0)	(0 / -23)	(-125 / -145)
006	TiNi	(-70 / -58)	(-45 / 20)	(15 / -80)	(-145 / -175)
008	TiNi	(-30 / -10)	(-5 / 22)	(20 / -30)	(-70 / -85)
019	TiNi	(-15 / 0)	(0 / 25)	(12 / -25)	(-47 / -70)
004	TiNiCu	(43 / 50)	-	(35 / 21)	-
022	TiNiCuCo	(-26 / -18)	-	(-40 / -45)	-
028	TiNiCuCo	(3 / 8)	-	(-6 / -9)	-

required in order to obtain sufficient signal strength. Hence, a certain averaging or superposition is obtained for inhomogeneous sample material. In $R(T)$ measurements, smaller sample portions are examined, usually only few square millimeters. In both cases, transformation temperatures are estimated by applying the tangent method.

Measurements reveal a single-step transformation for some materials and a two-step transformation for others. Without having performed a structural analysis, it is concluded based on literature that the single-step transformation takes place between martensite (B19 or B19′) and austenite (B2), whereas an intermediate R-phase is involved in two-step transformations [42]. The peak temperatures of the alleged R⇆A transformation usually exhibit a rather small hysteresis between forward and reverse transformation. In the case of TiNi film sample 006, the temperature range had to be extended to $-180\,°C$ in order to capture a second peak associated with the R→M transformation. In the case of TiNiFe foil samples annealed at $T_H = 400$ or $450\,°C$, a second peak could not even be detected in the extended temperature range. The latent heat of the alleged R⇆A transformation is lower than that of a full M(⇆R)⇆A transformation. Nevertheless their elastocaloric effect size in TiNi foil samples annealed at $T_H = 450\,°C$ is almost identical as for samples with $T_H = 500\,°C$, although the latter exhibit a clear two-step transformation. In addition, samples show perfect superelastic behavior with a transformation strain above 5% and no signs of one-way shape memory effect although the transformation peak temperature is right at room temperature. These findings provoke the question, whether a DSC or $R(T)$ measurement, limited to the temperature of liquid nitrogen as the lowest measurement temperature, really capture the full phase transformation that is accessed in tensile test experiments. In my opinion, the observed mechanical behavior cannot be explained by a mere

---

explain certain deviations of measured temperature and actual sample temperature. Furthermore, stress states may be induced by the spring contacts in the electrical resistance measurement setup, hindering the sample from thermal expansion/contraction.

stress-induced R$\leftrightarrows$A transformation for the samples in question, and the latent heat determined by DSC does not represent the full latent heat available for the elastocaloric effect.

The thermal measurements provide information about the temperature regime in which a material may be employed for elastocaloric cooling. Ideally, the difference δT between ambient temperature (i.e. the intended operation temperature of a device) and austenite finish temperature of the material should be higher than the adiabatic temperature change during unloading:

$$\delta T = T_{amb} - A_f \overset{!}{>} |\Delta T_{ad}| \qquad (4.1)$$

On the other hand, the maximum δT is limited by mechanical constraints: Stress-induced transformation has to take place at stresses below the yield stress at which irreversible damage to the material occurs:

$$\sigma_{crit} + \Delta T_{ad} \cdot \frac{d\sigma_{crit}}{dT} \overset{!}{<} \sigma_{yield} \qquad (4.2)$$

The proportionality between temperature intervals and stress intervals is established by the Clausius-Clapeyron coefficient $d\sigma_{crit}/dT$ (Section 2.3.3, Eq. 2.15).

In order to cover wider temperature spans within a single device, arrays of material elements with adjusted transformation properties may be considered, each element being operated in its own suitable temperature regime. A continuous array may be realized in a single sample with graded properties, achieved, e.g., by a stoichiometry gradient along the sample length.

Elastocaloric effect size. The elastocaloric effect size is determined from tensile tests under adiabatic conditions by IR measurements. Mass-specific transformation enthalpies $Q_{load,unload}$ are estimated based on the adiabatic temperature change ΔT_{ad} and the specific heat capacity of the material c_p:

$$Q \approx c_p \cdot \Delta T_{ad} \qquad (4.3)$$

In contrast to thermocouples or other kinds of temperature sensors employed in earlier experiments, IR thermography provides a method for contactless temperature measurement, disturbing the temperature evolution of the sample as little as possible. However, in order to achieve reliable measurements, samples are covered with a thin layer of black carbon. Because of the thin sample geometry, the additional heat capacity of this layer has to be considered. The estimated increase of total heat capacity, based on layer mass and heat capacity of graphite, is about 6%.

At lower strain rates, the observed temperature changes are lower than in the adiabatic limit. However, this does not imply that the transformation enthalpy is

lower in this case, but rather that heat exchange with the environment is faster than heat release and absorption. Therefore, transformation enthalpy would be underestimated by IR-based evaluation in case the strain rate is too low. This has to be considered when comparing literature values for the elastocaloric effect in different materials. In some cases, the assurance of adiabatic conditions is not clearly stated or different strain rates are employed during loading and unloading (e.g., Ref. [228]).

Among the materials investigated herein, the highest temperature changes are observed for TiNi-based foils and films. A self-cooling of $-17\,\mathrm{K}$ is obtained for TiNiFe foils annealed at $T_H = 500\,^\circ\mathrm{C}$. For TiNi films, the self-cooling is up to $-15\,\mathrm{K}$. The other materials show lower effect sizes. Values reported in literature for bulk material indicate that there is still room for improvement. In a recent publication, Pieczyska et al. report on a TiNi bulk sample undergoing a maximum temperature change of close to 60 K [96]. This phenomenal temperature change seems feasible when assuming a latent heat of $30\,\mathrm{J\,g^{-1}}$ and a typical heat capacity of $0.5\,\mathrm{J\,g^{-1}\,K^{-1}}$ but was not confirmed by other research groups yet.

Usually, the adiabatic temperature change (and thus the estimated enthalpy, assuming constant c_p) is higher for loading than for unloading. This asymmetry is plausible, since irreversible processes like dissipation due to internal friction contribute to heating and counteract cooling (compare Eq. 3.3b). The quaternary low-hysteresis TiNiCuCo films exhibit a remarkable exception in that they show a reversed asymmetry. This phenomenon might be understood if the austenite phase had a higher specific heat capacity than the martensite – which was however not observed in DSC measurements (see Fig. 4.24). Another reason might be a difference in heat transfer due to changes in thermal conductivity. These, however, should not be relevant anymore in the adiabatic limit. Hence, a convincing explanation is still to be found.

When comparing the enthalpies of thermally induced transformation (determined by DSC) with those of stress-induced transformation (estimated by the IR-method), higher enthalpies of the thermal transformation are generally observed. This difference has to be considered when judging the cooling potential of a particular material. In some cases, DSC values have been used for calculation of material efficiencies in literature [13]. The reason for the discrepancy might be a still-to-be-explained fundamental difference between the thermally induced and stress-induced phase transformation. A more obvious explanation is given by the assumption that the sample volume is not fully transformed to martensite even at the end of the superelastic plateau. Most samples investigated herein are polycrystalline, hence it seems plausible that some grains or variants are hindered by internal stresses and may not undergo stress-induced phase transformation. Hence, only a total volume fraction below 100% contributes to the elastocaloric effect. The phenomenon is discussed in literature under the terms of residual or 'lazy' austenite, referring to austenite fractions that transform to martensite only if stress is increased beyond the end of the superelastic plateau [45, 297, 298]. In the tensile test experiments described above, the maximum applied strain is

adjusted to be just below the end of the stress plateau, hence fractions of 'lazy austenite' would not be accessed.

The competition between heat release/absorption in the sample and heat exchange with the environment due to conduction and air convection is quantified by the time constants determined from tensile tests. For foil and film samples, adiabatic conditions are reached at a strain rate of $0.2\,\mathrm{s}^{-1}$. Assuming a strain interval of 5%, stress-induced (and reverse) phase transformation takes place within a quarter of a second. In comparison, the time constants estimated from time-dependent temperature equalization in the sample center are between 1 to $1.5\,\mathrm{s}$. Close to the sample fixations, time constants are lower due to the stronger influence of thermal conduction. With respect to microcooling applications, heat exchange between sample and heat sink/source thus has to proceed within $250\,\mathrm{ms}$ or faster in order to keep the impact of parasitic heat flows sufficiently low.

Mechanical performance. In the previous sections, mechanical performance has been studied for two limiting cases: the quasi-static and the adiabatic limit. Quasi-static experiments have been performed to determine basic material properties such as elastic moduli, Clausius-Clapeyron coefficients, critical stresses and stress hysteresis independently of self-heating and cooling effects. Results are summarized in Table 4.4. A compilation of representative quasi-static stress-strain characteristics of the investigated materials is shown in Fig. 4.43. A comparison reveals that critical stresses (plateau stresses), transformation strains and hysteresis greatly vary among the materials. These deviations have to be considered when designing an elastocaloric cooling device, since they have a direct impact on the required force and stroke of the actuator for mechanical loading. The lowest hysteresis is found in fatigue-free TiNiCuCo films, whereas CuAlBe wires exhibit the largest hysteresis and a transformtion strain beyond 20%. Such a high reversible strain makes sample fixation very challenging.
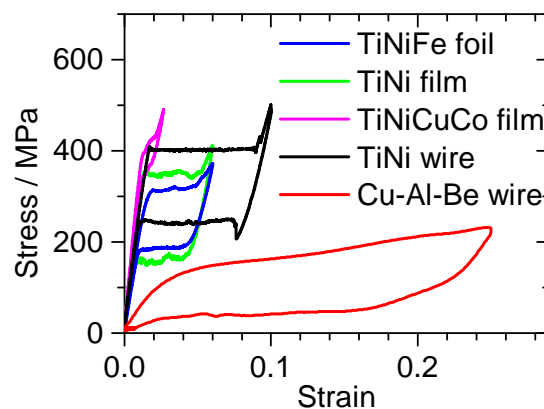
Figure 4.43: Comparison of quasi-static stress-strain characteristics of pseudoelastic materials investigated in this thesis.

Table 4.4: Summary of mechanical and elastocaloric material performance, determined by tensile test and infrared thermography. (* untrained sample).

Name	Material	E_A [GPa]	E_M [GPa]	σ_{crit}^{AM} [MPa]	σ_{crit}^{MA} [MPa]
018-a	TiNiFe foil, RD, $T_H = 450\,°C$	22.7	16.6	475	340
018-b	TiNiFe foil, TD, $T_H = 450\,°C$	21.0	19.0	530	400
018-c	TiNiFe foil, 45°, $T_H = 450\,°C$	23.8	18.0	465	340
018-g	TiNiFe foil, RD, $T_H = 500\,°C$	21.9	17.0	370	185
018-h	TiNiFe foil, RD, $T_H = 400\,°C$	18.8	15.0	455	335
018-i	TiNiFe foil, TD, $T_H = 400\,°C$	19.1	16.1	480	365
006-a	TiNi film	32.6	25.5		
006-b	TiNi film	35.9*	22.8*	465	445
006-c	TiNi film	36.7*	20.1*	490	410
006-d	TiNi film	32.8*	20.2*	500	410
008-b	TiNi film	35.9*	27.9*	400	285
019-c	TiNi film	32.4*	24.8*	375	315
021-b	TiNiCuCo film	26.6	14.9	480	445
022-a	TiNiCuCo film	34.8	20.6	390	365
022-b	TiNiCuCo film	35.3	17.8	450	425
028-d	TiNiCuCo film	35.8	17.8	235	180
029-a	TiNi wire	24.4	15.5	400	205
027-c	CuAlBe wire	4.7	4.5	130	50

Name	$\Delta\sigma$ [MPa]	ΔW_{iso} [MPa]	ΔW_{ad} [MPa]	$\Delta\varepsilon$ [%]	ΔT_{load} [K]	ΔT_{unload} [K]	τ_{load} [s]	τ_{unload} [s]
018-a	160	5.4	9.5	3.1	20.2	-15.9	1.32	1.25
018-b	145	5.5	9.7	2.5	18.8	-14.4	1.79	1.72
018-c	160	5.8	10.1	3.5	9.2	-6.7	1.57	1.75
018-g	185	5.0	8.8	> 4.2	21.6	-17.3	1.26	1.41
018-h	130	4.3	7.9	2.8	13.4	-11.1	1.18	1.35
018-i	130	3.1	5.4					
006-a	90	3.3	7.0				1.06	0.71
006-b	130*	3.3	6.0	> 3.8	17.7	-17.1	0.95	0.96
006-c	85 / 130*	3.2	7.5	> 3.7	17.7	-15.6	0.95	0.96
006-d	100 / 135*	3.2	6.9	3.7	16.4	-15.1	1.11	1.36
008-b	120 / 200*	5.5	8.8	> 3.9	18.3	-12.1	0.94	1.13
019-c	180							
021-b	70	1.3	2.8		7.5	-10.2	0.87	0.75
022-a	60	0.7	2.2		9.3	-12.4	1.02	0.83
022-b	55	0.6	1.8		7.4	-9.8	1.48	1.00
028-d	80	1.0	3.0	1.4	7.1	-5.4	1.8	1.5
029-a	160	12.7	29.7	7.0	27.3	-18.6	2.15	2.67
027-c	140	26.6		> 20	8.8	-5.5	1.58	1.08

However, the more realistic condition for practical applications is the adiabatic limit, because high cycling rates are desired in order to reach high pumping powers. This case should therefore be considered in performance estimations. The mechanical work input, obtained by numerical integration of stress-strain characteristics, increases with strain rate and reaches a maximum in the adiabatic limit. This effect is consistently observed for all investigated materials and is caused by self-heating and cooling, respectively [61]. In the course of mechanical loading (within the forward stress plateau), the sample temperature continuously increases due to heat release and in consequence, the critical stress for phase transformation increases as well according to the Clausius-Clapeyron relation. Upon unloading, the reverse phenomenon occurs: The critical stress for reverse transformation is lowered by self-cooling and stress-induced martensite is stabilized. As a result, the stress-strain loop is enlarged in both directions: towards higher stresses during loading and towards lower stresses during unloading. In the adiabatic limit, further increase of the strain rate does not lead to further increase of the work input, since the maximum temperature changes are already reached. Note that this kind of behavior is only observed when tensile test experiments are performed according to the procedure described above. Here, mechanical loading and unloading start with the sample being at ambient temperature. In case the halting steps for temperature equalization are left out (as in many studies reported in literature), unloading starts from an elevated temperature level and an actual maximum of work input ΔW occurs at an intermediate strain rate [61–63].
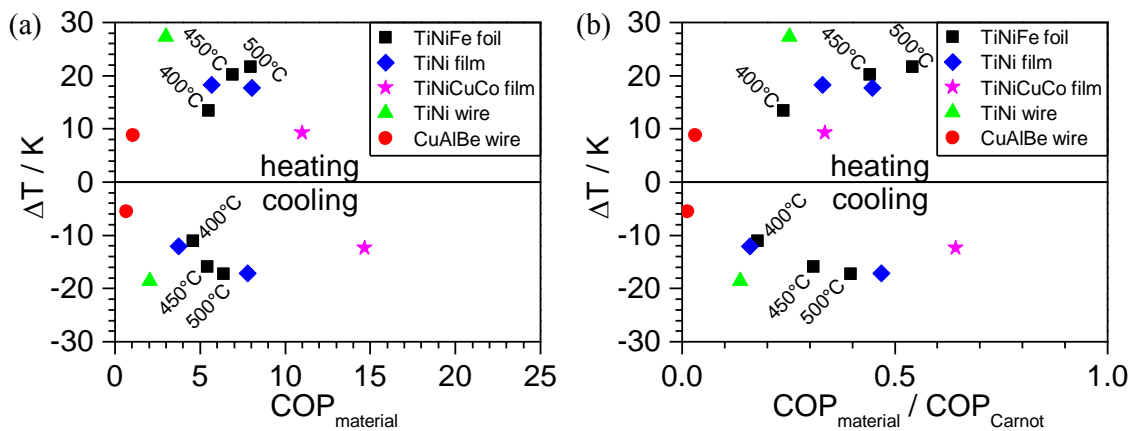
Figure 4.44: (a) Adiabatic temperature changes ΔT and material coefficients of performance $COP_{material}$ of the investigated materials. (b) Material COPs normalized by Carnot COPs. Annealing temperature T_H is indicated for cold-rolled foils.

Material coefficient of performance. In order to compare the potential cooling capacities of the investigated samples, material coefficients of performance (also called material efficiency η in literature) are calculated, which are given by the ratio of released/absorbed heat Q and work input ΔW:

$$COP_{material} = Q/\Delta W \tag{4.4}$$

In order to obtain realistic values, ΔW is determined from tensile tests under adiabatic conditions. Released and absorbed heat Q_{load} and Q_{unload} are also determined from tensile tests by multiplying the observed adiabatic temperature changes with the heat capacity [226], rather than using latent heat values from DSC measurements [13]. The highest COP for cooling of 15 is obtained for sputter-deposited TiNiCuCo films due to their particularly low hysteresis [300]. The adiabatic temperature changes of these quaternary films are somewhat lower than for binary TiNi samples, but this is overcompensated by a very low hysteresis. In comparison, sputter-deposited TiNi films reach a cooling COP of up to 7.7 in the trained state (i.e. having a rather narrow cigar-shaped stress-strain characteristic). In the case of cold-rolled TiNiFe foils, cooling COPs of up to 10.5 are reached for samples annealed at $500\,°C$ and loaded in rolling direction [295]. The COPs of the wire samples are considerably lower. A COP of 1.8 is obtained for the commercial TiNi wire[5] and in case of the CuAlBe wire, COP is below one. Note that all COPs given above assume full recovery of the unloading work. Work recovery has to be implemented on the device level to reach maximum efficiency. The calculated material COPs have to be seen in relation to the Carnot efficiency (Eq. 2.9a): From a thermodynamic point of view, higher COPs may be reached when the temperature lift is lower. Fig. 4.44 gives an overview over the adiabatic temperature changes and material COPs of the invetitgated materials in absolute values (a), as well as relative to the Carnot COP defined by Equations 2.9b and 2.9a (b). For COP calculation, a density of $6500\,\mathrm{kg\,m^{-3}}$ and a heat capacity of $0.5\,\mathrm{J\,g^{-1}\,K^{-1}}$ have been assumed (except for TiNi and TiNiCuCo films, for which c_p values have been measured).

The functional properties of SMA may be tuned, e.g., by variation of stoichiometry, additional alloying elements or heat treatments. However, in most cases hysteresis and latent heat cannot be tuned independently in the same material. Therefore, a trade-off has to be found between elastocaloric effect size, mechanical hysteresis and, of course, cyclic stability.

Cycle dependence.   In a typical cooling or heat pumping device, the active material has to undergo millions of cycles throughout the device lifetime. Assuming operation at $1\,\mathrm{Hz}$ over $12\,\mathrm{h}$ a day, for 10 years, as Cui et al. did in their example, results in a total number of $68\,000\,000$ cycles [13]. Therefore, cyclic stability is crucial for every practical application. Extensive fatigue studies are certainly required, but lie out of the scope of this thesis. However, sample behavior during the first tens to hundreds of cycles was investigated, during which sample performance changes most rapidly.

---

[5]This low value is not necessarily representative for other TiNi wires – higher COPs have been reported by other authors [13, 86].

It has to be discriminated between structural fatigue and functional fatigue. The former refers to the mechanical stability and integrity of a SMA material, e.g., a tendency for crack formation and growth, and depends on the microstructure as well as the sample surface quality. The latter, functional fatigue, relates to the stability of the desired functional material properties, which are pseudoelastic behavior and elastocaloric effect in the present case, and depends on microstructure as well. Thus, both types of fatigue may be counteracted by optimization of stoichiometry and chemical composition and are therefore a central task in material development and fabrication.

Recent results obtained by the group of Eckhard Quandt have shown the tremendous impact of crystallographic compatibility between martensite and austenite, the existence of Ti_2Cu precipitates forming epitaxial interfaces with both, martensite and austenite, as well as a small grain size [103, 120, 122] on structural and functional fatigue. Newly developed sputter-deposited TiNiCuCo films have been investigated in this thesis with respect to their elastocaloric properties and Lüders-band formation. In the experiments, sample lifetime was limited due to fracture of the relatively brittle samples. In comparison, (non-brittle) cold-rolled TiNiFe foils accumulated small plastic strains upon mechanical cycling without reduction of temperature change and failed after several hundreds of cycles due to fracture. It is believed that the lifetime of both, TiNiCuCo films and TiNiFe foils could be drastically increased by applying a surface treatment like electropolishing. In the experiments of Chluba et al., polished films survived more than ten million pseudoelastic cycles [120].
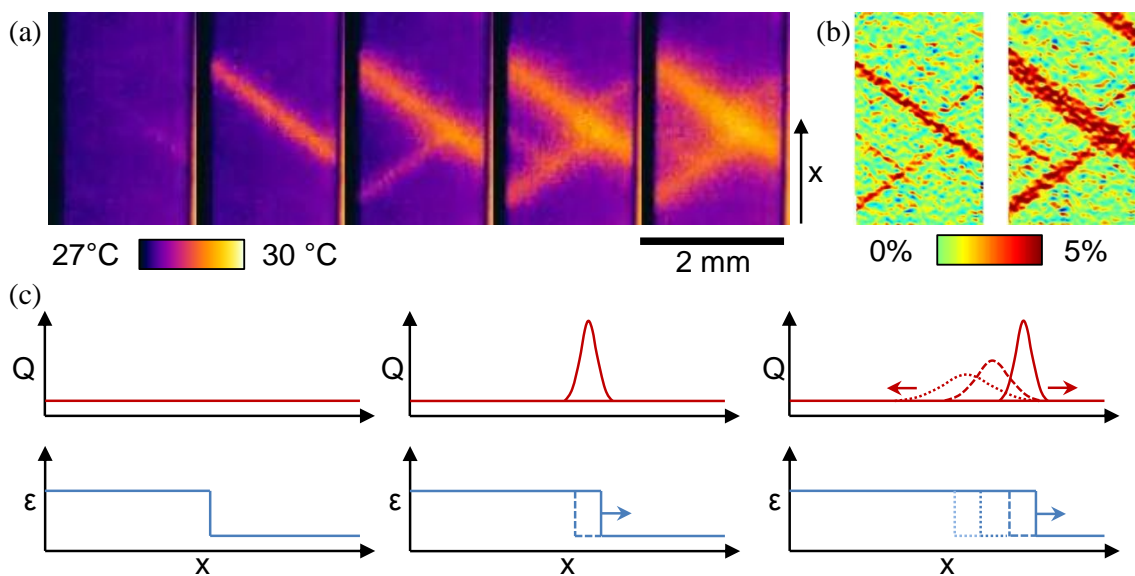
Figure 4.45: Correlation of strain bands and temperature bands. (a,b) TiNiCuCo sample loaded at a strain rate of $0.02\,\mathrm{s}^{-1}$ in x-direction: (a) IR thermograms in intervals of $10\,\mathrm{ms}$; (b) local strain maps from DIC for an interval of $100\,\mathrm{ms}$. (c) Schematic correlation of moving strain band interface and heat release. Compare Ref. [300]. (Sample 028-d)

Local phenomena.   Due to the particular way stress-induced phase transformation proceeds on the local scale, local phenomena have to be considered particularly in the context of microcooling applications. In many SMAs, most prominently binary TiNi-based alloys, transformation is nucleation-growth-driven. This leads to the formation and propagation of strain bands (Lüders bands) during stress-induced martensitic and reverse transformation. Lüders-like transformation behavior manifests in the macroscopic stress-strain characteristic as stress plateaus during loading and unloading, respectively. Strain bands are defined regions with elevated local strain in the direction of applied force, neighboring regions with lower strain. Their boundaries represent (mesoscopically) sharp interfaces between predominantly martensitic and austenitic parts of a sample. During tensile test, the overall sample length increases by growth of martensitic regions during loading, and decreases by shrinkage of those regions during unloading. Due to the localized phase transformation at the moving interface, heat release or absorption also proceeds highly localized (Fig. 4.45 (c)).

In this chapter, local phase transformation is studied by two complementary methods: digital image correlation and infrared thermography. Figs. 4.45 (a) and (b) show an example, where a particular region of a TiNiCuCo film sample was observed by both methods at once during a tensile test at intermediate strain rate well below the adiabatic limit. A comparison reveals that closely correlated band patterns are found by both methods. However, the information gained by either method is not quite the same. The difference is indicated schematically in Fig. 4.45 (c). Local strain maps obtained from DIC detect the absolute position of strain bands (provided that an image of an unstressed sample free of bands is used as reference for evaluation). Austenitic and martensitic regions may be discriminated by local strain level, since martensite variants orient in the direction of applied strain. IR measurements, on the other hand, reveal the change of phase fractions, i.e. the creation or movement of interfaces, as a function of time. A motionless strain band cannot be detected by IR thermography, which represents a kind of time-derivative of the DIC measurement. Furthermore, existing temperature bands are rapidly blurred and averaged out by inevitable heat conduction along the sample. Forward and reverse transformation may be discriminated by the fact that the exothermal A→M transformation leads to local heating, whereas the endothermal M→A transformation leads to cooling. Heat release and absorption is thus highly inhomogeneous in samples showing Lüders-like transformation behavior. This has to be considered in microcooling, where the occurring strain- and temperature bands are of similar size as the device itself.

As the experiments in section 4.2.2 show (in accorance with literature reports on thicker TiNi samples), the dynamics of Lüders-bands strongly depends on strain rate. The methods of DIC and IR measurement are both suitable only for certain ranges of strain rate. DIC can be applied for very low (quasi-static) to medium rates, whereas at higher rates the exposure time gets too short to obtain reasonably sharp images.[6] IR thermography, on the other hand, is suitable for medium

---

[6]For the given experimental setup, DIC is furthermore limited to a frame rate of 10 Hz and a

to high rates[7], since measurable temperature changes are required. Hence, strain rate-dependence of local effects was studied by IR thermography. Experiments reveal that the number of temperature bands increases with strain rate (Fig. 4.30-4.34). While only one or two bands are observed for a rate of $1 \times 10^{-3}\,\text{s}^{-1}$, an increasingly dense network of bands occurs with increasing rate. Note that these may either originate from the formation of new, or the propagation of existing phase interfaces. The explanation for this behavior lies in the self-heating and cooling of elastocaloric materials: Whenever a martensitic region grows during mechanical loading, heat release at the moving interface leads to local heating, inhibiting further movement of the very same interface, because higher temperature stabilizes austenite. Hence, formation of a new (or movement of a previously still-standing) interface at a different location becomes energetically more favorable. The same explanation applies during unloading, where local undercooling stabilizes martensite and inhibits reverse transformation.[8] In the adiabatic limiting case, which is desirable for practical application in order to exploit the maximum elastocaloric temperature change, the distribution of thermal bands is so dense that homogeneous temperature is obtained quickly due to heat conduction. Hence, heat transfer in microcooling is affected the least by local phenomena when strain rate is in the adiabatic limit.

Among the materials studied herein, strain- and temperature bands have been found in TiNiFe foils, as-fabricated TiNi films, as well as TiNiCuCo films with low critical stress. In all cases, bands are oriented in the same angle of $55°$ with respect to loading direction. Since all samples are polycrystalline, crystal orientation may be discarded as explanation. According to simulation studies of F. Wendler, the angle naturally arises from the transformation matrix for geometries with negligible thickness, whereas for thicker bulk geometries, higher angles up to $90°$ are obtained [304]. Depending on material and strain rate, bands may intersect or be predominantly oriented in one direction. In the case of textured cold-rolled foils, loading in TD seems to prefer one particular orientation. This finding is in accordance with literature [74].

In two kinds of samples no strain bands could be observed: in binary TiNi films after training and in as-fabricated TiNiCuCo films with high critical stress (batch 022). In both cases, the stress-strain characteristic does not contain stress plateaus with sharp onset. For the TiNiCuCo sample, the observation is unexpected and may be correlated with ambient temperature: It was observed that with increasing ambient temperature the plateaus get steeper and more rounded. Another explanation may be found in the production process. The TiNiCuCo films not exhibiting sharp Lüders bands were fabricated by alternatingly depositing TiNiCu

---

sample section of $2 \times 3\,\text{mm}^2$.

[7]Up to $100\,\text{Hz}$ could be achieved with the IR equipment used herein; IR cameras with cooled semiconductor detectors easily reach frame rates in the kHz regime.

[8]Note that in contrast to homogeneous heat release (absorption), temperature changes exceeding the adiabatic limit are locally possible in materials showing Lüders-like behavior, when local temperature is already raised (lowereded) due to heat release (absorption) in surrounding regions.

and Co layers. Possibly, homogenization by rapid thermal annealing remained incomplete, resulting in gradients of critical stresses across the sample thickness.

5 Material simulation

Simulations play a crucial role in understanding and predicting physical material behavior. Within the past decades, various models for the description of shape memory effect and superelasticity have been proposed. The models assess the behavior on different length scales ranging from the atomic level (ab-initio) to the device level. In this chapter, pseudoelasticity including the elastocaloric effect shall be described on the material level by a computationally simple model that allows simulation of a whole sample, in contrast to only infinitesimal volume fractions or unit cells. This two-phase phenomenological model is based on experimentally accessible properties of the investigated material.

5.1 Finite element model

In the following, a model of pseudoelastic material behavior including the elastocaloric effect is introduced [299]. The model was formulated by Tanaka [138] in its original one-dimensional form and was further developed and generalized to 2D by Ikuta [139] and to 3D by Kohl and Krevet [140]. Krevet et al. also applied the model on a device level [141] and integrated the elastocaloric effect [142]. It is chosen here for relying on experimentally determined parameters. The model is implemented in the finite element software COMSOL Multiphysics with the modules 'Heat transfer' and 'Solid mechanics'.

5.1.1 Two-phase model

The model considers isotropic material properties, which represent a reasonable approximation in many polycrystalline SMA materials. The phase fraction of oriented martensite (i.e. variant orientation in tensile direction) is implemented as an internal variable ξ. Correspondingly, the phase fraction of austenite is given by $1 - \xi$. In order to account for hysteresis, the evolution of martensitic phase fraction is defined separately for forward ('AM') and reverse ('MA') direction as follows:

$$\xi^{AM}(T, \sigma^*) = f(k^{AM} \cdot [T - T_0^{AM} - c^{AM} \cdot \sigma^*]) \tag{5.1a}$$

$$\xi^{MA}(T, \sigma^*) = f(k^{MA} \cdot [T - T_0^{MA} - c^{MA} \cdot \sigma^*]) \tag{5.1b}$$

The phase fraction is defined locally and depends on local temperature T and effective local stress σ^*. Based on the above formulation, the temporal evolution of the phase fraction can be expressed by:

$$\frac{d\xi}{dt} = \frac{\partial\xi}{\partial\sigma^*} \cdot \frac{d\sigma^*}{dt} + \frac{\partial\xi}{\partial T} \cdot \frac{dT}{dt} \tag{5.2}$$

In the present case, the scalar variable σ^* is determined by the Tresca stress.[1] The material-specific parameters T_0^{AM} and T_0^{MA} represent the peak temperatures of martensitic and reverse transformation, c^{AM} and c^{MA} describe the linear dependence of critical stresses (plateau stresses) σ_{crit}^{AM} and σ_{crit}^{MA} on temperature according to the Clausius-Clapeyron relationship:

$$c^{AM} = \left(\frac{d\sigma_{crit}^{AM}}{dT}\right)^{-1}, \quad c^{MA} = \left(\frac{d\sigma_{crit}^{MA}}{dT}\right)^{-1} \tag{5.3}$$

The width (or temperature span) of the forward and reverse transformation is adjusted by the fit parameters k^{AM} and k^{MA}. The function $f(x)$ describes a soft step function which is defined here following the suggestion of Ref. [142] as:

$$f(x) = \frac{1}{1 + e^x} \tag{5.4}$$

The mechanical rule of mixture is formulated based on the assumption that the contributions of martensitic and austenitic phase fraction to the total stress in each volume element are mechanically coupled in parallel. This kind of mechanical behavior is commonly referred to as Voigt model (compare, e.g., Ref. [135]):

$$\sigma = (1 - \xi) \cdot E_A \cdot \varepsilon + \xi \cdot E_M \cdot (\varepsilon - \varepsilon_T), \tag{5.5}$$

where ε refers to the absolute local strain, ε_T represents the transformation strain in case of fully oriented (stress-induced) martensite, and E_A and E_M are the elastic moduli of austenite and martensite phase.

The release and absorption of latent heat due to martensitic and reverse phase transformation is accounted for by introducing a local heat source term:

$$Q_L(T, \sigma^*) = L \cdot \rho \cdot \dot{\xi}(T, \sigma^*) \tag{5.6}$$

depending on the time derivative of the phase fraction $\dot{\xi} = d\xi/dt$, the specific latent heat L and the mass density ρ. The latent heat is assumed to be identical for forward and reverse transformation; possible contributions to heat release

---

[1] In this work, the effective stress is defined by the Tresca stress: $\sigma^* = \max(|\sigma_I - \sigma_{II}|; |\sigma_{II} - \sigma_{III}|; |\sigma_{III} - \sigma_I|)$. In previous works [142], the effective stress was described by the von Mises stress: $\sigma^* = \sqrt{\sigma_x^2 + \sigma_y^2 + \sigma_z^2 - \sigma_x\sigma_y - \sigma_x\sigma_z - \sigma_y\sigma_z + 3(\tau_{xy}^2 + \tau_{xz}^2 + \tau_{yz}^2)}$.

due to irreversible processes like dissipation are neglected in the model. Heat transfer within the elastocaloric material is described by the following differential equation, assuming isotropic thermal properties and taking into account the sensible heat, the advection, release and absorption of latent heat due to phase transformation Q_L, as well as losses due to heat conduction Q_C:

$$\rho \cdot C_p \cdot \dot{T} + \rho \cdot C_p \cdot \vec{u} \cdot \nabla T = \nabla \cdot (\kappa \cdot \nabla T) + Q_L + Q_C. \tag{5.7}$$

The material parameters m, C_p and κ refer to the mass, specific heat capacity and thermal conductivity, respectively. $\vec{u} = \dot{\vec{r}}$ is the velocity of material at position $\vec{r}$. The parameters are assumed to be identical for martensite and austenite phase for sake of simplicity. This assumption is justifiable for the mass and heat capacity of TiNi-based alloys. However, heat conductivities of austenite and martensite have been reported to differ, which is neglected here [56].

5.1.2 Initial and boundary conditions

(a) Boundary conditions
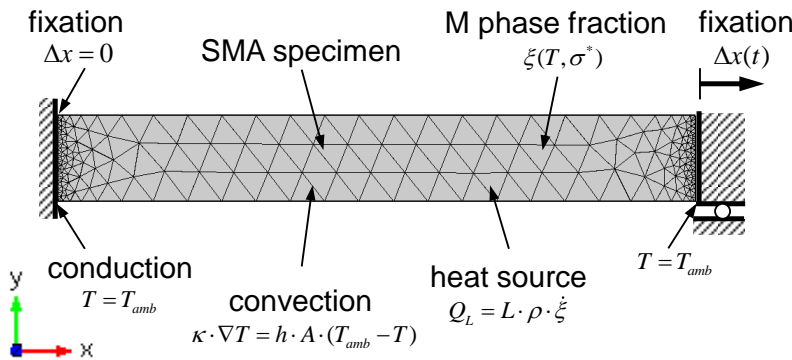
(b) Rule of mixture
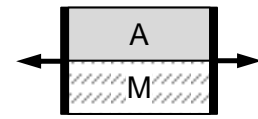
Figure 5.1: Thermal and mechanical boundary conditions of the phenomenological two-phase model (a) and mechanical rule of mixture (b).

The thermo-mechanical performance of the elastocaloric material is simulated for an ambient temperature T_{amb} well above the phase transformation temperatures. The initial sample temperature is homogeneous and equal to the ambient temperature. Hence the material can be considered to be fully austenitic, $\xi = 0$. In this case, the sample is assumed to be mechanically stress-free.

An overview over the boundary conditions is shown in Fig. 5.1. The simulation of uniaxial loading and unloading experiments is defined by the mechanical boundary conditions at the sample ends ($x = 0$ and $x = l_0$). While the position and cross-section of the sample end at $x = 0$ are held constant throughout the simulation, the opposing sample end is subjected to a prescribed displacement $\Delta x(t)$ in x-direction while the cross-section is held constant as well. $\Delta x(t)$

descibes a linear time-dependent length increase until reaching an engineering strain ε_{max} within the sample, a waiting period at constant position in order to allow for heat release, a linear time-dependent length decrease until reaching the initial sample length, and a second waiting period for heat absorption. The lateral faces of the sample are mechanically free. Decreasing of the cross-section with increasing sample length due to volume conservation is considered by the model based on the Poisson's ratio ν. Phase fraction is evaluated by ξ^{AM} during loading (i.e. increasing sample length) and by ξ^{MA} during unloading.

In order to start with a defined state in the sample at the beginning of unloading, the maximum strain ε_{max} is usually chosen in such a way that the martensitic phase fraction ξ^{AM} approaches 1 in the whole sample after the loading step. Simulation of pseudoelastic sub-loops is also possible with the model, but requires additional modifications introducing a phase fraction memory term. In this case, a field of the local phase fraction of all volume elements is saved in a text file at the end of the loading step. This phase fraction distribution is then re-loaded and treated as initial condition for the unloading step. The phenomenological model is only applied to the respective phase fraction that had transformed to martensite during loading, whereas the remaining austenite fraction is left unaffected by the model. Implementation is realized with COMSOL in combination with the Matlab live link.

The thermal boundary conditions at the sample ends ($x = 0$ and $x = l_0$) are held constant at $T = T_{amb}$. This condition (Dirichlet condition) assumes that the sample fixations act as infinite temperature reservoirs immediately compensating any temperature variations, which is a worst-case assumption in the context of elastocaloric cooling. The other extreme, the von Neumann conditions, would assume perfectly insulating interfaces at the sample ends. A convective heat transfer term is applied to the remaining, lengthwise sample faces:

$$\vec{n} \cdot (-\kappa \cdot \nabla T) = -h \cdot (T_{amb} - T) \tag{5.8}$$

where $\vec{n}$ is the normal vector of the surface, κ the thermal conductivity and h the heat transfer coefficient.

5.1.3 Model extension for description of localized behavior

In order to better reflect localized behavior (see discussion below) like Lüders-like strain bands and local interactions between martensitic and austenitic regions, a modification is performed on the model. The model parameters k^{AM} and k^{MA} are increased by an order of magnitude in order to make the transformation sharper and obtain sharp onsets of the pseudoelastic plateaus, which thus become virtually horizontal. The model adopts a bi-stable character, allowing only phase fractions equal to zero or one, except for a very narrow stress/temperature regime.
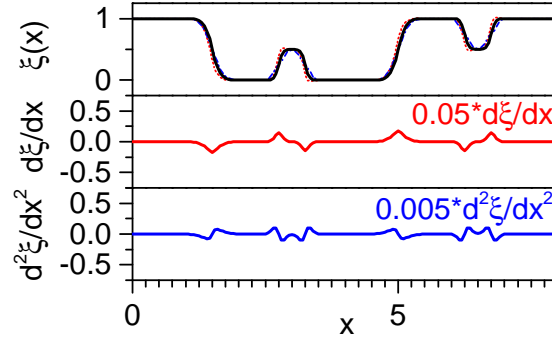
Figure 5.2: Hypothetical phase fraction profile as a function of longitudinal position x and corresponding first and second spatial derivatives. The sum of the black and the red, as well as the black and the blue curve are included as dashed lines in the upper plot.

This is closer to the experimentally observed Lüders-like behavior than the originial model described above, which allows all phase fractions between zero and one. Since the modification leads to numerical instabilities and periodic artefacts in finite element simulation, a gradient term is added to the differential formulation of the constitutive equation 5.2:

$$\frac{d\xi}{dt} = \frac{\partial \xi}{\partial \sigma^*} \cdot \frac{d\sigma^*}{dt} + \frac{\partial \xi}{\partial T} \cdot \frac{dT}{dt} + \beta_{int}\frac{d^2\xi}{d\vec{x}^2} \tag{5.9}$$

The gradient term is proportional to the second spatial derivative of the phase fraction and leads to a smoothing of interfaces between austenitic ($\xi = 0$) and martensitic regions ($\xi = 1$). Fig. 5.2 shows a hypothetical (one-dimensional) phase fraction profile, as well as the corresponding first and second derivative. A comparison for ascending and descending flanks of $\xi(x)$ shows that adding a first-derivative term would prefer the movement of phase interfaces in one particular direction (either to the left or to the right, depending on the sign of the gradient term). Adding a second-derivative, on the other hand, smoothes existing interfaces and annihilates regions with intermediate phase fractions (i.e. mixtures of austenite and martensite). In terms of physical interpretation, the gradient term represents the influence of already transformed regions on untransformed neighboring regions.

For practical reasons related to the COMSOL implementation, the function $f(x)$ is defined as the antiderivative of the Gaussian bell curve in this case instead of the exponential function (Equation 5.4). This modification does not influence the simulation results, which was verified using $\beta_{int} = 0$ and the same $k^{AM,MA}$ as in the previous section.
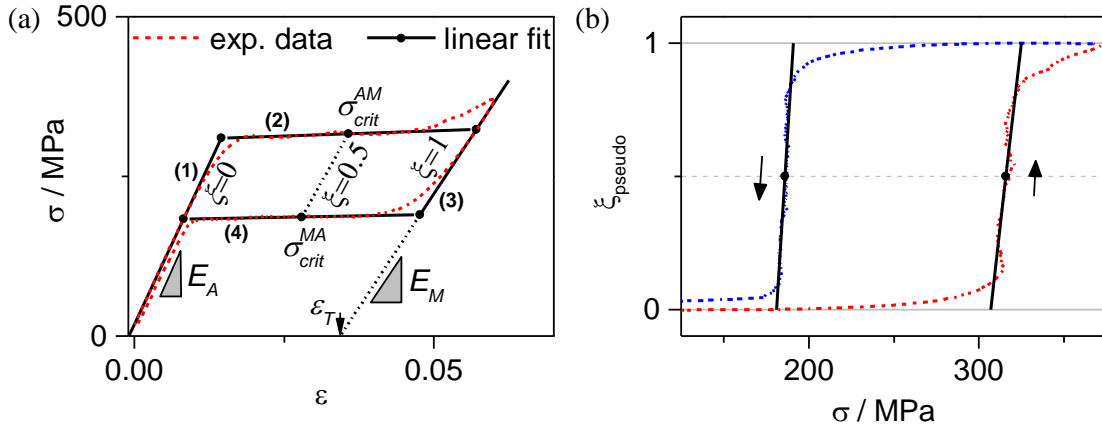
Figure 5.3: Determination of model parameters. (a) Approximation of experimental stress-strain curve by linear fits. (b) 'Pseudo phase fraction' estimated by applying the rule of mixture to experimental data.

5.2 Determination of parameters

The material parameters required by the model are determined from experimental data. For this purpose, the experimentally obtained stress-strain characteristic[2] is approximated by four straights, as indicated in Fig 5.3, in order to obtain the fit parameters s_{1-4} and E_{1-3}:

$$\sigma = s_1 + E_1 \cdot \varepsilon \tag{5.10a}$$

$$\sigma = s_2 + E_2 \cdot \varepsilon \tag{5.10b}$$

$$\sigma = s_3 + E_3 \cdot \varepsilon \tag{5.10c}$$

$$\sigma = s_4 + E_4 \cdot \varepsilon \tag{5.10d}$$

The first and third equation are interpreted as elastic loading of the sample in pure austenite ($\xi = 0$) and unloading in pure oriented martensite state ($\xi = 1$). Hence, the elastic moduli of austenite and martensite are directly obtained: $E_A = E_1$ and $E_M = E_3$. The transformation strain is given by the difference of both curves at zero stress:

$$\varepsilon_T = s_1/E_1 - s_3/E_3 \tag{5.11}$$

The pseudoelastic (forward and reverse) plateaus are approximated by the second and fourth linear equation, taking into account that the plateaus may have a certain inclination as well. According to the rule of mixture (equation 5.5), the

---

[2]Note that the experimental stress-strain curve considers the engineering strain and therefore represents a macroscopic information about the sample. The model, on the other hand, is formulated on a local scale. Therefore, it would be more precise to determine model parameters from local stress-strain characteristics obtained from digital image correlation.

model describes the mechanical state of the material as a linear superposition of the elastic austenite and martensite curve, weighted with the respective phase fractions. Hence, the center points of the two plateau lines represent states where the martensitic phase fraction is exactly one half. The critical stresses σ_{crit}^{AM} and σ_{crit}^{MA} are defined here as the stresses at these points. By determining the critical stresses for different ambient temperatures and applying linear fits to the $\sigma_{crit}(T)$-data, the Clausius Clapeyron coefficients and model parameters c^{AM} and c^{MA} are obtained (compare equation 5.3).

The state of equal martensite and austenite phase fraction is described by the step function (equation 5.4) in the case the argument equals zero: $f(0) = 0.5$. Based on the arguments in equations 5.1 and inserting the parameters $T = T_{amb}$, $c^{AM,MA}$ and $\sigma^* = \sigma_{crit}^{AM,MA}$, the phase transformation peak temperatures are calculated:

$$T_0^{AM} = T_{amb} - c^{AM} \cdot \sigma_{crit}^{AM} \tag{5.12a}$$

$$T_0^{MA} = T_{amb} - c^{MA} \cdot \sigma_{crit}^{MA} \tag{5.12b}$$

Model parameters k^{AM} and k^{MA} describe the temperature span of the phase transformation and also determine the inclination of the pseudoelastic plateaus. The plateaus are horizontal in the case of infinite values for k^{AM} and k^{MA}. In the more realistic case of a finite plateau slope, the parameters can be determined from experimental data by approximating a 'pseudo phase fraction'. For this purpose, the expression for the phase fraction (equation 5.1) is simplified by Taylor expansion of f around zero ($f(k \cdot x)|_{x \to 0} \approx 1/2 - (k/4) \cdot x$) and differentiated with respect to stress:

$$\left. \frac{d\xi}{d\sigma^*} \right|_{\xi \to \frac{1}{2}} \approx -k \cdot \frac{c}{4} \tag{5.13a}$$

$$k^{AM} = \frac{4}{c^{AM}} \cdot \frac{d\xi^{AM}}{d\sigma^*}, \quad k^{MA} = \frac{4}{c^{MA}} \cdot \frac{d\xi^{MA}}{d\sigma^*} \tag{5.13b}$$

For estimation of the phase fraction dependency on stress, a pseudo phase fraction is calculated from the experimental stress-strain curve by re-arranging the rule of mixture (equation 5.5):

$$\xi_{pseudo} = \frac{\sigma - s_1 - E_1 \cdot \varepsilon}{s_3 - s_1 + (E_3 - E_1)\varepsilon} \tag{5.14}$$

The resulting $\xi_{pseudo}(\sigma)$ is plotted against the stress (see Fig. 5.3 (b)) and used for calculation of $d\xi_{pseudo}/d\sigma$, as well as k^{AM} and k^{MA}.

The latent heat L is estimated from the experimentally observed adiabatic temperature change ΔT_{ad} during fast unloading and the heat capacity c_p determined by differential scanning calorimetry: $L = c_p \cdot \Delta T_{ad}$. In previous work, phase transformation temperatures and latent heat for modelling where obtained fom

differential scanning calorimetry as well [142]. However, in the present case the DSC values lead to poor agreement of simulated and experimental stress-strain characteristics and the elastocaloric effect size was overestimated. The discrepancy between latent heats estimated from tensile tests and DSC measurement was also discussed in the previous chapter. Therefore, the values for simulation are derived from tensile test and infrared data.

Since mass densities ρ, Poisson's rations ν and thermal conductivities κ could not be measured, literature values for binary NiTi are used here for the simulation of all materials. The heat transfer coefficient h is adjusted to obtain optimal agreement with experimental time constants for heat exchange. The selected value lies within the typical range of heat transfer coefficients for free air convection (compare Section 2.1.2).

5.3 Results and discussion

Table 5.1: Experimentally determined model parameters for selected samples (*literature value for NiTi, **literature value for NiTi in austenite phase [56], ***estimation). Identification numbers of samples are included to allow for comparison with Chapter 4.

Sample	TiNiFe foil	TiNi films				TiNiCuCo films	
	018-g	006-d new	006-d degr.	019-c new	019-c degr.	022-a	028-d
E_A / MPa	23.0	34.3	33.1	30.0	24.0	33.2	34.2
E_M / MPa	15.0	20.2	24.2	22.0	24.0	19.4	23.8
ε_T	0.034	0.0265	0.0226	0.035	0.024	0.00197	0.011
L / $\mathrm{J\,g^{-1}}$	9.0	7.2	7.2	7.2	7.2	5.0	3.0
c_p / $\mathrm{J\,g^{-1}\,K^{-1}}$	0.45	0.45	0.45	0.45	0.45	0.42	0.45
$d\sigma_c^{MA}/dT$ / $\mathrm{MPa\,K^{-1}}$	7.77	9.0	9.0	8.75	8.75	11.4	8.5
$d\sigma_c^{AM}/dT$ / $\mathrm{MPa\,K^{-1}}$	7.1	9.0	9.0	8.75	8.75	11.4	8.5
T_0^{MA} / K	272.4	251.4	255.9	268.9	275.0	264.4	281.32
T_0^{AM} / K	253.5	236.9	241.3	249.2	259.0	258.75	267.45
k^{MA}	2.0	0.6	0.15	4.5	0.2	0.73	4.5
k^{AM}	2.0	0.55	0.15	4.5	0.2	0.63	4.5
β_{int}				4e-6			4e-6
ρ / $\mathrm{kg\,m^{-3}}$				6500*			
ν				0.33*			
κ / $\mathrm{W\,cm^{-1}\,K^{-1}}$				0.18**			
h / $\mathrm{W\,m^{-2}\,K^{-1}}$				18***			

Following the routines described above, model parameters are determined for a

selection of foil and film samples. The parameters are summarized in Table 5.1. The simulated sample performance will be discussed in the following.

5.3.1 TiNiFe foils
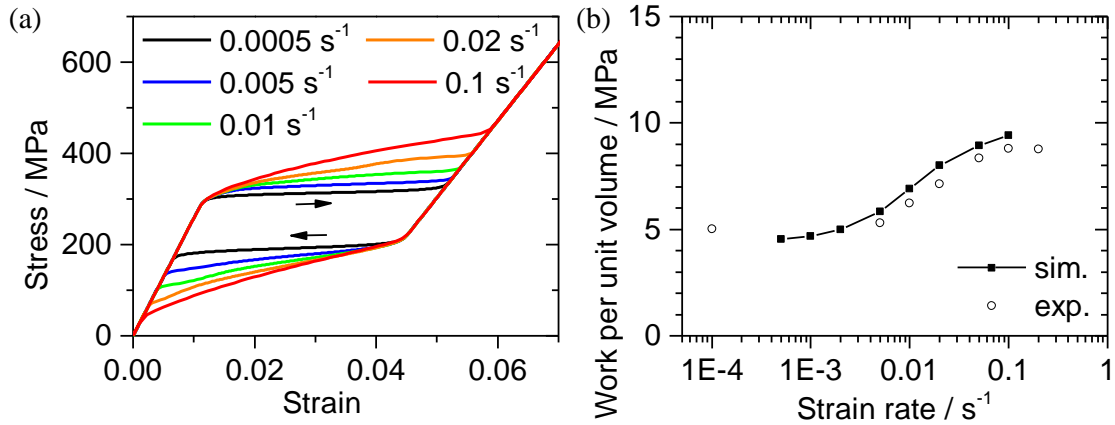
Figure 5.4: Simulated stress-strain characteristics (a) and work input ΔW (b) in dependence of strain rate for a cold-rolled TiNiFe foil sample (loaded in RD, $T_H = 500\,°C$). (Sample 018-g)

Mechanical performance. Simulation is performed for a TiNi foil sample annealed at $T_H = 500\,°C$ and loaded in rolling direction (RD). Fig. 5.4 (a) shows simulated stress-strain characteristics for different strain rates. Data is taken from the center of the simulated sample. Under quasi-static conditions ($d\varepsilon/dt = 0.0005s^{-1}$) the pseudoelastic plateaus of loading and unloading are almost horizontal. With increasing strain rate, both plateaus become steeper, until reaching their maximum slope in the adiabatic limit. As the comparison of experimental and simulated data in Fig. 5.4 (b) shows, the phenomenologic model also captures the effect of work input increase with increasing strain rate accurately. The simulated work input for the adiabatic limit is slightly higher than the experimentally determined value, because the maximum strain was higher in the simulation in order to guarantee $\xi = 1$ throughout the sample at the end of the loading step.

Elastocaloric performance. The temperature evolution $T(t)$ during loading and unloading, as well as the corresponding maximum temperature changes as a function of strain rate are shown in Fig. 5.5. Again, a comparison with experimental data shows good agreement for the peak temperatures during unloading. The peak temperatures during loading, however, are underestimated by simulation by about $4\,K$. The reason for this discrepancy is that for the cold-rolled TiNiFe foil samples, self-heating yields higher temperature changes than self-cooling. On the other hand, the model assumes an identical latent heat L to be
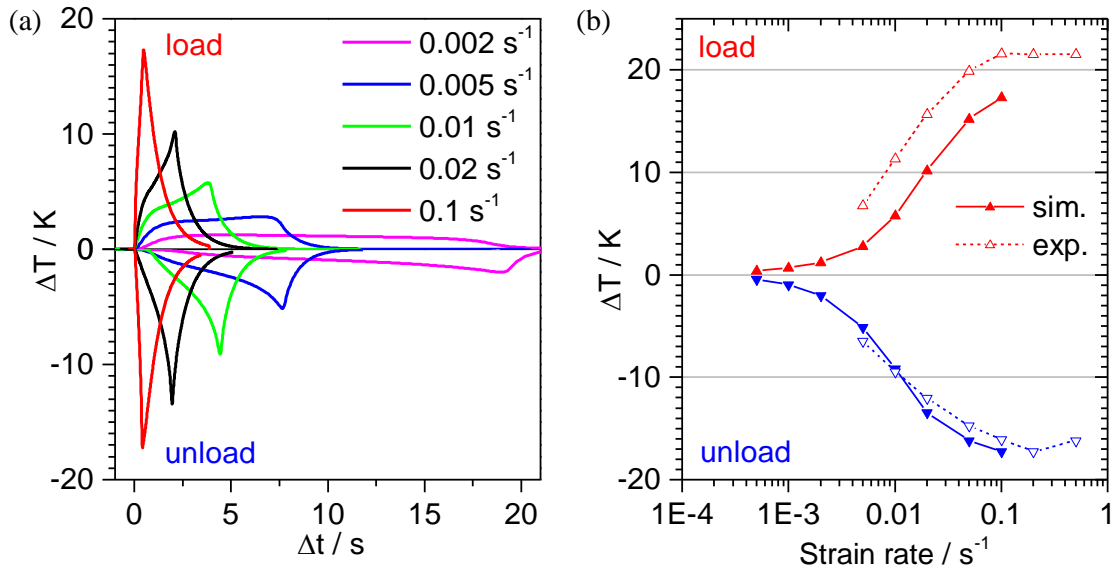
Figure 5.5: Simulated time-dependent temperature evolution (a) and maximum temperature changes during loading and unloading (b) as a function of strain rate for a cold-rolled TiNiFe foil sample (loaded in RD, $T_H = 500\,°C$). (Sample 018-g)

released during loading, as is absorbed during unloading in order to guarantee conservation of energy. Irreversible processes that could create additional heat, are not considered here.
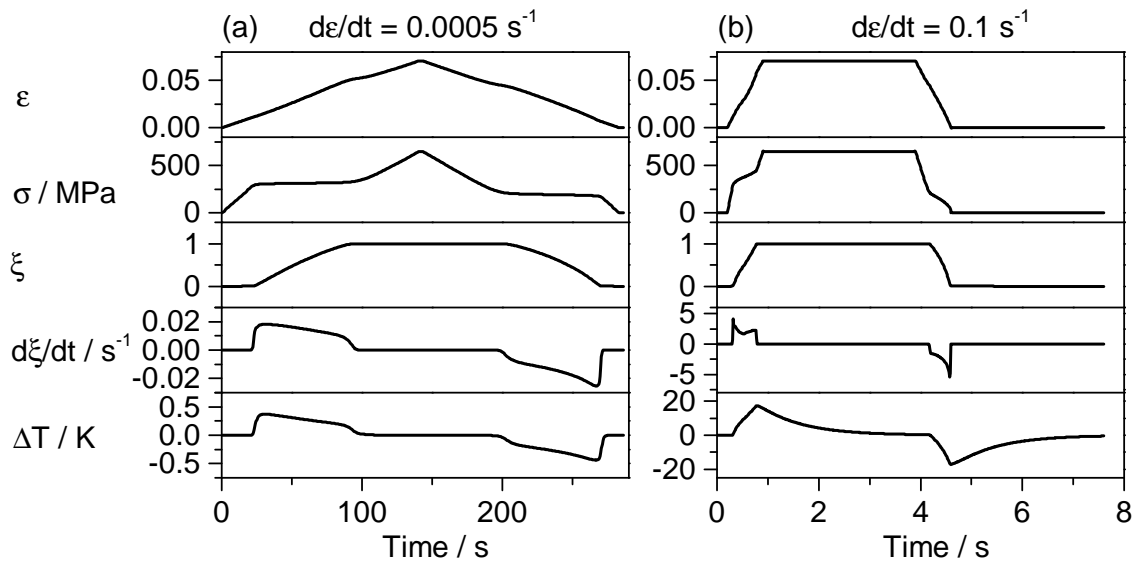
Figure 5.6: Simulation of local strain ε, stress σ, martensite phase fraction ξ and its time derivative $\dot{\xi}$, as well as temperature T as a function of time for a cold-rolled TiNiFe foil sample (loaded in RD, $T_H = 500\,°C$). The two different strain rates represent quasi-static (a) and adiabatic conditions (b). (Sample 018-g)

A comparison of the time-dependent temperature evolution reveals a clear asymmetry between pseudoelastic loading and unloading. The effect can be under-

stood by considering the time-dependent local variables strain, stress and phase fraction. These are depicted in Fig. 5.6 for a slow (quasi-static) and a fast (adiabatic) strain rate. Since the model predicts a rather homogeneous strain distribution in all sample regions not too close to the fixations, local strain essentialy follows the engineering strain prescribed by the mechanical boundary conditions, i.e. it increases and decreases linearly during loading and unloading, respectively. The stress shows typical plateaus corresponding to stress-induced martensite and reverse transformation. Accordingly, the martensite phase fraction ξ increases from 0 to 1 during the loading plateau and decreases from 1 to 0 during the unloading plateau. The time-dependence of the phase fraction is clearly non-linear. From the time derivative $\dot{\xi}$ it can be seen that during loading, the phase transformation rate starts at a high level and then slowly decreases, whereas during unloading it starts at a lower value and slowly increases with time. This asymmetry is caused by the different elastic moduli of austenite and martensite, $E_A > E_M$ in the present case. In the model, the phase fraction is controlled by stress (compare equation 5.1) whereas the simulated tensile experiment is strain-controlled, i.e. at a constant strain rate $d\varepsilon/dt$. Due to the higher elastic modulus E_A, the stress increase rate and thus the predicted phase transformation rate will be highest in the predominantly austenitic sample ($\xi \approx 0$) and decrease with increasing martensite fraction. The same argument applies to the unloading as well. Since the volume heat source Q_L is proportional to the change of phase fraction $\dot{\xi}$, the asymmetry directly affects the temperature evolution. Under quasi-static conditions, temperature changes are very small and closely follow the course of $\dot{\xi}$. In the adiabatic case, on the other hand, temperature increases/decreases until phase transformation is completed at the end of the stress plateaus. Self-heating is slightly decelerating in the course of loading, whereas self-cooling is accelerating during unloading.

The difference between E_A and E_M affects the asymmetry between heat release during forward and absorption during reverse transformation in a second way. The time interval for elastic loading in the austenite state and subsequently passing the A→M stress plateau is the same as the time interval for elastic unloading in the martensite state and passing the M→A plateau, since the strain rate is identical in both cases. However, the elastic unloading lasts longer than the elastic loading due to the lower elastic modulus of the martensite. Consequentially, the time for passing the unloading plateau is shorter than the that for the loading plateau and the latent heat is absorbed in a shorter time than it has been released before. At strain rates below the adiabatic limit, the maximum temperature change $|\Delta T|$ during unloading is higher than during loading, as can be seen in Fig. 5.5 (b). Note that heat conductivities of austenite and martensite are assumed to be the same by the model.

The temperature profiles show, however, certain deviations from experimentally observed profiles (compare experimental and simulated temperature curves, Fig. 4.9 (a) and Fig. 5.5 (a), respectively). These are caused by Lüders-like strain and temperature bands which are observed in the experiment, but not reflected by

the model, and lead to sudden local temperature increase or drop. This will be
further discussed below.
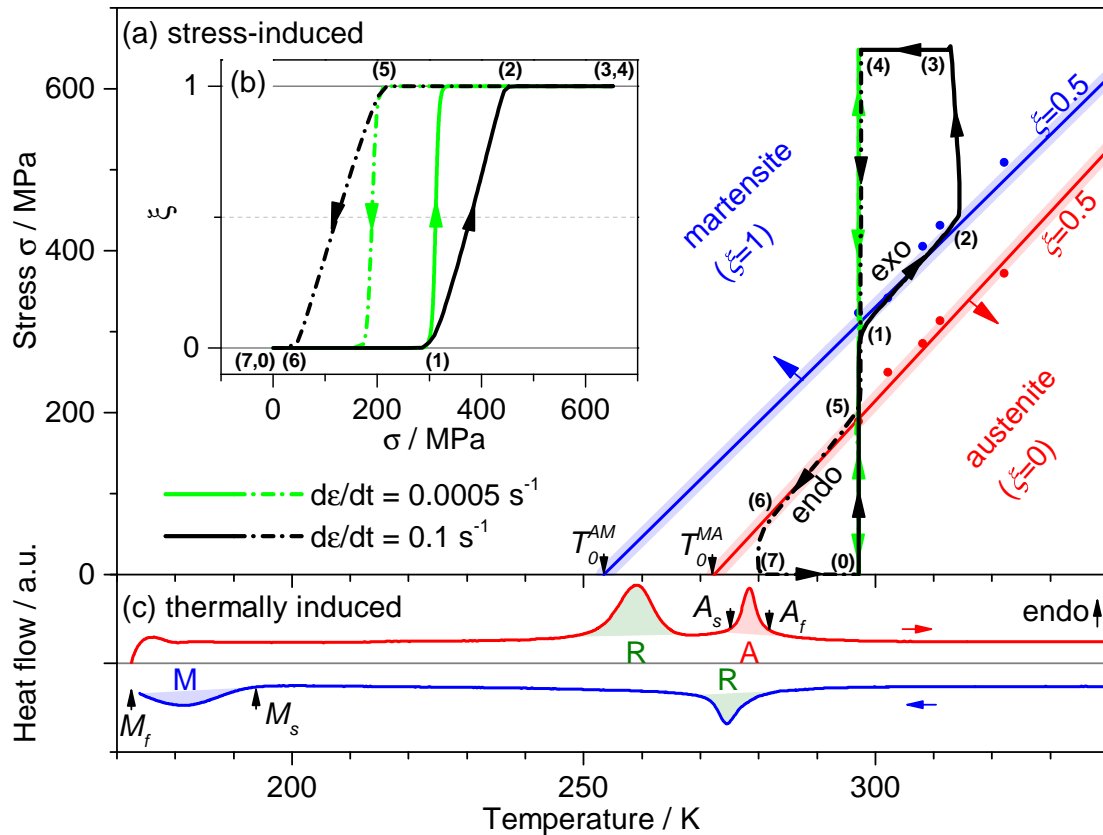
Figure 5.7: Comparison of stress-induced and thermally induced phase transformation. (a) Tanaka-type phase diagram of cold-rolled TiNiFe sample annealed at $T_H = 500\,°C$ assuming a one-step transformation between austenite and martensite (compare Fig. 2.16 (a)). Center lines ($\xi = 0.5$) of the phase transformation regions are indicated by solid red and blue lines. Simulated transformation paths of a sample loaded at two different rates are shown. (b) Martensitic phase fraction during loading and unloading. (c) Experimental DSC curve including phase transformation temperatures, indicating that the transformation is actually two-step. Extrapolated transformation temperatures at zero stress T_0^{AM} and T_0^{MA} (a) do not agree with the peak temperatures observed by DSC (c), indicating that the linear Clausius-Clapeyron relation does not hold in the regime of low stresses (compare Fig. 2.11). (Sample 018-g)

Stress-induced vs. thermal phase transformation. Finally, the course of stress-induced phase transformation shall be discussed and compared with thermally induced phase transformation. Fig. 5.7 (a) shows a Tanaka-type phase diagram (in the stress-temperature plane) of the TiNiFe foil sample. The phase transformation regions are indicated by their center lines in red (M→A) and blue (A→M). These lines represent states with phase fraction $\xi = 0.5$ and are deter-

mined by the experimental temperature-dependent critical stresses (indicated by bullets). In between both lines lies the region of coexisting phases, in which the sample may be either martensitic or austenitic, depending on mechanical history. The trajectories of two simulated tensile experiments are indicated, the corresponding evolution of phase fraction is shown in the inset (b). At the rather low strain rate close to quasi-static conditions (green curve), the trajectory is essentially vertical, since self-heating and cooling are negligible. In the case of a high strain rate (black curve), the sample starts in a stress-free state (0) and stays at ambient temperature upon stress-increase, until approaching the martensitic transformation region (blue line) (1). While crossing this region ((1)→(2)), the phase fraction increases from 0 to 1 and the sample heats up. The width of the transformation region is determined by the model parameter k^{AM}. Loading is continued until point (3), followed by a waiting period until point (4) during which the sample releases heat and cools down to room temperature again. During subsequent unloading, the sample stays at ambient temperature until approaching the reverse transformation region (red line) (5). While crossing the region, the sample temperature drops due to self-cooling, until reaching a fully austenitic state again (6). The sample is unloaded until fully stress-free (7) and reaches the initial state again after temperature equalization. A comparison of the phase diagram with an experimental DSC curve (Fig. 5.7 (c)) reveals considerable differences between the transformation temperatures T_0^{AM} and T_0^{MA} of the phenomenological model and the corresponding thermal phase transformation temperatures $(M_s + M_f)/2$ and $(A_s + A_f)/2$. Whilst $A_{s,f}$ are slightly higher than T_0^{MA}, $M_{s,f}$ are more than $70\,°C$ below T_0^{AM}. This finding indicates that the assumpion of a linear dependence of critical stresses on temperature, on which the model is based, does not hold for the whole stress range. This is also shown by experimental data of Churchill et al., see Fig. 2.11. In addition, the intermediate R-phase transformation is neglected by the model. At low stress, considerable non-linearity is required to establish consistency between stress-induced and thermally induced phase transformation data. Hence the model should only be applied to samples at ambient temperatures well above the A_f temperature.

5.3.2 TiNiCuCo and TiNi films

TiNiCuCo films. In the previous section it was shown that the phenomenological model successfully describes the dynamics of heat release/absorbtion and exchange with the environment, but does not capture the effect of Lüders-like band formation. In the following, the model is applied to a sputter-deposited TiNiCuCo film sample that does not reveal any strain or temperature bands even in the as-produced state. As Fig. 5.8 (a) shows, the experimental stress-strain characteristic can be approximated accurately. The steeper stress plateaus of the sample are reproduced in simulation by selecting low values for the fit parameters k^{AM} and k^{MA}. The increase of work input with increasing strain rate is reproduced very accurately (Fig. 5.8 (b)).
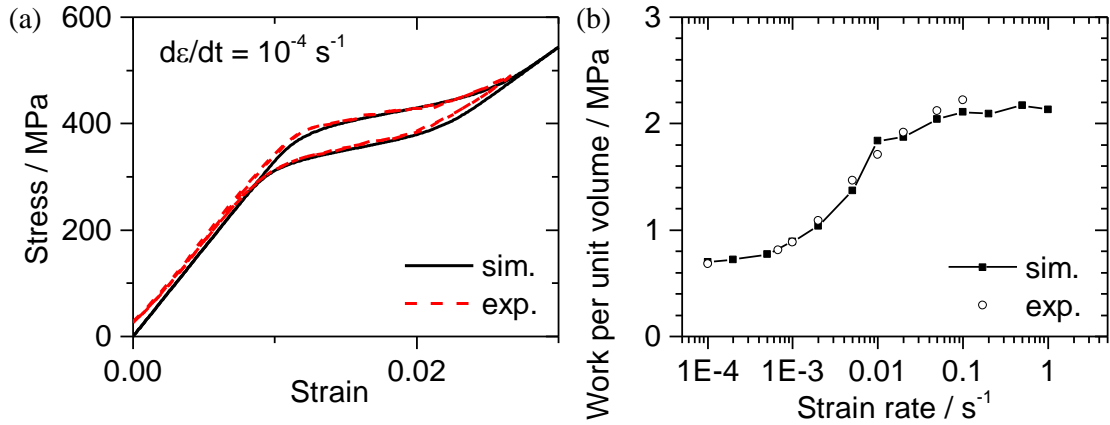
Figure 5.8: Experimental and simulated stress-strain characteristic (a) and work input ΔW (b) as a function of strain rate for a sputter-deposited TiNiCuCo film sample. (Sample 022-a)
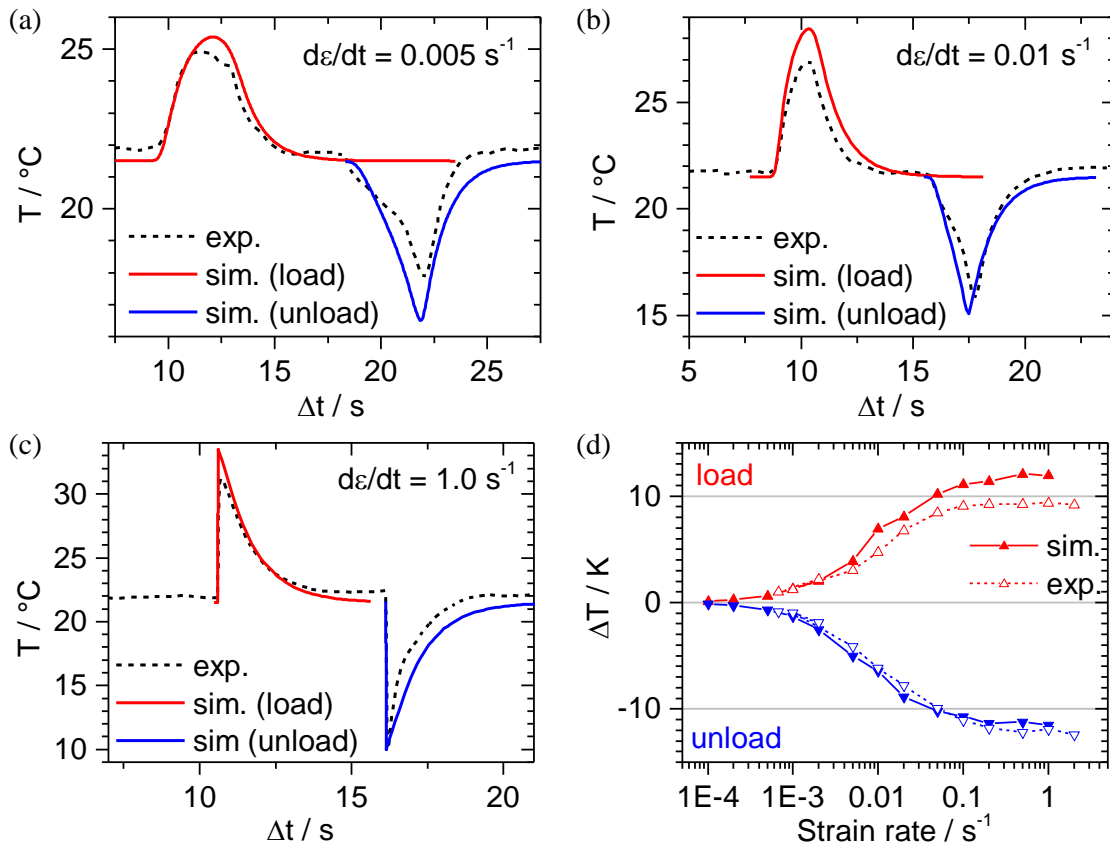
Figure 5.9: Simulated time-dependent temperature evolution (a-c) and maximum temperature changes during loading and unloading (d) as a function of strain rate for a sputter-deposited TiNiCuCo film sample. (The time axis of the simulated profiles has been shifted for optimal coincidence with experimental data). (Sample 022-a)

The corresponding maximum temperature changes shown in 5.9 (d) are in very close agreement with experimental data as well in the case of loading. The self-heating during loading is somewhat overestimated, since the experimentally observed self-heating effect is lower than the self-cooling effect (which is not yet fully understood). In Figs. 5.9 (a-c) the experimental and simulated temperature evolution is compared for three different strain rates. In all three cases, the shape of the profiles and the asymmetry between loading and unloading is captured well by the model. Hence, in this case where neither experiment nor simulation reveal localized temperature bands during tensile loading and unloading of the sample, the model accurately describes the temperature evolution in the sample and its effect on the stress-strain characteristic.
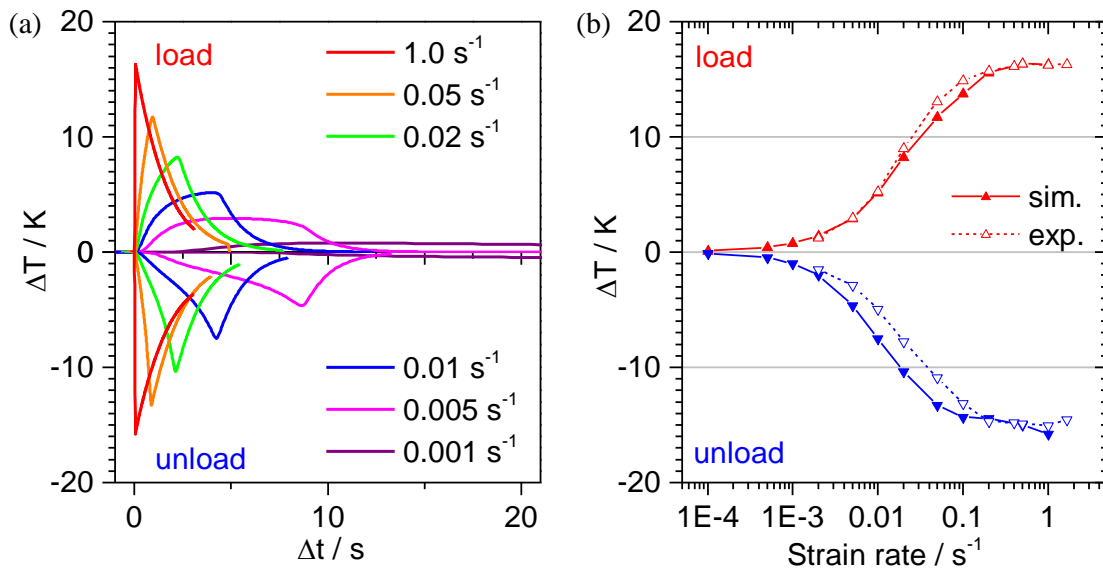
Figure 5.10: Simulated time-dependent temperature evolution (a) and maximum temperature changes during loading and unloading (b) as a function of strain rate for a sputter-deposited TiNi film sample in the degraded state. Compare Ref. [299]. (Sample 006-d)

Trained TiNi films. For comparison, the temperature evolution is also simulated for a TiNi film sample in the degraded state, hence not showing localized bands – compare Fig. 4.22 in the previous chapter. As the results in Fig. 5.10 show, reasonable agreement between experimental and simulated data is achieved. Though, the increase of temperature drop with increasing strain rate is predicted by the model at slightly lower strain rates than actually observed in the experiment. Since self-heating and cooling are almost identical in this case, both – self heating and cooling – are predicted correctly.

As-fabricated TiNi films – localized effects. As has been demonstrated in detail in Section 4.2.1, as-fabricated TiNi films show pronounced localized effects
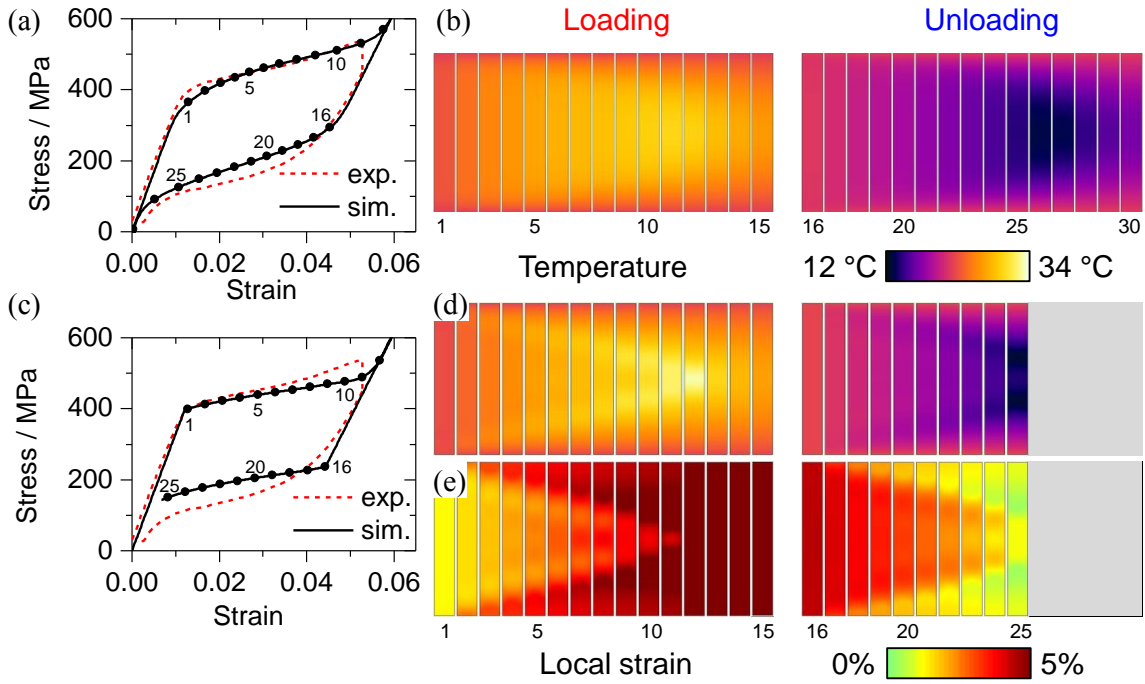
Figure 5.11: Stress-strain characteristic and spatially resolved temperature evolution of a TiNi film sample loaded and unloaded at a strain rate of $0.02\,\text{s}^{-1}$, simulated with the base model (a,b) and the model extended by a gradient term (c,d). In the latter case, the strain distribution (e) reveals the formation of strain bands starting close to the fixations. Stress and strain values corresponding to the temperature profiles on the right are marked by numbered bullets in the stress-strain characteristics on the left. Compare Ref. [299]. (Sample 019-c)

including temperature bands. In order to reproduce these effects, a modifiction is performed on the phenomenological model, as described in section 5.1.3. Stress-strain characteristics and corresponding spatially resolved temperature maps obtained with the original and the extended model are shown in 5.11 (a,b). The base model predicts a rather homogeneous temperature distribution (Fig. 5.11 (a)). Due to heat conduction through the clamping, highest temperature changes occur in the sample center. Unlike in the experiments, no temperature bands are found. In the extended model, the parameters k^{AM} and k^{MA} are increased from 0.45 to 4.5 and a gradient term with the weighting $\beta_{int} = 4 \cdot 10^{-6}$ is introduced. In this case, simulation predicts two hot temperature bands during loading, each forming at one of the two clampings and then propagating inwards. The highest temperature is reached when both bands unite in the sample center. During unloading, the same observation is made with two cold temperature bands, again initiating at the clampings. Corresponding strain bands are observed in the strain maps. This can be explained by the additional stress at the clamping, introduced by the mechanical boundary conditions, and the thermal Dirichlet conditions. In the experiment, these conditions are realized by the SMA samples being sandwiched between two alumina plates and fixed by a two-component adhesive.

A striking deviation between simulated and experimental sample behavior is found concerning the band propagation during unloading. In the experiment, bands tend to follow roughly the reverse course with respect to loading. The effect is associated with phase interfaces that are still present after loading and act as nucleation centers of the reverse transformation. The model, on the other hand, does not contain memory terms, therefore the nucleation sites are determined solely by the thermal and mechanical boundary conditions. The observation of bands starting at the sample fixation during both, loading and unloading, is made in an experiment on a cold-rolled TiNiFe foil which is loaded until well beyound the forward stress plateau, as can be seen in Fig. 4.11.

5.4 Conclusion

A phenomenological model based on the work of Tanaka [138] was modified to include the elastocaloric effect and applied here for the simulation of thin TiNi-based film and foil samples. A straightforward routine for obtaining the required model parameters from experimental data is presented. The parameters are mainly based on stress-strain characteristics obtained from tensile tests. Therefore, it is possible to accurately reproduce experimental stress-strain curves. By proper adjustment of the parameters, the model is adapted to different shapes of stress-strain characteristics with nearly horizontal as well as inclined stress plateaus. The sharpness of the plateau onset is however coupled to the inclination and may not be adjusted separately. Steeper plateaus automatically have softer/ more rounded onsets.

In addition to mechanical data, experimentally determined heat capacities and adiabatic temperature changes measured by infrared thermography are considered in order to describe heat release and absorption due to stress-induced martensitic and reverse transformation. Thus, temperature changes are closely reproduced, provided that ΔT_{load} and ΔT_{unload} are roughly equal.

In contrast to earlier implementations [142], characteristics of the thermally induced phase transformation obtained by DSC like latent heat L and phase transformation temperatures A_s, A_f, M_s and M_f do not enter the model.

Based on these parameters, the strain-rate and ambient temperature-dependence of the thermo-mechanical sample behavior, including the increase of plateau slopes as well as saturation of work input and temperature changes in the adiabatic limit, is predicted by the model in accordance with experimental observations. Thermal coupling with the environment is considered by conduction through the clampings as well as convection acting on the open sample surface. A comparison of experimental and simulated data as a function of strain rate shows that the balance between heat release/absorption on the one hand and heat exchange with the environment on the other is described correctly.

The temperature evolution (of an exemplary test area in the sample center) shows characteristic asymmetries between loading and unloading, which are explained by the different elastic moduli of martensite and austenite phase. During loading, the rate of heat release is highest in the beginning and then decreases with increasing strain (and martensite phase fraction). During unloading, heat absorption begins at a lower rate and then increases. Also, the duration is shorter than that of heat release.

Since the base model produces rather smooth distributions of strain, phase fraction and temperature change, it is not capable of reproducing Lüders-like strain and temperature bands. Correspondingly, results are most accurate for samples that do not show these localized effects in reality.

In order to include localized effects, a modification is performed in the base model by introducing a gradient term proportional to the second spatial derivative of the phase fraction. With this modification, the formation of two thermal bands starting from the clamping is predicted, as it is indeed observed in experiments for low strain rates. The pronounced increase in band number at higher strain rates, the interface sharpness and orientation of the bands is however not captured by the model in its current form. In the case of high strain rates above the adiabatic limit, the number of thermal bands observed in experiments is so high that the sample temperature homogenizes in a very short time due to heat conduction. In this case, the model without gradient term extension seems to be an appropriate approximation.

In conclusion, the phenomenological model is a valuable tool for predicting the performance of samples for elastocaloric microcooling under various conditions. Furthermore, it grants access to the martensitic phase fraction which cannot be measured in simple tensile test experiments and provides an important contribution to a deeper understanding of the mechanisms of heat absorption, release and exchange with the environment.

(a) Experiment

(b) Phase field model

loading   unloading
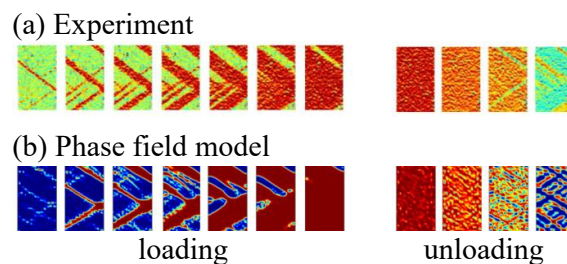
Figure 5.12: (a) Chronological series of strain profiles of a TiNiCuCo sample during tensile test at a strain rate of $0.02\,\mathrm{s}^{-1}$ (red = martensite, green = austenite). (b) Very similar strain patterns are reproduced by a 2D phase field model implemented by Frank Wendler (strain rate $0.01\,\mathrm{s}^{-1}$, red = martensite, blue = austenite). Modified from Ref. [304].

For the understanding of detailed band formation and propagation mechanisms as well as number of bands as a function of strain rate, other models seem to

be more appropriate than the simple Tanaka-type model. Band formation was described in a one-dimensional approximation by phase field models [150–153] and Seelecke-Müller-Achenbach models (*Seelecke et al., in preparation*). In recent work at the Karlsruhe Institute of Technology, Frank Wendler combined these approaches and included stochastic spatial variations of critical stresses in order to represent material inhomogeneities (Ref. [304], *submitted*). The model was implemented in 2D and 3D and is able to predict band number, band angle and cyclic reproducibility (history effect) of strain and temperature bands. Fig. 5.12 shows the striking similarity between experimentally observed and simulated strain bands in a TiNiCuCo film sample.

6 Demonstrator development

In chapter 4, the elastocaloric effect was studied in a number of materials by uni-axial tensile tests, from which important information about the elastocaloric temperature change, work input and time constants was obtained. However, since the surrounding air acts as heat sink as well as heat source in this type of experiment, no actual heat pumping is performed. The aim of the present chapter is to implement the principle of elastocaloric cooling and heat pumping in a real device on a miniature scale. In the first section, a design concept is developed, targeting the challenges of heat transfer and mechanical loading in small dimensions. Subsequently the dimensioning, fabrication and experimental characterization of first-of-its-kind demonstrators is described, supported by simple models for mechanical and thermal performance. Finally, results are discussed and alternative concepts for elastocaloric microcooling are introduced.

6.1 Device concept

In a general heat pumping device, heat is actively transported from a reservoir at low temperature level T_{cold} ('heat source') to a second reservoir at elevated temperature level $T_{hot} > T_{cold}$ ('heat sink'), which are both separated from each other. Depending on which one of the reservoirs shall be temperature-controlled, the device is operated as cooling device or heat pump. Energy has to be introduced in order to drive the process, since heat spontaneously only flows from hot to cold reservoirs in a closed system according to the second law of thermodynamics. In the following, a concept for heat transfer and mechanical loading of elastocaloric materials with flat geometry is developed for elastocaloric microcooling.

6.1.1 Thermal coupling: Solid-to-solid heat transfer

Elastocaloric SMA materials are solid, hence elastocaloric cooling (/heat pumping) is considered to be a solid-state cooling technology. Generally, the heat sources and sinks can either be solid, liquid or gaseous. Although a gas flow serving as heat transfer medium is discussed in literature, e.g., for air conditioning applications (compare Fig. 3.8 on page 64), this approach seems rather inappropriate for miniature-scale applications due to the low heat capacity of gases. Liquids, on the other hand, are well suited for heat transfer in microcooling and

find application, e.g., in passive elements like heat pipes and micro heat exchangers. However, the integration of microfluidic components like pumps and valves increases system complexity. Therefore, an approach of heat transfer by conduction between the SMA and solid heat sources and sinks is selected in this work, because it allows for simple and effective device concepts.

The performance of the solid-to-solid concepts depends on the thermal mass (i.e. heat capacity) of heat source and sink. Sources/sinks with lower thermal mass (with respect to the active elastocaloric material) can be cooled/heated more rapidly, but they also have a higher surface-to-volume ratio, leading to higher parasitic heat flows. In the limiting case of infinite thermal mass, on the other hand, heat transfer is most effective but the temperature change over time is zero. Hence, the choice of source and sink mass is a trade-off and has to be adapted to the intended application. For cooling applications, the heat sink should have a much higher thermal mass than the source.

The contact resistance plays a crucial role in solid-to-solid heat transfer by conduction. It depends on the roughness of the surfaces in contact, the contact area and contact force. Therefore, a high surface quality and perfect alignment of the surfaces is required. Contact resistance may be reduced by introduction of thermally conductive interface layers [15, 18, 305]. However, it has been shown that these layers introduce additional interfaces, again increasing complexity and affecting contact resistance [16, 17].

6.1.2 Mechanical handling: Bridge concepts
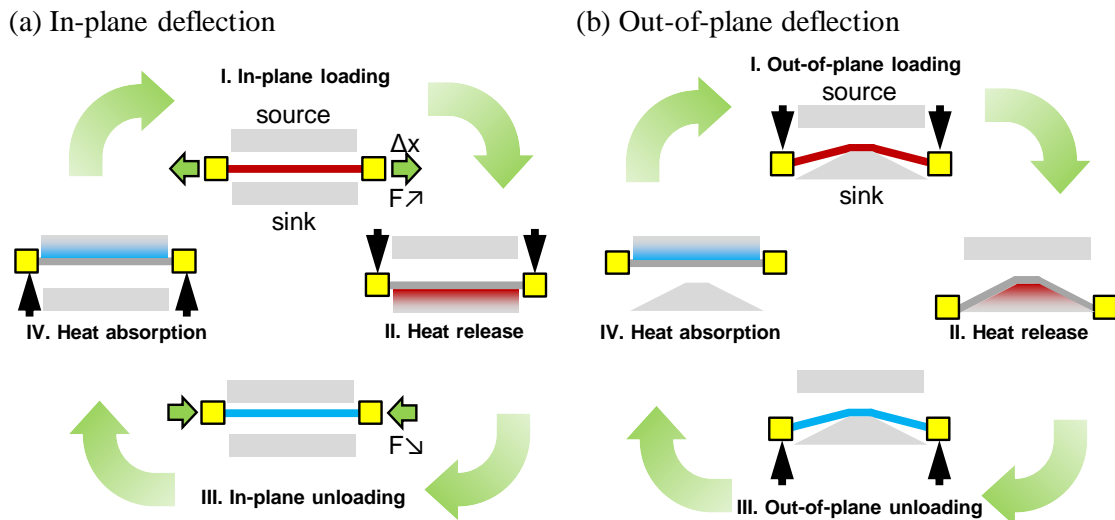
Figure 6.1: Schematic of elastocaloric microcooling devices based on (a) in-plane and (b) out-of-plane deflection of a single SMA bridge.

An obvious way of transferring heat between two solid bodies is to bring these bodies into physical contact to each other in order to allow for heat conduction.

This approach is particularly promising for thin sample geometries like foils and films, since they provide a very large surface for heat transfer, compared to their volume. Elastocaloric heat pumping based on solid-to-solid heat transfer can be achieved by modified uniaxial tensile loading, as shown in Fig. 6.1 (a). Between the loading step (I.) and the unloading step (III.), a heat transfer step (II.) is introduced, where a solid heat sink is brought into contact to the elastocaloric foil to absorb heat released by the A→M transformation. (This step has been achieved by air convection in the previous experiments, compare Chapter 4). Correspondingly, a second heat transfer step (IV.) is introduced in between unloading and loading step, during which a solid heat source is brought into contact to the foil after M→A transformation for heat absorption. The concept requires an actuator for loading and unloading of the SMA sample and a second actuator for switching between heat source and sink. It can be regarded as a most simple form of a heat switch. A meso-scale demonstrator following this approach has been built by Schmidt et al. [288].

A significant simplification of the solid-to-solid concept is introduced by switching from in-plane to out-of-plane deflection of the SMA element. The modified concept is based on freestanding SMA film or foil bridges attached to a support frame on both ends.[1] Stress-induced phase transformation is obtained by applying a force in the bridge center in normal direction to the bridge plane, deflecting it in out-of-plane direction. Due to the thin geometry, the occuring bending forces are small enough to be neglected. In the concept depicted in Fig. 6.1 (b), the SMA bridge is pressed against the convex surface of a heat sink during the loading step (I.). The released latent heat is directly transferred to the sink (II.), hence loading and heat transfer step are combined. After a sufficient time for heat transfer, the bridge is rapidly removed from the convex surface and thereby unloaded leading to self-cooling (III.). The cold bridge is then brought into contact to the flat surface of the heat source, from which it absorbs heat (IV.). This single-bridge layout relies on a single actuator for loading/unloading and thermal contact switching.

The schematic force-displacement characteristics of a thin pseudoelastic sample loaded in in-plane and out-of-plane direction are shown in Fig. 6.2. The same sample geometry and stress-strain behavior are assumed in both cases. Elastic moduli and transformation strain represent typical values for cold-rolled TiNiFe foils. The forces and displacements are referred to the driving actuator. In the case of out-of-plane loading, the strain within each half-bridge of length l_0, deflected by Δh, is given by:

$$\varepsilon = \sqrt{1 + (\Delta h/l_0)^2} - 1 \tag{6.1}$$

---

[1]This layout is inspired by microtechnology-compatible actuation concepts for SMA micro valves, in which a number of intersecting SMA bridges is used to open and close a fluidic channel by out-of-plane deflection [296]. By combining two SMA valve actuators to form an antagonistic pair, bistable valves and switches are realized [306, 307].

Inverting the equation, the deflection neccessary to apply the strain ε may be calculated by:

$$\Delta h(\varepsilon) = l_0 \cdot \sqrt{(1 + \varepsilon)^2 - 1} \qquad (6.2)$$

The out-of-plane force F_x, depending on the in-plane force F and the deflection angle α, is given by

$$F_x = F \cdot \sin(\alpha) = F \cdot \frac{\Delta h}{\sqrt{l_0^2 + \Delta h^2}} \qquad (6.3)$$

The intervals of elastic loading/unloading adopt the shape of parabolic branches and the stress plateaus (which are horizontal for in-plane loading) become linearly increasing. The mechanical work required for stress-induced transformation of the SMA bridge is given by the area under the loading trajectory of the device. This work has to be introduced by the external driving actuator. During unloading, the device can be regarded as a loaded spring that can in principle perform mechanical work by itself. The unloading work is marked by the shaded areas in Fig. 6.2 (b). Only the difference between both areas (colored areas in Fig. 6.2 (b)) is consumed by the heat pumping process. The loading and unloading work are identical for in-plane and out-of-plane loading. However, the forces are reduced whereas the displacements (or amplitudes) are increased in the latter case, leading to different requirements on the driving actuator.
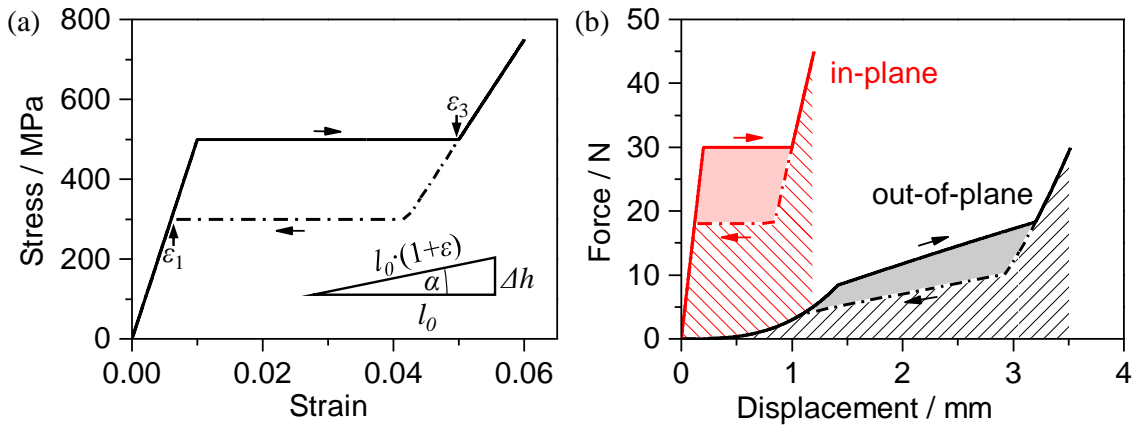
Figure 6.2: (a) Schematic stress-strain characteristic of a pseudoelastic material. (b) Corresponding simulated force-displacement curves for a sample loaded in-plane by a force in longitudinal direction (red curve) and out-of-plane by applying a perpendicular force in the sample center (black curve) for a sample geometry of $20 \times 2 \times 0.03\,\mathrm{mm}^3$.

(a) Application of pre-strain

(b) Device operation

(c) Force-displacement – individual bridges

(d) Force-displacement – coupled bridges
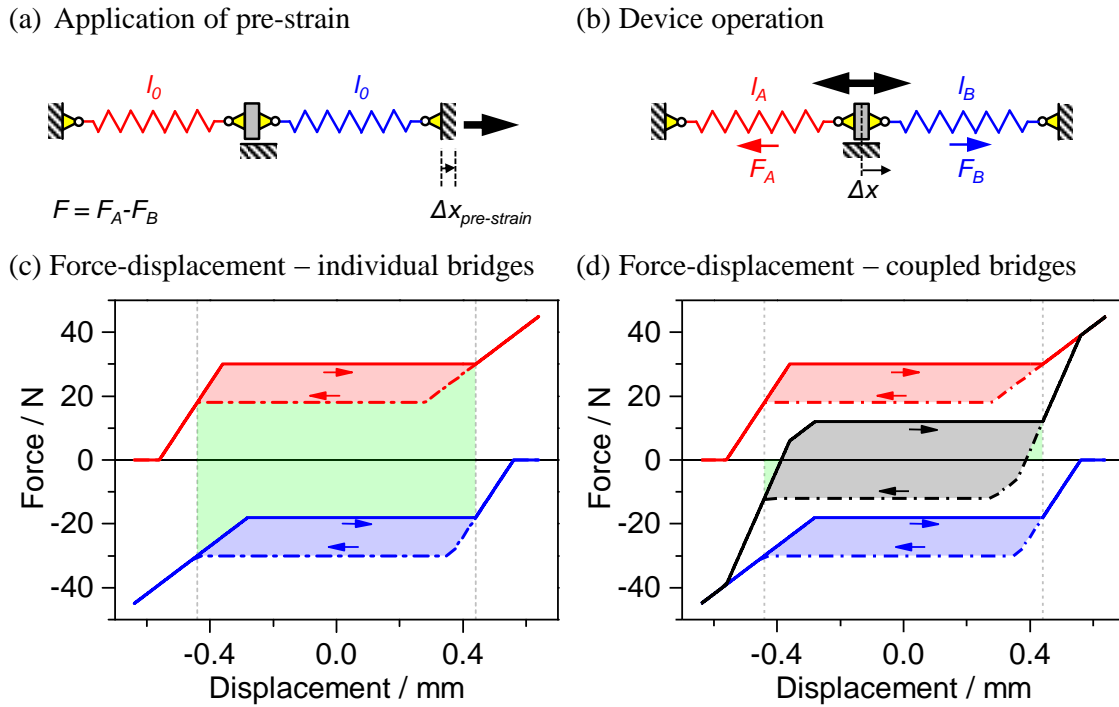
Figure 6.3: Antagonistic device obtained by coupling of two single bridge devices for in-plane deflection. Mechanical equivalent circuits are shown (a) for pre-straining and (b) device operation. (c) Simulated force-displacement characteristics of two individual bridges (red and blue) as well as (d) resulting characteristic of coupled device (black), assuming a bridge length of $l_0 = 20\,\mathrm{mm}$ and cross-section of $2 \times 0.03\,\mathrm{mm}^2$. Recoverable work is indicated in green.

6.1.3 Mechanical handling: Antagonistic concepts

For the coefficient of performance of the heat pumping devices, work input is of equal importance as the elastocaloric heat pumping power. Therefore, intelligent concepts of force application are required in order to obtain optimal performance. One might, e.g., consider integrating a piezoelectric or electromagnetic generator in the device for converting the unloading work into electricity. However, a large fraction of the unloading work may be utilized in a much simpler fashion by intelligently coupling the SMA element to a second, counteracting SMA element. In this case, both bridges form an antagonistic pair and mechanical work is transferred between both elements during the operation cycle – the work required from external actuation is greatly reduced. Coupling is achieved, for instance, by connecting two single bridge devices along length direction and deflecting them in-plane (Fig. 6.3), or by connecting the devices by a perpendicular spacer in the center and deflecting them out-of-plane (Fig. 6.4).

In Figs. 6.3 and 6.4, schematic force-displacement characteristics of two individual SMA devices ((c), red and blue), as well as the resulting characteristic of the coupled device ((d), black) are shown. Quasi-static operation without self-

(a) Application of pre-strain

(b) Device operation

(c) Force-displacement – individual bridges

(d) Force-displacement – coupled bridges
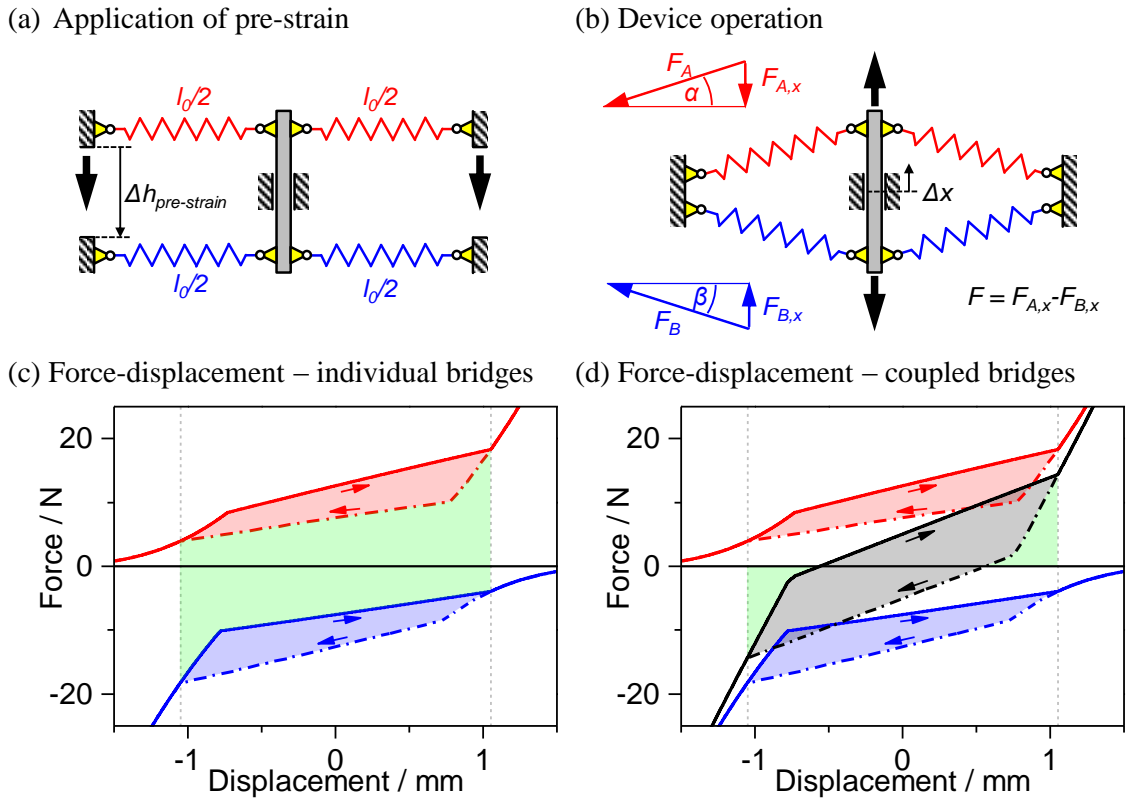
Figure 6.4: Antagonistic device obtained by coupling of two single bridge devices for out-of-plane-plane deflection. Mechanical equivalent circuits are shown (a) for pre-straining and (b) device operation. (c) Simulated force-displacement characteristics of two individual bridges (red and blue) as well as (d) resulting characteristic of coupled device (black), assuming a bridge length of $l_0 = 20\,\text{mm}$ and cross-section of $2 \times 0.03\,\text{mm}^2$. Recoverable work is indicated in green.

heating and -cooling effects is assumed. The dissipated work is indicated by red, blue and grey shading, respectively. The work that may in principle be recovered during unloading is marked in green. In order to take the maximum advantage from the antagonistic principle, the bridges are pre-strained with respect to each other in such a way that the starting ($\varepsilon = \varepsilon_1$, compare Fig. 6.2) and end points ($\varepsilon = \varepsilon_3$) of both pseudoelastic loops coincide (see dashed vertical lines).[2] For in-plane operation, the optimum pre-deflection is

$$\Delta x_{prestrain} = l_0 \cdot (\varepsilon_1 + \varepsilon_3) \tag{6.4}$$

---

[2]It should be remarked that in the case of in-plane coupling, the device is in an undefined condition during application of pre-strain. Both coupled bridges reach the forward stress plateau after initial elastic loading, and since the forces are equal and displacement-independent in the plateau region, it is not defined which fraction of the pre-strain each bridge experiences. However, in the case of out-of-plane coupling the pre-strain is distributed symmetrically between both bridges due to the finite slope of the loading/unloading plateaus.

For out-of-plane operation, the optimum spacer heigh is calculated using equation 6.2:

$$\Delta h_{prestrain} = \Delta h(\varepsilon_1) + \Delta h(\varepsilon_3) \tag{6.5}$$

By applying the optimum pre-strain, the two pseudoelastic loops of both bridges coincide to a single loop for the coupling element in between the bridges and the deflection amplitude $\Delta x_{min} - \Delta x_{max}$ is the same as for each single bridge device. The work input ΔW for a full operation cycle of the coupled device is exactly twice the work input for each single device. Furthermore, the work input for in-plane and out-of-plane loading is identical. However, loading and unloading work are greatly reduced in the coupled devices. This shall be discussed now with the help of numerical examples. In the above diagrams (Figs. 6.3 and 6.4 (c)), the loading work W_{load} for both devices together is $0.0518\,\mathrm{N\,m}$ and the dissipated work ΔW is $0.018\,24\,\mathrm{N\,m}$. Hence, the work input performed by the actuator accounts for 284% of the required minimum ΔW, or in other words, about two third of the work could have been recovered. The work input for the in-plane coupled device (6.3 (d)), on the other hand, is reduced to $0.018\,56\,\mathrm{N\,m}$ which is only 1.8% more than the dissipated work ΔW. In the out-of-plane coupled device (6.4 (d)), the ratio is slightly less favorable for geometric reasons: the work input for the coupled device is $0.019\,87\,\mathrm{N\,m}$, which is about 10% more than ΔW.

In conclusion, the proposed antagonistic concepts are not capable of recovering the full unloading work $W_{unload} = W_{load} - \Delta W$, but a great fraction of it, so that additional measures for work recovery, like eletromagnetic generators, may be omitted without a pronounced loss in coefficient of performance. A second advantage of the antagonistic concepts is that the maximum forces of the driving actuator are reduced. In case of in-plane coupling, the maximum force is equal to the force difference between loading and unloading plateau of a single bridge device.

Due to the advantages of out-of-plane loading discussed above, a cooling cycle based on this operation mode will be discussed in the following. The coupling may be achieved in two different ways, which are fully equivalent from the mechanical point of view: The SMA bridges may be either pre-strained in a convex manner by a spacer in the centers of both bridges, or in a concave manner by a clamp in the center. Both concepts are shown schematically in Fig. 6.5. For convex coupling (Fig. 6.5 (a)), a heat sink with inclined surfaces is located in between the two coupled bridges (leaving room for free movement of the spacer) and acts as sink for both bridges. The heat source is split into two blocks – one located above the upper, the other below the lower brigde. During the first operation half-cycle, the coupled device is moved upwards, releasing strain from the upper bridge while straining the lower bridge to the maximum. As soon as contact is achieved, the upper bridge absorbs latent heat from the upper heat source, while the lower bridge releases heat to the common heat sink. In the second half-cycle, the roles of both bridges are reversed: The device is moved downwards, until the

upper bridge reaches the sink to release heat, whereas the lower bridge absorbs heat from the lower heat source.

The operation of the convexely coupled device (Fig. 6.5 (b)) is very similar, except that the heat source – located in between the coupled bridges in this case – is cooled twice during each cycle, whereas the heat sink is split into two blocks.

(a) Convex double bridge   (b) Concave double bridge

I. Out-of-plane loading   II. Heat release to sink
III. Out-of-plane unloading IV. Heat absorption from source
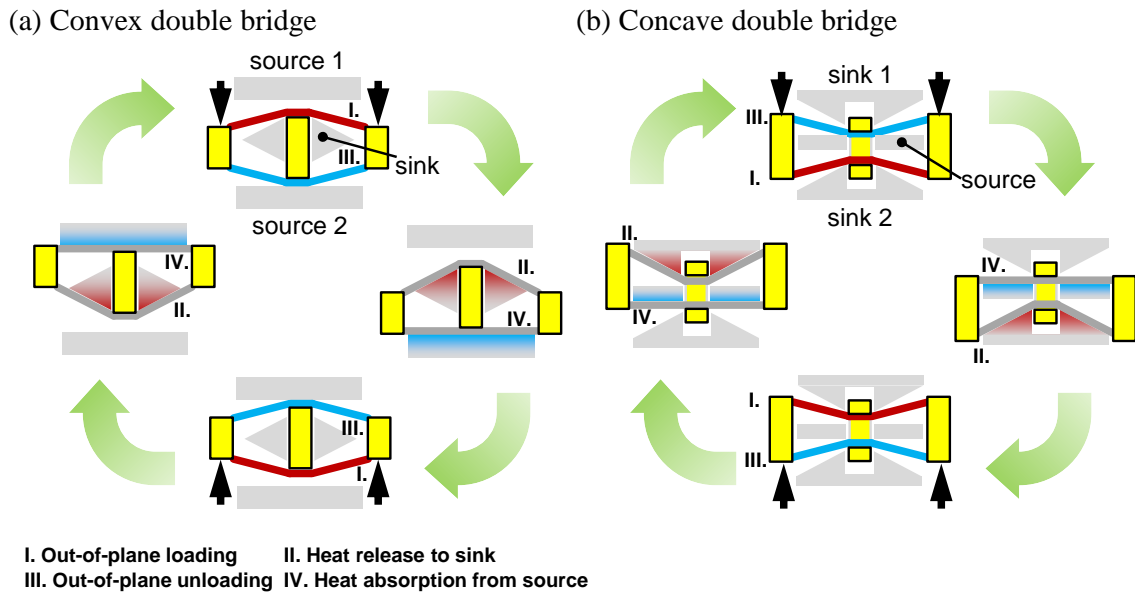
Figure 6.5: Schematic of elastocaloric microcooling devices based on antagonistically coupled SMA double bridge devices operated in out-of-plane mode. Bridges may be coupled either in a convex (a) or concave manner (b).

6.1.4 Actuation

In the above concepts for elastocaloric microcooling, a strong but compact actuator is required in order to induce stress-induced phase transformation in the active material. For the investigated materials and geometries, forces of several $10\,\text{N}$ at strokes in the order of 1 to $10\,\text{mm}$ are required. The concepts based on out-of-plane deflection somewhat reduce the requirements on force while requiring higher strokes.

In order to fully benefit from the fast heat transfer in elastocaloric films and foils, the velocity of the actuator should allow an operation at several Hz. These high requirements make it unlikely that a chip-scale actuator directly integrated in the microcooling device will fullfill them. Therefore, it is assumed that in general an external actuator will be required to drive the cooling or heat pumping device. The most common actuator types suitable for this task will be shortly reviewed in the following.

- Electric (rotary) motors are very common, can provide high forces (e.g., using gears) and are reasonably efficient. They produce a rotary motion which has to be converted to a linear motion mechanically, for instance using a spindle drive or an excentric wheel.

- Electric linear motors or the somewhat simpler voice coils represent a suitable alternative, as they work by the same electromagnetic principle, but create a linear motion directly. They can provide high forces (up to the kN range), high velocities (up to $5\,\mathrm{m\,s^{-1}}$) and arbitrary strokes, while being reasonably efficient.

- Piezoelectric actuators can produce high forces (up to kN) and very high velocities. Multilayer stack actuators find application, e.g., in Diesel injectors. Efficiency is high due to the capacitive operation principle. However, strokes are very low (in the order of 0.1% of the stack height) and maximum force is only achieved at zero displacement.

- Hydraulic drives are compact and can produce high forces but require additional equipment for operation.

- Shape memory alloy actuators can produce high forces and strokes, but they are very unefficient and not appropriate for cooling applications due to their thermal operation principle.

6.2 Demonstrator implementation and performance

The elastocaloric microcooling concepts described above are implemented in first-of-its-kind demonstrators. In the first part of this section, the performance of devices based on a single SMA bridge is investigated in order to study basic design parameters such as size, geometry and arrangement of heat sinks, sources and SMA films. In these designs, work recovery is not yet included. Enhanced demonstrator designs based on two antagonistically coupled SMA bridges are developed in the second part, implementing recovery of a large fraction of the input work. Due to availability and reasonable cyclic stability, cold-rolled TiNiFe foils are used as standard material in most of the experiments.

6.2.1 Single bridge devices – foil material

The solid-to-solid heat transfer concept described above is based on SMA bridges that are fixed on both ends and deflected out-of-plane. Devices are fabricated from rectangular SMA foil (/film) samples having a width of $2\,\mathrm{mm}$ ($1.75\,\mathrm{mm}$) and bridge length of $20\,\mathrm{mm}$. These are attached to a support frame on both ends with a two-component adhesive (EPO-TEK 353ND) by sandwiching the SMA foil between two frames. Support frames are fabricated from alumina with a thickness of $0.5\,\mathrm{mm}$. In cases where alumina frames may not be applied due to brittleness,

Table 6.1: Overview of SMA bridge demontrators developed in this work. Legend: SB – single bridge device, DB – convexely coupled double bridge device, iDB – concavely coupled double bridge device, T_{H1} – annealed at $T_H = 450\,°C$, $m_{sink/source}$ – masses of heat sink/source segments, $C_{p,sink/source}$ – lumped heat capacity of sink/source.

Name	Type	Material	Cross-section [mm²]	m_{sink} [g]	m_{source} [g]	$C_{p,sink}$ [J K⁻¹]	$C_{p,source}$ [J K⁻¹]
D02	SB 1st gen.	TiNiFe foil, RD, T_{H1}	2.00×0.030	1.63	0.86	0.61	0.32
D03	SB 1st gen.	TiNi film (021)	1.75×0.020	1.63	0.86	0.61	0.32
D04	SB 1st gen.	TiNi film (006)	1.75×0.020	1.63	0.86	0.61	0.32
D05	SB 2nd gen.	TiNiFe foil, RD, T_{H1}	2.00×0.030	$2 \times 0.13 + 0.49$	3×0.13	0.29	0.15
D06		TiNiFe foil, RD, T_{H1}	2.00×0.030	$2 \times 0.13 + 0.49$	3×0.13	0.29	0.15
D07	SB 2nd gen.	TiNi film (021)	1.75×0.020	$2 \times 0.13 + 0.49$	3×0.13	0.29	0.15
D09	SB 3rd gen.	TiNiFe foil, RD, T_{H1}	2.00×0.030	$2 \times 0.13 + 0.49$	3×0.13	0.29	0.15
D11	SB 4th gen.	TiNiFe foil, RD, T_{H1}	2.00×0.030	0.131	0.124	0.05	0.048
D12	SB 4th gen.	TiNiFe foil, RD, T_{H1}	2.00×0.030	0.131	0.124	0.05	0.048
D13	SB 4th gen.	TiNiCuCo film (032)	1.75×0.020	0.125	0.124	0.048	0.048
D01	DB 1st gen.	TiNiFe foil, RD, T_{H1}	2.00×0.030	-	2×0.86	-	0.65
D08	DB 2nd gen.	TiNiFe foil, RD, T_{H1}	2.00×0.030	-	6×0.13	-	0.2
D10	DB 2nd gen.	TiNiFe foil, RD, T_{H1}	2.00×0.030	-	6×0.13	-	0.2
D17	DB 3rd gen.	TiNiFe foil, RD, T_{H1}	2.00×0.030	16.8	4×0.235	62	0.32
D14	iDB 3rd gen.	TiNiFe foil, RD, T_{H1}	2.00×0.030	4×0.324	4×0.18	0.5	0.28
D15	iDB 3rd gen.	TiNiFe foil, RD, T_{H1}	3.00×0.030	4×0.324	4×0.18	0.5	0.28
D16	iDB 3rd gen.	TiNiFe foil, RD, T_{H1}	2.00×0.050	4×0.324	4×0.18	0.5	0.28

frames are fabricated from stainless steel. An assembled bridge device is shown in Fig. 6.7 (a).
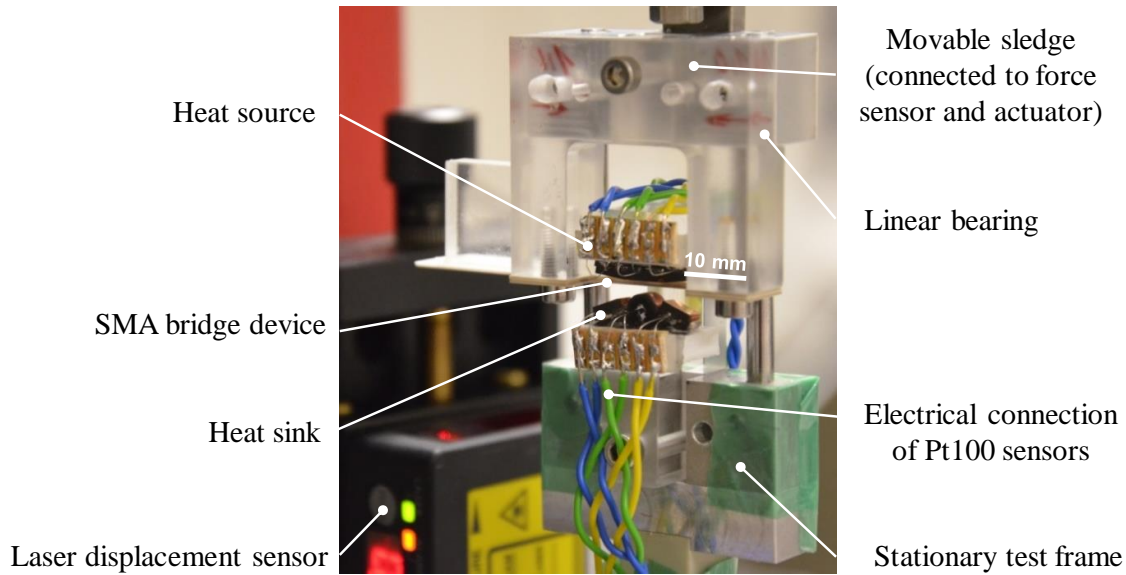
Figure 6.6: Experimental setup for characterization of elastocaloric miniature-scale heat pumping demonstrators based on solid-to-solid heat transfer.

For heat pumping experiments, bridge devices are mounted to the movable sledge of a testing frame as shown in Fig. 6.6. The sledge has a linear guidance in z-direction and is connected to the external actuator. In the following proof-of-principle experiments, the tensile testing machine plays the role of the actuator.

The machine has the advantage of providing a force and displacement measurement, as well as comparability with the tensile experiments described in chapter 4. Heat sources and sinks are fabricated from copper/brass by wire erosion and drilling. The surfaces intended for contact with the SMA bridges are polished with SiC polishing paper of grade 4000. The sink and source components are attached to polymer frames holding them in place. These, in turn, are mounted to the stationary part of the testing frame. For direct temperature measurement, Pt100 temperature sensors (class A) with dimensions of $3 \times 1 \times 0.5\,\mathrm{mm}^3$ and an accuracy of $0.2\,\mathrm{K}$ are attached to the outer side of each sink/source metal part (i.e. the side opposite to the one in contact with SMA bridge). In addition, the front faces are covered with black carbon to enable infrared thermography.
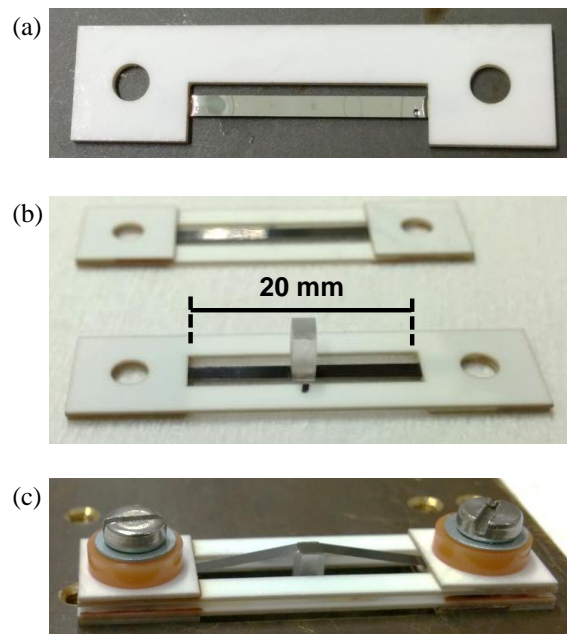
Figure 6.7: Fabrication of SMA bridge devices for elastocaloric microcooling. (a) SMA bridge is attached to alumina frame with both ends. For coupled devices, a polymer spacer is placed in the center of a single bridge device (b), then a second bridge device is mounted on top and pre-strained using an auxiliary frame (c). The devices are bonded with a thermally cured two-component epoxy adhesive.

As shown in Fig. 6.8, several generations of single bridge heat pumping devices are built, each implementing design optimizations based on the performance results of the previous generation. The devices are characterized using the test frame. Details about heat sink/source mass, as well as the utilized elastocaloric material, are summarized in Table 6.1. Identification numbers consisting of a capital 'D' and two digits are assigned to each demonstrator. These numbers are also indicated in figure captions for orientation. In the first device generation (e.g., demonstrator D02), heat sink and source are realized as monolithic brass blocks, the sink having a tent shape with inclination angle $15.5°$ whereas the source surface is flat. Since the lumped heat capacities of sink and source are orders of magnitude higher than that of the SMA bridge, temperature changes are rather
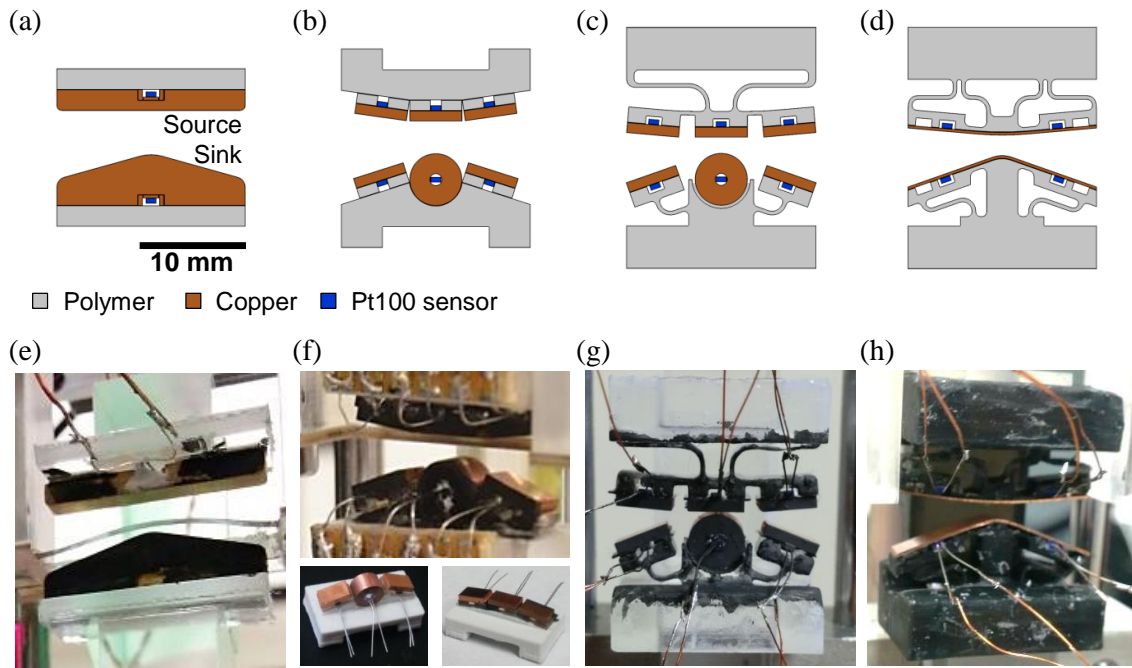
Figure 6.8: Elastocaloric miniature heat pumping demonstrators based on a single SMA bridge. In the first device generation (a,e) tent-shaped heat sink and flat heat source are monolithic. The second generation (b,f) comprises segmented heat sources and sinks. The source elements are arranged to form a slightly convex surface. Thermal contact between sink/source and SMA bridge is further improved in the third generation (c,g) by embedding sink/source segments in polymeric compliant mechanisms. In a forth generation (d,h), sink and source segments are replaced by continuous metal sheet stripes in order to omit sharp edges.

low. Since the TiNiFe foil samples accumulate a small amount of plastic strain during the first operation cycles (compare Fig. 4.10), the thermal contact between SMA bridge and flat heat source surface rapidly degrades.

For these reasons the heat sink and source are each assembled from three copper segments with smaller mass in the second device generation. The segments are attached to a (rigid) polymer frame produced by 3D printing, allowing a more flexible adaption of inclination angles. Each segment is equipped with a Pt100 temperature sensor, thus providing a coarse spatial resolution of the temperature change measurement. The central segment has the shape of a cylinder with diameter $5\,\text{mm}$ and a depth of $3\,\text{mm}$. The SMA bridge is pressed against this segment with maximum force during loading, therefore it is prepared to not have any sharp edges. The remaining five segments are rectangular with the dimensions $5 \times 3 \times 1\text{mm}^3$. The segments of the heat source are arranged in a slightly convex manner as well, in order to allow good thermal contact to the SMA bridge. This slight slope of the segments leads to a strain of 1% in the bridge during contact, which is higher than typical plastic strain due to training, but on the other hand

lower than the onset strain of the stress plateaus. The results of device characterization are shown in Fig. 6.9. Temperature changes are significantly improved compared to the first demonstrator. During operation at $0.68\,\text{Hz}$, the heat sink[3] is heated by $4.4\,\text{K}$ whereas the source is cooled by $-3.1\,\text{K}$. For a lower operation frequency, temperature changes are lower. As infrared thermograms show, parts of the polymer frame, which are in direct contact to the metal segments of heat sink / source, are heated and cooled as well.
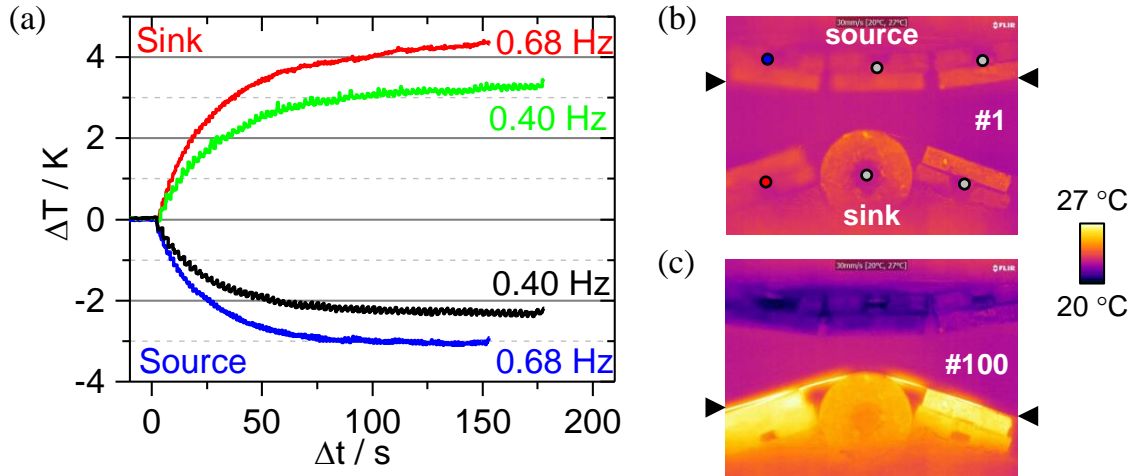
Figure 6.9: Characterization of temperature changes of single-bridge heat pumping demonstrator with segmented heat source and sink on rigid polymer frame (2nd generation). The SMA bridge is fabricated from cold-rolled TiNiFe foil. (a) Temperature change of heat source and sink, measured by Pt100 sensors, during operation at the two frequencies $0.40\,\text{Hz}$ and $0.68\,\text{Hz}$. IR thermograms are shown on the right for the first (b) and hundredth cycle (c) at $0.68\,\text{Hz}$. Compare Ref. [308]. (D05)

In the second demonstrator generation, the SMA bridge still has to be aligned very carefully with respect to the source and sink to allow for good thermal contact. In case of a small tilt, one part of the bridge is mechanically overloaded at the sharp edge of a sink / source segment, whereas another part is not yet in contact to the sink / source, resulting in inhomogeneous heat transfer. In order to tackle this issue, compliant mechanisms are introduced in the third demonstrator generation, which allow adaptation of the sink and source segments to the inclination of the SMA bridge. The compliant mechanisms are produced by modern stereo-lithographic 3D printing technology (Formlabs Form1+) from a liquid polymer resin. They consist of meandering structures with a thickness of $400\,\mu\text{m}$ and a depth of $3\,\text{mm}$. The shape and thickness of the compliant structures are adjusted by several design iterations and experimental validation. An additional advantage of these structures is that they decrease the cross-section of support frame material acting as parasitic heat bridge. A possible disadvantage

---

[3]These temperature changes are measured in the outer sink segments; the cylindrical segment in the center has a higher mass and therefore lower temperature change.

is that the contact forces between sink/source segments and SMA bridge are reduced, increasing the thermal contact resistance. The performance of a device with compliant support structures operated at $0.75\,\mathrm{Hz}$ is shown in Fig. 6.10, exhibiting similar temperature changes of sink and source as the device with rigid support structures (although heating of the sink is increased). This result means that either parasitic heat flows are similar in both cases, or the advantage of more gentle stressing of the SMA bridge is compensated by decreased thermal contact due to lower contact forces. However, contact of all sink/source segments with the SMA bridge is improved.
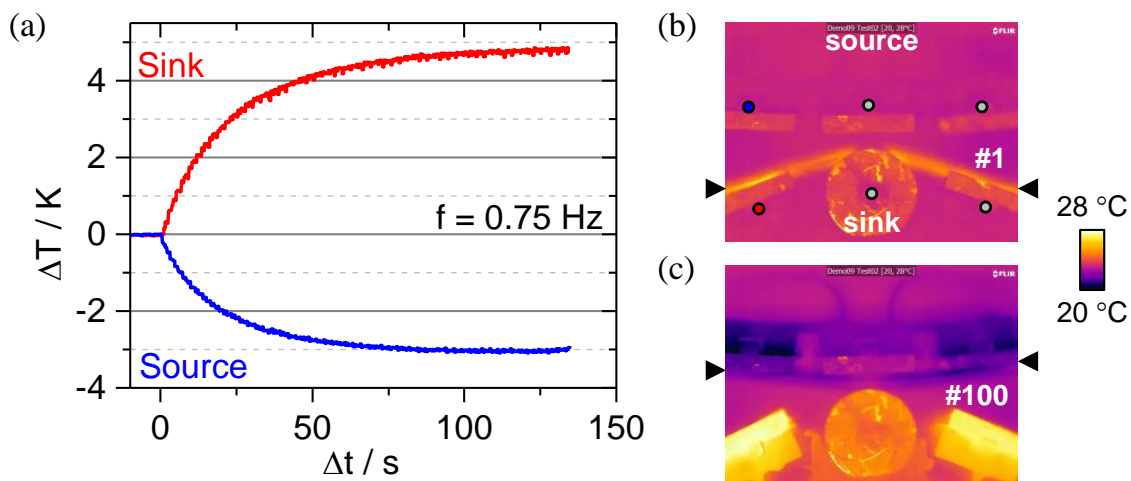
Figure 6.10: Characterization of temperature changes of single-bridge heat pumping demonstrator with segmented heat source and sink supported by polymer compliant mechanism (3rd generation). The SMA bridge is fabricated from cold-rolled TiNiFe foil. (a) Average temperature change of heat source and sink, measured by Pt100 sensors, during operation at a frequency of $0.75\,\mathrm{Hz}$. IR thermograms are shown on the right for the first (b) and hundredth cycle (c). Compare Ref. [294]. (D09)

In a further design variation (fourth generation), copper segments of sink and source are replaced by two continuous stripes of copper sheet, respectively. The stripes are bent to the desired deflection angle ($19.37°$ for the sink and $5.0°$ for the source). The design eliminates sharp edges of individual copper segments and maximizes the contact area between SMA bridge and sink/source. At the same time, the capability to adapt the SMA bridge alignment is maintained by integrating compliant mechanisms within the polymer frame. As Fig. 6.11 shows, temperature changes of source and sink are again very similar to the previous devices, although the lumped heat capacities of sink and source are lower in this case (see table 6.1). Since the copper sheet stripes have a considerably higher surface-to-volume ratio, heat transfer between sink/source and SMA film is more efficient, but thermal losses due to convection and conduction through frame structures are increased as well. A close-up of the sink temperature evolution at two different operation frequencies (inset in Fig. 6.11 (a)) shows that overall cooling is higher at the higher frequency, but temperature oscillations are higher

for the lower frequency. Hence, more heat is absorbed by the SMA bridge during each contact with the sink in case of the lower frequency.
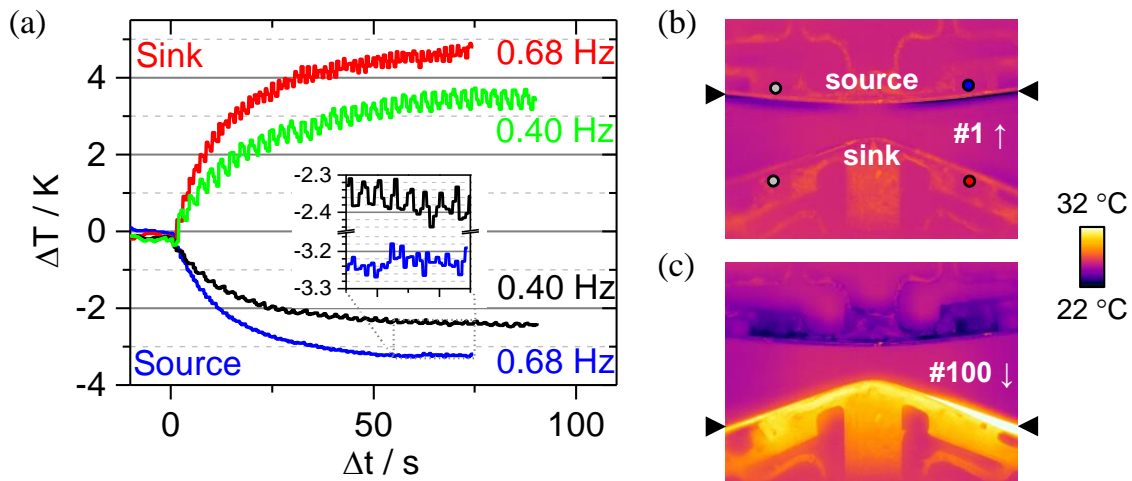
Figure 6.11: Characterization of temperature changes of single-bridge heat pumping demonstrator with heat source and sink fabricated from copper sheet, supported by polymer compliant mechanism (4th generation). The SMA bridge is fabricated from cold-rolled TiNiFe foil. (a) Average temperature change of heat source and sink, measured by Pt100 sensors, during operation at the two frequencies $0.40\,\mathrm{Hz}$ and $0.68\,\mathrm{Hz}$. IR thermograms are shown on the right for the first (b) and hundredth cycle (c). (D12)

The performance results of selected demonstrators are summarized in Table 6.2. The table includes device identifiers (D02 etc.), experimental conditions, data of thermal and mechanical performance, as well as estimated coefficients of performance. Thermal performance is evaluated based on initial temperature change rate, maximum temperature changes with respect to room temperature[4] and time constants for reaching stationary conditions.[5] Based on the lumped heat capacities of sink and source, as well as the initial temperature change rate during the first cycles, heat flows absorbed from the source and released to the sink (cooling and heating power) are estimated. Mechanical input power is estimated by numerical integration of the force-displacement loop, multiplied with the operation frequency. Based on these figures, a coefficient of performance is calculated for each demonstrator. Note that full recovery of the unloading work is assumed although not implemented in the demonstrator setup, and the efficiency of the driving actuator is not considered. A temperature lift of $7.9\,\mathrm{K}$ is reached by 3rd generation demonstrator 'D09'. The COP for cooling is 2.9 in this case (corresponding to 8% of the Carnot efficiency for cooling), whereas the COP for heating is 7.3 (corresponding to 20% of Carnot), hence more than twice the cooling COP.

---

[4]In case the temperature change of individual copper segments was different, the segment showing maximum temperature change was selected and the same temperature change was assumed for the other segments having the same heat capacity.

[5]Time constants are obtained by exponential fit of time-dependent temperature evolution measured by Pt100 segments.

Table 6.2: Performance of selected single bridge demontrators. Legend: # – experiment number, cycles – number of cycles in the experiment, f – operation frequency, $t_{contact}$ – heat transfer time, F_{max} – maximum applied force, Δx – stroke, $\frac{dT}{dt}{}_{sink/source}$ – initial temperature change rate of sink/source, $\tau_{sink/source}$ – time constants for reaching steady state (exponential fit), $\Delta T_{sink/source}$ – maximum temperature change of sink/source after specified number of cycles, $P_{heat/cool}$ – estimated heating/cooling power of device, P_{mech} – mechanical input power, assuming full work recovery, $COP_{heat/cool}$ – coefficient of performance for heating/cooling, assuming full work recovery.

Name/#	Cycles	f [Hz]	$t_{contact}$ [s]	F_{max} [N]	Δx [mm]	$\frac{dT}{dt}{}_{sink}$ [K s^{-1}]	$\frac{dT}{dt}{}_{source}$ [K s^{-1}]	τ_{sink} [s]	τ_{source} [s]
D02 / 8	100	0.68	0.4	20	6.4	0.03	-0.05	53.4	48.6
D05 / 1	100	0.68	0.4	24	6.0	0.20	-0.17	28.7	23.6
D05 / 2	69	0.40	0.9	24	6.0	0.15	-0.09	32.2	25.6
D09 / 2	100	0.75	0.3	22	4.8	0.21	-0.16	24.9	21.0
D11 / 1	92	0.73	0.4	30	6.1	0.30	-0.23	17.0	10.2
D12 / 1	50	0.68	0.1	30	6.4	0.48	-0.25	14.5	13.2
D12 / 2	35	0.40	0.5	30	6.4	0.28	-0.15	21.4	15.4
D07 / 1	100	0.72	0.4	11	5.9	0.21	-0.15	10.5	9.1
D07 / 2	48	0.69	0.4	14	6.5	0.14	-0.09	20.0	17.0
D13 / 3	8	0.75	0.15	30	4.4	0.19	-0.30	21.2	5.6

Name/#	ΔT_{sink} [K]	ΔT_{source} [K]	P_{heat} [mW]	P_{cool} [mW]	P_{mech} [mW]	COP_{heat}	COP_{cool}
D02 / 8	1.3	-1.7	20.1	16.6	3.0	6.7	5.5
D05 / 1	4.4	-3.1	26.3	25.5	17.3	1.5	1.5
D05 / 2	3.3	-2.4	19.2	13.5	8.5	2.3	1.6
D09 / 2	4.8	-3.1	61.0	24.0	8.3	7.3	2.9
D11 / 1	5.1	-2.9	15.0	11.0	9.8	1.5	1.1
D12 / 1	4.9	-3.3	24.0	12.0	9.4	2.6	1.3
D12 / 2	3.7	-2.5	14.0	7.2	5.0	2.8	1.4
D07 / 1	2.5	-1.7	26.1	23.1	8.0	3.3	2.9
D07 / 2	2.7	-1.6	-	15.4	5.0	-	3.1
D13 / 3	1.5	-2.0	9.1	14.4	5.0	1.8	2.9

1st generation demonstrator 'D02' reaches a higher cooling COP of 5.5 (5.7% of Carnot), which is due to the much higher thermal mass of sink and source, leading to a low temperature lift of $3\,\mathrm{K}$. Considering the Carnot efficiency (Eq. 2.9a), it is easier to reach high COPs when the temperature lift is low.

A number of lessons can be learned from the above experiment with single-bridge elastocaloric cooling devices, which shall be summarized in the following:

- Demonstrators reach temperature differences of up to $8\,\mathrm{K}$ between sink and source, corresponding to 50% of the self-cooling of elastocaloric TiNiFe foils observed in uniaxial tensile tests.

- In the frequency range accessible by the experimental setup used herein (0.6 to $0.75\,\mathrm{Hz}$, depending on actuation stroke), highest temperature differences between sink and source are reached at maximum frequency, suggesting that higher temperature differences may be expected upon further increasing the frequency.

- However, temperature oscillations are higher at lower frequencies, indicating that at the highest frequency, a smaller fraction of the total latent heat is transferred from or to the SMA bridge. The thermal contact needs to be improved, e.g., by increasing contact forces or decreasing the thermal contact resistance.

- Infrared thermograms of heat pumping devices during operation reveal inhomogeneous heating/cooling of segmented heat sinks/sources, suggesting that SMA bridges are not fully transformed in some cases and/or thermal contact between SMA bridge and sink/source segments varies.

- Despite implementation of several design variations and varying the lumped heat capacities, final temperature changes of heat sources and sinks are in a similar range (except for the first device generation). Advantages and disadvantages of the design changes partly compensate each other. Improvement of the thermal contact between sink/source and SMA bridge may be achieved by increasing the spring constant of compliant mechanisms in order to increase contact forces. In case of small heat source and sink segments, their inceased surface-to-volume ratio becomes a disadvantage since it increases parasitic heat flow. Therefore, heat sinks and souces with higher lumped heat capacity allow for more efficient heat pumping.

- A clear advantage of integrating compliant structures in the heat source and sink (3rd device generation) is that thermal contact of the SMA bridge is more even, tolerating small miss-alignments in the setup and omitting stress peaks in the SMA material.

- Device coefficients of performance for cooling of up to 3.1 are reached, when work recovery is assumed.

- COPs increase with increasing mass (lumped heat capacity) of the source and sink, since lower surface-to-volume ratios lead to lower parasitic heat flows. Obviously, the time constants for reaching stationary conditions increase as well.

6.2.2 Single bridge devices – film material
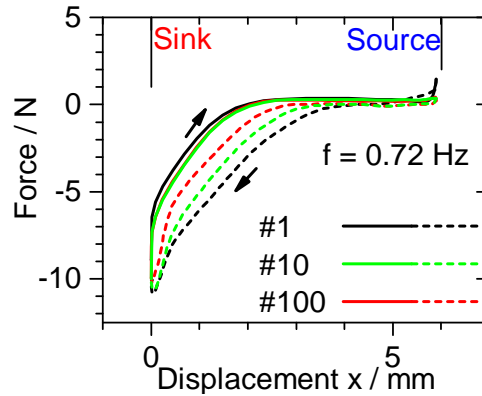
Figure 6.12: Force-displacement characteristic of single-bridge heat pumping demonstrator (2nd generation) operated with sputter-deposited TiNi film of $20\,\mu m$ thickness at $0.72\,Hz$ for 100 cycles. Contact force at the heat sink is negative, since movement from source to sink proceeds in negative z-direction. (D07)

After achieving proof-of-principle of the single-bridge heat pumping concept using TiNiFe foil bridges, demonstrators based on sputter-deposited film material are investigated in the following. A device comprising a TiNi film bridge with the dimensions $20 \times 1.75 \times 0.02\,\text{mm}^3$ is built according to the 2nd generation design scheme (compare Fig. 6.8 (b)). The force-displacement characteristic of the device operated at $0.72\,Hz$ for 100 cycles is shown in Fig. 6.12. The mechanical behavior clearly changes with increasing cycle number: The force-displacement loop adopts an increasingly narrow shape and stabilizes after 100 cycles. The reason for this behavior is the strong degratation of sputter-deposited TiNi films as described in chapter 4.2.1, leading to accumulation of plastic strain and buckling of the bridge. In order to investigate the cooling performance of a degraded (trained) sample, a second experimental sweep is performed with the same film device. For this purpose, the actuation stroke is increased in such a way that the film device is again in full contact to the sink and source segments at the reversal points. The device is operated at $0.69\,Hz$ for another 49 cycles, until mechanical failure of the film occurs.

The thermal performance of the device during both experimental sweeps is shown in Fig. 6.13. During the first sweep, the temperatures of heat sink/source rapidly increase/decrease, until stationary conditions are reached after 25 cycles. During these cycles, the film bridge accumulates plastic strain, leading to poor contact,
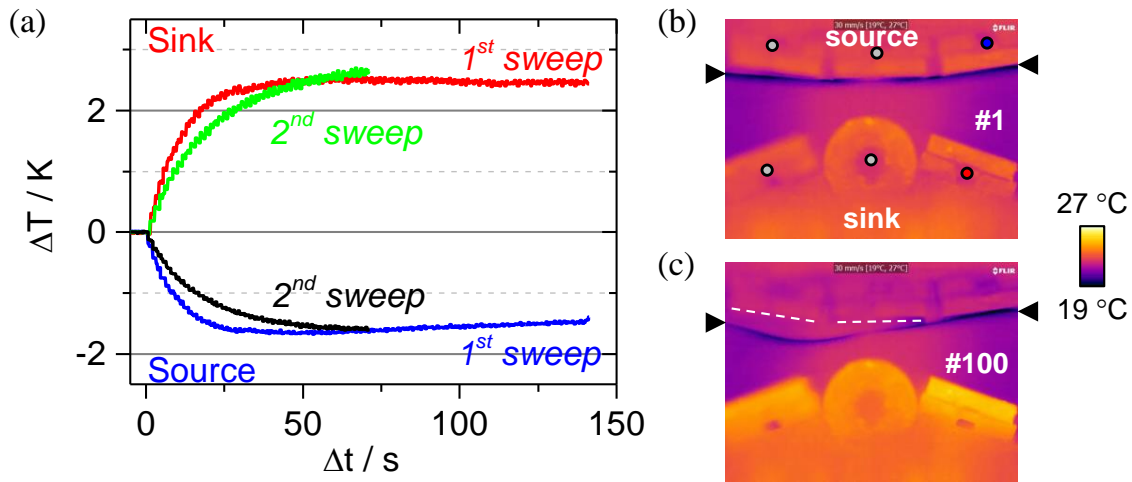
Figure 6.13: Characterization of temperature changes of single-bridge heat pumping demonstrator (2nd generation) operated with sputter-deposited TiNi film of $20\,\mu m$ thickness. (a) Average temperature change of heat souce and sink, measured by Pt100 sensors. Two consecutive experimental sweeps are performed at the frequencies $0.72\,Hz$ and $0.69\,Hz$, respectively. IR thermograms are shown on the right for the first (b) and hundredth cycle (c) of the first sweep. In (c), the surface of the heat source segments is indicated by dashed lines. Compare Ref. [301]. (D07)

especially between film and heat source. The resulting gap between bridge and source is marked in Fig. 6.13 (c), showing a thermogram acquired during the 100th cycle. During the second sweep, started after re-establishing good contact by increasing the stroke, the estimated cooling/heating power is reduced by about one third while the time constant for reaching stationary conditions is doubled, compared to the first sweep. However, after 49 cycles the temperature changes of $+2.7$ and $-1.8\,K$ are very close to those obtained in the first sweep. The coefficient of performance of the device operated with a degraded TiNi film is even slightly increased to 3.1 (compared to 2.9 for the as-fabricated film), because the mechanical work input ΔW is reduced for the trained material. In conclusion, sputter-deposited TiNi film samples can be employed for efficient elastocaloric heat pumping despite the strong degradation effects they exhibit. However, the presumed high dislocation density might limit the lifetime of the device, which has to be examined in a future study. In order to obtain reasonable thermal contact to the heat source (and sink), the films have to be trained for a number of cycles in order to reach stable behavior.

The performance of fatigue-free sputter-deposited TiNiCuCo films is investigated in a demonstrator according to the 4th generation design using a film bridge with the dimensions $20\times3\times0.039\,mm^3$. Due to the increased brittleness of the material, heat source and sink are fabricated from copper sheet in order to omit sharp edges (compare Fig. 6.8 (d)). Nevertheless the device failed after 8 cycles of operation at $0.75\,Hz$ due to fracture at several points of the film. The thermal and mechanical
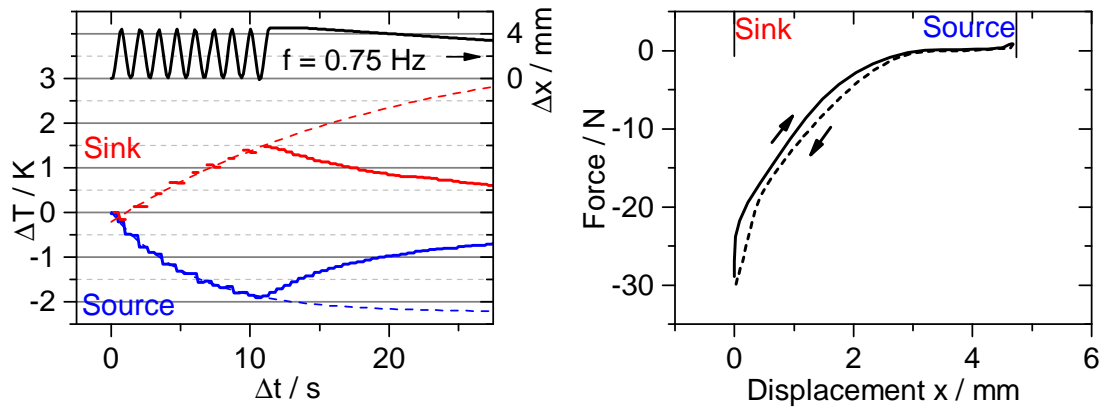
Figure 6.14: Characterization of temperature changes of single-bridge heat pumping demonstrator (3rd generation) operated with sputter-deposited TiNiCuCo film of $39\,\mu m$ thickness. (a) Average temperature change of heat source and sink during operation at $0.72\,Hz$, measured by Pt100 sensors. (b) Force-displacement characteristic of the device. Compare Ref. [301]. (D13)

device performance is shown in Fig. 6.14. Whithin 8 cycles the heat source is cooled by $-2.0\,K$ while the sink is heated by $1.5\,K$. Note that the same unexpected asymmetry as in the uniaxial tensile tests is observed, the heating effect being 25% lower than the cooling effect. The copper sheets representig heat source and sink are designed to have the same heat capacity. However, the polymeric support structures differ slightly between source and sink, possibly leading to a stronger heat bridge at the source. The cooling COP of the device (assuming work recovery) is 2.9.

6.2.3 Coupled devices

In the above section the concept of miniature heat pumping based on elastocaloric film and foil bridge devices was verified and a number of design optimizations were introduced. However, the work ΔW_{unload} stored in the bridge devices after loading is not recovered during unloading. In the following, antagonistic concepts will be investigated, allowing for recovery of a large fraction of the unloading work and therefore approaching the optimum coefficient of performance.

Antagonistic devices coupled in a convex manner are fabricated from two single bridge devices with a spacer in between, as shown in Fig. 6.7. Analogously to the experiments on single bridge devices, several design variants are evaluated (Fig. 6.15). In the first generation device two monolithic heat source blocks with flat surface are placed above and below the coupled double bridge. During operation, the double bridge is alternatingly pressed against the upper and the lower source. Due to slight buckling of the relaxed bridges, however, the cooling effect is negligible. Therefore, heat sources are divided into three segments each in the second generation device. The outer segments are arranged with a
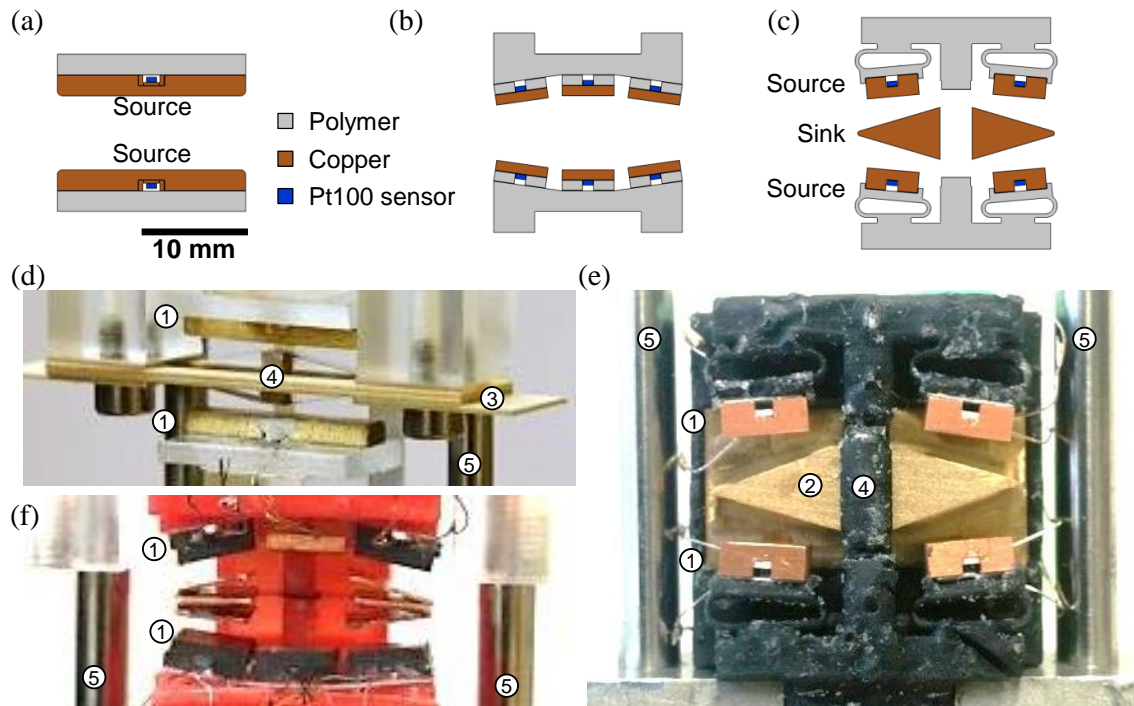
Figure 6.15: Heat pumping demonstrators based on two antagonistic SMA bridge coupled in a convex manner. (a,d) First generation, (b,f) second generation and (d,e) third generation. Demonstrator components are: (1) heat source, (2) heat sink, (3) alumina frame, (4) spacer, (5) linear guidance. Compare Ref. [294].

slight inclination of $8.07°$, corresponding to a strain of 1% in the bridge during contact. Thus the SMA bridges are never fully released during operation and buckling is omitted. The device does not contain a solid heat sink but instead relies on the surrounding air for heat removal. The thermal and mechanical performance of the device are shown in Figs. 6.16 and 6.17. The force-displacement characteristic comprises two sub-loops corresponding to the coupled device being pressed against the upper and lower heat source, respectively. During free motion between both sinks, the device is force-free. The temperature evolution of the device operated at $0.84\,\mathrm{Hz}$ shown in Fig. 6.16 (a) reveals a cooling of the outer source segments of up to $-1.3\,\mathrm{K}$. The estimated cooling coefficient of performance is 1.2. The spacer and the center segments of the source, in contrast, are slightly heated up with increasing cycle number, indicating that heat release to the surrounding air is not sufficiently effectiv. Infrared thermograms reveal that the fully strained bridges are still hot when unloading begins.

For this reason, a solid heat sink, fabricated from brass and having a much higher heat capacity than the heat source, is integrated in the third generation device ((2) in Fig. 6.15 (e)). The sink contains two triangular fingers, reaching in between the coupled SMA bridges and leaving space for free movement of the spacer in between (4). In this case, the spacer is part of the 3D-printed polymer frame, being supported by compliant structures. The heat sources are assembled from four segments placed above and below the coupled bridge device (1) and supported
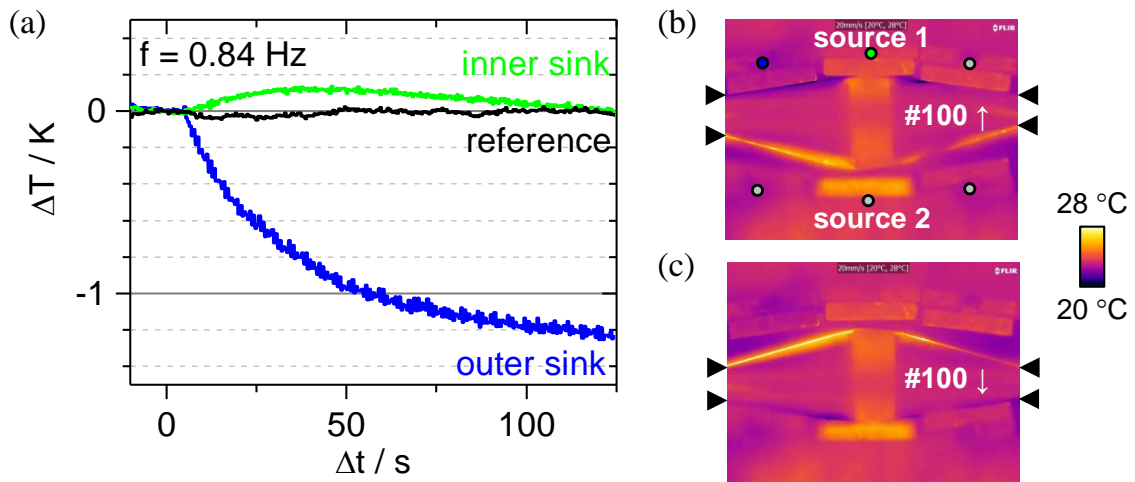
Figure 6.16: Characterization of temperature changes of convexely coupled antagonistic heat pumping demonstrator with segmented heat sources (2nd generation). Two SMA bridges fabricated from cold-rolled TiNiFe foil are pre-strained by a polymer spacer. (a) Temperature change of heat source segments, measured by Pt100 sensors, during operation at $0.84\,\mathrm{Hz}$. IR thermograms are shown on the right for the first (b) and hundredth cycle (c) at $0.68\,\mathrm{Hz}$. Compare Ref. [308]. (D08)
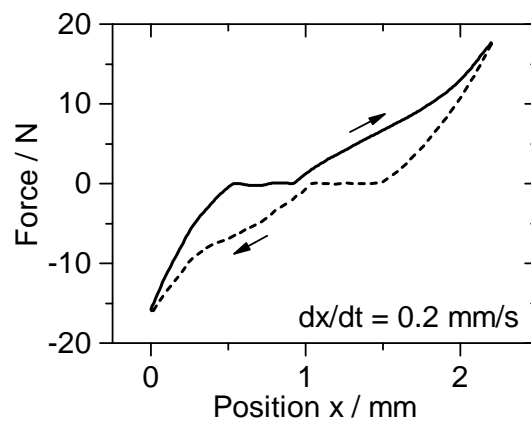
Figure 6.17: Force-displacement characterisitc of convexely coupled antagonistic heat pumping demonstrator with segmented heat sources (2nd generation). Compare Ref. [308]. (D08)

by compliant structures as well. The SMA bridges are assembled in-situ and pre-strained by screws. The device is operated at $0.76\,\text{Hz}$ and reaches a maximum cooling of the source segments by $5.0\,\text{K}$, whereas the sink is only slightly heated by $0.5\,\text{K}$ due to its higher mass (Fig. 6.18). Infrared thermograms reveal that the source segments are cooled inhomogeneously because full phase transformation of the SMA bridges is not reached. The device coefficient of performance is 3.2 for cooling and 2.0 for heating.
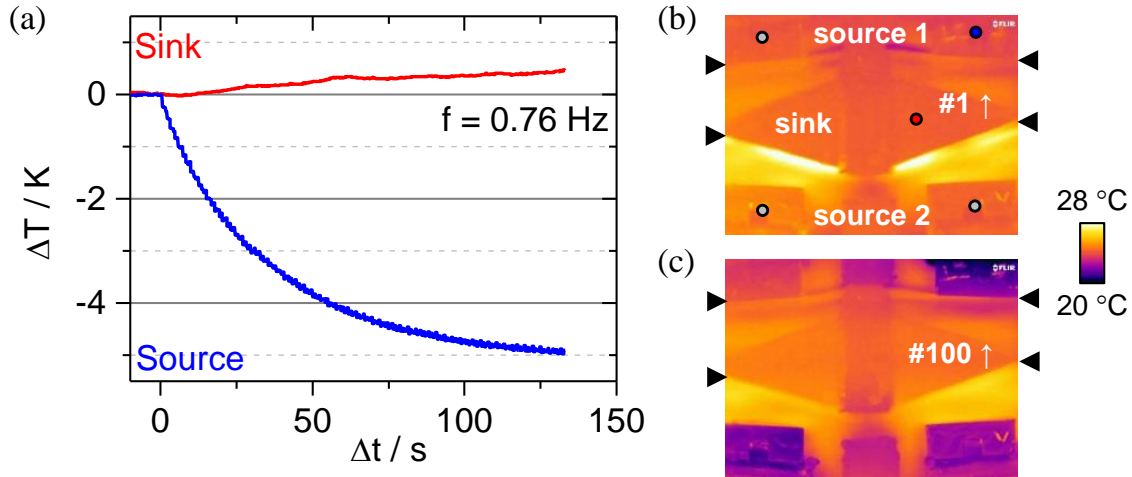
Figure 6.18: Characterization of temperature changes of convexely coupled antagonistic heat pumping demonstrator (3rd generation) with segmented heat sources supported by compliant structures, and a solid heat sink. Two SMA bridges fabricated from cold-rolled TiNiFe foil are pre-strained by a polymer spacer. (a) Average temperature change of heat sink and source segments, measured by Pt100 sensors, during operation at $0.76\,\text{Hz}$. IR thermograms are shown on the right for the first (b) and hundredth cycle (c). Compare Ref. [294]. (D17)

In the convexely coupled antagonistic device the heat source is distributed in two parts above and below the coupled SMA bridges. In the context of microcooling applications, however, it might be desired to have the cooling power concentrated in a small spot, whereas the heat sink may be distributed over a larger area. Therefore, a second type of coupled bridge device is developed, comprising SMA bridges pre-strained in a concave manner, a single heat source (which, however, consists of four copper sements attached to a polymer part) and distributed heat sinks.

The schematic setup and demonstrator components are shown in Fig. 6.19. Heat source (1) and sink (2) are both assembled from four individual copper sements attached to polymeric compliant structures. The source is placed in between the SMA bridges, the two parts of the sink are placed above and below. The bridges are attached to stainless steel frames (6) and are pre-strained during assembly within the test frame. Spacers (7) are placed between the outer ends of the bridges whereas the bridge centers are coupled by a clamp in their centers (4) on a linear guidance (3) and pre-strained by a screw. The coupled bridges are attached to a
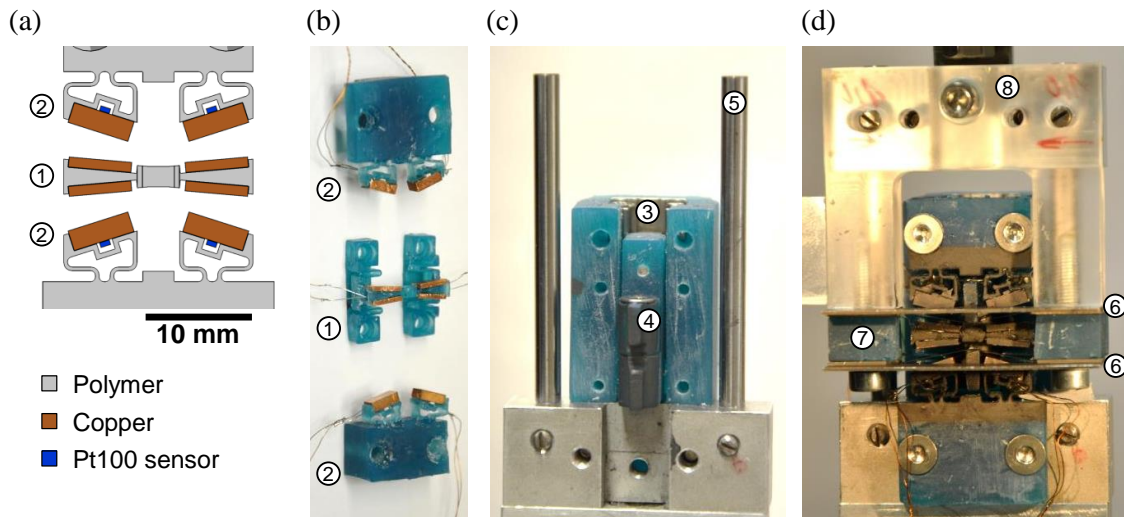
Figure 6.19: Heat pumping demonstrators based on two antagonistic SMA bridges coupled in a concave manner. (a) Schematic setup, (b) heat sink and source, (c) Linear guidance and clamp, (d) assembled demonstrator. Demonstrator components are: (1) heat source with compliant mechanism (2) heat sink with compliant mechanism, (3) linear guidance for clamp, (4) pre-straining clamp, (5) linear guidance for coupled bridge device, (6) bridge devices on stainless steel frames, (7) outer spacer, (8) linear guidance for coupled bridge device. Compare Ref. [294].

second linear guidance (8) which is connected to the actuator. Clamp and frame structures are fabricated by 3D-printing.

The thermal and mechanical performance of the device are shown in Figs. 6.20 and 6.21. Again, the force-displacement characteristic consists of two subloops corresponding to the displacement intervals, during which the device is in contact to source and sink. The differing size of the loops in Fig. 6.21 results from unsymmetric loading. When operating the device at $0.76\,\mathrm{Hz}$, the heat source and sink are cooled/heated by $-4.4\,\mathrm{K}$ and $5.0\,\mathrm{K}$, respectively. The coefficient of performance is 3.1 for cooling and 4.9 for heating.

The performance results of the coupled device demonstrators are summarized in Table 6.3.
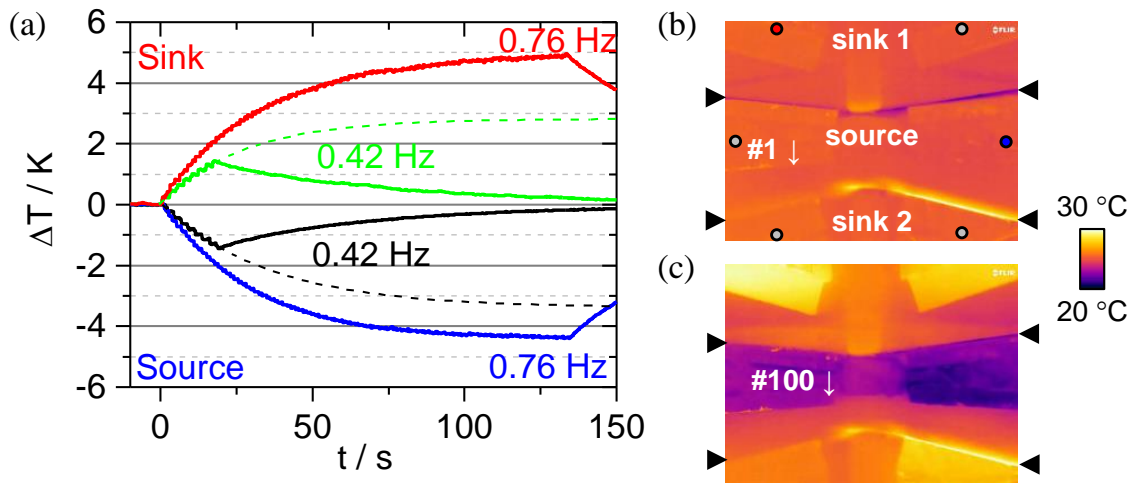
Figure 6.20: Characterization of temperature changes of concavely coupled antagonistic heat pumping demonstrator with segmented heat sources and sinks supported by compliant structures. Two SMA bridges fabricated from cold-rolled TiNiFe foil are pre-strained by a polymer clamp. (a) Average temperature change of heat sink and source segments, measured by Pt100 sensors, during operation at the two frequencies $0.76\,\text{Hz}$ and $0.40\,\text{Hz}$. IR thermograms are shown on the right for the first (b) and hundredth cycle (c) at $0.76\,\text{Hz}$. Compare Ref. [294]. (D14)
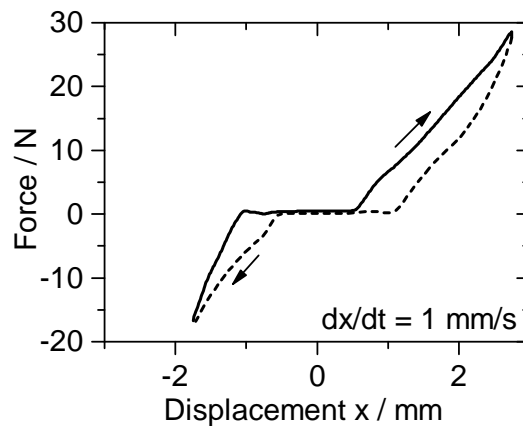
Figure 6.21: Force-displacement characteristic of concavely coupled antagonistic heat pumping demonstrator with segmented heat sources and sinks. Compare Ref. [294]. (D14)

Table 6.3: Performance of selected coupled bridge demontrators. Legend: # - experiment number, cycles – number of cycles in the experiment, f – operation frequency, $t_{contact}$ – heat transfer time, F_{max} – maximum applied force, Δx – stroke, $\frac{dT}{dt}_{sink/source}$ – initial temperature change rate of sink/source, $\tau_{sink/source}$ – time constants for reaching steady state (exponential fit), $\Delta T_{sink/source}$ – maximum temperature change of sink/source after specified number of cycles, $P_{heat/cool}$ – estimated heating/cooling power of device, P_{mech} – mechanical input power, assuming full work recovery, $COP_{heat/cool}$ – coefficient of performance for heating/cooling, assuming full work recovery.

Name/#	Cycles	f [Hz]	$t_{contact}$ [s]	F_{max} [N]	Δx [mm]	$\frac{dT}{dt}_{sink}$ [K s^{-1}]	$\frac{dT}{dt}_{source}$ [K s^{-1}]	τ_{sink} [s]	τ_{source} [s]
D08 / 4	100	0.84	0.35	20	1.9	-	-0.05	-	31.7
D17 / 2	100	0.76	0.1	25	4.2	0.006	-0.16	63.0	35.4
D14 / 2	8	0.42	0.5	30	4.3	0.10	-0.09	27.3	34.9
D14 / 3	100	0.76	0.1	30	4.3	0.14	-0.16	34.4	30.0
D16 / 6	100	0.71	0.3	35	3.9	0.20	-0.15	30.1	28.5

Name/#	ΔT_{sink} [K]	ΔT_{source} [K]	P_{heat} [mW]	P_{cool} [mW]	P_{mech} [mW]	COP_{heat}	COP_{cool}
D08 / 4	-	-1.3	-	10	8.1	-	1.2
D17 / 2	0.5	-5.0	384.0	51.0	16.0	2.0	3.2
D14 / 2	1.4	-1.4	50.0	25.2	8.7	5.7	2.9
D14 / 3	5.0	-4.4	70.0	45.0	14.4	4.9	3.1
D16 / 6	5.2	-4.6	100.0	42.0	15.9	6.3	2.6

6.3 Heat transfer model

In order to understand the thermal performance of the elastocaloric heat pumping devices, heat transfer is modelled with a simple lumped-element model (LEM) implemented by Frank Wendler [294]. In contrast to the phenomenological model discussed in the previous chapter, the LEM assumes homogeneous temperature within the SMA foil, the sink and the source (compare also Table 2.1 in Chapter 2.1.4). Since it is very difficult to measure thermal contact resistances in the devices, the model provides an important means to estimate the contact resistances and heat flows in the experimental setup. For symmetry reasons, only a quarter of the coupled device needs to be modeled.

A thermal equivalent circuit of the elastocaloric miniature heat pump based on solid-to-solid heat transfer is shown in Fig. 6.22. The model comprises three elements, representing the SMA bridge, heat sink and heat source, respectively. Each of the elements experiences convective as well as conductive losses to the environment, referred to as $\dot{Q}_{conv,\alpha}$ and $\dot{Q}_{cond,\alpha}$, respectively ($\alpha = 1 \ldots 3$). The stress-strain characteristic of the SMA is approximated by linear segments, assuming
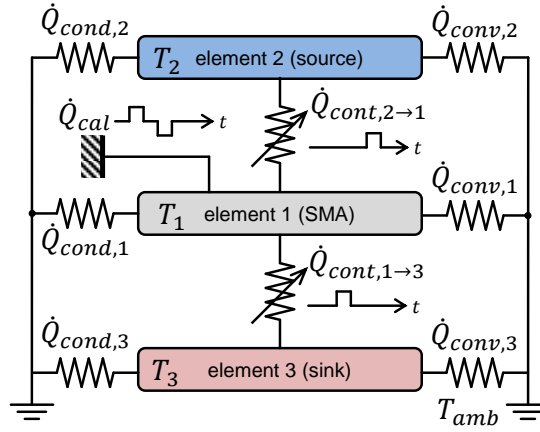
Figure 6.22: Thermal lumped-element model of heat transfer in a SMA bridge-based microcooling device. The model comprises a heat source, heat sink and SMA bridge element. Heat transfer by conduction of bridge and sink/source in contact, as well as parasitic heat flows by air convection and conduction to the fixation are considered. Compare Ref. [294].

horizontal stress plateaus and neglecting self-heating effects on the plateau stresses (compare Fig. 6.2). Within the stress plateau region, phase fraction ξ is assumed to increase homogeneously and linearly with increasing strain. The beginning of the plateau corresponds to 0% martensite, whereas the martensitic phase fraction reaches 100% at the end of the plateau. The heat source term $\dot{Q}_{cal}$ representing release and absorption of latent heat L within the SMA is proportional to the time-dependent change of phase fraction $\dot{\xi}$, which in turn is proportional to the strain rate $\dot{\varepsilon}$ ($\Delta\varepsilon_T$ is the plateau width):

$$\dot{Q}_{cal} = L \cdot \dot{\xi} = L \cdot \frac{\dot{\varepsilon}}{\Delta\varepsilon_T} \tag{6.6}$$

The heat equations describing the elastocaloric heat pump are:

$$C_p^1 \dot{T}_1 = -\dot{Q}_{conv,1} - \dot{Q}_{cond,1} + \dot{Q}_{cont,2\to1} - \dot{Q}_{cont,1\to3} + \dot{Q}_{cal} \tag{6.7a}$$

$$C_p^2 \dot{T}_2 = -\dot{Q}_{conv,2} - \dot{Q}_{cond,2} - \dot{Q}_{cont,2\to1} \tag{6.7b}$$

$$C_p^3 \dot{T}_3 = -\dot{Q}_{conv,3} - \dot{Q}_{cond,3} + \dot{Q}_{cont,1\to3} \tag{6.7c}$$

where $\dot{Q}_{conv,\alpha} = A_{conv,\alpha}(t) \cdot h_{conv,\alpha} \cdot (T_\alpha - T_{amb})$ represents convective losses, $\dot{Q}_{cond,\alpha} = A_{cond,\alpha}(t) \cdot h_{cond,\alpha} \cdot (T_\alpha - T_{amb})$ conductive losses of element α and $\dot{Q}_{cont,1\alpha\to\beta} = A_{cont,\alpha\beta} \cdot h_{cont,\alpha\beta} \cdot (T_\alpha - T_\beta)$ solid-to-solid heat transfer between elements α and β across the time-dependent contact area $A_{cont,\alpha\beta}$.

The movement of the SMA element during a cooling cycle is schematically shown in Fig. 6.23. Although only heat transfer of one bridge is considered, the counteracting bridge has to be considered for correct description of the mechanical
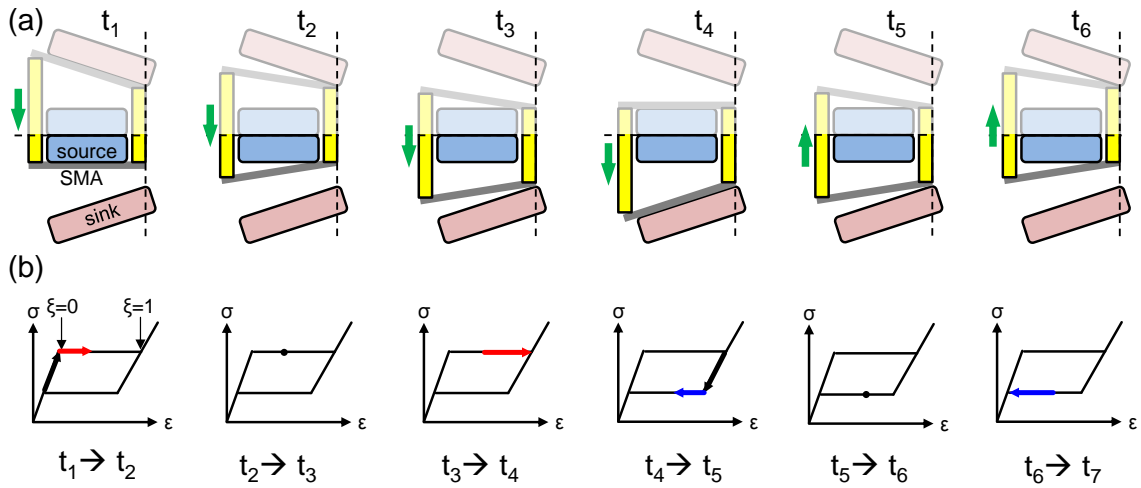
Figure 6.23: Mechanical behavior of concavely coupled double bridge device. (a) Schematic condition of the coupled device (only left half is shown) at time steps $t_1 \ldots t_6$ during a heat pumping cycle. (b) Stress-strain states of the lower bridge. Red arrows indicate heat release, blue arrows heat absorption.

device behavior. Strain and phase fraction within the SMA are calculated as a function of the device position. During mechanical loading of the lower bridge (downward movement, $t_1 \to t_4$), martensitic phase fraction increases from 0 to 1 and the bridge is heated up. However, self-heating only takes place during time intervals $t_1 \to t_2$, when the bridge is removed from the heat source, and $t_3 \to t_4$, when it is brought into contact to the lower heat sink. During the intermediate time interval $t_2 \to t_3$, both bridges are in force equilibrium during free movement of the coupled device and internal strain as well as phase fraction stay constant – hence, heat release is interrupted. Similarly, during mechanical unloading of the lower bridge (upward movement), self-cooling occurs during the intervals $t_4 \to t_5$ and $t_6 \to t_7$, whereas it is interrupted during interval $t_5 \to t_6$. For simplification, the model assumes that, in force equilibrium, both bridges have the same strain. In reality, the force equilibrium depends on whether the coupled device has been in contact to the upper or lower heat sink before due to mechanical hysteresis.

Geometries (volumes and surface areas) and heat capacities of the lumped elements are set to the experimental values of demonstrator D14. Heat transfer coefficients $h_{conv,\alpha}$, $h_{cond,\alpha}$ and $h_{cont,\alpha\beta}$ are adjusted in order to match experimentally measured temperature evolutions of sink and source for the operation frequencies 0.42 and $0.76\,\mathrm{Hz}$. As Fig. 6.24 shows, close agreement is reached for appropriate choice of heat transfer coefficients. The heat transfer coefficient for convection is set to $5\,\mathrm{W\,m^{-2}\,K^{-1}}$. Heat transfer coefficents for solid-to-solid contact between SMA and sink as well as SMA and source are estimated to $1200\,\mathrm{W\,m^{-2}\,K^{-1}}$ and $300\,\mathrm{W\,m^{-2}\,K^{-1}}$, respectively, in order to optimally fit experimental data. The considerably higher value for contact to the sink is attributed to the higher contact force. Simulation is also performed for the higher frequency $1.52\,\mathrm{Hz}$ wich could
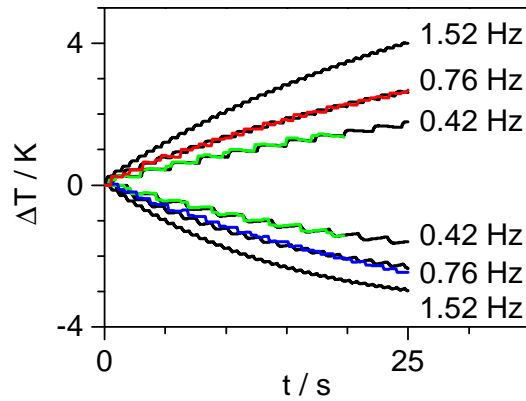
Figure 6.24: Temperature evolution in coupled bridge-based elastocaloric cooling device, simulated by thermal lumped-element model. Heat transfer is simulated for three different operating frequencies (black curves). Experimental data is included as colored curves. Compare Fig. 6.20 and Ref. [294].

not be reached in experiment. The result shows that higher heating/cooling rates and higher temperature lifts are feasible by increasing the operation frequency. Hence, the heat pumping capability was not yet fully exploited in the experiments described above.

6.4 Fatigue and device failure

The cooling devices characterized above usually had a limited lifetime due to mechanical failure of the SMA bridges. Failed devices are shown in Fig. 6.25, indicating the cycle number and location of fracture. In the case of single bridge devices, fracture locations are statistically scattered across the whole bridge length. In the case of coupled devices, on the other hand, fracture occured in one of the coupled bridges directly at the edge of the bridge frame in most cases, indicating that these locations are particularly stressed during cyclic operation. Scanning electron microscopy images (Fig. 6.26) of the breaking edges reveal a rough surface with possible crack nucleation points for both, film and foil samples. Lifetime of a bridge was between 85 and 256 cycles, which is clearly too low for practical applications.

The samples used for demonstrator experiments are cut from as-fabricated cold-rolled TiNiFe foil. Hence, sample surfaces are very likely to contain micro-cracks and other seeds for fracture. Lifetime of pseudoelastic SMA samples under tensile load can be tremendously increased by electropolishing or other polishing methods [110–112], which unfortunately could not be applied in the present work due to lack of equipment. The aim of the experiments has been to provide a proof-of-principle, for which the lifetime of untreated samples was sufficient.

When targeting technical application, a careful polishing of the SMA bridges prior to integration in a microcooling system will be necessary. Also, bridge lifetime may be increased by optimizing the loading conditions. Amongst others, options for improvement include more gentle acceleration and deceleration of the device and eliminating sharp edges at the heat sources and sinks, as well as support frames of the bridges.
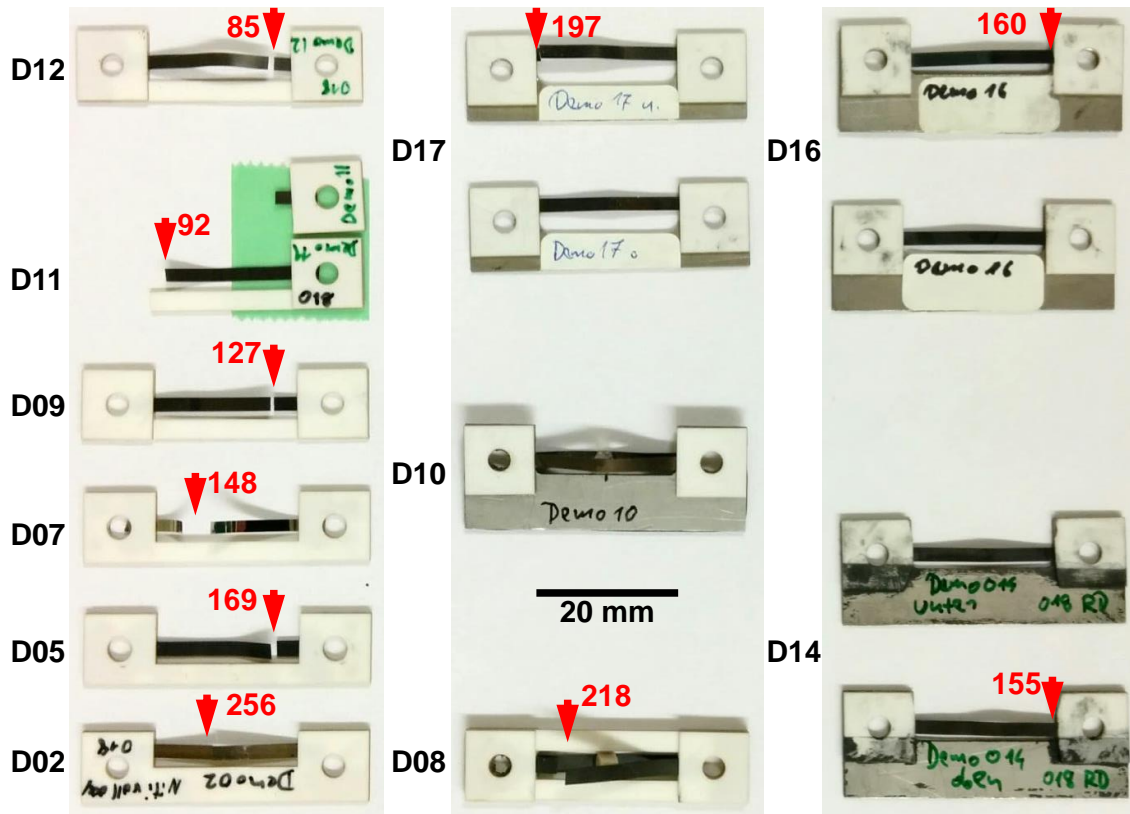
Figure 6.25: SMA bridge-based cooling failed by mechanical breaking during cyclic operation. The number of operation cycles until failure as well as the position of fracture are indicated.

6.5 Discussion

In this chapter, concepts for elastocaloric microcooling based on thin SMA foils and films have been presented. The concepts are based on out-of-plane deflection of freestanding SMA bridges, requiring only a single linear actuator for operation. Compared to in-plane actuation, the required maximum forces are reduced, whereas stroke is increased. By coupling two pre-strained bridges to form an antagonistic pair, partial recovery of unloading work is implemented. While the work input $\Delta W = W_{load} - W_{unload}$ is identical for in-plane and out-of-plane coupling, the total work input W_{load} is somewhat lower for in-plane coupling. In case of out-of-plane coupling, stress plateaus adopt a finite slope and coupled
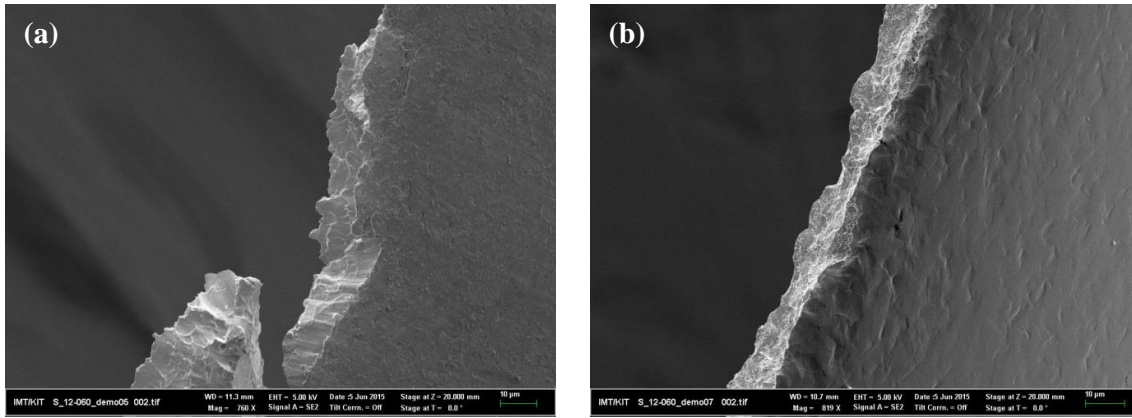
Figure 6.26: Scanning electron microscopy (SEM) images of the breaking edge in failed SMA bridge devices: (a) cold-rolled TiNiFe foil and (b) sputter-deposited TiNi film sample.

devices have two points of force equilibrium. Mechanical history determines, in which one of the two equilibrium states the device is found. The equilibrium state leads to an interruption of phase transformation and corresponding self-heating/cooling during loading/unloading of the device.

Heat transfer is realized by solid-to-solid contact between SMA and heat source / sink segments fabricated from copper. Thermal switching is performed by the same actuator as mechanical loading and unloading. The mechanism can be regarded a simple form of a thermal switch. Heat pumping performance may be increased by improving thermal contact. This might be achieved, for instance, by increasing contact forces or introducing flexible, thermally conductive interface layers. In the presented device layouts, compliant mechanisms produced by 3D printing are introduced in order to improve alignment of sink and source with respect to the SMA bridges. The spring constants of these clompliant mechanisms may be further optimized.

Sample lifetime of unpolished, mechanically structured TiNiFe foils was sufficient for proof-of-principle experiments, but has to be increased considerably for practical application. This might be achieved by electro-polishing or other polishing procedures, eliminating crack seeds.

Although the presented concepts are aimed at miniature-scale applications, total heat pumping power may be upscaled by massive *parallelization*. Meso-scale applications benefit from the fast heat transfer in thin foils and films in just the same way as microcooling applications. Grund et al. have shown a route for parallel fabrication of SMA devices for out-of-plane actuation [309], and Barth et al. fabricated antagonistic devices for bi-stable microvalves [306, 307]. A very similar fabrication process might be applied for fabrication of cooling devices.

In the presented device concepts, the temperature lift is ultimately limited by the adiabatic temperature change ΔT_{ad} of the elastocaloric material. In case this

temperature lift is not sufficient for the intended application, the lift might be increased by *cascading* of cooling devices.

6.6 Alternative concepts for elastocaloric microcooling

In the present work, a cooling device concept based on solid-to-solid heat transfer was chosen due to its simplicity. However, many of the device concepts reviewed in chapter 3 may be applied for elastocaloric microcooling as well, each having specific advantages and disadvantages. In the following, alternative design routes for elastocaloric cooling are presented, considering the special requirements of miniature-scale applications. These may serve as a guideline for future development.

A convenient way of transporting heat, e.g., between two solid heat exchangers, is by using a liquid heat transfer medium. A liquid easily adapts arbitrary surfaces (such as in porous materials) and may be directed and controlled by channels, valves and pumps. The majority of magnetocaloric cooling demonstrators rely on solid-to-liquid heat transfer. In vapor compression the active medium itself is a liquid during half of the cooling cycle.

In an elastocaloric heat pump based on solid-to-liquid heat transfer, the active SMA material has to be integrated into a fluidic system, leading to various constructional challenges. On the other hand, fluid control provides great flexibility in the timing of heat transfer. In contrast to the solid-to-solid concept, heat transfer to source and sink may begin simultaneously with heat release/absorption in the active material, since strong thermal coupling is guaranteed. In many cases, heat is transferred from the fluid to solid heat sources and sinks using heat exchangers.

As applications in IC cooling, inkjet printing, bio technology and many other fields show, fluid control using valves and pumps is in principle microtechnology-compatible. Heat exchangers may also be fabricated in a microtechnology compatible way [10, 263].

6.6.1 Static concept

The first fluid-based layout presented here will be referred to as 'static concept' since heat source and sink remain static during device operation. Similar concepts have been proposed in literature, which work analogously to a heat engine operated in reverse direction. An overview of corresponding concepts from literature is given in Fig. 3.7 on page 63.
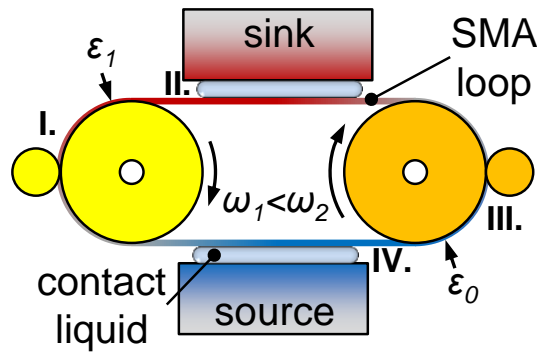
Figure 6.27: Schematic of static concept for elastocaloric microcooling based on a closed SMA loop.

For small-scale application, a simple layout with few components is required. A closed loop of SMA film or foil band may be used as active material, which is continuously driven through a cycle in such a way that it alternatingly enters two liquid baths acting as heat sink and source. Alternatively, thin liquid films may be used to thermally couple the band to a solid heat source and sink, as shown in the schematic of Fig. 6.27. In order to achieve stress-induced phase transformation, the band has to be stressed in one part of the cycle and relaxed in the other. This can be obtained by guiding the band across several rolls turning at two different velocities. If one of the rolls is, for instance, rotating 5% faster than its neighboring roll and both rolls have the same diameter, then the SMA band will be strained by 5% when passing from the slower to the faster roll. Strain will be released when the band passes from the faster to the slower roll.

A serious challenge of the static concept is the fabrication of a closed loop of SMA band material. The material junction has to withstand bending forces, as well as repeated stress-induced martensite and reverse transformation over millions of cycles. A closed loop of SMA film or foil band may be fabricated, e.g., by sputtering SMA films on a cylindrical target [310] or cutting rings from a sufficiently thin-walled SMA tube.

A meso-scale demonstrator for the static elastocaloric concept was constructed by Massy Mehran in his master thesis [303]. The setup is shown in Fig. 6.28. In this case, closed loops of pseudoelastic TiNi wires (Memry / SAES Getters) with a diameter of $254\,\mu\mathrm{m}$ are used as active material, which are fabricated by laser-welding the ends of a wire piece and additionaly applying a stainless steel crimp for mechanical protection of the weld. In the demonstrator, an array of five wire loops is guided by a number of rolls. Two of the rolls, which are used to apply force to the wire loops, are coupled to each other by a gear belt. The desired maximum strain in the wire is adjusted by the gear transmission ratio. The force is applied to the wire by guiding it through tapered slits in the two rolls. The other rolls are freely movable. The heat source is realized as a liquid bath filled with a small amount of water (see 6.28 (b); not shown in the schematic (a)), through which the wire loops are guided after releasing the strain. Afterwards, strain
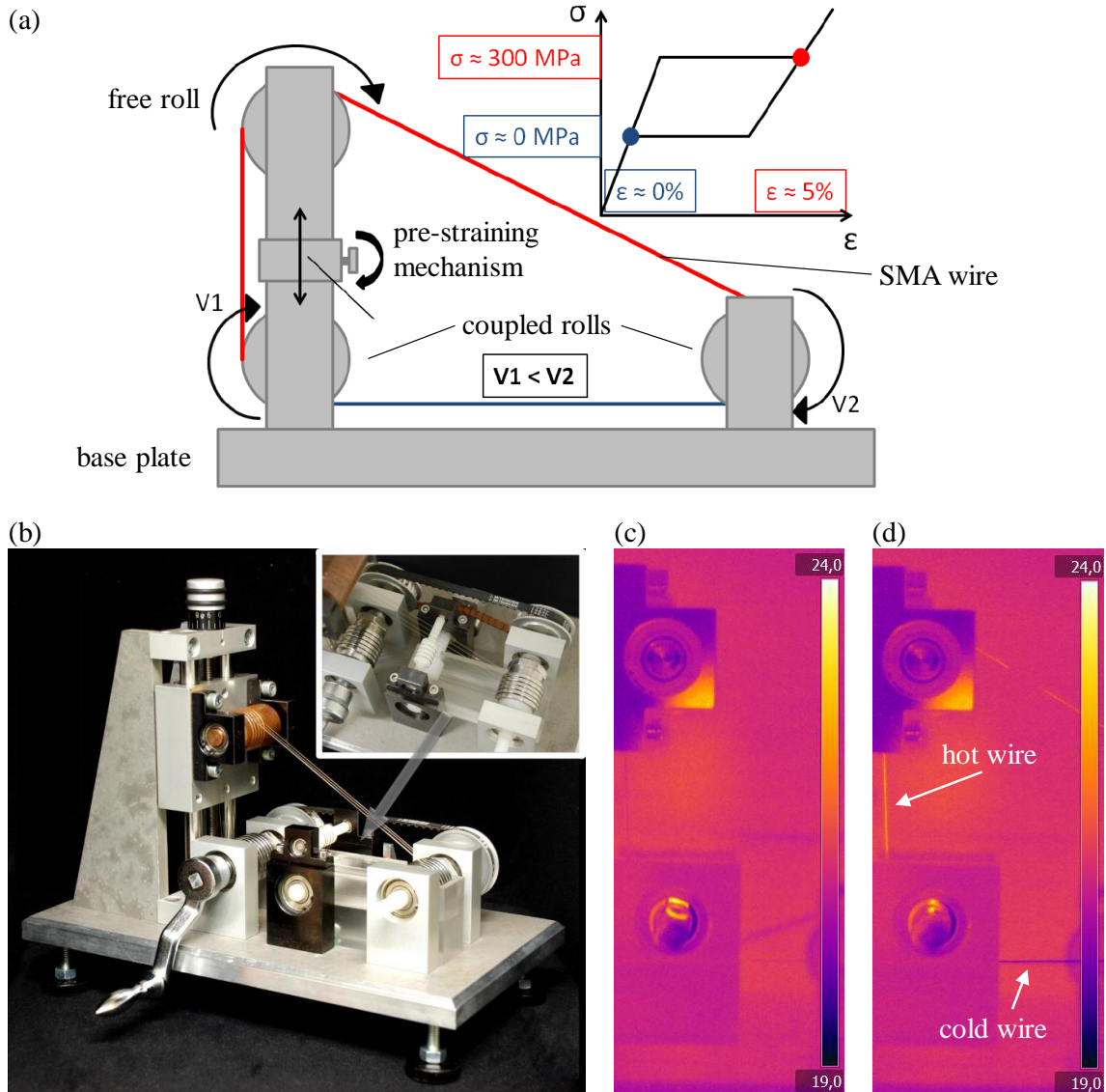
Figure 6.28: Mesoscale demonstrator for the static elastocaloric concept developed in the master thesis of Massy Mehran. (a) Schematic of the device: a bundle of closed SMA wire loops is guided around three rolls. One roll is freely movable, whereas the other two are coupled by a gear belt and rotate with slightly different velocities. Prior to operation, the wire loops are pre-strained. (b) Photograph of the demonstrator. A comparison of IR thermograms of the still-standing (c) and hand-operated demonstrator (d) reveals elastocaloric cooling and heating in the wire. Figures modified from Ref. [303].

is applied and heat is released to a heat sink roll made from copper, as well as the surrounding air. Infrared measurements reveal that the setup is in principle working, as part of the wire is continuously cooling during operation, whereas the remaining wire is releasing heat. However, due to the high thermal mass of the liquid bath as well as losses to the guiding rolls, the cooling effect measured in the liquid bath is negligible. In order to improve the setup, the ratio of active SMA material and heat sink/source has to be drastically increased and the rolls should be fabricated from a material with lower thermal conductivity (e.g., glass, ceramics or a hard polymer).

6.6.2 Regenerator concept

Components:
(1) SMA regenerator beds
(2) Heat transfer fluid circuit
(3) Heat sink
(4) Heat source
(5) Linear motor
(6) Fluid displacer

Operation steps:
I. Loading
II. Heat release to sink
III. Unloading
IV. Heat absorption from source
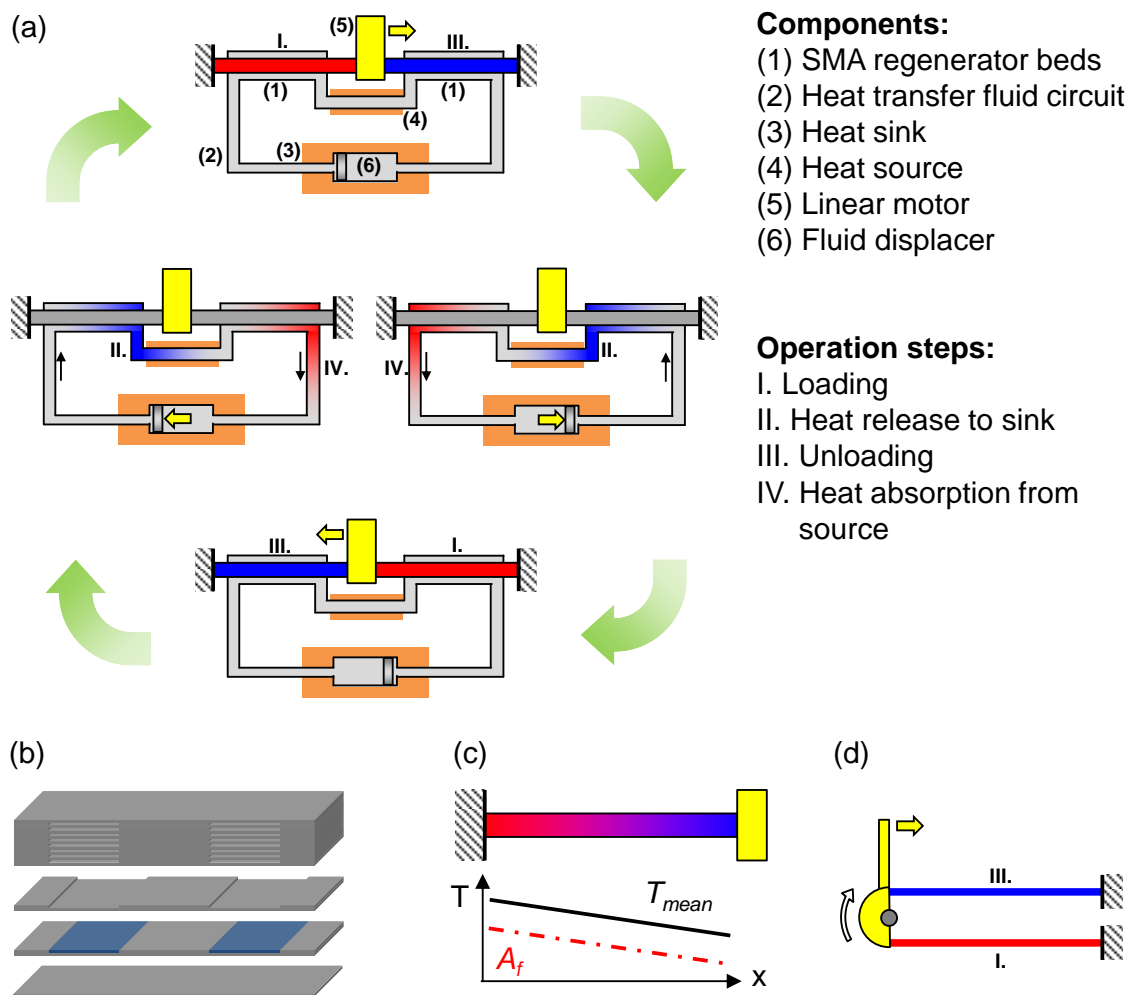
Figure 6.29: Active regenerator concept for elasocaloric microcooling. The setup contains two regenerator beds of SMA films or foils forming an antagonistic pair. Heat exchange is realized with a heat transfer fluid pumped back and forth within a closed fluid circuit.

The concept of active regeneration was described in section 3.2.3 and is particu-

larly promising since it allows for temperature lifts exceeding the adiabatic temperature change of the active material. The current world record for the temperature lift of an elastocaloric device was achieved by Tušek and co-workers using a TiNi foil-based regenerator device having a single regenerator bed [291].
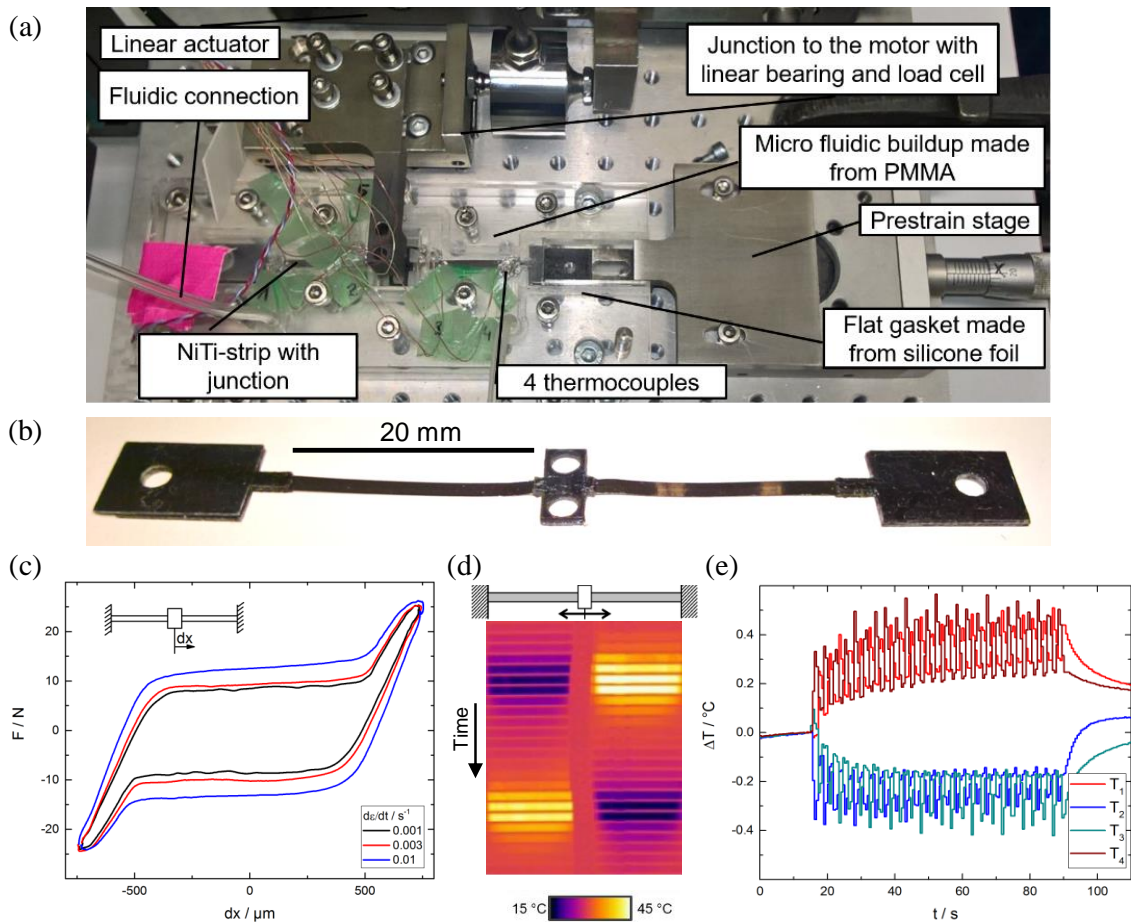
Figure 6.30: Demonstrator implementing the concept of active elastocaloric regeneration on a small scale, developed in the master thesis of Florian Brüderlin. (a) Experimental setup, (b) coupled device comprising two cold-rolled TiNiFe foil elements with the dimensions $20 \times 2 \times 0.03 \, \text{mm}^3$ which are connected in length direction. (c) Force-displacement characteristic of the coupled device operated at different strain rates. (d) Chronological series of IR thermograms of the device operated in air at a strain rate of $0.1 \, \text{s}^{-1}$. (e) Time-dependent temperature evolution of the heat transfer fluid in a heat pumping experiment at $0.33 \, \text{Hz}$, measured by thermocouples at the inlets and outlets of both regenerator beds. Figures modified from Ref. [311].

Here, a somewhat simpler device concept targeted at small-scale cooling, which on the other hand includes work recovery, is proposed in the following. The schematic device layout and cooling cycle are shown in Fig. 6.29 (a). The layout comprises two regenerator beds of elastocaloric foils or films which are coupled to form an antagonistic pair (in-plane; compare also section 6.1.3). The regenerator beds are connected by a microchannel loop containing a heat transfer fluid,

which is guided through the heat sink and source. During each operation half-cycle, one of the regenerator beds is mechanically loaded (I.) while the other one is unloaded (III.). The the heat transfer fluid is pumped through the microchannel in such a way, that fluid is transported from the cold bed to the heat source (or 'cold heat exchanger' CHEX) and from the hot bed to the sink ('hot heat exchanger', HHEX). During the second operation half-cycle, the roles of both regenerator beds are reversed and the fluid is pumped in opposite direction. After a sufficient run-in phase, stationary temperature gradients are obtained along both regenerator beds. The setup does not require any valves and fluid pumping might be achieved by a displacer driven by electrostatic or electromagnetic forces.

A particular challenge of active regenerators is the temperature gradient along the active material. According to the Clausius-Clapeyron relation, the cold end of each SMA film stripe would undergo stress-induced transformation at a lower stress than the hot end, which might lead to premature device failure. An optimal solution would be pseudoelastic SMA films having gradient of transformation temperatures along the length-direction (Fig. 6.29 (c)). Such films may be produced by co-sputtering using two targets with different stoichiometry, since transformation temperatures sensibly depend on chemical composition.

In order to increase the mass of active material while maintaining a high surface-to-volume ratio, arrays of elastocaloric films might be used (Fig. 6.29 (b)). An alternative for coupling the films in length direction migth be coupling them to a rotary joint as indicated in Fig. 6.29 (d). This way, films may be arranged parallely in a more compact way and a leverage may be used to scale-up actuation forces.

A first prototype combining active elastocaloric regeneration and heat recovery by the antagonistic principle was developed by Florian Brüderlin in his master thesis [311]. The setup is shown in Fig. 6.30. A microchannel was micro-milled into a acrylic glass (PMMA) plate (Fig. 6.30 (a)), in which two coupled TiNiFe foil stripes are inserted (Fig. 6.30 (b)). The length of both regenerator beds is $20\,mm$, width and thickness of the foils are $2\,mm$ and $30\,\mu m$, respectively. The regenerator porosity (total volume minus volume fraction of active material) is about 80%. The TiNiFe foils are loaded by an electromagnetic linear motor (ESR Pollmeier) with a maximum force of $200\,N$. Water is used as heat transfer fluid, which is pumped back and forth by piezoelectric micro pumps (Bartels).

The force-displacement characteristics for different strain rates, as well as the elastocaloric temperature change measured by IR thermography of the device operated without fluid in the channel are shown in Figs. 6.30 (c) and (d). A preliminary result of the heat pumping performance at a cycling frequency of $0.33\,Hz$ is shown in Fig. 6.30 (e). Temperature measurements by thermocouples at both ends of each regenerator bed reveal a maximum temperature lift of $0.8\,K$. Considerable improvements are expected in future experiments by increasing the mass of active material as well as regenerator porosity (e.g., in the experiment of Tušek [291] porosity was 50%), reducing thermal losses and increasing the cycling frequency.

6.6.3 Heat switches

I. Loading of SMA
II. Heat release to sink
III. Unloading of SMA
IV. Heat absorption from source
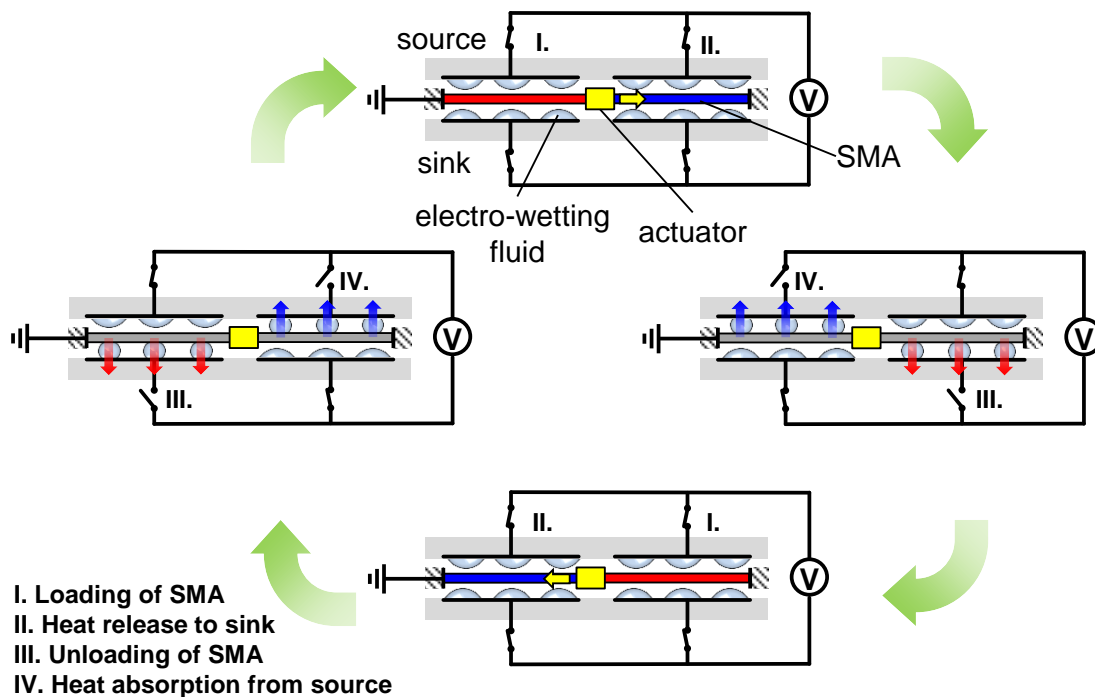
Figure 6.31: Heat switch concept for elastocaloric micocooling based on electro wetting. An antagonistic pair of SMA films is used as active material. Thermal contact is established by fluid drops controlled by electrical fields between the SMA films and heat sink/source.

Very compact heat pumping devices for small-scale applications may be realized using heat switches to direct heat flows between active material and heat source/sink.

In the following, a concept is proposed in which heat switching is achieved by electro wetting [191, 312]. The schematic layout is shown in Fig. 6.31. Again, a pair of SMA foils or films coupled in length direction is used as active material in order to achieve work recovery. The SMA foils are placed in the small gap between two plates representing heat source and sink. Specially designed micro-electrodes are arranged on the surface of each plate heading towards the SMA foils, covered by a thin hydrophobic film. In order to establish thermal contact between sink/source and SMA foils, a number of fluid droplets is placed in between both. Due to the hydrophobic film, the contact angle will be high and each droplet contacts the elecrode plane as well as the SMA, acting as a heat bridge. When thermal contact needs to be turned off in order to direct heat flows, a strong electric field is applied to the drops via the micro electrodes, causing them to wet the electrode surface and loose contact to the SMA. The electrodes may be realized as comb-like structures or concentric rings alterntingly connected to the voltage potential and ground electrode. Alternatively, the electrically coductive SMA foils may be used as common ground electrode, as indicated in the scheme.

An even more flexible way of distribution heat and cold using electro wetting is represented by digital microfluidics [313]. Using arrays or matrices of flat electrodes which can be switched individually, drops of heat transfer fluid (or liquid specimens, analytes or the like to be cooled) may be directed towards and away from the elastocaloric material.

6.6.4 Comparison

A comparison of the proposed concepts for elastocaloric small-scale cooling is given in Table 6.4. Each of the concepts has its specific advantages and disadvantages. Due to its compactness, the thermal switch concept would be the most convincing for small-scale applications. However, an efficient heat switch mechanism is still to be identified. As said before, the solid-to-solid heat transfer concept developed within this thesis may be regarded as a very simple kind of heat switch, since the mechanical (and therefore also thermal) contact between SMA film and sink/source is switched. Due to the out-of-plane deflection, only a single actuator is required for this, but on the other hand devices can not be built as flat as in case of the alternative concepts. It was shown above that temperature lifts in the order of $10\,\mathrm{K}$ are feasible with a single cooling stage.

In case the adiabatic temperature change of the active material is not sufficient for the target application, several cooling stages have to be connected in series to form a cascade. Alternatively, the regenerator concept may be used, which allows for high temperature changes in a single stage (provided that the regenerator length is chosen appropriately). For optimal operation, an elastocaloric regenerator requires SMA films having a functional gradient of the transformation temperatures along the film length, adapted to the steady-state temperature profile reached along the regenerator bed. Such films may be produced by sputter deposition and are already under development at the University of Kiel.

In order to achieve active regeneration in a still very compact setup, a combination of the regenerator concept with digital microfluidics might be a solution. With the help of electrically controlled microfluidics, a small amount of heat transfer fluid might be shifted ('pumped') forth and backwards along the regenerator bed without the neccessity of any pumps or valves.

Table 6.4: Comparison of different concepts for elastocaloric cooling in miniature scale.

Concept	Advantages	Disadvantages
Solid-to-solid heat transfer	• Simplicity: Only a single linear actuator required • Fluid-free • Compact	• Temperature lift $\leq \Delta T_{ad}$ • High mechanical stressing of SMA films/foils • May induce mechanical vibrations in setup
Static concept	• Sink and source in rest, active material circulating / 'flowing' • Work recovery intrinsic (coupling of rolls)	• Temperature lift $\leq \Delta T_{ad}$ • Relative movement of active material with respect to sink/source complicates heat transfer • Strong mechanical contact force of rolls leads to high parasitic heat flows
Regenerator	• Temperature lift $\gg \Delta T_{ad}$ feasible • Independent control of SMA (un)loading and heat transfer	• Complexity (fluid channel, pump/displacer, valves) • Fluid involved, having relatively high thermal mass
Heat switch	• Potentially very compact • No additional moving parts; sink/source and active material mechanically de-coupled	• Temperature lift $\leq \Delta T_{ad}$ • Fuid control system involving high electric fields (depending on heat switch technology)

7 Conclusion and Outlook

The aim of this work was to explore the potential of the elastocaloric effect for miniaturized cooling applications. The elastocaloric performance of several samples with thin geometries has been investigated by uniaxial tensile tests in combination with infrared thermography and digital image correlation. Material investigation has been supplemented by finite element simulation using a phenomenological Tanaka-type shape memory model. Finally, the experimental findings have been used to design and implement first-of-its-kind demonstrators for elastocaloric miniature-scale cooling. In the following, the results will be summarized and an outlook for future development will be given.

Elastocaloric materials In order to perform cooling and heat pumping on a small scale, thin shape memory alloy samples are required. These have the advantage of allowing for particularly effective heat transfer due to their large surface-to-volume ratio. In this work, polycrystalline samples of three major SMA classes – kindly provided by cooperation partners – have been studied: TiNi-based, Cu-based and magnetic shape memory alloys. While results on the latter two revealed the need for further improvement in structural and functional properties, TiNi-based alloys turned out to be highly promising for elastocaloric cooling. Tensile tests are performed on samples of cold-rolled TiNiFe foils, as well as sputter-deposited TiNi and TiNiCuCo films having thicknesses of 30 and $20\,\mu m$, respectively. Similar investigations have been reported before in literature, however, in these cases samples have been by at least a factor of ten thicker. Furthermore, in contrast to previous work, special emphasis was put here on heat exchange and the elastocaloric self-cooling effect during mechanical *unloading* of the pseudoelastic materials.

The thermo-mechanical sample performance was shown to be strongly dependent on strain rate. In the case of quasi-static experiments, mechanical hysteresis is lowest and elastocaloric temperature changes are negligible because heat exchange with the environment is much faster than release and absorbtion of latent heat. Upon increasing the strain rate, mechanical hysteresis and temperature change increase as well, until saturating at a maximum value for strain rates above the adiabatic limit of $0.2\,s^{-1}$. In elastocaloric applications, high cycling frequencies are desired in order to reach high heat pumping powers. Therefore, the hysteresis under adiabatic conditions is technically more relevant than the hysteresis under quasi-static conditions. The increase of hysteresis is a direct consequence of the increasing *self-heating* and *self-cooling* effect: The rate of heat

release and absorption is directly determined by the strain rate during loading and unloading. On the other hand, heat exchange with the environment due to air convection and conduction through the sample fixation is only dependent on thermal boundary conditions, and has a time constant in the order of $1\,\mathrm{s}$ in the present investigation. Under adiabatic conditions, a maximum heating of $21\,\mathrm{K}$ and a cooling of $-17\,\mathrm{K}$ was obtained by TiNiFe foil samples. For TiNi films, the effect was a few Kelvin lower, and for the TiNiFe foils, the cooling effect of $-12\,\mathrm{K}$ was unexpectedly more pronounced than the heating effect of $9\,\mathrm{K}$.

The elastocaloric performance is measured by the material coefficient of performance (COP), which is the ratio of transported heat (estimated from IR measurement and heat capacity) and the mechanical work input (area enclosed by the stress-strain characterisitic). The highest COP is obtained for TiNiCuCo films due to their very low hysteresis. In all cases, the latent heats determined by differential scanning calorimetry were by at least a factor of two higher than the latent heat estimated from IR measurements during tensile experiments. This finding seems to be an indication for a fundamental difference between thermally and stress-induced martensitic phase transformation. In literature, it is sometimes explained by an incomplete stress-induced transformation, preserving a fraction of 'lazy austenite'. By achieving a better understanding of this effect and possibly overcoming it, elastocaloric cooling performance could be greatly increased.

The elastocaloric effect was found to be strongly localized due to the formation of Lüders-like strain bands and closely related temperature bands. These bands are consistently oriented in an angle of $\pm 55°$ with respect to loading direction for all three investigated TiNi-based samples. Simulations of localized band formation (performed by F. Wendler at KIT) using a thermodynamic phase-field model show that the band angle depends on sample geometry rather than being an intrinsic material property [304]. In accordance with literature reports on thicker samples, the number of bands increases from only one or two in the quasi-static limiting case up to a dense network in the adiabatic limit. In case of TiNiFe foils, band formation is dependent on rolling-induced texture. The TiNi film samples revealed strong functional degradation, leading to cigar-shaped stress-strain relationships and a vanishing of sharp strain bands within the first few load-unload cycles. In the TiNiCuCo films, Lüders bands were either very stable upon cyclic loading, or did not occur at all. A possible reason may be the different fabrication techniques. In the latter case, films were produced by alternatingly depositing TiNiCu and Co layers, which might have been homogenized incompletely during annealing.

Besides the adiabatic temperature change and mechanical performance, a third crucial material parameter is cyclic stability. In a typical application, the elastocaloric material has to withstand millions of load-unload cycles without severe structural and functional fatigue. Newly developed quaternary TiNiCuCo films (which are amongst the materials characterized in this work) have recently received great attention due to their extraordinary microstructural properties and

crystallographic compatibility between the martensitic variants and the austenite lattice. These new low-hysteresis materials point out the direction for future development in elastocaloric cooling. In order to pave the way for commercial applications, however, the materials have to be fabricated in large quantities and become commercially availible. Currently, the fabrication of fatigue-free films relies on sputter-deposition, which yields very high purity alloys with low thickness, but is rather expensive. Cold-rolling is capable of producing larger quantities of sheet material, but becomes increasingly challenging with decreasing foil thickness and is not applicable for brittle materials. A third production route to be considered is melt-spinning, which requires further optimization in order to deliver structurally stable films.

The large latent heat of classical near-equiatomic TiNi, as well as the superior cyclic stability of ternary TiNiCu indicate that the TiNi-system is currently the most promising for elastocaloric cooling, and material development should be focused on finding corresponding optimized ternary and quaternary alloys.

Material simulation In order to obtain a deeper understanding of the elastocaloric sample behavior, finite element simulations have been performed. A phenomenological Tanaka-type model has been chosen for its simplicity and because it is based on experimentally accessible material parameters. This model combined with a heat transfer model allowed for close approximation of the mechanical behavior as well as very good reproduction of the elastocaloric effect and heat transfer dynamics as a function of strain rate in samples *without* localized Lüders-like effects. The increase of mechanical hysteresis and self-heating and cooling with increasing strain rate was captured solely by including latent heat and Clausius-Clapeyron relation between critical stresses and temperature.

By assuming a very sharp transformation and adding a spatial gradient term to the model, basic band formation and propagation behavior could be described as well. However, bands were not as sharp as in the experiment, and the increasing band number at high strain rates could not be reproduced.

The model is therefore primarily suitable for simulation of averaged elastocaloric heat generation/absorption and might be used for simulation of thermo-mechanical material performance in real devices. For simulation of thermal performance at the device level, a *lumped element model* was used, which proved to be sufficient to closely reproduce the heating and cooling performance of demonstrators. In terms of achieving a better understanding of Lüders-like band formation, thermodynamic models like the Seelecke-Müller-Achenbach models in combination with a phase field approach are probably a more promising choice for future work [304]. The extended model contains more fundamental material properties like the interfacial energy of the martensite-austenite interface. It is able to capture rate-dependent number and distribution of strain bands, band orientation as well as temperature bands in very close agreement with experimental observations.

Elastocaloric devices Chapter 6 of this work was dedicated to the development of an elastocaloric heat pumping demonstrator. While the major requirements on an elastocaloric material are a large adiabatic temperature change, reversibility over large number of operation cycles, rapid heat transfer and a low work input, the task of a heat pumping device is to separate heat flows in a most efficient way.

Among the different possible heat transfer modes, a heat transfer concept based on conduction between the SMA and a solid heat sink and source in direct (*solid-to-solid*) contact was chosen for its simplicity. Due to the thin geometry of the samples, martensitic transformation could be induced by *out-of-plane* deflection of SMA bridges fixed on both ends. In this case, loading is performed in a quasi-tensile way, while bending forces are negligible. By alternatingly pressing a SMA bridge against the convex surface of a heat sink, followed by the flat surface of a heat source, the steps of loading/unloading and the thermal contact switching could be united. The device is operated by a single linear actuator, which is required for elastocaloric cooling in any case to provide the mechanical driving field. The presented heat transfer mechanism can be considered as a simple form of a heat switch.

In order to increase the device-level coefficient of performance, *work recovery* is implemented by coupling two SMA bridges to form antagonistic pairs: Both bridges are operated with a phase shift of half a cooling cycle and mechanical work stored in the bridge being unloaded is constantly transferred to the respective counteracting bridge. By this method, most of the unloading work can be recovered. In order to obtain the maximum possible work recovery, more than two devices would have to be coupled, as is done for example in the drum-like or continuously operated device schemes shown in Figures 3.7 and 3.8.

Antagonistic devices are built using TiNiFe foil bridges of $20\,\text{mm}$ length, $2\,\text{mm}$ width and $30\,\mu\text{m}$ thickness by coupling two bridges with a spacer in between. Coupling is performed either in a concave or convex way, which is completely equivalent except for the positions of heat sink and source. The sink and source are fabricated from several individual copper segments placed on compliant polymer structures produced by 3D printing. These structures allow for self-alignment of the sink/source surfaces with respect to the SMA bridge. A maximum temperature lift of $9.4\,\text{K}$ between source and sink is obtained by a coupled device operated at $0.75\,\text{Hz}$. The ratio of heat capacities between SMA and sink/source was 1:128 and 1:72, respectively. The estimated heating and cooling powers are 70 and $45\,\text{mW}$ and the device-level COPs are 4.9 and 3.1 for heating and cooling, respectively. Lumped-element simulations indicate that even higher temperature lifts are feasible by increasing the operation frequency (which could not be realized due to limitations of the actuator used here). Further performance increase may also be achieved by optimizing the solid-to-solid heat transfer, e.g., by increasing contact forces and contacting areas, as well as by introducing thermally conductive interface layers.

Experiments also revealed that the temperature lift could not be increased by decreasing the masses of sink and source. This observation points out a challenge of small-scale applications: Surface-to-volume ratios do not only increase for the SMA element, but also for other parts of the device, which leads to increased parasitic heat flows. Therefore, thermal insulation is of particular importance.

The temperature lift of the proposed device scheme is ultimately limited by the adiabatic temperature change of the elastocaloric material. Since the temperature change is up to $20\,\mathrm{K}$ for the investigated materials, and up to three times higher values have been reported for bulk TiNi in literature, this may be already sufficient for many applications. In case higher temperature lifts are required, several devices could be coupled thermally in series by *cascading*.

A kind of continuous cascade of infinitesimal portions of material is realized in the concept of *active regeneration*. In this approach, heat transfer is accomplished using a fluid which is pumped back and forth a regenerator bed filled with caloric material. Maximum temperature lifts are no longer limited by the material's adiabatic temperature change, but rather by thermal boundary conditions and geometrical properties of the device. Recently, Tušek et al. reported a relatively compact elastocaloric regenerator setup (when neglecting the actuator size) reaching a temperature lift of more than $15\,\mathrm{K}$ and COPs of up to 7, which is to date the best experimentally achieved performance of an elastocaloric device. The concept of active regeneration may be also very attractive for microcooling. Digital microfluidics provide a very flexible way of handling small amounts of liquids on a chip scale, without the need for pumps or valves. Heating and cooling could be combined with chemical analysis steps, e.g., in lab-on-chip systems or DNA cyclers. For an optimum operation of elastocaloric regeneration, novel materials with *functional gradients* have to be developed. This way, transformation temperatures may be adapted to the temperature profile along the regenerator bed under steady-state operation.

The current work was aimed at small-scale cooling and temperature control applications as required for instance in microelectronics, chemical and biological analysis or certain medical applications. However, the advantage of fast heat transfer in thin samples is equally useful for meso- and macroscale applications. Higher total cooling powers may be obtained by massive parallelization of SMA bridge devices into large *distributed arrays*. Similar to magnetocalorics, wine coolers may be envisioned as pilot application.

Despite the presence of shape memory alloys for already half a century, the potential of elastocaloric cooling was underestimated and neglected for a long time. However, starting from the early 2010s, progress in material as well as device development has attracted interest and created awareness in public funding agencies as well as commercial enterprises. Hopefully, the increased efforts will eventually lead to first commercial application within the next decade. A challenge still to be tackled is the identification of actuators capable of providing the huge mechanical forces to drive the cooling process, while at the same time being reasonably compact, energy-efficient and quiet.

Acknowledgement

Bibliography

[1] W. Goetzler, R. Zogg, J. Young, and C. Johnson, "Energy savings potential and RD&D opportunities for non-vapor-compression HVAC technologies", *Navigant Consulting Inc., prepared for US Department of Energy*, 2014.

[2] C. Park, H. Lee, Y. Hwang, and R. Radermacher, "Recent advances in vapor compression cycle technologies", *International Journal of Refrigeration*, vol. 60, pp. 118–134, 2015. DOI: `10.1016/j.ijrefrig.2015.08.005`.

[3] G. E. Moore, "Cramming more components onto integrated circuits, reprinted from electronics, volume 38, number 8, april 19, 1965, pp.114 ff.", *IEEE Solid-State Circuits Newsletter*, vol. 20, no. 3, pp. 33–35, 2006. DOI: `10.1109/n-ssc.2006.4785860`.

[4] V. Pastukhov, Y. Maidanik, C. Vershinin, and M. Korukov, "Miniature loop heat pipes for electronics cooling", *Applied Thermal Engineering*, vol. 23, no. 9, pp. 1125–1135, 2003. DOI: `10.1016/s1359-4311(03)00046-2`.

[5] Y. Maydanik, S. Vershinin, M. Korukov, and J. Ochterbeck, "Miniature loop heat pipes – a promising means for cooling electronics", *IEEE Transactions on Components and Packaging Technologies*, vol. 28, no. 2, pp. 290–296, 2005. DOI: `10.1109/tcapt.2005.848487`.

[6] L. Vasiliev, "Micro and miniature heat pipes – electronic component coolers", *Applied Thermal Engineering*, vol. 28, no. 4, pp. 266–273, 2008. DOI: `10.1016/j.applthermaleng.2006.02.023`.

[7] K. Schubert, J. Brandner, and M. Fichtn, "Microstructure devices for applications in thermal and chemical process engineering", *Microscale Thermophysical Engineering*, vol. 5, no. 1, pp. 17–39, 2001. DOI: `10.1080/108939501300005358`.

[8] J. Schütze, H. Ilgen, and W. Fahrner, "An integrated micro cooling system for electronic circuits", *IEEE Transactions on Industrial Electronics*, vol. 48, no. 2, pp. 281–285, 2001. DOI: `10.1109/41.915406`.

[9] J.-Y. Chang, H. S. Park, J. I. Jo, and S. Julia, "A system design of liquid cooling computer based on the micro cooling technology", in *Thermal and Thermomechanical Proceedings 10th Intersociety Conference on Phenomena in Electronics Systems, 2006. ITHERM 2006.*, Institute of Electrical & Electronics Engineers (IEEE), 2006. DOI: `10.1109/itherm.2006.1645337`.

[10] J. J. Brandner, L. Bohn, T. Henning, U. Schygulla, and K. Schubert, "Microstructure heat exchanger applications in laboratory and industry", *Heat Transfer Engineering*, vol. 28, no. 8-9, pp. 761–771, 2007. DOI: `10.1080/01457630701328528`.

[11] C. B. Vining, "An inconvenient truth about thermoelectrics", *Nature Materials*, vol. 8, no. 2, pp. 83–85, 2009. DOI: `10.1038/nmat2361`.

[12] S. Fähler, U. K. Rößler, O. Kastner, J. Eckert, G. Eggeler, H. Emmerich, P. Entel, S. Müller, E. Quandt, and K. Albe, "Caloric effects in ferroic materials: New concepts for cooling", *Advanced Engineering Materials*, vol. 14, no. 1-2, pp. 10–19, 2011. DOI: `10.1002/adem.201100178`.

[13] J. Cui, Y. Wu, J. Muehlbauer, Y. Hwang, R. Radermacher, S. Fackler, M. Wuttig, and I. Takeuchi, "Demonstration of high efficiency elastocaloric cooling with large ΔT using NiTi wires", *Appl. Phys. Lett.*, vol. 101, no. 7, p. 073 904, 2012. DOI: `10.1063/1.4746257`.

[14] W. Demtröder, *Experimentalphysik 1 – Mechanik und Wärme*. Springer, 2005, ISBN: 978-3540260349.

[15] F. Sarvar, D. Whalley, and P. Conway, "Thermal interface materials – a review of the state of the art", in *2006 1st Electronic Systemintegration Technology Conference*, Institute of Electrical and Electronics Engineers (IEEE), 2006. DOI: `10.1109/estc.2006.280178`.

[16] B. Gotsmann and M. A. Lantz, "Quantized thermal transport across contacts of rough surfaces", *Nature Materials*, vol. 12, no. 1, pp. 59–65, 2012. DOI: `10.1038/nmat3460`.

[17] M. Bahrami, M. M. Yovanovich, and J. R. Culham, "Thermal contact resistance at low contact pressure: Effect of elastic deformation", *International Journal of Heat and Mass Transfer*, vol. 48, no. 16, pp. 3284–3293, 2005. DOI: `10.1016/j.ijheatmasstransfer.2005.02.033`.

[18] R. Prasher, "Thermal interface materials: Historical perspective, status, and future directions", *Proceedings of the IEEE*, vol. 94, no. 8, pp. 1571–1586, 2006. DOI: `10.1109/jproc.2006.879796`.

[19] FLIR Systems, AB. (–). The ultimate infrared handbook for R&D professionals – a resource guide for using infrared in the research and development industry, URL: `http://www.flirmedia.com/MMC/THG/Brochures/T559243/T559243_EN.pdf` (visited on 10/15/2016).

[20] Wikipedia. (2016). Lumped element model, URL: `https://en.wikipedia.org/wiki/Lumped_element_model` (visited on 10/15/2016).

[21] J. S. Brown and P. A. Domanski, "Review of alternative cooling technologies", *Applied Thermal Engineering*, vol. 64, no. 1-2, pp. 252–262, 2014. DOI: `10.1016/j.applthermaleng.2013.12.014`.

[22] S. Qian, D. Nasuta, A. Rhoads, Y. Wang, Y. Geng, Y. Hwang, R. Radermacher, and I. Takeuchi, "Not-in-kind cooling technologies: A quantitative comparison of refrigerants and system performance", *International Journal of Refrigeration*, vol. 62, pp. 177–192, 2016. DOI: `10.1016/j.ijrefrig.2015.10.019`.

[23] N. Ashraf, K Casey, L. Chow, S Corban, M. Drost, A. Gumm, Z Hao, A. Hasan, J. Kapat, L Kramer, M Newton, K. Sundaram, J Vaidya, C. Wong, and K Yerkes, "Design and analysis of a meso-scale refrigerator", *ASME-PUBLICATIONS-HTD*, vol. 364, pp. 109–116, 1999.

[24] S. Munkejord, H. Mæhlum, G. Zakeri, P. Nekså, and J. Pettersen, "Micro technology in heat pumping systems", *International Journal of Refrigeration*, vol. 25, no. 4, pp. 471–478, 2002. DOI: `10.1016/s0140-7007(00)00036-0`.

[25] T. C. Ernst and S. Garimella, "Wearable engine-driven vapor-compression cooling system for elevated ambients", *Journal of Thermal Science and Engineering Applications*, vol. 1, no. 2, p. 025 001, 2009. DOI: `10.1115/1.3159478`.

[26] J. R. Barbosa, G. B. Ribeiro, and P. A. de Oliveira, "A state-of-the-art review of compact vapor compression refrigeration systems and their applications", *Heat Transfer Engineering*, vol. 33, no. 4-5, pp. 356–374, 2012. DOI: `10.1080/01457632.2012.613275`.

[27] S. Jeong, "How difficult is it to make a micro refrigerator?", *International Journal of Refrigeration*, vol. 27, no. 3, pp. 309–313, 2004. DOI: `10.1016/j.ijrefrig.2003.11.004`.

[28] L. E. Bell, "Cooling, heating, generating power, and recovering waste heat with thermoelectric systems", *Science*, vol. 321, no. 5895, pp. 1457–1461, 2008. DOI: `10.1126/science.1158899`.

[29] S. Riffat and X. Ma, "Thermoelectrics: A review of present and potential applications", *Applied Thermal Engineering*, vol. 23, no. 8, pp. 913–935, 2003. DOI: `10.1016/s1359-4311(03)00012-7`.

[30] D. Zhao and G. Tan, "A review of thermoelectric cooling: Materials, modeling and applications", *Applied Thermal Engineering*, vol. 66, no. 1-2, pp. 15–24, 2014. DOI: `10.1016/j.applthermaleng.2014.01.074`.

[31] W. He, G. Zhang, X. Zhang, J. Ji, G. Li, and X. Zhao, "Recent development and application of thermoelectric generator and cooler", *Applied Energy*, vol. 143, pp. 1–25, 2015. DOI: `10.1016/j.apenergy.2014.12.075`.

[32] G. Hwang, A. Gross, H. Kim, S. Lee, N. Ghafouri, B. Huang, C. Lawrence, C. Uher, K. Najafi, and M. Kaviany, "Micro thermoelectric cooler: Planar multistage", *International Journal of Heat and Mass Transfer*, vol. 52, no. 7-8, pp. 1843–1852, 2009. DOI: `10.1016/j.ijheatmasstransfer.2008.10.014`.

[33] T. C. Harman, "Quantum dot superlattice thermoelectric materials and devices", *Science*, vol. 297, no. 5590, pp. 2229–2232, 2002. DOI: `10.1126/science.1072886`.

[34] I. Chowdhury, R. Prasher, K. Lofgreen, G. Chrysler, S. Narasimhan, R. Mahajan, D. Koester, R. Alley, and R. Venkatasubramanian, "On-chip cooling by superlattice-based thin-film thermoelectrics", *Nature Nanotech*, vol. 4, no. 4, pp. 235–238, 2009. DOI: `10.1038/nnano.2008.417`.

[35] A. Majumdar, "Thermoelectric devices: Helping chips to keep their cool", *Nature Nanotech*, vol. 4, no. 4, pp. 214–215, 2009. DOI: `10.1038/nnano.2009.65`.

[36] R. M. Atta, "Solar water condensation using thermoelectric coolers", *International Journal of Water Resources and Arid Environments*, vol. 1, no. 2, pp. 142–145, 2011.

[37] W. Glatz, S. Muntwyler, and C. Hierold, "Optimization and fabrication of thick flexible polymer based micro thermoelectric generator", *Sensors and Actuators A: Physical*, vol. 132, no. 1, pp. 337–345, 2006. DOI: `10.1016/j.sna.2006.04.024`.

[38] L. Goncalves, J. Rocha, C. Couto, P. Alpuim, and J. Correia, "On-chip array of thermoelectric peltier microcoolers", *Sensors and Actuators A: Physical*, vol. 145-146, pp. 75–80, 2008. DOI: `10.1016/j.sna.2007.10.062`.

[39] I.-Y. Huang, J.-C. Lin, K.-D. She, M.-C. Li, J.-H. Chen, and J.-S. Kuo, "Development of low-cost micro-thermoelectric coolers utilizing MEMS technology", *Sensors and Actuators A: Physical*, vol. 148, no. 1, pp. 176–185, 2008. DOI: `10.1016/j.sna.2008.07.017`.

[40] L. M. Goncalves, J. G. Rocha, C Couto, P Alpuim, G. Min, D. M. Rowe, and J. H. Correia, "Fabrication of flexible thermoelectric microcoolers using planar thin-film technologies", *Journal of Micromechanics and Microengineering*, vol. 17, no. 7, S168–S173, 2007. DOI: `10.1088/0960-1317/17/7/s14`.

[41] K. Otsuka and C. M. Wayman, *Shape memory materials*. Cambridge university press, 1999.

[42] J. Shaw, C. Churchill, and M. Iadicola, "Tips and tricks for characterizinf shape memory alloy wire: Part 1 – differential scanning calorimetry and basic phenomena", *Experimental Techniques*, vol. 32, no. 5, pp. 55–62, 2008. DOI: `10.1111/j.1747-1567.2008.00410.x`.

[43] C. B. Churchill and J. A. Shaw, "Shakedown response of conditioned shape memory alloy wire", in *Behavior and Mechanics of Multifunctional and Composite Materials 2008*, M. J. Dapino and Z. Ounaies, Eds., SPIE-Intl Soc Optical Eng, 2008. DOI: `10.1117/12.778726`.

[44] R. Zarnetta, R. Takahashi, M. L. Young, A. Savan, Y. Furuya, S. Thienhaus, B. Maaß, M. Rahim, J. Frenzel, H. Brunken, Y. S. Chu, V. Srivastava, R. D. James, I. Takeuchi, G. Eggeler, and A. Ludwig, "Identification of quaternary shape memory alloys with near-zero thermal hysteresis and unprecedented functional stability", *Adv. Funct. Mater.*, vol. 20, no. 12, pp. 1917–1923, 2010. DOI: `10.1002/adfm.200902336`.

[45] X. Wang, B. Verlinden, and J. V. Humbeeck, "Deformation behavior after stress-induced martensite transformation in a Ti-50.8 at.% Ni alloy", *MATEC Web of Conferences*, vol. 33, N. Schryvers and J. V. Humbeeck, Eds., p. 03 018, 2015. DOI: `10.1051/matecconf/20153303018`.

[46] J. Frenzel, E. George, A. Dlouhy, C. Somsen, M.-X. Wagner, and G. Eggeler, "Influence of Ni on martensitic phase transformations in NiTi shape memory alloys", *Acta Materialia*, vol. 58, no. 9, pp. 3444–3458, 2010. DOI: `10.1016/j.actamat.2010.02.019`.

[47] J. Frenzel, A. Wieczorek, I. Opahle, B. Maaß, R. Drautz, and G. Eggeler, "On the effect of alloy composition on martensite start temperatures and latent heats in Ni–Ti-based shape memory alloys", *Acta Materialia*, vol. 90, pp. 213–231, 2015. DOI: `10.1016/j.actamat.2015.02.029`.

[48] C. Zamponi, H. Rumpf, B. Wehner, J. Frenzel, and E. Quandt, "Superelasticity of free-standing NiTi films depending on the oxygen impurity of the used targets", *Mat.-wiss. u. Werkstofftech.*, vol. 35, no. 5, pp. 359–364, 2004. DOI: `10.1002/mawe.200400748`.

[49] J. Frenzel, Z. Zhang, C. Somsen, K. Neuking, and G. Eggeler, "Influence of carbon on martensitic phase transformations in NiTi shape memory alloys", *Acta Materialia*, vol. 55, no. 4, pp. 1331–1341, 2007. DOI: `10.1016/j.actamat.2006.10.006`.

[50] J. Otubo, O. Rigo, A. Coelho, C. Neto, and P. Mei, "The influence of carbon and oxygen content on the martensitic transformation temperatures and enthalpies of NiTi shape memory alloy", *Materials Science and Engineering: A*, vol. 481-482, pp. 639–642, 2008. DOI: `10.1016/j.msea.2007.02.137`.

[51] C. Somsen, H Zähres, J Kästner, E. Wassermann, T Kakeshita, and T Saburi, "Influence of thermal annealing on the martensitic transitions in Ni–Ti shape memory alloys", *Materials Science and Engineering: A*, vol. 273, pp. 310–314, 1999.

[52] A. S. Mahmud, H. Yang, S. Tee, G. Rio, and Y. Liu, "Effect of annealing on deformation-induced martensite stabilisation of NiTi", *Intermetallics*, vol. 16, no. 2, pp. 209–214, 2008. DOI: `10.1016/j.intermet.2007.09.003`.

[53] S. A. Wilson, R. P. Jourdain, Q. Zhang, R. A. Dorey, C. R. Bowen, M. Willander, Q. U. Wahab, M. Willander, S. M. Al-hilli, O. Nur, E. Quandt, C. Johansson, E. Pagounis, M. Kohl, J. Matovic, B. Samel, W. van der Wijngaart, E. W. Jager, D. Carlsson, Z. Djinovic, M. Wegener, C. Moldovan, R. Iosub, E. Abad, M. Wendlandt, C. Rusu, and K. Persson, "New materials

for micro-scale sensors and actuators", *Materials Science and Engineering: R: Reports*, vol. 56, no. 1-6, pp. 1–129, 2007. DOI: `10.1016/j.mser.2007.03.001`.

[54] Y. Bellouard, "Shape memory alloys for microsystems: A review from a material research perspective", *Materials Science and Engineering: A*, vol. 481-482, pp. 582–589, 2008. DOI: `10.1016/j.msea.2007.02.166`.

[55] A. Nespoli, S. Besseghini, S. Pittaccio, E. Villa, and S. Viscuso, "The high potential of shape memory alloys in developing miniature mechanical devices: A review on shape memory alloy mini-actuators", *Sensors and Actuators A: Physical*, vol. 158, no. 1, pp. 149–160, 2010. DOI: `10.1016/j.sna.2009.12.020`.

[56] J. M. Jani, M. Leary, A. Subic, and M. A. Gibson, "A review of shape memory alloy research, applications and opportunities", *Materials & Design*, vol. 56, pp. 1078–1113, 2014. DOI: `10.1016/j.matdes.2013.11.084`.

[57] M. Zainal, S. Sahlan, and M. Ali, "Micromachined shape-memory-alloy microactuators and their application in biomedical devices", *Micromachines*, vol. 6, no. 7, pp. 879–901, 2015. DOI: `10.3390/mi6070879`.

[58] S. Miyazaki and K. Otsuka, "Deformation and transition behavior associated with the R-phase in Ti-Ni alloys", *Metallurgical Transactions A*, vol. 17, no. 1, pp. 53–63, 1986. DOI: `10.1007/bf02644442`.

[59] C. Churchill, J. Shaw, and M. Iadicola, "Tips and tricks for characterizing shape memory alloy wire: Part 2 – fundamental isothermal responses", *Experimental Techniques*, vol. 33, no. 1, pp. 51–62, 2009. DOI: `10.1111/j.1747-1567.2008.00460.x`.

[60] K. Otsuka and X. Ren, "Physical metallurgy of Ti–Ni-based shape memory alloys", *Progress in Materials Science*, vol. 50, no. 5, pp. 511–678, 2005. DOI: `10.1016/j.pmatsci.2004.10.001`.

[61] Y. He and Q. Sun, "On non-monotonic rate dependence of stress hysteresis of superelastic shape memory alloy bars", *International Journal of Solids and Structures*, vol. 48, no. 11-12, pp. 1688–1695, 2011. DOI: `10.1016/j.ijsolstr.2011.02.017`.

[62] Y. J. He and Q. P. Sun, "Rate-dependent damping capacity of NiTi shape memory alloy", *Solid State Phenomena*, vol. 172-174, pp. 37–42, 2011. DOI: `10.4028/www.scientific.net/ssp.172-174.37`.

[63] E. Pieczyska, S. Gadaj, W. Nowacki, K. Hoshio, Y. Makino, and H. Tobushi, "Characteristics of energy storage and dissipation in TiNi shape memory alloy", *Science and Technology of Advanced Materials*, vol. 6, no. 8, pp. 889–894, 2005. DOI: `10.1016/j.stam.2005.07.008`.

[64] K. Otsuka and X. Ren, "Recent developments in the research of shape memory alloys", *Intermetallics*, vol. 7, no. 5, pp. 511–528, 1999.

[65] T. Duerig, A Pelton, and D Stöckel, "An overview of nitinol medical applications", *Materials Science and Engineering: A*, vol. 273, pp. 149–160, 1999.

[66] L. Machado and M. Savi, "Medical applications of shape memory alloys", *Braz J Med Biol Res*, vol. 36, no. 6, 2003. DOI: 10.1590/s0100-879x2003000600001.

[67] N. Morgan, "Medical shape memory alloy applications — the market and its products", *Materials Science and Engineering: A*, vol. 378, no. 1-2, pp. 16–23, 2004. DOI: 10.1016/j.msea.2003.10.326.

[68] X. Zhang, P. Feng, Y. He, T. Yu, and Q. Sun, "Experimental study on rate dependence of macroscopic domain and stress hysteresis in NiTi shape memory alloy strips", *International Journal of Mechanical Sciences*, vol. 52, no. 12, pp. 1660–1670, 2010. DOI: 10.1016/j.ijmecsci.2010.08.007.

[69] S. Mao, J. Luo, Z. Zhang, M. Wu, Y. Liu, and X. Han, "EBSD studies of the stress-induced B2-B19′ martensitic transformation in NiTi tubes under uniaxial tension and compression", *Acta Materialia*, vol. 58, no. 9, pp. 3357–3366, 2010. DOI: 10.1016/j.actamat.2010.02.009.

[70] J. Shaw and S. Kyriakides, "On the nucleation and propagation of phase transformation fronts in a NiTi alloy", *Acta Materialia*, vol. 45, no. 2, pp. 683–700, 1997. DOI: 10.1016/s1359-6454(96)00189-9.

[71] J. Zurbitu, S. Kustov, A. Zabaleta, E. Cesari, and J. Aurrekoetxe, "Thermomechanical behaviour of NiTi at impact", in *Shape Memory Alloys*, InTech, 2010, ISBN: 978-953-307-106-0. DOI: 10.5772/9985.

[72] J Shaw, "Thermomechanical aspects of NiTi", *Journal of the Mechanics and Physics of Solids*, vol. 43, no. 8, pp. 1243–1281, 1995. DOI: 10.1016/0022-5096(95)00024-d.

[73] P. Sittner, Y. Liu, and V. Novak, "On the origin of lüders-like deformation of NiTi shape memory alloys", *Journal of the Mechanics and Physics of Solids*, vol. 53, no. 8, pp. 1719–1746, 2005. DOI: 10.1016/j.jmps.2005.03.005.

[74] K Kim and S Daly, "The effect of texture on stress-induced martensite formation in nickel–titanium", *Smart Mater. Struct.*, vol. 22, no. 7, p. 075 012, 2013. DOI: 10.1088/0964-1726/22/7/075012.

[75] S. Daly, G. Ravichandran, and K. Bhattacharya, "Stress-induced martensitic phase transformation in thin sheets of nitinol", *Acta Materialia*, vol. 55, no. 10, pp. 3593–3600, 2007. DOI: 10.1016/j.actamat.2007.02.011.

[76] Y. Xiao, P. Zeng, L. Lei, and H. Du, "Local mechanical response of superelastic NiTi shape-memory alloy under uniaxial loading", *Shap. Mem. Superelasticity*, vol. 1, no. 4, pp. 468–478, 2015. DOI: 10.1007/s40830-015-0037-9.

[77] E. A. Pieczyska, S. P. Gadaj, W. K. Nowacki, and H. Tobushi, "Phase-transformation fronts evolution for stress- and strain-controlled tension tests in TiNi shape memory alloy", *Exp Mech*, vol. 46, no. 4, pp. 531–542, 2006. DOI: 10.1007/s11340-006-8351-y.

[78] S. Gadaj, W. Nowacki, and H Tobushi, "Temperature evolution during tensile test of TiNi shape memory alloy", *Archives of Mechanics*, vol. 51, no. 6, pp. 649–663, 1999.

[79] H. Louche, P. Schlosser, D. Favier, and L. Orgéas, "Heat source processing for localized deformation with non-constant thermal conductivity. Application to superelastic tensile tests of NiTi shape memory alloys", *Exp Mech*, vol. 52, no. 9, pp. 1313–1328, 2012. DOI: `10.1007/s11340-012-9607-3`.

[80] Y. Xiao, P. Zeng, and L. Lei, "Experimental investigation on local mechanical response of superelastic NiTi shape memory alloy", *Smart Mater. Struct.*, vol. 25, no. 1, p. 017 002, 2015. DOI: `10.1088/0964-1726/25/1/017002`.

[81] A. Maynadier, M. Poncelet, K. Lavernhe-Taillard, and S. Roux, "One-shot measurement of thermal and kinematic fields: InfraRed image correlation (IRIC)", *Exp Mech*, vol. 52, no. 3, pp. 241–255, 2011. DOI: `10.1007/s11340-011-9483-2`.

[82] Z Li, "The initiation and growth of macroscopic martensite band in nanograined NiTi microtube under tension", *International Journal of Plasticity*, vol. 18, no. 11, pp. 1481–1498, 2002. DOI: `10.1016/s0749-6419(02)00026-8`.

[83] Q.-P. Sun and Z.-Q. Li, "Phase transformation in superelastic NiTi polycrystalline micro-tubes under tension and torsion – from localization to homogeneous deformation", *International Journal of Solids and Structures*, vol. 39, no. 13-14, pp. 3797–3809, 2002. DOI: `10.1016/s0020-7683(02)00182-8`.

[84] P. Feng and Q Sun, "Experimental investigation on macroscopic domain formation and evolution in polycrystalline NiTi microtubing under mechanical force", *Journal of the Mechanics and Physics of Solids*, vol. 54, no. 8, pp. 1568–1603, 2006. DOI: `10.1016/j.jmps.2006.02.005`.

[85] P. Schlosser, H. Louche, D. Favier, and L. Orgéas, "Image processing to estimate the heat sources related to phase transformations during tensile tests of NiTi tubes", *Strain*, vol. 43, no. 3, pp. 260–271, 2007. DOI: `10.1111/j.1475-1305.2007.00350.x`.

[86] J. Tušek, K. Engelbrecht, L. P. Mikkelsen, and N. Pryds, "Elastocaloric effect of Ni-Ti wire for application in a cooling device", *J. Appl. Phys.*, vol. 117, no. 12, p. 124 901, 2015. DOI: `10.1063/1.4913878`.

[87] F Maquin, F Pierron, S Avril, and F. Scarpa, "Heat generation assessment of the phase transformation in an SMA ribbon", in *Proceedings of 2006 SEM, June 4 -7, San Louis, MS*, Conference Organiser: SEM, Jun. 2006.

[88] M. Schmidt, J. Ullrich, A. Wieczorek, J. Frenzel, A. Schütze, G. Eggeler, and S. Seelecke, "Thermal stabilization of NiTiCuV shape memory alloys: Observations during elastocaloric training", *Shap. Mem. Superelasticity*, vol. 1, no. 2, pp. 132–141, 2015. DOI: `10.1007/s40830-015-0021-4`.

[89] C. Efstathiou, H. Sehitoglu, J. Carroll, J. Lambros, and H. Maier, "Full-field strain evolution during intermartensitic transformations in single-crystal NiFeGa", *Acta Materialia*, vol. 56, no. 15, pp. 3791–3799, 2008. DOI: 10.1016/j.actamat.2008.04.033.

[90] G. J. Pataky, E. Ertekin, and H. Sehitoglu, "Elastocaloric cooling potential of NiTi, Ni_2FeGa, and CoNiAl", *Acta Materialia*, vol. 96, pp. 420–427, 2015. DOI: 10.1016/j.actamat.2015.06.011.

[91] E. Vives, S. Burrows, R. S. Edwards, S. Dixon, L. Mañosa, A. Planes, and R. Romero, "Temperature contour maps at the strain-induced martensitic transition of a Cu–Zn–Al shape-memory single crystal", *Appl. Phys. Lett.*, vol. 98, no. 1, p. 011 902, 2011. DOI: 10.1063/1.3533403.

[92] G. Murasawa, S. Yoneyama, T. Sakuma, and M. Takashi, "Influence of cyclic loading on inhomogeneous deformation behavior arising in NiTi shape memory alloy plate", *MATERIALS TRANSACTIONS*, vol. 47, no. 3, pp. 780–786, 2006. DOI: 10.2320/matertrans.47.780.

[93] C Efstathiou and H Sehitoglu, "Local transformation strain measurements in precipitated NiTi single crystals", *Scripta Materialia*, vol. 59, no. 12, pp. 1263–1266, 2008. DOI: 10.1016/j.scriptamat.2008.08.030.

[94] G. Murasawa, K. Kitamura, S. Yoneyama, S. Miyazaki, K. Miyata, A. Nishioka, and T. Koda, "Macroscopic stress–strain curve, local strain band behavior and the texture of NiTi thin sheets", *Smart Mater. Struct.*, vol. 18, no. 5, p. 055 003, 2009. DOI: 10.1088/0964-1726/18/5/055003.

[95] E. Pieczyska, "Activity of stress-induced martensite transformation in TiNi shape memory alloy studied by infrared technique", *Journal of Modern Optics*, vol. 57, no. 18, pp. 1700–1707, 2010. DOI: 10.1080/09500341003725748.

[96] E. A. Pieczyska, H Tobushi, and K Kulasinski, "Development of transformation bands in TiNi SMA for various stress and strain rates studied by a fast and sensitive infrared camera", *Smart Mater. Struct.*, vol. 22, no. 3, p. 035 007, 2013. DOI: 10.1088/0964-1726/22/3/035007.

[97] E. A. Pieczyska, M. Staszczak, V. Dunić, R. Slavković, H. Tobushi, and K. Takeda, "Development of stress-induced martensitic transformation in TiNi shape memory alloy", *J. of Materi Eng and Perform*, vol. 23, no. 7, pp. 2505–2514, 2014. DOI: 10.1007/s11665-014-0959-y.

[98] C. Bechtold, C. Chluba, R. L. de Miranda, and E. Quandt, "High cyclic stability of the elastocaloric effect in sputtered TiNiCu shape memory films", *Appl. Phys. Lett.*, vol. 101, no. 9, p. 091 903, 2012. DOI: 10.1063/1.4748307.

[99] Y. Song, X. Chen, V. Dabade, T. W. Shield, and R. D. James, "Enhanced reversibility and unusual microstructure of a phase-transforming material", *Nature*, vol. 502, no. 7469, pp. 85–88, 2013. DOI: 10.1038/nature12532.

[100] K Gall and H. Maier, "Cyclic deformation mechanisms in precipitated NiTi shape memory alloys", *Acta Materialia*, vol. 50, no. 18, pp. 4643–4657, 2002.

[101] E. Hornbogen, "Review thermo-mechanical fatigue of shape memory alloys", *Journal of Materials Science*, vol. 39, no. 2, pp. 385–399, 2004. DOI: `10.1023/b:jmsc.0000011492.88523.d3`.

[102] G. Eggeler, E. Hornbogen, A. Yawny, A. Heckmann, and M. Wagner, "Structural and functional fatigue of NiTi shape memory alloys", *Materials Science and Engineering: A*, vol. 378, no. 1-2, pp. 24–33, 2004. DOI: `10.1016/j.msea.2003.10.327`.

[103] C. Chluba, W. Ge, T. Dankwort, C. Bechtold, R. L. de Miranda, L. Kienle, M. Wuttig, and E. Quandt, "Effect of crystallographic compatibility and grain size on the functional fatigue of sputtered TiNiCuCo thin films", *Phil. Trans. R. Soc. A*, vol. 374, no. 2074, p. 20 150 311, 2016. DOI: `10.1098/rsta.2015.0311`.

[104] A Ishida and M Sato, "Thickness effect on shape memory behavior of Ti-50.0at.%Ni thin film", *Acta Materialia*, vol. 51, no. 18, pp. 5571–5578, 2003. DOI: `10.1016/s1359-6454(03)00420-8`.

[105] Y. Chen and C. A. Schuh, "Size effects in shape memory alloy microwires", *Acta Materialia*, vol. 59, no. 2, pp. 537–553, 2011. DOI: `10.1016/j.actamat.2010.09.057`.

[106] S. M. Ueland and C. A. Schuh, "Superelasticity and fatigue in oligocrystalline shape memory alloy microwires", *Acta Materialia*, vol. 60, no. 1, pp. 282–292, 2012. DOI: `10.1016/j.actamat.2011.09.054`.

[107] S. M. Ueland, Y. Chen, and C. A. Schuh, "Oligocrystalline shape memory alloys", *Adv. Funct. Mater.*, vol. 22, no. 10, pp. 2094–2099, 2012. DOI: `10.1002/adfm.201103019`.

[108] S. M. Ueland and C. A. Schuh, "Grain boundary and triple junction constraints during martensitic transformation in shape memory alloys", *J. Appl. Phys.*, vol. 114, no. 5, p. 053 503, 2013. DOI: `10.1063/1.4817170`.

[109] S. M. Ueland and C. A. Schuh, "Transition from many domain to single domain martensite morphology in small-scale shape memory alloys", *Acta Materialia*, vol. 61, no. 15, pp. 5618–5625, 2013. DOI: `10.1016/j.actamat.2013.06.003`.

[110] K. Engelbrecht, J. Tušek, S. Sanna, D. Eriksen, O. V. Mishin, C. R. H. Bahl, and N. Pryds, "Effects of surface finish and mechanical training on Ni-Ti sheets for elastocaloric cooling", *APL Mater.*, vol. 4, no. 6, p. 064 110, 2016. DOI: `10.1063/1.4955131`.

[111] K. Fushimi, M. Stratmann, and A. W. Hassel, "Electropolishing of NiTi shape memory alloys in methanolic H_2SO_4", *Electrochimica Acta*, vol. 52, no. 3, pp. 1290–1295, 2006. DOI: `10.1016/j.electacta.2006.07.030`.

[112] E. S. Lee and T. H. Shin, "An evaluation of the machinability of nitinol shape memory alloy by electrochemical polishing", *Journal of Mechanical Science and Technology*, vol. 25, no. 4, pp. 963–969, 2011. DOI: `10.1007/s12206-011-0209-2`.

[113] J. Racek, P. Šittner, L. Heller, J. Pilch, M. Petrenec, and P. Sedlák, "Corrosion of NiTi wires with cracked oxide layer", *J. of Materi Eng and Perform*, vol. 23, no. 7, pp. 2659–2668, 2014. DOI: `10.1007/s11665-014-0925-8`.

[114] J. Racek, M. Stora, P. Šittner, L. Heller, J. Kopeček, and M. Petrenec, "Monitoring tensile fatigue of superelastic NiTi wire in liquids by electrochemical potential", *Shap. Mem. Superelasticity*, vol. 1, no. 2, pp. 204–230, 2015. DOI: `10.1007/s40830-015-0020-5`.

[115] J. Racek, P. Šittner, L. Heller, J. Pilch, P. Sedlák, and L. Kadeřávek, "Electrochemistry of NiTi wires/springs subjected to static/cyclic loadings", *Materials Today: Proceedings*, vol. 2, S965–S969, 2015. DOI: `10.1016/j.matpr.2015.07.442`.

[116] J. Cui, Y. S. Chu, O. O. Famodu, Y. Furuya, J. Hattrick-Simpers, R. D. James, A. Ludwig, S. Thienhaus, M. Wuttig, Z. Zhang, and I. Takeuchi, "Combinatorial search of thermoelastic shape-memory alloys with extremely small hysteresis width", *Nature Materials*, vol. 5, no. 4, pp. 286–290, 2006. DOI: `10.1038/nmat1593`.

[117] Z. Zhang, R. D. James, and S. Müller, "Energy barriers and hysteresis in martensitic phase transformations", *Acta Materialia*, vol. 57, no. 15, pp. 4332–4352, 2009. DOI: `10.1016/j.actamat.2009.05.034`.

[118] R. Zarnetta, P. J. S. Buenconsejo, A. Savan, S. Thienhaus, and A. Ludwig, "High-throughput study of martensitic transformations in the complete Ti–Ni–Cu system", *Intermetallics*, vol. 26, pp. 98–109, 2012. DOI: `10.1016/j.intermet.2012.03.044`.

[119] X. Chen, V. Srivastava, V. Dabade, and R. D. James, "Study of the cofactor conditions: Conditions of supercompatibility between phases", *Journal of the Mechanics and Physics of Solids*, vol. 61, no. 12, pp. 2566–2587, 2013. DOI: `10.1016/j.jmps.2013.08.004`.

[120] C. Chluba, W. Ge, R. L. de Miranda, J. Strobel, L. Kienle, E. Quandt, and M. Wuttig, "Ultralow-fatigue shape memory alloy films", *Science*, vol. 348, no. 6238, pp. 1004–1007, 2015. DOI: `10.1126/science.1261164`.

[121] C. Chluba, H. Ossmer, C. Zamponi, M. Kohl, and E. Quandt, "Ultra-low fatigue quaternary TiNi-based films for elastocaloric cooling", *Shap. Mem. Superelasticity*, vol. 2, no. 1, pp. 95–103, 2016. DOI: `10.1007/s40830-016-0054-3`.

[122] T. Dankwort, J. Strobel, C. Chluba, W. Ge, V. Duppel, M. Wuttig, E. Quandt, and L. Kienle, "Martensite adaption through epitaxial nano transition layers in TiNiCu shape memory alloys", *J Appl Cryst*, vol. 49, no. 3, pp. 1009–1015, 2016. DOI: `10.1107/s160057671600710x`.

[123] S. Kibey, H. Sehitoglu, and D. Johnson, "Energy landscape for martensitic phase transformation in shape memory NiTi", *Acta Materialia*, vol. 57, no. 5, pp. 1624–1629, 2009. DOI: `10.1016/j.actamat.2008.12.008`.

[124] K. G. Vishnu and A. Strachan, "Phase stability and transformations in NiTi from density functional theory calculations", *Acta Materialia*, vol. 58, no. 3, pp. 745–752, 2010. DOI: `10.1016/j.actamat.2009.09.019`.

[125] Y. Zhong, K. Gall, and T. Zhu, "Atomistic characterization of pseudoelasticity and shape memory in NiTi nanopillars", *Acta Materialia*, vol. 60, no. 18, pp. 6301–6311, 2012. DOI: `10.1016/j.actamat.2012.08.004`.

[126] T. Ezaz, J. Wang, H. Sehitoglu, and H. Maier, "Plastic deformation of NiTi shape memory alloys", *Acta Materialia*, vol. 61, no. 1, pp. 67–78, 2013. DOI: `10.1016/j.actamat.2012.09.023`.

[127] E. Patoor, D. C. Lagoudas, P. B. Entchev, L. C. Brinson, and X. Gao, "Shape memory alloys, part I: General properties and modeling of single crystals", *Mechanics of Materials*, vol. 38, no. 5-6, pp. 391–429, 2006. DOI: `10.1016/j.mechmat.2005.05.027`.

[128] D. C. Lagoudas, P. B. Entchev, P. Popov, E. Patoor, L. C. Brinson, and X. Gao, "Shape memory alloys, part II: Modeling of polycrystals", *Mechanics of Materials*, vol. 38, no. 5-6, pp. 430–462, 2006. DOI: `10.1016/j.mechmat.2005.08.003`.

[129] F. Auricchio and J. Lubliner, "A uniaxial model for shape-memory alloys", *International Journal of Solids and Structures*, vol. 34, no. 27, pp. 3601–3618, 1997. DOI: `10.1016/s0020-7683(96)00232-6`.

[130] H. Prahlad and I. Chopra, "Comparative evaluation of shape memory alloy constitutive models with experimental data", *Journal of Intelligent Material Systems and Structures*, vol. 12, no. 6, pp. 383–395, 2001. DOI: `10.1106/104538902022599`.

[131] M. Kohl, *Entwicklung von Mikroaktoren aus Formgedächtnislegierungen*. Forschungszentrum Karlsruhe, 2002.

[132] R. C. Smith, S. Seelecke, M. Dapino, and Z. Ounaies, "A unified framework for modeling hysteresis in ferroic materials", *Journal of the Mechanics and Physics of Solids*, vol. 54, no. 1, pp. 46–85, 2006. DOI: `10.1016/j.jmps.2005.08.006`.

[133] S. J. Furst, J. H. Crews, and S. Seelecke, "Numerical and experimental analysis of inhomogeneities in SMA wires induced by thermal boundary conditions", *Continuum Mech. Thermodyn.*, vol. 24, no. 4-6, pp. 485–504, 2012. DOI: `10.1007/s00161-012-0238-9`.

[134] S. J. Furst and S. Seelecke, "Modeling and experimental characterization of the stress, strain, and resistance of shape memory alloy actuator wires with controlled power input", *Journal of Intelligent Material Systems and Structures*, vol. 23, no. 11, pp. 1233–1247, 2012. DOI: `10.1177/1045389x12445036`.

[135] L. C. Brinson and M. S. Huang, "Simplifications and comparisons of shape memory alloy constitutive models", *Journal of Intelligent Material Systems and Structures*, vol. 7, no. 1, pp. 108–114, 1996. DOI: `10.1177/1045389x9600700112`.

[136] K. Tanaka and S. Nagaki, "A thermomechanical description of materials with internal variables in the process of phase transitions", *Ingenieur-Archiv*, vol. 51, no. 5, pp. 287–299, 1982. DOI: `10.1007/bf00536655`.

[137] K. Tanaka, "A thermomechanical sketch of shape memory effect: One-dimensional tensile behavior", *RES MECHANICA*, vol. 18, no. 3, pp. 251–263, 1986.

[138] K. Tanaka, S. Kobayashi, and Y. Sato, "Thermomechanics of transformation pseudoelasticity and shape memory effect in alloys", *International Journal of Plasticity*, vol. 2, no. 1, pp. 59–72, 1986. DOI: `10.1016/0749-6419(86)90016-1`.

[139] K. Ikuta and H. Shimizu, "Two dimensional mathematical model of shape memory alloy and intelligent SMA-CAD", in *Proceedings IEEE Micro Electro Mechanical Systems*, Institute of Electrical & Electronics Engineers (IEEE), 1993. DOI: `10.1109/memsys.1993.296958`.

[140] M. Kohl and B. Krevet, "Smart materials – fundamentals and applications. 3D simulation of a shape memory microactuator.", *MATERIALS TRANSACTIONS*, vol. 43, no. 5, pp. 1030–1036, 2002. DOI: `10.2320/matertrans.43.1030`.

[141] B. Krevet and M. Kohl, "Modeling and FEM simulation of shape memory microactuators", *Materials Science Forum*, vol. 583, pp. 229–256, 2008. DOI: `10.4028/www.scientific.net/msf.583.229`.

[142] B. Krevet, V. Pinneker, M. Rhode, C. Bechthold, E. Quandt, and M. Kohl, "Evolution of temperature profiles during stress-induced transformation in NiTi thin films", *Materials Science Forum*, vol. 738-739, pp. 287–291, 2013. DOI: `10.4028/www.scientific.net/msf.738-739.287`.

[143] L. Brinson, "One-dimensional constitutive behavior of shape memory alloys: Thermomechanical derivation with non-constant material functions and redefined martensite internal variable", *Journal of Intelligent Material Systems and Structures*, vol. 4, no. 2, pp. 229–242, 1993. DOI: `10.1177/1045389x9300400213`.

[144] L. Brinson and R. Lammering, "Finite element analysis of the behavior of shape memory alloys and their applications", *International Journal of Solids and Structures*, vol. 30, no. 23, pp. 3261–3280, 1993. DOI: `10.1016/0020-7683(93)90113-l`.

[145] M. Brocca, L. Brinson, and Z. Bažant, "Three-dimensional constitutive model for shape memory alloys based on microplane model", *Journal of the Mechanics and Physics of Solids*, vol. 50, no. 5, pp. 1051–1077, 2002. DOI: `10.1016/s0022-5096(01)00112-0`.

[146] R Mehrabi and M Kadkhodaei, "3D phenomenological constitutive modeling of shape memory alloys based on microplane theory", *Smart Mater. Struct.*, vol. 22, no. 2, p. 025 017, 2013. DOI: `10.1088/0964-1726/22/2/025017`.

[147] E Patoor, A Eberhardt, and M Berveiller, "Micromechanical modelling of the shape behavior", in *Proceedings of the Symposium on Phase Transformation in Shape Memory Alloys*, vol. 189, ASME International Congress and Exposition, 1994, pp. 23–37.

[148] G. Caginalp and W. Xie, "Phase-field and sharp-interface alloy models", *Physical Review E*, vol. 48, no. 3, pp. 1897–1909, 1993. DOI: `10.1103/physreve.48.1897`.

[149] N. T. Tsou, J. E. Huber, and Y. C. Shu, "A sharp interface model of compatible twin patterns in shape memory alloys", *Smart Mater. Struct.*, vol. 21, no. 9, p. 094 010, 2012. DOI: `10.1088/0964-1726/21/9/094010`.

[150] R. S. Qin and H. K. Bhadeshia, "Phase field method", *Materials Science and Technology*, vol. 26, no. 7, pp. 803–811, 2010. DOI: `10.1179/174328409x453190`.

[151] C Mennerich, F Wendler, M Jainta, and B Nestler, "A phase-field model for the magnetic shape memory effect", *Archives of Mechanics*, vol. 63, no. 5-6, pp. 549–571, 2011.

[152] M. Mamivand, M. A. Zaeem, and H. E. Kadiri, "Shape memory effect and pseudoelasticity behavior in tetragonal zirconia polycrystals: A phase field study", *International Journal of Plasticity*, vol. 60, pp. 71–86, 2014. DOI: `10.1016/j.ijplas.2014.03.018`.

[153] L. Dong, R. Zhou, X. Wang, G. Hu, and Q. Sun, "On interfacial energy of macroscopic domains in polycrystalline NiTi shape memory alloys", *International Journal of Solids and Structures*, vol. 80, pp. 445–455, 2016. DOI: `10.1016/j.ijsolstr.2015.10.006`.

[154] J. A. Shaw, "Simulations of localized thermo-mechanical behavior in a NiTi shape memory alloy", *International journal of plasticity*, vol. 16, no. 5, pp. 541–562, 2000.

[155] M. A. Iadicola and J. A. Shaw, "Rate and thermal sensitivities of unstable transformation behavior in a shape memory alloy", *International Journal of Plasticity*, vol. 20, no. 4-5, pp. 577–605, 2004. DOI: `10.1016/s0749-6419(03)00040-8`.

[156] B. Azadi, R. Rajapakse, and D. Maijer, "Multi-dimensional constitutive modeling of SMA during unstable pseudoelastic behavior", *International Journal of Solids and Structures*, vol. 44, no. 20, pp. 6473–6490, 2007. DOI: `10.1016/j.ijsolstr.2007.02.039`.

[157] H Soul and A Yawny, "Thermomechanical model for evaluation of the superelastic response of NiTi shape memory alloys under dynamic conditions", *Smart Materials and Structures*, vol. 22, no. 3, p. 035 017, 2013. DOI: `10.1088/0964-1726/22/3/035017`.

[158] D. Depriester, A. Maynadier, K. Lavernhe-Taillard, and O. Hubert, "Thermomechanical modelling of a NiTi SMA sample submitted to displacement-controlled tensile test", *International Journal of Solids and Structures*, vol. 51, no. 10, pp. 1901–1922, 2014. DOI: 10.1016/j.ijsolstr.2014.01.027.

[159] J. Frenzel, Z. Zhang, K. Neuking, and G. Eggeler, "High quality vacuum induction melting of small quantities of NiTi shape memory alloys in graphite crucibles", *Journal of Alloys and Compounds*, vol. 385, no. 1-2, pp. 214–223, 2004. DOI: 10.1016/j.jallcom.2004.05.002.

[160] A. S. Mahmud, Y. Liu, and T. hyun Nam, "Gradient anneal of functionally graded NiTi", *Smart Mater. Struct.*, vol. 17, no. 1, p. 015 031, 2008. DOI: 10.1088/0964-1726/17/01/015031.

[161] Q. S. Zheng and Y. Liu, "Prediction of the detwinning anisotropy in textured NiTi shape memory alloy", *Philosophical Magazine A*, vol. 82, no. 4, pp. 665–683, 2002. DOI: 10.1080/01418610208243195.

[162] Y. Sutou, T. Omori, R. Kainuma, K. Ishida, and N. Ono, "Enhancement of superelasticity in Cu-Al-Mn-Ni shape-memory alloys by texture control", *Metall and Mat Trans A*, vol. 33, no. 9, pp. 2817–2824, 2002. DOI: 10.1007/s11661-002-0267-2.

[163] Y. Liu, "The superelastic anisotropy in a NiTi shape memory alloy thin sheet", *Acta Materialia*, vol. 95, pp. 411–427, 2015. DOI: 10.1016/j.actamat.2015.03.022.

[164] R. L. de Miranda, C. Zamponi, and E. Quandt, "Micropatterned freestanding superelastic TiNi films", *Advanced Engineering Materials*, vol. 15, no. 1-2, pp. 66–69, 2012. DOI: 10.1002/adem.201200197.

[165] V. V. Khovaylo, V. V. Rodionova, S. N. Shevyrtalov, and V. Novosad, "Magnetocaloric effect in "reduced" dimensions: Thin films, ribbons, and microwires of heusler alloys and related compounds", *Phys. Status Solidi B*, vol. 251, no. 10, pp. 2104–2113, 2014. DOI: 10.1002/pssb.201451217.

[166] *Test method for transformation temperature of nickel-titanium alloys by thermal analysis*, ASTM F2004-05, 2010. DOI: 10.1520/f2004-05r10.

[167] *Test method for determining specific heat capacity by differential scanning calorimetry*, ASTM E1269-11, 2011. DOI: 10.1520/e1269-11.

[168] *Prüfung von Kunststoffen und Polymeren – Thermische Analyse – Dynamische Differenzkalorimetrie (DDK)*, DIN 53765:1994-03, 1994.

[169] P. S. Gill, S. R. Sauerbrunn, and M. Reading, "Modulated differential scanning calorimetry", *Journal of Thermal Analysis*, vol. 40, no. 3, pp. 931–939, 1993. DOI: 10.1007/bf02546852.

[170] Y. Zheng, J. Schrooten, L. Cui, and J. V. Humbeeck, "Constrained thermoelastic martensitic transformation studied by modulated DSC", *Acta Materialia*, vol. 51, no. 18, pp. 5467–5475, 2003. DOI: 10.1016/s1359-6454(03)00412-9.

[171] G. D. Sandrock, "Premartensitic behavior of the electrical resistivity of NiTi", *Metallurgical and Materials Transactions B*, vol. 5, no. 1, pp. 299–301, 1974.

[172] V. Novák, P. Šittner, G. Dayananda, F. Braz-Fernandes, and K. Mahesh, "Electric resistance variation of NiTi shape memory alloy wires in thermomechanical tests: Experiments and simulation", *Materials Science and Engineering: A*, vol. 481-482, pp. 127–133, 2008. DOI: `10.1016/j.msea.2007.02.162`.

[173] *Industrial platinum resistance thermometers and platinum temperature sensors*, DIN EN 60751:2009-05, 2009.

[174] M. Sutton, C. Mingqi, W. Peters, Y. Chao, and S. McNeill, "Application of an optimized digital correlation method to planar deformation analysis", *Image and Vision Computing*, vol. 4, no. 3, pp. 143–150, 1986. DOI: `10.1016/0262-8856(86)90057-0`.

[175] C. Eberl, D. Gianola, X. Wang, M. He, A. Evans, and K. Hemker, "A method for in situ measurement of the elastic behavior of a columnar thermal barrier coating", *Acta Materialia*, vol. 59, no. 9, pp. 3612–3620, 2011. DOI: `10.1016/j.actamat.2011.02.034`.

[176] C Eberl, R. Thompson, and D. Gianola. (2006). Free digital image correlation and tracking functions, URL: `http://de.mathworks.com/matlabcentral/fileexchange/12413-digital-image-correlation-and-tracking` (visited on 12/12/2012).

[177] Elsevier. (2016). Scopus citation database, URL: `https://www.scopus.com` (visited on 11/06/2016).

[178] A. Kitanovski, U. Plaznik, U. Tomc, and A. Poredoš, "Present and future caloric refrigeration and heat-pump technologies", *International Journal of Refrigeration*, vol. 57, pp. 288–298, 2015. DOI: `10.1016/j.ijrefrig.2015.06.008`.

[179] K. A. Gschneidner and V. K. Pecharsky, "Magnetocaloric materials", *Annual Review of Materials Science*, vol. 30, no. 1, pp. 387–429, 2000. DOI: `10.1146/annurev.matsci.30.1.387`.

[180] V. K. Pecharsky and K. A. Gschneidner, "Some common misconceptions concerning magnetic refrigerant materials", *J. Appl. Phys.*, vol. 90, no. 9, p. 4614, 2001. DOI: `10.1063/1.1405836`.

[181] B. Yu, Q Gao, B Zhang, X. Meng, and Z Chen, "Review on research of room temperature magnetic refrigeration", *International Journal of Refrigeration*, vol. 26, no. 6, pp. 622–636, 2003. DOI: `10.1016/s0140-7007(03)00048-3`.

[182] K. A. Gschneidner, V. K. Pecharsky, and A. O. Tsokol, "Recent developments in magnetocaloric materials", *Rep. Prog. Phys.*, vol. 68, no. 6, pp. 1479–1539, 2005. DOI: `10.1088/0034-4885/68/6/r04`.

[183] A. Planes, L. Mañosa, and M. Acet, "Magnetocaloric effect and its relation to shape-memory properties in ferromagnetic heusler alloys", *Journal of Physics: Condensed Matter*, vol. 21, no. 23, p. 233 201, 2009. DOI: `10.1088/0953-8984/21/23/233201`.

[184] J. Liu, T. Gottschall, K. P. Skokov, J. D. Moore, and O. Gutfleisch, "Giant magnetocaloric effect driven by structural transitions", *Nature Materials*, vol. 11, no. 7, pp. 620–626, 2012. DOI: `10.1038/nmat3334`.

[185] K. Gschneidner and V. Pecharsky, "Thirty years of near room temperature magnetic cooling: Where we are today and future prospects", *International Journal of Refrigeration*, vol. 31, no. 6, pp. 945–961, 2008. DOI: `10.1016/j.ijrefrig.2008.01.004`.

[186] B. Yu, M. Liu, P. W. Egolf, and A. Kitanovski, "A review of magnetic refrigerator and heat pump prototypes built before the year 2010", *International Journal of Refrigeration*, vol. 33, no. 6, pp. 1029–1060, 2010. DOI: `10.1016/j.ijrefrig.2010.04.002`.

[187] R. Bjørk, C. Bahl, A. Smith, and N. Pryds, "Review and comparison of magnet designs for magnetic refrigeration", *International Journal of Refrigeration*, vol. 33, no. 3, pp. 437–448, 2010. DOI: `10.1016/j.ijrefrig.2009.12.012`.

[188] A. Kitanovski and P. W. Egolf, "Innovative ideas for future research on magnetocaloric technologies", *International Journal of Refrigeration*, vol. 33, no. 3, pp. 449–464, 2010. DOI: `10.1016/j.ijrefrig.2009.11.005`.

[189] K. Nielsen, J. Tusek, K. Engelbrecht, S. Schopfer, A. Kitanovski, C. Bahl, A. Smith, N. Pryds, and A. Poredos, "Review on numerical modeling of active magnetic regenerators for room temperature applications", *International Journal of Refrigeration*, vol. 34, no. 3, pp. 603–616, 2011. DOI: `10.1016/j.ijrefrig.2010.12.026`.

[190] F. Scarpa, G. Tagliafico, and L. Tagliafico, "Classification proposal for room temperature magnetic refrigerators", *International Journal of Refrigeration*, vol. 35, no. 2, pp. 453–458, 2012. DOI: `10.1016/j.ijrefrig.2011.09.010`.

[191] A. Kitanovski, J. Tušek, U. Tomc, U. Plaznik, M. Ožbolt, and A. Poredoš, *Magnetocaloric energy conversion*. Springer International Publishing, 2015, ISBN: 978-3-319-08741-2. DOI: `10.1007/978-3-319-08741-2`.

[192] E. Brück. (2015). Magnetocaloric refrigeration: Reinventing the fridge, URL: `https://creator-space.basf.com/content/basf/creatorspace/en/blog/2015/02/magnetocaloric_refri.html` (visited on 11/11/2016).

[193] BASF. (2015). Premiere of cutting-edge magnetocaloric cooling appliance, URL: `https://www.youtube.com/watch?v=Py9IaztpKzs` (visited on 11/11/2016).

[194] L. Mañosa, A. Planes, and M. Acet, "Advanced materials for solid-state refrigeration", *J. Mater. Chem. A*, vol. 1, no. 16, p. 4925, 2013. DOI: 10.1039/c3ta01289a.

[195] X. Moya, S. Kar-Narayan, and N. D. Mathur, "Caloric materials near ferroic phase transitions", *Nature Materials*, vol. 13, no. 5, pp. 439–450, 2014. DOI: 10.1038/nmat3951.

[196] S. Crossley, N. D. Mathur, and X. Moya, "New developments in caloric materials for cooling applications", *AIP Advances*, vol. 5, no. 6, p. 067153, 2015. DOI: 10.1063/1.4922871.

[197] B. Lu and J. Liu, "Mechanocaloric materials for solid-state cooling", *Sci. Bull.*, vol. 60, no. 19, pp. 1638–1643, 2015. DOI: 10.1007/s11434-015-0898-5.

[198] A. Chauhan, S. Patel, R. Vaish, and C. R. Bowen, "A review and analysis of the elasto-caloric effect for solid-state refrigeration devices: Challenges and opportunities", *MRS Energy & Sustainability*, vol. 2, 2015. DOI: 10.1557/mre.2015.17.

[199] L. Mañosa and A. Planes, "Mechanocaloric effects in shape memory alloys", *Phil. Trans. R. Soc. A*, vol. 374, no. 2074, p. 20150310, 2016. DOI: 10.1098/rsta.2015.0310.

[200] I. Takeuchi and K. Sandeman, "Solid-state cooling with caloric materials", *Phys. Today*, vol. 68, no. 12, pp. 48–54, 2015. DOI: 10.1063/pt.3.3022.

[201] S. Qian, Y. Geng, Y. Wang, J. Ling, Y. Hwang, R. Radermacher, I. Takeuchi, and J. Cui, "A review of elastocaloric cooling: Materials, cycles and system integrations", *International Journal of Refrigeration*, vol. 64, pp. 1–19, 2016. DOI: 10.1016/j.ijrefrig.2015.12.001.

[202] D. Guyomar, Y. Li, G. Sebald, P.-J. Cottinet, B. Ducharne, and J.-F. Capsal, "Elastocaloric modeling of natural rubber", *Applied Thermal Engineering*, vol. 57, no. 1-2, pp. 33–38, 2013. DOI: 10.1016/j.applthermaleng.2013.03.032.

[203] Z. Xie, G. Sebald, and D. Guyomar, "Elastocaloric effect dependence on pre-elongation in natural rubber", *Appl. Phys. Lett.*, vol. 107, no. 8, p. 081905, 2015. DOI: 10.1063/1.4929395.

[204] M. Trček, M. Lavrič, G. Cordoyiannis, B. Zalar, B. Rožič, S. Kralj, V. Tzitzios, G. Nounesis, and Z. Kutnjak, "Electrocaloric and elastocaloric effects in soft materials", *Phil. Trans. R. Soc. A*, vol. 374, no. 2074, p. 20150301, 2016. DOI: 10.1098/rsta.2015.0301.

[205] K. Aizu, "Possible species of ferromagnetic, ferroelectric, and ferroelastic crystals", *Phys. Rev. B*, vol. 2, no. 3, pp. 754–772, 1970. DOI: 10.1103/physrevb.2.754.

[206] N. T. Trung, L. Zhang, L. Caron, K. H. J. Buschow, and E. Brück, "Giant magnetocaloric effects by tailoring the phase transitions", *Appl. Phys. Lett.*, vol. 96, no. 17, p. 172504, 2010. DOI: 10.1063/1.3399773.

[207] S. G. Lu, B. Rožič, Q. M. Zhang, Z. Kutnjak, X. Li, E. Furman, L. J. Gorny, M. Lin, B. Malič, M. Kosec, R. Blinc, and R. Pirc, "Organic and inorganic relaxor ferroelectrics with giant electrocaloric effect", *Appl. Phys. Lett.*, vol. 97, no. 16, p. 162 904, 2010. DOI: `10.1063/1.3501975`.

[208] S. Aksoy, T. Krenke, M. Acet, E. F. Wassermann, X. Moya, L. Mañosa, and A. Planes, "Tailoring magnetic and magnetocaloric properties of martensitic transitions in ferromagnetic heusler alloys", *Applied Physics Letters*, vol. 91, no. 24, p. 241 916, 2007. DOI: `10.1063/1.2825283`.

[209] W. Geng, Y. Liu, X. Meng, L. Bellaiche, J. F. Scott, B. Dkhil, and A. Jiang, "Giant negative electrocaloric effect in antiferroelectric la-doped $Pb(ZrTi)O_3$ thin films near room temperature", *Advanced Materials*, vol. 27, no. 20, pp. 3165–3169, 2015. DOI: `10.1002/adma.201501100`.

[210] E. Stern-Taulats, A. Gràcia-Condal, A. Planes, P. Lloveras, M. Barrio, J.-L. Tamarit, S. Pramanick, S. Majumdar, and L. Mañosa, "Reversible adiabatic temperature changes at the magnetocaloric and barocaloric effects in $Fe_{49}Rh_{51}$", *Appl. Phys. Lett.*, vol. 107, no. 15, p. 152 409, 2015. DOI: `10.1063/1.4933409`.

[211] S. Nikitin, G. Myalikgulyev, M. Annaorazov, A. Tyurin, R. Myndyev, and S. Akopyan, "Giant elastocaloric effect in FeRh alloy", *Physics Letters A*, vol. 171, no. 3-4, pp. 234–236, 1992. DOI: `10.1016/0375-9601(92)90432-1`.

[212] L. Mañosa, D. González-Alonso, A. Planes, M. Barrio, J.-L. Tamarit, I. S. Titov, M. Acet, A. Bhattacharyya, and S. Majumdar, "Inverse barocaloric effect in the giant magnetocaloric La–Fe–Si–Co compound", *Nature Communications*, vol. 2, p. 595, 2011. DOI: `10.1038/ncomms1606`.

[213] L. Mañosa, A. Planes, E. Vives, E. Bonnot, and R. Romero, "The use of shape memory alloys for mechanical refrigeration", *Functional Materials Letters*, vol. 02, no. 02, pp. 73–78, 2009. DOI: `10.1142/s1793604709000594`.

[214] A. Smith, C. R. Bahl, R. Bjørk, K. Engelbrecht, K. K. Nielsen, and N. Pryds, "Materials challenges for high performance magnetocaloric refrigeration devices", *Advanced Energy Materials*, vol. 2, no. 11, pp. 1288–1318, 2012. DOI: `10.1002/aenm.201200167`.

[215] P. Nordblad, "Magnetocaloric materials: Strained relations", *Nature Materials*, vol. 12, no. 1, pp. 11–12, 2012. DOI: `10.1038/nmat3516`.

[216] V. I. Zverev, A. M. Tishin, and M. D. Kuz'min, "The maximum possible magnetocaloric ΔT effect", *J. Appl. Phys.*, vol. 107, no. 4, p. 043 907, 2010. DOI: `10.1063/1.3309769`.

[217] X. Moya, E. Defay, V. Heine, and N. D. Mathur, "Too cool to work", *Nat Phys*, vol. 11, no. 3, pp. 202–205, 2015. DOI: `10.1038/nphys3271`.

[218] T. Correia and Q. Zhang, Eds., *Electrocaloric materials*. Springer Berlin Heidelberg, 2014, ISBN: 978-3-642-40264-7. DOI: `10.1007/978-3-642-40264-7`.

[219] M. Valant, "Electrocaloric materials for future solid-state refrigeration technologies", *Progress in Materials Science*, vol. 57, no. 6, pp. 980–1009, 2012. DOI: 10.1016/j.pmatsci.2012.02.001.

[220] M. Ožbolt, A. Kitanovski, J. Tušek, and A. Poredoš, "Electrocaloric refrigeration: Thermodynamics, state of the art and future perspectives", *International Journal of Refrigeration*, vol. 40, pp. 174–188, 2014. DOI: 10.1016/j.ijrefrig.2013.11.007.

[221] G. Zhang, Q. Li, H. Gu, S. Jiang, K. Han, M. R. Gadinski, M. A. Haque, Q. Zhang, and Q. Wang, "Ferroelectric polymer nanocomposites for room-temperature electrocaloric refrigeration", *Advanced Materials*, vol. 27, no. 8, pp. 1450–1454, 2015. DOI: 10.1002/adma.201404591.

[222] Y. Liu, J. F. Scott, and B. Dkhil, "Direct and indirect measurements on electrocaloric effect: Recent developments and perspectives", *Applied Physics Reviews*, vol. 3, no. 3, p. 031 102, 2016. DOI: 10.1063/1.4958327.

[223] Z. Kutnjak, B. Rožič, and R. Pirc, "Electrocaloric effect: Theory, measurements, and applications", *Wiley Encyclopedia of Electrical and Electronics Engineering*, 2015.

[224] E. Bonnot, R. Romero, L. Mañosa, E. Vives, and A. Planes, "Elastocaloric effect associated with the martensitic transition in shape-memory alloys", *Phys. Rev. Lett.*, vol. 100, no. 12, 2008. DOI: 10.1103/physrevlett.100.125901.

[225] M. Annaorazov, S. Nikitin, A. Tyurin, S. Akopyan, and R. Myndyev, "Heat pump cycles based on the AF–F transition in Fe–Rh alloys induced by tensile stress", *International Journal of Refrigeration*, vol. 25, no. 8, pp. 1034–1042, 2002. DOI: 10.1016/s0140-7007(02)00028-2.

[226] J Quarini and A Prince, "Solid state refrigeration: Cooling and refrigeration using crystalline phase changes in metal alloys", *Proceedings of the Institution of Mechanical Engineers, Part C: Journal of Mechanical Engineering Science*, vol. 218, no. 10, pp. 1175–1179, 2004. DOI: 10.1243/0954406042369062.

[227] C Rodriguez and L. Brown, "The thermal effect due to stress-induced martensite formation in β-CuAlNi single crystals", *Metallurgical and Materials Transactions A*, vol. 11, no. 1, pp. 147–150, 1980.

[228] L. Mañosa, S. Jarque-Farnos, E. Vives, and A. Planes, "Large temperature span and giant refrigerant capacity in elastocaloric Cu-Zn-Al shape memory alloys", *Applied Physics Letters*, vol. 103, no. 21, p. 211 904, 2013. DOI: 10.1063/1.4832339.

[229] F. Xiao, T. Fukuda, and T. Kakeshita, "Inverse elastocaloric effect in a Ti-Ni alloy containing aligned coherent particles of Ti_3Ni_4", *Scripta Materialia*, vol. 124, pp. 133–137, 2016. DOI: 10.1016/j.scriptamat.2016.07.016.

[230] P. Álvarez-Alonso, C. Aguilar-Ortiz, E. Villa, A. Nespoli, H. Flores-Zúñiga, and V. Chernenko, "Conventional and inverse elastocaloric effect in Ni-Fe-Ga and Ni-Mn-Sn ribbons", *Scripta Materialia*, vol. 128, pp. 36–40, 2017. DOI: `10.1016/j.scriptamat.2016.09.033`.

[231] J. Tušek, K. Engelbrecht, and N. Pryds, "Elastocaloric effect of a Ni-Ti plate to be applied in a regenerator-based cooling device", *Science and Technology for the Built Environment*, vol. 22, no. 5, pp. 489–499, 2016. DOI: `10.1080/23744731.2016.1176809`.

[232] L. C. Brown, "The thermal effect in pseudoelastic single crystals of β-CuZnSn", *Metallurgical Transactions A*, vol. 12, no. 8, pp. 1491–1494, 1981. DOI: `10.1007/bf02643695`.

[233] F. Xiao, T. Fukuda, and T. Kakeshita, "Significant elastocaloric effect in a Fe-31.2Pd (at. %) single crystal", *Appl. Phys. Lett.*, vol. 102, no. 16, p. 161 914, 2013. DOI: `10.1063/1.4803168`.

[234] F. Xiao, T. Fukuda, T. Kakeshita, and X. Jin, "Elastocaloric effect by a weak first-order transformation associated with lattice softening in an Fe-31.2Pd (at.%) alloy", *Acta Materialia*, vol. 87, pp. 8–14, 2015. DOI: `10.1016/j.actamat.2015.01.004`.

[235] F. Xiao, M. Jin, J. Liu, and X. Jin, "Elastocaloric effect in $Ni_{50}Fe_{19}Ga_{27}Co_4$ single crystals", *Acta Materialia*, vol. 96, pp. 292–300, 2015. DOI: `10.1016/j.actamat.2015.05.054`.

[236] Y. Xu, B. Lu, W. Sun, A. Yan, and J. Liu, "Large and reversible elastocaloric effect in dual-phase $Ni_{54}Fe_{19}Ga_{27}$ superelastic alloys", *Appl. Phys. Lett.*, vol. 106, no. 20, p. 201 903, 2015. DOI: `10.1063/1.4921531`.

[237] B. Lu, F. Xiao, A. Yan, and J. Liu, "Elastocaloric effect in a textured polycrystalline Ni-Mn-In-Co metamagnetic shape memory alloy", *Applied Physics Letters*, vol. 105, no. 16, p. 161 905, 2014. DOI: `10.1063/1.4899147`.

[238] W. Sun, J. Liu, B. Lu, Y. Li, and A. Yan, "Large elastocaloric effect at small transformation strain in $Ni_{45}Mn_{44}Sn_{11}$ metamagnetic shape memory alloys", *Scripta Materialia*, vol. 114, pp. 1–4, 2016. DOI: `10.1016/j.scriptamat.2015.11.021`.

[239] Z. Xie, G. Sebald, and D. Guyomar, "Comparison of direct and indirect measurement of the elastocaloric effect in natural rubber", *Appl. Phys. Lett.*, vol. 108, no. 4, p. 041 901, 2016. DOI: `10.1063/1.4940378`.

[240] E. V. Morozov, D. S. Kuchin, V. V. Koledov, and V. G. Shavrov, "Solid state cooling based on elastocaloric effect in latex rubber", *Materials Science Forum*, vol. 845, pp. 73–76, 2016. DOI: `10.4028/www.scientific.net/msf.845.73`.

[241] H. Schmid, "On ferrotoroidics and electrotoroidic, magnetotoroidic and piezotoroidic effects", *Ferroelectrics*, vol. 252, no. 1, pp. 41–50, 2001. DOI: `10.1080/00150190108016239`.

[242] T. Castán, A. Planes, and A. Saxena, "Thermodynamics of ferrotoroidic materials: Toroidocaloric effect", *Phys. Rev. B*, vol. 85, no. 14, 2012. DOI: 10.1103/physrevb.85.144429.

[243] A. Saxena and A. Planes, Eds., *Mesoscopic phenomena in multifunctional materials*. Springer Berlin Heidelberg, 2014, ISBN: 978-3-642-55375-2. DOI: 10.1007/978-3-642-55375-2.

[244] M. M. Vopson, "The multicaloric effect in multiferroic materials", *Solid State Communications*, vol. 152, no. 23, pp. 2067–2070, 2012. DOI: 10.1016/j.ssc.2012.08.016.

[245] M. M. Vopson, "Theory of giant-caloric effects in multiferroic materials", *Journal of Physics D: Applied Physics*, vol. 46, no. 34, p. 345 304, 2013. DOI: 10.1088/0022-3727/46/34/345304.

[246] H. Meng, B. Li, W. Ren, and Z. Zhang, "Coupled caloric effects in multiferroics", *Physics Letters A*, vol. 377, no. 7, pp. 567–571, 2013. DOI: 10.1016/j.physleta.2012.12.033.

[247] S. Patel, A. Chauhan, and R. Vaish, "Multiple caloric effects in ($Ba_{0.865}Ca_{0.135}$ $Zr_{0.1089}Ti_{0.8811}Fe_{0.01}$)$O_3$ ferroelectric ceramic", *Appl. Phys. Lett.*, vol. 107, no. 4, p. 042 902, 2015. DOI: 10.1063/1.4927558.

[248] H. Ursic, V. Bobnar, B. Malic, C. Filipic, M. Vrabelj, S. Drnovsek, Y. Jo, M. Wencka, and Z. Kutnjak, "A multicaloric material as a link between electrocaloric and magnetocaloric refrigeration", *Scientific Reports*, vol. 6, p. 26 629, 2016. DOI: 10.1038/srep26629.

[249] G. V. Brown, "Magnetic heat pumping near room temperature", *J. Appl. Phys.*, vol. 47, no. 8, p. 3673, 1976. DOI: 10.1063/1.323176.

[250] U. Plaznik, J. Tušek, A. Kitanovski, and A. Poredoš, "Numerical and experimental analyses of different magnetic thermodynamic cycles with an active magnetic regenerator", *Applied Thermal Engineering*, vol. 59, no. 1-2, pp. 52–59, 2013. DOI: 10.1016/j.applthermaleng.2013.05.019.

[251] A. Kitanovski, U. Plaznik, J. Tušek, and A. Poredoš, "New thermodynamic cycles for magnetic refrigeration", *International Journal of Refrigeration*, vol. 37, pp. 28–35, 2014. DOI: 10.1016/j.ijrefrig.2013.05.014.

[252] A. Rowe, "Thermodynamics of active magnetic regenerators: Part I", *Cryogenics*, vol. 52, no. 2-3, pp. 111–118, 2012. DOI: 10.1016/j.cryogenics.2011.09.005.

[253] A. Rowe, "Thermodynamics of active magnetic regenerators: Part II", *Cryogenics*, vol. 52, no. 2-3, pp. 119–128, 2012. DOI: 10.1016/j.cryogenics.2011.09.007.

[254] J. Tušek, A. Kitanovski, and A. Poredoš, "Geometrical optimization of packed-bed and parallel-plate active magnetic regenerators", *International Journal of Refrigeration*, vol. 36, no. 5, pp. 1456–1464, 2013. DOI: 10.1016/j.ijrefrig.2013.04.001.

[255] J. Tušek, A. Kitanovski, S. Zupan, I. Prebil, and A. Poredoš, "A comprehensive experimental analysis of gadolinium active magnetic regenerators", *Applied Thermal Engineering*, vol. 53, no. 1, pp. 57–66, 2013. DOI: `10.1016/j.applthermaleng.2013.01.015`.

[256] K. Bartholomé, T. Hess, A. Mahlke, and J. König, "New concept for magnetocaloric heat pumps based on thermal diodes and latent heat transfer", in *7th International Conference on Magnetic Refrigeration at Room Temperature (Thermag VII). Proceedings: Turin, Italy, September 11-14, 2016.*, IIF-IIR, 2016, ISBN: 9782362150166.

[257] J. König and K. Bartholomé, "Klimatisierungseinrichtung mit zumindest einem Wärmerohr, insbesondere Thermosiphon", Patent DE102014010476 B3, Dec. 2015. URL: `https://www.google.de/patents/DE102014010476B3`.

[258] U. Tomc, J. Tušek, A. Kitanovski, and A. Poredoš, "A new magnetocaloric refrigeration principle with solid-state thermoelectric thermal diodes", *Applied Thermal Engineering*, vol. 58, no. 1-2, pp. 1–10, 2013. DOI: `10.1016/j.applthermaleng.2013.03.063`.

[259] D. Silva, B. Bordalo, A. Pereira, J. Ventura, and J. Araújo, "Solid state magnetic refrigerator", *Applied Energy*, vol. 93, pp. 570–574, 2012. DOI: `10.1016/j.apenergy.2011.12.002`.

[260] S. L. Ghirlanda, S. Kim, C. F. Hernandez, M. M. Rahman, and S. Bhansali, "Simulation and experimental validation of a magnetocaloric microcooler", in *Heat Transfer, Volume 3*, ASME International, 2006. DOI: `10.1115/imece2006-15358`.

[261] S. Kim, B. Bethala, S. Ghirlanda, S. N. Sambandam, and S. Bhansali, "Design and fabrication of a magnetocaloric microcooler", in *Microelectromechanical Systems*, ASME International, 2005. DOI: `10.1115/imece2005-82720`.

[262] S. Kim, S. Ghirlanda, C. Adams, B. Bethala, S. N. Sambandam, and S. Bhansali, "Design, fabrication and thermal characterization of a magnetocaloric microcooler", *International Journal of Energy Research*, vol. 31, no. 6-7, pp. 717–727, 2007. DOI: `10.1002/er.1287`.

[263] A. Pereira, J. Oliveira, J. Soares, J. Ventura, J. Sousa, and J. Araújo, "Simulations of refrigeration on integrated circuits using micro-channels", *Journal of Non-Crystalline Solids*, vol. 354, no. 47-51, pp. 5295–5297, 2008. DOI: `10.1016/j.jnoncrysol.2008.06.122`.

[264] A. M. Pereira, J. C. Soares, J. Ventura, J. B. Sousa, J. P. Araujo, and J. C.R. E. Oliveira, "Influence of micro-channel shape and magnetic material on the magneto-refrigeration process of integrated circuits", *Journal of Nanoscience and Nanotechnology*, vol. 10, no. 4, pp. 2590–2593, 2010. DOI: `10.1166/jnn.2010.1421`.

[265] D. J. Silva, B. D. Bordalo, A. M. Pereira, J. Ventura, J. C.R. E. Oliveira, and J. P. Araújo, "The effect of coolants on the performance of magnetic micro-refrigerators", *Journal of Nanoscience and Nanotechnology*, vol. 14, no. 6, pp. 4337–4340, 2014. DOI: `10.1166/jnn.2014.8205`.

[266] H. Gu, X. Qian, X. Li, B. Craven, W. Zhu, A. Cheng, S. C. Yao, and Q. M. Zhang, "A chip scale electrocaloric effect based cooling device", *Appl. Phys. Lett.*, vol. 102, no. 12, p. 122 904, 2013. DOI: `10.1063/1.4799283`.

[267] R. I. Epstein and K. J. Malloy, "Electrocaloric devices based on thin-film heat switches", *J. Appl. Phys.*, vol. 106, no. 6, p. 064 509, 2009. DOI: `10.1063/1.3190559`.

[268] Y. S. Ju, "Solid-state refrigeration based on the electrocaloric effect for electronics cooling", *Journal of Electronic Packaging*, vol. 132, no. 4, p. 041 004, 2010. DOI: `10.1115/1.4002896`.

[269] H. Gu, B. Craven, X. Qian, X. Li, A. Cheng, and Q. M. Zhang, "Simulation of chip-size electrocaloric refrigerator with high cooling-power density", *Appl. Phys. Lett.*, vol. 102, no. 11, p. 112 901, 2013. DOI: `10.1063/1.4796184`.

[270] M. Schmidt, S.-M. Kirsch, S. Seelecke, and A. Schütze, "Elastocaloric cooling: From fundamental thermodynamics to solid state air conditioning", *Science and Technology for the Built Environment*, vol. 22, no. 5, pp. 475–488, 2016. DOI: `10.1080/23744731.2016.1186423`.

[271] S. Qian, J. Ling, Y. Hwang, R. Radermacher, and I. Takeuchi, "Thermodynamics cycle analysis and numerical modeling of thermoelastic cooling systems", *International Journal of Refrigeration*, vol. 56, pp. 65–80, 2015. DOI: `10.1016/j.ijrefrig.2015.04.001`.

[272] E. H. Schiller, "Heat engine driven by shape memory alloys: Prototyping and design", Master's thesis, Virginia Polytechnic Institute and State University, 2002.

[273] R. M. Banks, "Energy conversion system", Patent US 3913326 A, Oct. 1975. URL: `https://www.google.ch/patents/US3913326`.

[274] J. J. Hugenroth, "Solid phase change refrigeration", Patent US 6367281 B1, Apr. 2002. URL: `https://patents.google.com/patent/US6367281B1/en`.

[275] G. L. Quarini, "Solid state cooling device", Patent WO 2002084185 A1, Oct. 2002. URL: `https://www.google.com/patents/WO2002084185A1?cl=en`.

[276] I. Takeuchi. (2016). Compact thermoelastic cooling system – 2016 building technologies office peer review, URL: `http://energy.gov/sites/prod/files/2016/04/f30/312109_Takeuchi_040616-950.pdf` (visited on 08/19/2016).

[277] S. Qian, Y. Wu, J. Ling, J. Muehlbauer, Y. Hwang, I. Takeuchi, and R. Radermacher, "Design, development and testing of a compressive thermoelastic cooling prototype", in *24th International Congress of Refrigeration (ICR2015), Yokohama, Japan*, 2015.

[278] S. Fähler and S. Fleischer. (2012). DFG Priority Programme 1599 – Caloric Effects in Ferroic Materials: New Concepts for Cooling, URL: http://www.ferroiccooling.de (visited on 08/19/2016).

[279] M. Schmidt, A. Schütze, and S. Seelecke, "Cooling efficiencies of a NiTi-based cooling process", in *Volume 1: Development and Characterization of Multifunctional Materials; Modeling, Simulation and Control of Adaptive Systems; Integrated System Design and Implementation*, ASME International, 2013. DOI: 10.1115/smasis2013-3249.

[280] A. L. Browne, M. Wittorf, N. L. Johnson, P. B. Usoro, P. W. Alexander, J. H. Brown, and X. Gao, "Heat transport system and method", Patent US 8511082 B2, Aug. 2013. URL: https://patents.google.com/patent/US8511082B2/en.

[281] J. Cui, I. Takeuchi, M. Wuttig, Y. Wu, R. Radermacher, Y. Hwang, and J. Muehlbauer, "Thermoelastic cooling", Patent US 20120273158 A1, Nov. 2012. URL: https://patents.google.com/patent/US20120273158A1/en.

[282] S. Ikegami, Y. Makino, K. Yasuo, H. Kim, M. Kojima, M. Okumoto, C. Piao, and L. Jiang, "Air conditioning device", Patent WO 2014122702 A1, Aug. 2014. URL: https://patents.google.com/patent/WO2014122702A1/en.

[283] S. Qian, J. Ling, Y. Hwang, and R. Radermacher, "Dynamic performance of a compression thermoelastic cooling air-conditioner under cyclic operation mode", in *International Refrigeration and Air Conditioning Conference*, Purdue University – Purdue e-Pubs, 2014, p. 2244. URL: http://docs.lib.purdue.edu/iracc/1411/.

[284] S. Qian, A. Alabdulkarem, J. Ling, J. Muehlbauer, Y. Hwang, R. Radermacher, and I. Takeuchi, "Performance enhancement of a compressive thermoelastic cooling system using multi-objective optimization and novel designs", *International Journal of Refrigeration*, vol. 57, pp. 62–76, 2015. DOI: 10.1016/j.ijrefrig.2015.04.012.

[285] S. Qian, J. Ling, J. Muehlbauer, Y. Hwang, and R. Radermacher, "Study on high efficient heat recovery cycle for solid-state cooling", *International Journal of Refrigeration*, vol. 55, pp. 102–119, 2015. DOI: 10.1016/j.ijrefrig.2015.03.023.

[286] R. K. Radermacher, I. Takeuchi, Y. Hwang, Y. Wu, S. Qian, and J. Ling, "Solid-state heating or cooling systems, devices, and methods", Patent US 20160084544 A1, Mar. 2016. URL: https://patents.google.com/patent/US20160084544A1/en.

[287] S. Qian, Y. Geng, Y. Wang, J. Muehlbauer, J. Ling, Y. Hwang, R. Radermacher, and I. Takeuchi, "Design of a hydraulically driven compressive elastocaloric cooling system", *Science and Technology for the Built Environment*, vol. 22, no. 5, pp. 500–506, 2016. DOI: `10.1080/23744731.2016.1171630`.

[288] M. Schmidt, A. Schütze, and S. Seelecke, "Experimental investigation on the efficiency of a control dependent NiTi-based cooling process", in *Volume 2: Mechanics and Behavior of Active Materials; Integrated System Design and Implementation; Bioinspired Smart Materials and Systems; Energy Harvesting*, ASME International, 2014. DOI: `10.1115/smasis2014-7561`.

[289] M. Schmidt, A. Schütze, and S. Seelecke, "Scientific test setup for investigation of shape memory alloy based elastocaloric cooling processes", *International Journal of Refrigeration*, vol. 54, pp. 88–97, 2015. DOI: `10.1016/j.ijrefrig.2015.03.001`.

[290] M. Schmidt, A. Schütze, and S. Seelecke, "Experimentelle untersuchung elastokalorischer kühlprozesse", *Tm - Technisches Messen*, vol. 83, no. 4, 2016. DOI: `10.1515/teme-2015-0110`.

[291] J. Tušek, K. Engelbrecht, D. Eriksen, S. Dall'Olio, J. Tušek, and N. Pryds, "A regenerative elastocaloric heat pump", *Nature Energy*, vol. 1, p. 16 134, 2016. DOI: `10.1038/nenergy.2016.134`.

[292] J. Tušek, K. Engelbrecht, R. Millán-Solsona, L. Mañosa, E. Vives, L. P. Mikkelsen, and N. Pryds, "The elastocaloric effect: A way to cool efficiently", *Advanced Energy Materials*, vol. 5, no. 13, p. 1 500 361, 2015. DOI: `10.1002/aenm.201500361`.

[293] J. Ullrich, M. Schmidt, A. Schütze, A. Wieczorek, J. Frenzel, G. Eggeler, and S. Seelecke, "Experimental investigation and numerical simulation of the mechanical and thermal behavior of a superelastic shape memory alloy beam during bending", in *Volume 2: Mechanics and Behavior of Active Materials; Integrated System Design and Implementation; Bioinspired Smart Materials and Systems; Energy Harvesting*, ASME International, 2014. DOI: `10.1115/smasis2014-7619`.

[294] H. Ossmer, F. Wendler, M. Gueltig, F. Lambrecht, S. Miyazaki, and M. Kohl, "Energy-efficient miniature-scale heat pumping based on shape memory alloys", *Smart Mater. Struct.*, vol. 25, no. 8, p. 085 037, 2016. DOI: `10.1088/0964-1726/25/8/085037`.

[295] H. Ossmer, S. Miyazaki, and M. Kohl, "The elastocaloric effect in TiNi-based foils", *Materials Today: Proceedings*, vol. 2, S971–S974, 2015. DOI: `10.1016/j.matpr.2015.07.443`.

[296] C. Megnin and M. Kohl, "Shape memory alloy microvalves for a fluidic control system", *Journal of Micromechanics and Microengineering*, vol. 24, no. 2, p. 025 001, 2013. DOI: `10.1088/0960-1317/24/2/025001`.

[297] G. Tan, Y. Liu, P. Sittner, and M. Saunders, "Lüders-like deformation associated with stress-induced martensitic transformation in NiTi", *Scripta Materialia*, vol. 50, no. 2, pp. 193–198, 2004. DOI: `10.1016/j.scriptamat.2003.09.018`.

[298] L. C. Brinson, I. Schmidt, and R. Lammering, "Stress-induced transformation behavior of a polycrystalline NiTi shape memory alloy: Micro and macromechanical investigations via in situ optical microscopy", *Journal of the Mechanics and Physics of Solids*, vol. 52, no. 7, pp. 1549–1571, 2004. DOI: `10.1016/j.jmps.2004.01.001`.

[299] H. Ossmer, F. Lambrecht, M. Gültig, C. Chluba, E. Quandt, and M. Kohl, "Evolution of temperature profiles in TiNi films for elastocaloric cooling", *Acta Materialia*, vol. 81, pp. 9–20, 2014. DOI: `10.1016/j.actamat.2014.08.006`.

[300] H. Ossmer, C. Chluba, M. Gueltig, E. Quandt, and M. Kohl, "Local evolution of the elastocaloric effect in TiNi-based films", *Shap. Mem. Superelasticity*, vol. 1, no. 2, pp. 142–152, 2015. DOI: `10.1007/s40830-015-0014-3`.

[301] H. Ossmer, C. Chluba, S. Kauffmann-Weiss, E. Quandt, and M. Kohl, "TiNi-based films for elastocaloric microcooling — fatigue life and device performance", *APL Mater.*, vol. 4, no. 6, p. 064 102, 2016. DOI: `10.1063/1.4948271`.

[302] M. Kazeminezhad and A. K. Taheri, "An experimental investigation on the deformation behavior during wire flat rolling process", *Journal of Materials Processing Technology*, vol. 160, no. 3, pp. 313–320, 2005. DOI: `10.1016/j.jmatprotec.2004.06.020`.

[303] M. Mehran, "Elastokalorische Wärmepumpe – Konstruktion und Bau eines Demonstrators", Master's thesis, Karlsruhe Institute of Technology, 2014.

[304] F. Wendler, H. Ossmer, C. Chluba, E. Quandt, and M. Kohl, "Phase-field simulation of elastocaloric cooling in sma films", *To be published*, 2016.

[305] D. Chung, "Thermal interface materials", *Journal of Materials Engineering and Performance*, vol. 10, no. 1, pp. 56–59, 2001. DOI: `10.1361/105994901770345358`.

[306] J Barth, B Krevet, and M Kohl, "A bistable shape memory microswitch with high energy density", *Smart Materials and Structures*, vol. 19, no. 9, p. 094 004, 2010. DOI: `10.1088/0964-1726/19/9/094004`.

[307] J. Barth, C. Megnin, and M. Kohl, "A bistable shape memory alloy microvalve with magnetostatic latches", *Journal of Microelectromechanical Systems*, vol. 21, no. 1, pp. 76–84, 2012. DOI: `10.1109/jmems.2011.2174428`.

[308] H. Ossmer, S. Miyazaki, and M. Kohl, "Elastocaloric heat pumping using a shape memory alloy foil device", in *2015 Transducers - 2015 18th International Conference on Solid-State Sensors, Actuators and Microsystems (TRANSDUCERS)*, Institute of Electrical & Electronics Engineers (IEEE), 2015. DOI: `10.1109/transducers.2015.7181026`.

[309] T. Grund, R. Guerre, M. Despont, and M. Kohl, "Transfer bonding technology for batch fabrication of SMA microactuators", *The European Physical Journal Special Topics*, vol. 158, no. 1, pp. 237–242, 2008. DOI: `10.1140/epjst/e2008-00681-3`.

[310] R. L. de Miranda, C Zamponi, and E Quandt, "Fabrication of TiNi thin film stents", *Smart Materials and Structures*, vol. 18, no. 10, p. 104 010, 2009. DOI: `10.1088/0964-1726/18/10/104010`.

[311] F. Brüderlin, "Design of a regeneration-based elastocaloric microcooling device", Master's thesis, Karlsruhe Institute of Technology, 2016.

[312] F. Mugele and J.-C. Baret, "Electrowetting: From basics to applications", *Journal of Physics: Condensed Matter*, vol. 17, no. 28, R705–R774, 2005. DOI: `10.1088/0953-8984/17/28/r01`.

[313] I. Barbulovic-Nad, H. Yang, P. S. Park, and A. R. Wheeler, "Digital microfluidics for cell-based assays", *Lab on a Chip*, vol. 8, no. 4, p. 519, 2008. DOI: `10.1039/b717759c`.